MACHINE LEARNING-EMPOWERED, ULTRASONIC GUIDED WAVE-BASED TESTING AND EVALUATION METHODS FOR RAILWAY TRACKS

DANG DAZHI

PhD

The Hong Kong Polytechnic University

2025

The Hong Kong Polytechnic University

Department of Civil and Environmental Engineering

Machine Learning-Empowered, Ultrasonic Guided Wave-Based Testing And Evaluation Methods For Railway Tracks

DANG Dazhi

A thesis submitted in partial fulfillment of the requirements for the degree of

Doctor of Philosophy

May 2025

CERTIFICATE OF ORIGINALITY

I hereby declare that this thesis is my own work and that, to the best of my knowledge and belief, it reproduces no material previously published or written, nor material that has been accepted for the award of any other degree or diploma, except where due acknowledgement has been made in the text.

_____ (Signed)

DANG Dazhi (Name of student)

ABSTRACT

The safe and efficient operation of modern railway systems relies heavily on robust health monitoring and defect inspection techniques to mitigate potential risks posed by track defects. Traditional ultrasonic inspection methods, while effective in identifying various types of railway defects, face significant limitations in terms of inspection efficiency, sensor durability, and adaptability to the expanding scale of railway networks. Thereupon, this thesis addresses these challenges by developing advanced guided wave testing (GWT) techniques for railway track inspections, integrating innovative sensing technologies and state-of-the-art signal processing methods to enhance the accuracy, reliability, and efficiency of rail defect detection and health evaluation.

The research first addresses the challenge in ultrasonic sensing efficiency and reliability. To fully adapt to the harsh environment of railway on-site monitoring, a novel hybrid sensing system for railway GWT is first proposed in Chapter 3, combining piezoelectric (PZT) actuators and fiber Bragg grating (FBG) sensors to generate and detect ultrasonic guided waves (UGWs). This system leverages the inherent advantages of FBG sensors, including their electromagnetic interference (EMI) resistance, durability, and cost-effectiveness. A high-speed optical interrogation strategy based on edge filters is designed to optimize the performance of FBG sensors in capturing UGW signals. Numerical simulations using COMSOL Multiphysics and experimental validations are

conducted to demonstrate the system's effectiveness in detecting rail defects, with a particular focus on wave propagation characteristics and defect sensitivity. The results reveal that UGWs generated and received by the proposed hybrid system can propagate on the rail interface and are highly sensitive to rail geometric inconsistencies.

Building on this hybrid sensing system, this thesis introduced comprehensive defect detection and identification frameworks to overcome the challenges in features extraction posed by perplexing UGW signals. A defect detection and evaluation framework is introduced in Chapter 4, utilizing nonlinear autoregressive models with exogenous inputs (NARX) and a probabilistic damage-sensitive feature (DSF) derived from the probability density function (PDF) of network prediction errors. Experimental studies are conducted to validate the framework, with three different types of railway defects configured to generate training and testing datasets. The NARX models are optimized through hyperparameter fine-tuning, achieving high detection accuracy. Large-scale testing further validates the framework, demonstrating an overall accuracy of 98.0% and confirming its robustness and effectiveness in real-world applications.

For further defect identification, an orthogonal matching pursuit (OMP)-based method is developed in Chapter 5, incorporating a customized interfering reflection components (IRC) dictionary to reconstruct defect-related reflective waves. This method leverages the sparse representation capabilities of the OMP algorithm to accurately identify crack locations. Numerical investigations are first conducted to

verify the effectiveness of the proposed approach, followed by experimental validations on a railway track segment. The results show that the proposed method can accurately predict crack locations with fitting errors of less than 6 mm, highlighting its potential for practical engineering applications. Comparative studies further demonstrate the superiority of the IRC dictionary in improving defect identification accuracy.

Finally, Chapter 6 proposes a rapid railway track diagnosis approach, using pencil lead break (PLB)-induced ultrasound as a cost-effective and portable excitation source for on-site inspections. This method is combined with adversarial autoencoders (AAEs) to process and analyze the ultrasonic signals, enabling the detection of subtle changes indicative of rail defects. A probabilistic damage indicator based on the Jensen-Shannon Divergence (JSD) is developed to evaluate rail health status. The proposed approach is validated through comparative studies in both laboratory and field tests, achieving 95.5% accuracy for intact rails and 97.3% for defective ones. The results demonstrate the method's potential for on-site inspections, offering a practical solution for rapid and reliable rail defect detection.

The proposed methods in Chapter 4-6, though developed based on machine learning (ML) algorithms, are not label-dependent, making them suitable for prospective engineering applications.

In conclusion, this thesis makes significant contributions to the field of railway GWT

by addressing key research gaps in sensing instrumentation, signal processing, and defect detection methodologies. The proposed techniques offer more efficient, durable, and reliable inspection methods for railway tracks. The findings have the potential to revolutionize intelligent railway maintenance strategies, enhancing safety and reducing operational costs. Future work is recommended to further validate these methods under real-world conditions, explore their scalability for large-scale railway networks, and investigate their applicability to a wider range of defect types and sizes.

LIST OF PUBLICATIONS

Journal Papers

Dang, D. Z., Lai, C. C., Ni, Y. Q., et al. (2023). Image Classification-Based Defect Detection of Railway Tracks Using Fiber Bragg Grating Ultrasonic Sensors. *Applied Sciences*, *13*(1). (SCI Q1)

Dang, D. Z., Wang, Y. W., & Ni, Y. Q. (2024). Nonlinear autoregression-based non-destructive evaluation approach for railway tracks using an ultrasonic fiber Bragg grating array. *Construction and Building Materials*, *411*. (SCI Q1)

Dang, D. Z., Wang, Y. W., & Ni, Y. Q. (2025). A novel guided wave testing method for identifying rail web cracks using optical fiber Bragg grating sensing and orthogonal matching pursuit. *Measurement*, *243*. (SCI Q1)

Dang, D. Z., Su, B. Y., Wang, Y. W., et al. (2025). A pencil lead break-triggered, adversarial autoencoder-based approach for rapid and robust rail damage detection. *Engineering Applications of Artificial Intelligence, 150.* (SCI Q1)

Zhang, Y., **Dang, D. Z.**, Wang, Y. W., & Ni, Y. Q. (2024). Damage identification for railway tracks using ultrasound guided wave and hybrid probabilistic deep learning. *Construction and Building Materials*, *418*. (SCI Q1)

Conference Papers

Dang, D. Z., Wang, Y. W., & Ni, Y. Q. (2023). Ultrasonic Guided Waves-Based Nonlinear Autoregressive Defect Detection for Railway Tracks Using Fiber Bragg Grating Sensing. *Proceedings of the 14th International Workshop on Structural Health Monitoring, 12-14 September 2023, Stanford University, California, USA.*

Patents

Dang, D. Z., Wang, Y. W., & Ni, Y. Q. (2024). A rail inspection method, system, and terminal, (China Invention Patent No. ZL202410832604.6). China National Intellectual Property Administration.

Dang, D. Z., Wang, Y. W., & Ni, Y. Q. (2025). An ultrasonic guided wave detection method and detection system for identifying rail cracks, (submitted on Mar 28, 2025, pending for approval). China National Intellectual Property Administration.

ACKNOWLEDGEMENT

There are so many people who have helped and supported me during my Ph.D. studies, and I would only fear that the limited pages and flat words may not fully convey my sincere gratitude. Therefore, I would like to specifically acknowledge the following.

I would first express my sincere gratitude to my chief supervisor, Professor Yi-Qing Ni, for providing me with a research position in CNERC-Rail, for providing me with the opportunity to pursue my Ph.D. studies at PolyU, and for being responsible guiding me towards excellence with his abundant knowledge and experience. As a world-renowned researcher, Professor Yi-Qing Ni has been universally acknowledged for what he has achieved in academia. However, I would also highly appreciate and acknowledge his sharp mind and in-depth insights and prospectives in discovering future trends in the research area of railway engineering and structural health monitoring. It is my greatest honor to look up to Prof. Ni and work under his supervision, as a member of CNERC-Rail from which I learnt how to conduct proper research studies.

I would also like to appreciate Dr. You-Wu Wang, who has been serving as my co-supervisor. Dr. You-Wu Wang has been helping me with my research throughout the 3-year period of time that I spent at PolyU and for that I will always be grateful. Dr. You-Wu Wang has been consistently patient and responsible, and generously offered hospitality to me when I first arrived in Hong Kong. I genuinely wish him all the best

in future endeavors.

My sincere thanks also go to those who helped and accompanied me throughout my stay in Hong Kong: Dr. Wen-Qiang Liu, Dr. Si-Yi Chen, Dr. Yang Zhang, Dr. Wai Kei Ao, Mr. Yu-Ling Wang, Mr. En-Ze Rui, Dr. Xin Ye, Mr. Jia-Hao Lu, Mr. Qi-Fan Zhou, Mr. Yan-Ke Tan, Mr. Lei Yuan, Mr. Wei-Jia Zhang, Ms. Qi Zhu. Thanks for your kindest help and assistance, and for simply being such amazing friends and always being supportive. And I would also express my thanks to other dear colleagues and friends at PolyU who I fail to mention here due to the limited pages. It has been my pleasure to meet and work with you all.

Finally, I would give special thanks to my dearest family who have been giving me everlasting love and support. I feel the luckiest person to be surrounded with their unconditional love and support, which keeps encouraging me to go further on my journey.

TABLE OF CONTENTS

LIST OF FIGURES

LIST OF TABLES

LIST OF ABBREVIATIONS

2D-FFT	two-dimensional Fast Fourier Transform
AAE	adversarial autoencoder
AE	autoencoder
AR	autoregressive
ARX	autoregressive with exogenous inputs
BMP	basic matching pursuit
BWT	bulk wave testing
BPD	balanced photodetector
CNN	convolutional neural network
CS	compressive sensing
DAS	distributed acoustic sensing
DNN	deep neural network
DOF	distributed optical fiber
DSF	damage-sensitive feature
EDI	energy-based damage index
EMAT	electromagnetic acoustic transducer
EMI	electromagnetic interference
FBG	fiber Bragg grating
FC	fully connected

FEM	finite element modelling
GAN	generative adversarial network
GWT	guided wave testing
HHT	Hilbert-Huang transform
HT	Hilbert transform
IRC	interfering reflection components
JSD	Jensen-Shannon divergence
KLD	Kullback-Leibler divergence
LM	Levenberg-Marquardt
LSTM	Long-Short Time Memory
LTC	local temporal coherence
LUT	laser ultrasonic testing
MISO	multi-input single-output
ML	machine learning
MP	matching pursuit
MSE	mean square error
NARX	nonlinear autoregressive models with exogenous inputs
NDT & E	non-destructive testing and evaluation
NLP	natural language processing
OMP	orthogonal matching pursuit
PCA	principal component analysis

PCC	peak coherence change
PDF	probability density function
PLB	pencil lead break
PLC	Planar Lightwave Circuit
PZT	Lead Zirconate Titanate
QN	quasi-Newton
RMSE	root mean square error
RNN	recurrent neural network
SADA	semi-supervised adversarial adaptation
SAFE	semi-analytical finite element
SCE	sigmoid cross entropy
SCG	scaled conjugate gradient
SH	shear horizontal
SHM	structural health monitoring
SLDV	scanning laser Doppler vibrometer
SNR	signal/noise ratio
STFT	short-time Fourier transform
SVM	support vector machine
ToF	time of flight
TSTL	task similarity transfer learning
UGW	ultrasonic guided wave

WOMP	weak orthogonal matching pursuit
WT	wavelet transform

CHAPTER 1 INTRODUCTION

1.1. Research Background and Motivation

The railway system plays a significant role in the modern world, guaranteeing convenient and efficient communications to meet the increasing demand for travelling and daily transportation. The safe operation and maintenance of such massive transport systems rely heavily on robust and reliable monitoring and inspection routines to rule out potential risks of occurrence of incidents.

Railway tracks, as the heart of the railway system, are constantly subjected to intensive and frequent service loads under harsh environmental conditions. It has been extensively reported that railway track defects are often the predominant cause of railway incidents ranging from vibration noises to major derailments (Dang et al., 2023; Sandström & Ekberg, 2009). **Figure 1-1** demonstrates railway defects observed during offline inspection routines in Hong Kong, which raised safety alarm for railway maintenance and operation. Railway corrugations, as demonstrated in **Figure 1-1(a)**, are often the main cause for high-pitch wheel-rail noise which can interrupt ride comfort especially in subways. A severe figure crack had developed into a broken rail as shown in **Figure 1-1(b)**, which raised enormous safety risks. Although many railway defects may not undermine the overall structural integrity at an early-developing stage, they tend to grow rapidly causing severe safety risks (J. Chen et al., 2018; Q. Wu et al., 2019)

leaving insufficient time for railway maintenance to react before disastrous incidents take place. Therefore, an early-in-time diagnostic system should be implemented to rule out potential risks brought by rail defects, such as fatigue cracks and rail fracture. In this sense, researchers and engineers of the railway industry have been exploring solutions to achieve automatic and efficient rail defect detection and health evaluation. However, those early-stage defects are of such minimum dimensions that they cannot always be visibly detected in engineering applications.

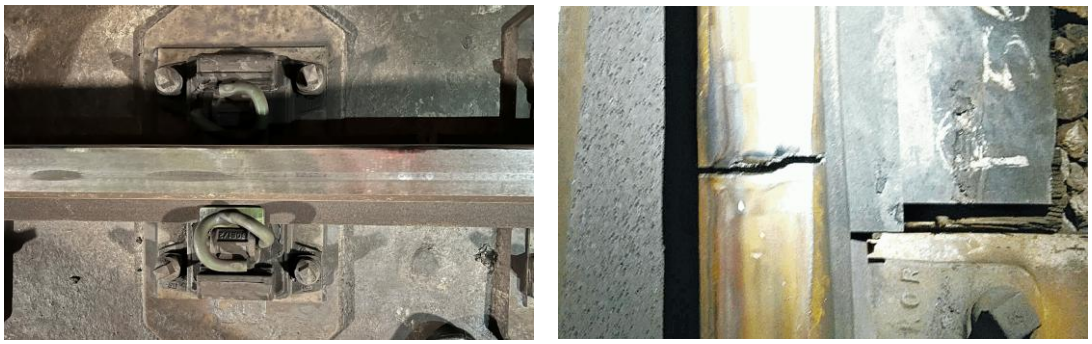

(a) (b)

Figure 1-1. Railway defects were discovered during site inspection. (a) rail corrugation near Diamond Hill Station, Tuen Ma Line, 2022; (b) rail head crack near Fo Tan depot, East Rail Line, 2017.

The recent development in non-destructive testing and evaluation (NDT & E) has enabled rapid and precise damage detection of railway damages without compromising structural integrity. Especially, ultrasound-based sensing methods have been widely studied and utilized on in-service railway lines as powerful defect inspectors (Bombarda et al., 2021; S. X. Chen et al., 2021; Pathak et al., 2019; Ramatlo et al., 2020). Ultrasonic sensors based on bulk wave testing (BWT) techniques are the most

used instruments, featuring high-precision inspection accuracies, which can effectively detect railway defects of various types. By integrating such sensors on portable hand-hold devices or mounting onto inspection vehicles, the inconsistency in material geometry can be intuitively revealed through the ultrasound scanning and imaging process. There have been successful BWT-based products, such as ultrasound inspection trolleys, which are currently being deployed on the subway and inter-city railway lines during offline hours.

However, the inspection efficiency of the current inspection methods still needs further improvement, considering the growing scale of modern railway lines. As mentioned, traditional BWT approaches rely on a scanning operation to cover a long-range railway line. The average inspection speed for a typical commercial inspection trolley is between 5 to 15 kilometers per hour, meaning that it could approximately take a month to complete the inspection of the railway line network for a middle-sized city. In contrast, guided wave testing (GWT) features long-range inspection capabilities, which is more suitable for railway engineering applications (Loveday & Wilcox, 2010). Ultrasonic guided waves (UGWs) can be excited and received via ultrasonic transducers. Unlike BWT which adopts a pulse-echo scheme, the pitch-catch mode is often deployed for GWT because UGWs can travel in the longitudinal direction of a rail and propagate for 10 to 1,000 meters depending on the specific configurations. The advancement in detecting range makes GWT a highly efficient tool for railway

inspections. Besides, it has been proven that UGWs are sensitive to various railway defects (Dang et al., 2024). Nevertheless, the challenges that prevent GWT from mass applications in railway inspection and monitoring can be concluded in 2 aspects: on the one hand, GWT requires more specified sensing instruments and configurations to generate guided waves propagating in longitudinal rails; on the other hand, the UGW signals are perplexing for analysis, due to the complex geometry of railway tracks resulting in multiple reflections.

First, **the efficiency and reliability of the ultrasonic sensing systems cannot meet the requirements for railway engineering**, which can be extremely demanding. The widely used piezoelectric sensors for railway online GWT are known to be easily affected by strong electromagnetic interference (EMI) of in-service railway lines (X. Sun et al., 2022). Due to this reason, the application for such sensing technique is limited to short-range offline inspection. Although electromagnetic shielding can increase the Signal/Noise ratio (SNR), the signal transmission via electric wires remains a major problem in field tests because the level of signal loss could be significant. In addition, piezoelectric sensors are typically expensive and fragile, which are not suitable for outdoor environments. On the other hand, optical fiber sensors, equipped with natural immunity to EMI, have prospective potential in railway monitoring projects. Currently such sensors have only been deployed to sense dynamic or static strain or temperature signal of railway tracks, with little research focusing on ultrasound

sensing applications. Recently, researchers have proposed optical Bragg grating (FBG) ultrasonic sensors, offering an innovative perspective to reveal damages on plate-like structures. Compared to traditional piezoelectric sensors, optical fiber sensors are more durable and cost-effective, but they rely heavily on high-speed optical interrogation techniques to demodulate and convert complex optical signals (e.g., optical intensity and wavelength) into comprehendible ultrasonic signals. In fact, to the best of the author's knowledge, it remains an unexplored area to study the feasibility of using optical sensors for railway GWT.

Second, **the signal processing and features extraction of UGW signals can be more challenging due to the perplexing waveforms**, compared to conventional BWT approaches. Although railway tracks are natural wave guides, it has been acknowledged that the complexity of rail geometry causes perplexing wave scattering and reflections at boundaries (K. Wang, Cao, et al., 2020); UGW signals collected from railway tracks are highly overlapped according to experimental findings by Z. Su et al. (2014) and such complex waveforms are almost uninterpretable, making it difficult to extract useful information that can reflect rail health status. As a result, commonly used damage-sensitive features (DSFs) lack generalization and representation of railway defects, such as waveform distortion, energy attenuation, and difference in time of flight (ToF). To address this issue, data-driven methods using machine learning (ML) models have been extensively researched to learn nonlinear representations of UGW signals

(Jamshidi et al., 2017; X. Wang, Liu, et al., 2022). Deep neural network (DNN) structures have been proved to have the capability of extracting hidden information of UGW signals to reveal structural damages. However, such automatic features extraction of DNN is based on a supervised learning manner, which leads to the third research gap addressed in this study.

Third, **despite the exceptional fitting performance, these ML models are label-dependent**, indicating that they require a manually labeled dataset for supervised training. However, most engineering scenarios will not meet this requirement due to the insufficiency in acquiring fully labeled datasets, especially when the amount of data is massive. For example, in the context of NDT for rails, the abundance of rail defect types brings inevitable difficulties in obtaining effective training data. Thereupon, the current challenge in this research lies in developing unsupervised ML methods to maximumly adapt to engineering applications, i.e., using clustering-based approaches (K. Wang, Zhang, et al., 2022). Extraordinarily complex models are often overfitted, which means that they may not possess generalizability. In contrast, developing rail health evaluation approaches based on unsupervised ML may overcome this challenge by introducing probabilistic analysis into defect detection and identification.

To address the research gaps discussed above, this study aims to explore comprehensive solutions towards online and offline GWT techniques ensuring overall integrity and reliability of the railway tracks. Advanced sensing technologies are first developed to

address the limitations of current PZT-dominant sensing instruments for railway GWT. Powerful ML algorithms are tailored to process and analyze the perplexing UGW signals, demonstrating railway health status. To this regard, DSFs are automatically extracted, and rail damage identification process can be carried out in an unsupervised manner. Both numerical and experimental validations are included in this research to support the proposed methodologies. The scalability and effectiveness of the methods proposed are tested and discussed in this thesis, bridging theoretical analysis, laboratory testing, and field applications. The long-term impact of this research will significantly contribute to intelligent railway maintenance by offering more efficient, durable, and generable railway inspection techniques, saving much labor cost.

1.2. Research Objectives

The main objectives of this research study are summarized as follows:

(1) To develop a guided wave inspection system for railway online monitoring based on optical fiber sensing technology, featuring high durability and reliability.

(2) To investigate effective rail damage detection and characterization methods based on the proposed sensing system in conjunction with high-performance machine learning models and signal processing techniques with exceptional robustness and generalizability.

(3) To develop GWT methods for offline rail inspections, using cost-effective and rapid ultrasound excitation sources for on-site operation, and machine learning techniques to characterize rail defects in a robust and accurate manner.

(4) To validate the proposed GWT methods via numerical modelling, laboratory experiments, and field tests.

1.3. Thesis Outline

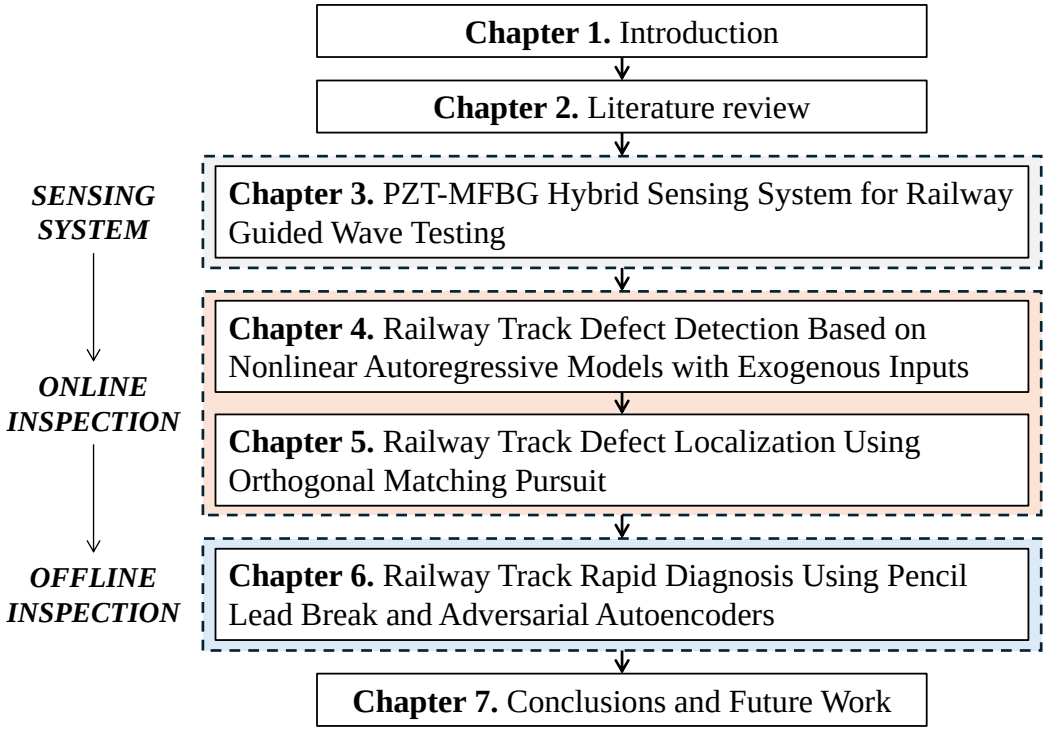

Figure 1-2. Thesis structure.

The thesis structure is demonstrated in **Figure 1-2**. This thesis is composed of 7 Chapters. The main contributions are included in Chapter 3, 4, 5, and 6, providing comprehensive solutions for railway GWT techniques from the aspects of sensing instrumentations, online monitoring techniques, and offline inspection techniques. The

detailed contents of each chapter are previewed as follows:

Chapter 1 introduces the research background, research objectives, and thesis outline in general.

Chapter 2 conducts a systematic review of recent advancement in the field of railway GWT technology, from sensing instrumentations to signal processing. An in-depth discussion session reflecting the research gaps is also included.

Chapter 3 proposes a hybrid sensing system for railway GWT using PZT as the actuator and FBG sensors as the ultrasound receiver. A multiplexing scheme for the FBG array is proposed based on edge filter interrogation techniques. A laboratory setup is first configured to demonstrate the effectiveness of the proposed sensing system, followed by a proof-of-concept simulation using COMSOL Multiphysics to conduct numerical investigations. The guided wave propagation mechanism and the directionality of FBG sensing are revealed through reconstructing the 3-D wave velocity field.

Chapter 4 demonstrates the application of the proposed hybrid sensing system in rail defect detection, using a novel defect detection method based on nonlinear autoregressive models. A specified probabilistic DSF is tailored to indicate rail health status, derived from the probability density function (PDF) of the network prediction errors. Experimental studies are conducted to verify the feasibility of the proposed method featuring various rail health status. A large-scale testing is also included further

proving the applicability and reliability of the proposed rail damage evaluation approach.

Chapter 5 is an extension of the contents introduced in Chapter 4, showcasing a novel rail defect identification method using the proposed sensing system, combined with an orthogonal matching pursuit (OMP)-based data processing technique. The characteristics of defect-related reflective wave mechanism are studied via finite element modelling. A dictionary composed of reflection components is proposed based on the findings through numerical simulations. The feasibility of the proposed method is validated on the numerical data of a 3-D railway segment and then further verified through experimental investigations. Comparative studies are also conducted to highlight the practical effectiveness of the method.

Chapter 6 proposes a novel and robust approach for offline rapid railway inspection, powered by an adversarial autoencoder (AAE) which learns effective representations of ultrasonic signals induced by pencil lead break (PLB). Then, a damage-sensitive indicator is developed based on the Jensen-Shannon Divergence (JSD) between the model output distributions of the baseline and an unknown signal. Both laboratory experiments and on-site verifications were carried out to validate the proposed approach. Further comparative studies are also conducted to demonstrate the adaptability and effectiveness of the proposed method against field testing environments.

Finally, Chapter 7 summarizes the research of this thesis and provides future prospectives regarding this research area. The significance of the study is also emphasized in this chapter.

CHAPTER 2 LITERATURE REVIEW

2.1. Ultrasonic Guided Waves in Railway Tracks

2.1.1. Bulk wave testing versus guided wave testing

A comparison between commonly used bulk wave testing (BWT) and guided wave testing (GWT) is schematically demonstrated in **Figure 2-1**. It is obvious that BWT approach generally requires a longitudinal scanning operation as the bulk wave only covers a specific transverse rail plane (Bombarda et al., 2021). Though BWT methods can present clear ultrasonic imaging of railway track defects and flaws, the inspection volume is limited by the probe position and location (Mićić et al., 2023). The defect size under detection should be above the half-wavelength level, therefore higher ultrasonic frequency bulk wave is usually applied when conducting BWT to railway tracks, which at the same time determines a shorter propagation range depending on the probe angle. For current engineering practices, manual inspection is the most adopted formality on railway sites, which requires experienced personnels equipped with handheld ultrasonic inspection instruments. Apart from that, ultrasonic probes are installed onto inspection vehicles to induce ultrasonic bulk wave on rail surface, but either approach cannot be efficiently carried out during operational period, especially considering the rapidly expanding size of the modern railway system.

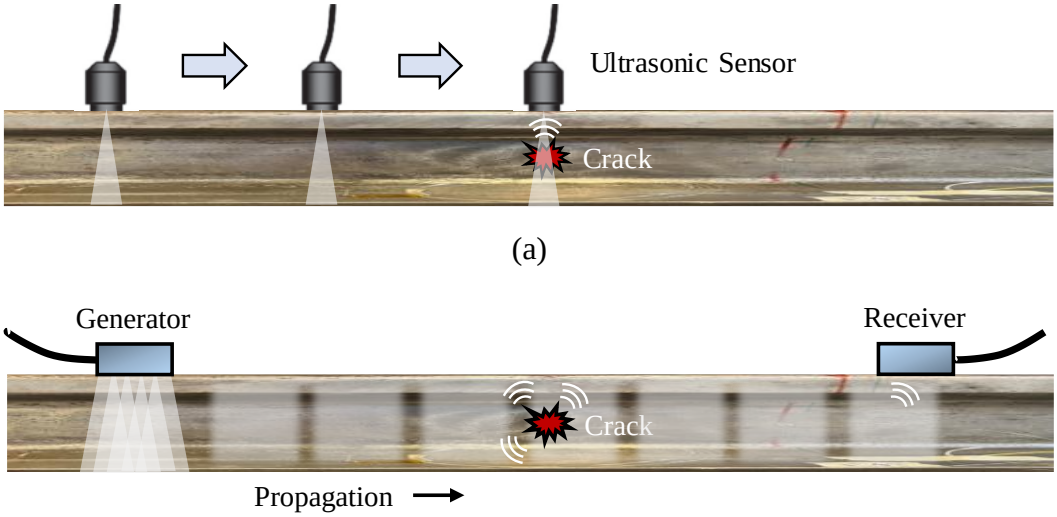

Figure 2-1. Comparison of (a) bulk wave inspection versus (b) guided wave inspection on the railway.

In comparison, GWT can cover a significantly longer range of rail segments for guided wave travels longitudinally. As shown in **Figure 2-1(b)** the UGW generated through multiple reflections and scatterings can sense the existence of railway defects which are revealed through analyzing signals picked up by the ultrasound receiver. The propagating route can last from meters to kilometers, according to successful attempts made by Loveday et al. (2020). Rail defects (mainly transverse cracks or squats) can be detected, located and prioritized in a pulse-echo configuration referring to EN 16729-3 (2018). It should be noted that the UGW generation should not be limited to the approach demonstrated in **Figure 2-1(b)**. Depending on the specific characteristics of the object being inspected (e.g., geometry and material), angle-beam excitation or comb excitation could also be chosen to effectively generate UGWs that cover the whole volume of the structure (Cawley, 2024; Rizzo et al., 2010).

Recent advances in GWT-based sensing systems have enabled the development of online monitoring of railway tracks. Pre-installed ultrasonic sensing instruments that are highly capable of generating and receiving UGWs can report potential railway defects of various kinds in a real-time manner.

2.1.2. Fundamentals of ultrasonic guided waves in railway tracks

UGW, when being deployed in the context of structural health monitoring, refers to ultrasonic mechanical wave propagating in structure media, featuring multi-modal, dispersive, and wave-attenuating behaviors (Mitra & Gopalakrishnan, 2016). The implementations of Lamb waves and Rayleigh waves have been extensively studied in the field of NDT (H. Lu et al., 2024; Rostami et al., 2020; Sha et al., 2021; X. Wang et al., 2010). Lamb waves are more generally used for defect detection of plate-like structures and shells bounded by stress free surfaces. While Rayleigh wave propagates near the free surface of the media and at higher frequency (Mitra & Gopalakrishnan, 2016), the most used scenarios are thicker plates or surface waves excited via certain configurations, for example, non-contact laser transduction (Masurkar et al., 2020).

However, the wave modes in railway tracks are much more complex. In most scenarios, it is difficult to excite single-mode guided waves that propagate in longitudinal rails. Numerous reflections and refractions against boundaries cause perplexing wave modes. Because of the complexity of wave modes in rails, researchers have innovatively

proposed diffuse ultrasonic waves-based methods to characterize the guided wave behaviors in railway tracks to diagnose the health status (X. Sun et al., 2022; K. Wang, Cao, et al., 2020). Having been proved effective, those methods have provided a novel prospective for guided wave-based inspections by comparing the waveforms acquired before and after the defect formation or development. It makes more sense to highlight signal processing than focusing on decoding the guided mode behaviors. Nevertheless, those methods lack generalizability when it comes to massive deployment on railway lines.

2.1.3. Mode selection of railway tracks

As introduced in previous sections, due to the multi-modal characteristics of UGWs in rail waveguides, it is critical to consider the selection of appropriate modes of propagation. The definition of an appropriate guided wave mode can differ in literature, but the common criteria include lower attenuation rate and concentrated energy in rail sections of interest (Loveday et al., 2020). Intuitively, the waves can travel further if the specified mode tends to attenuate slower in the longitudinal direction, which is highly desirable for GWT. Another key factor for model selection is to select guided wave modes that should interact with defects to be detected, located at certain parts of the rail section. For instance, some modes are dominated by rail head deformation thus reacting strongly from rail head defects. Thereupon, the mode shapes should be obtained priorly for mode selection.

It is easier to obtain the analytical solution of the dispersion characteristics of waveguides with simple cross section, such as cylinder, ellipse, and rectangle (Ge et al., 2022). Although rails are natural waveguides, the complexity of rail geometry inevitably causes much difficulty in computing modal shapes induced by guided waves. According to previous research on analysis of wave propagation (Shi et al., 2019; P. Zhang et al., 2021), the governing differential elasto-dynamic equations and associated boundary conditions should be first obtained followed by transforming into frequency-wavenumber domain. For a rail section, these equations are either too perplexing or impossible to format. Thereupon, numerical approaches have been studied to calculate dispersion properties of rails. Loveday (2012) summarized conventional finite element modelling (FEM) approaches, which basically follow 3 steps: 1) modelling a length of the rail segment with appropriate boundary conditions applied at each end; 2) obtaining the natural modes of the rail segment; 3) Obtaining the mode shapes while determining what fraction of a wavelength they correspond; 4) Obtaining the wavenumber-frequency dispersion curve by repeating the above procedures. The problem regarding this FEM configuration is that it is required to model various lengths of the rail to repeatedly obtain comprehensive dispersion results, which can be extremely time-consuming. Alternatively, semi-analytical finite element (SAFE) models have been proposed and used to compute dispersion properties of the railway tracks (Xing et al., 2020). This method has been universally acknowledged by researchers because only a bi-dimensional element discretization of the railway track cross section is required for

dispersion calculations (Xing et al., 2019), which has reduced the computational costs significantly. In addition, the SAFE approach has the advantage of avoiding the polynomial approximation of the displacement field.

Figure 2-2 demonstrates the dispersion analysis results via SAFE. The rail dispersion properties are modelled in COMSOL Multiphysics software. The nonlinear relations between the frequency and the wavenumber and the phase velocities are obtained and shown in the figure. To further demonstrate the nature of mode selection, the author chooses 3 modes at the frequency of 30 kHz, as shown in **Figure 2-2(b)**, and their corresponding mode shapes are shown in **Figure 2-2(c)**. Apparently, mode 1 is rail web-dominant; mode 2 is sensitive to rail foot displacement; mode 3 reflects rail head deformation. In engineering applications, it is vital to determine the types of defects to be detected, and the placement of transducers based on modal analysis. Although it is almost impossible to obtain single-mode UGW propagation, the purpose for mode selection based on SAFE is to maximize the proportion of modes desired to generate UGWs that are more sensitive to specific types of defects. It is also worth mentioning that mode 2 and 3 are symmetrical, which are usually priorly considered in practical applications. The SAFE method is also applicable for railway turnout featuring variable cross-sectional characteristics, which has been reported in the publication of R. Chen et al. (2021). By integrating a variety of cross sections with smooth change in geometry characteristics, a dispersive surface can be created to guide the mode selection process.

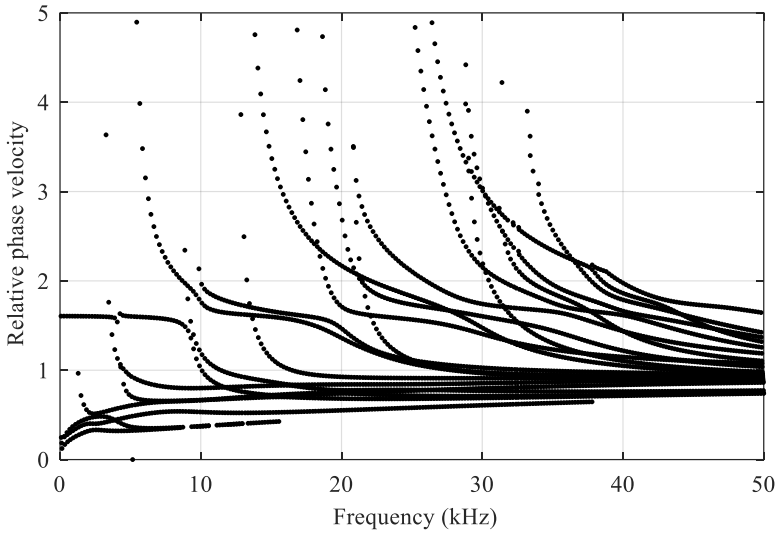

(a)

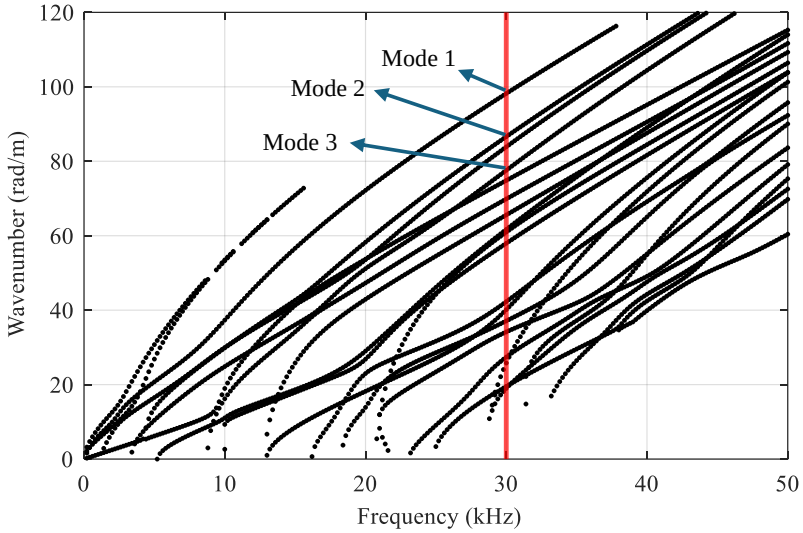

(b)

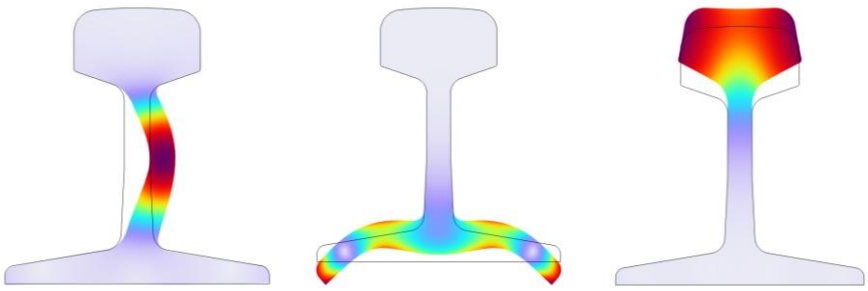

(c)

Figure 2-2. SAFE analysis of a BS100 standard railway track: (a) frequency-wavenumber curves; (b) frequency-group velocity curves; (c) selected modes shapes (from left to right: mode 1, mode 2, mode 3).

After obtaining the modal characteristics of the railway track, it is then important to determine the excitation strategy based on the selected mode. However, for railway tracks with such complex geometry, it is almost impossible to precisely excite a particular wave mode point of the dispersion curve. The phase velocity spectrum and frequency spectrum inevitably results in multiple modes existing simultaneously. Nevertheless, as Rose et al. (2012) have stated, "these are concerns, though, for another day". The common solution is to simply find the rail surface with the maximum degree of deformation and install sensors on or near that surface. This method has been adopted in most research work presented (Ramatlo et al., 2022; Xing et al., 2019, 2020; P. Zhang et al., 2021), which has been proved to be effective. As introduced in the work of R. Chen et al. (2021), the vertical displacement of finite element node for a specified mode is extracted and the node with the maximum amplitude is selected as the excitation position of the rail cross section. Similar concept has also been proposed by Xing et al. (2020). Shi et al. (2019) verified the selected modes by conducting FEM investigations and placed a signal pick-up array on the rail web with a fixed gap of 5 mm. The obtained signal included both time and spatial information, thus can be processed via two-dimensional Fast Fourier Transform (2D-FFT) to identify the excited guided wave modes. The calculated results are demonstrated in wavenumber-frequency domain to be compared with the dispersive curves of the rail section. **Figure 2-3** shows the results for 2D-FFT of simulated results in literature (Shi et al., 2019), which correspond to the selected modes in **Figure 2-2**. The excitation positions, as shown in **Figure 2-3(a)**, **(b)**,

and **(c)**, are the element nodes where maximum displacement takes place corresponding to each mode. This finding supports the basic principle for guided wave selection process though it should also be pointed out that this excitation configuration is rather complicated and idealized for field applications.

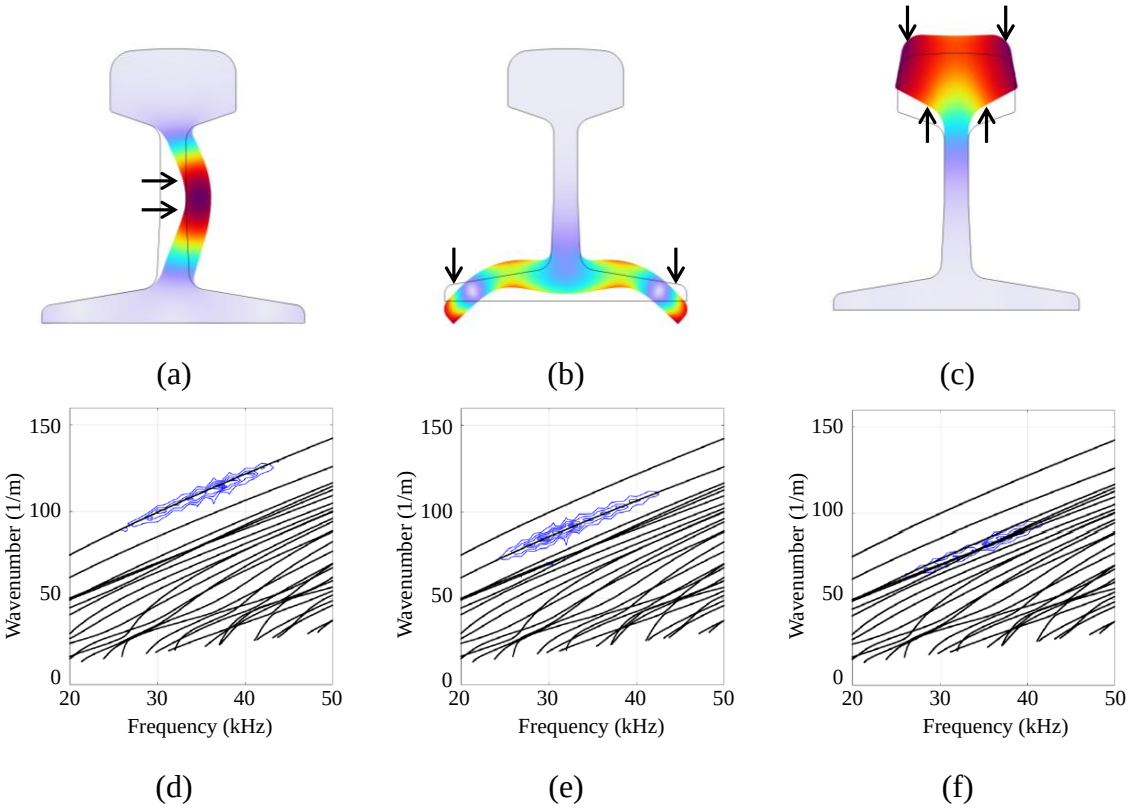

Figure 2-3. Excitation positions and frequency-wavenumber curves (Shi et al., 2019) corresponding to the selected modes: (a) & (d) Mode 1, (b) & (e) Mode 2, (c) & (f) Mode 3.

However, those successful applications of mode selection for railway track inspection mostly adopted ultrasonic excitation frequencies below the level of 100 kHz (Ramatlo et al., 2020), mainly because the guided wave modes above that threshold can be challenging to calculate and thus cannot be controlled in field applications. The selected

guided wave modes, although have been proved to be effective in detecting commonly seen rail defects, cannot reveal early-stage defects with minimum dimensions. The low-frequency ultrasonic excitation generates UGWs with longer wavelengths that may not be sensitive to minor defects, such as corrugations (Xie et al., 2022) and fatigue cracks (Chowdhury & Sehitoglu, 2016). However, higher-frequency UGW excitation frequency bands will inevitably lead to a higher density of modes (dispersion curves) in the frequency-wavenumber space, which is computationally demanding. The nonlinearities in material behaviors under high-frequency excitation also make SAFE not applicable for analysis.

Since it can be extremely difficult to conduct analysis in a traditional numerical approach, it is thus rational to set out to extract key information from the data. By introducing physics-based information into signal processing, Ramatlo et al. (2022) successfully characterized the UGW behavior of monitored long-range rail segments with welding defects. Such practice has enabled generalization in GWT of long-range railway tracks, which is a promising research area especially with the aid of the extensively developing data mining and ML technologies.

2.2. Ultrasonic Guided Wave Sensing and Transducing Techniques

2.2.1. Lead Zirconate Titanate (PZT) sensors

Piezoelectric sensors have been widely used for transducing and receiving UGWs on

rails and have been proven to be highly effective in laboratories and on railway sites (Gong et al., 2022; Loveday, 2012; Xue et al., 2023). The working principle for such ultrasonic sensors is that the PZT materials enable piezoelectric effect to measure changes in pressure or strain by converting those physical quantities to an electrical charge. According to literatures (Mićić et al., 2023; Ramatlo et al., 2018; Xiong et al., 2023), those sensors are extremely sensitive to transverse and longitudinal wave modes.

There are a variety of commercial PZT sensors available. PZT wafers (**Figure 2-4a**) are most used in laboratory because they are cost-effective enough to be disposal. But the exposed electrode may be interfered with by the electromagnetic field of the environment, therefore it needs further isolation against EMI. Acoustic emission sensors (**Figure 2-4b**) can be much more expensive than PZT wafers (S. Guo et al., 2022; X. Zhang, Sun, et al., 2020). They are specially designed for sensing minor acoustic signals known as acoustic emission events, meaning that they feature extremely high sensitivity. Apart from that, practical experience has commented that such type of sensors may record little useful information under a triggering acquisition mode. Sometimes subtle interference may result in a low SNR. While most PZTs are quite large in sizes, film sensors (**Figure 2-4c**) featuring excellent flexibility has gained popularity (Y. Zhang et al., 2024) in guided wave sensing. Consequently, such sensors can be smoothly implemented onto rail surface. But the sensitivity and reliability of such flexible material-based sensors are not as stable as traditional PZT wafers.

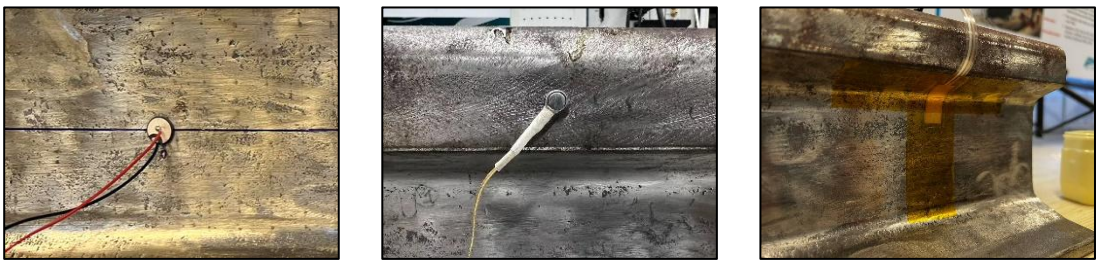

(a) (b) (c)

Figure 2-4. Different types of PZT sensors: (a) PZT wafer; (b) acoustic emission sensor; (c) film sensor.

For engineering applications, it is essential for sensors to be durable against harsh field conditions. Particularly, the quality of ultrasonic signals can be greatly compromised due to the severe EMI of railway environments. The materials used for manufacturing PZTs determine that they should be sensitive to ambient EMI, especially if the electrodes are exposed to air. Even with proper internal electromagnetic shielding to reduce high frequency noise, most PZTs still suffer from interference by strong electrical noise environments, such as railway sites.

2.2.2. Electromagnetic acoustic transducers (EMATs)

Figure schematically demonstrates the working principle of PZT and EMAT for sensing ultrasonic waves. Compared to traditional PZTs that converts electric signals into pressure against structural surface (under the generation mode), EMAT uses Lorentz force via a coil of electrified wire, a permanent magnet, and a conductive metal to generate periodic high-frequency vibrations forming ultrasonic waves as shown in **Figure 2-5**. It should be noted that due to the characteristics of Lorentz force

mechanism, no out-of-space displacement is generated from this process (Fang & Tse, 2019; W. Guo et al., 2023). Consequently, EMATs are considered an effective approach to excite shear horizontal (SH) guided waves (Hu et al., 2021; X. Li et al., 2023; Miao & Li, 2021). The probe arrangements for PZTs and EMATs are quite similar. For most circumstances, a pitch-catch pulsed ultrasonic system is expected, with one probe being the guided wave generator and another being the detector. When UGW encounters surface or subsurface defects, the defect echo is captured and presented on an oscilloscope. For railway inspection, it is also feasible to conduct B-scan imaging using EMATs or air-coupled instruments as guided wave transducers owing to the non-contact characteristic (Hu et al., 2021; Mariani & Lanza di Scalea, 2018).

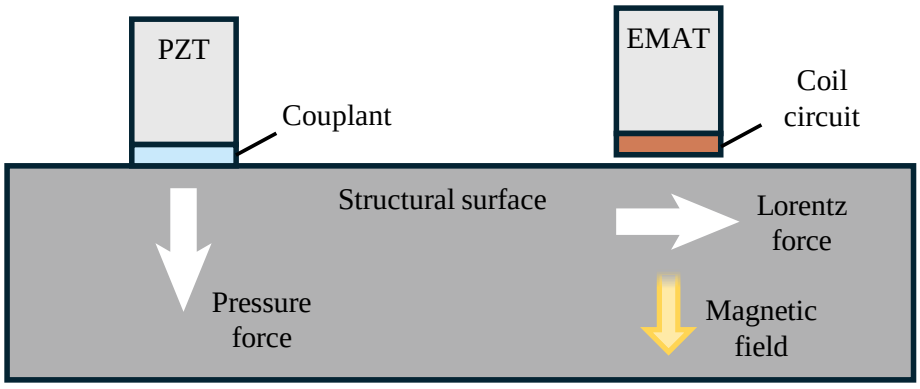

Figure 2-5. Comparison of piezoelectric PZT and EMAT.

The EMAT can detect UGWs maximumly over 10 meters depending on the wavelengths used for detection. In field applications, EMATs are often used to detect defects of proficiencies of pipelines, especially welding and corners where corrosion and cracks may occur. However, the main drawback for EMATs is identical to that of PZTs, that is, they are prone to EMI. Apart from that, EMATs are not quite lift-off

effective (S. W. Han et al., 2016; Mariani et al., 2017; Petcher et al., 2014).

2.2.3. Laser ultrasonic testing (LUTs)

Recent developments in laser technology have enabled applications on UGW generation and detection, especially in the field of railway track inspection. A scanning laser vibrometer can offer consistent measurement points to form an array to enhance the spatial resolution, which makes this technique superior to conventional ultrasonic transducers. Such laser-based methods can also achieve fully non-contact sensing in a manner that is free of lift-off effect.

However, this non-contact sensing pattern can also cause the obvious disadvantage of lower SNR related to impedance mismatch and loss of signal energy in the air-coupled propagation process (Pathak et al., 2019). Although efforts have been made to enhance the stability and signal quality of laser ultrasonic systems in laboratory via the means of advanced post signal processing techniques and machine learning algorithms (Ghafoor et al., 2022), it remains a major issue considering future deployment on railway sites where the operating environment can be further worse. As ultrasonic transducers, laser ultrasonic testing (LUT) can generate UGWs on rail surfaces in various frequency bands, which are composed of both bulk waves and guided waves in most circumstances. Nevertheless, the signals generated through an air-coupled laser source can be of low quality mainly due to the low-energy excitation causing the

difference in magnitudes of elastic waves (Ghafoor et al., 2021), resulting in difficulties in reproducible testing. As ultrasonic sensing modules, LUT can reconstruct the full wavefield using a scanning configuration, compared to traditional PZTs and EMATs, laser ultrasonic technique does not require multiple transducers to be mounted on the target structure to construct an array. In the experimental study illustrated in the work of Sha et al. (2021), a scanning laser Doppler vibrometer (SLDV) was adopted to measure the guided wavefield of a plate-like structure. The SLDV accurately extracted out-of-plane velocities in a square grid including more than 140,000 measuring points at the sampling frequency of 512 kHz. Similar experimental configurations were adopted by other researchers to receive UGWs on rails (Jiang et al., 2021; Pathak et al., 2019), featuring an even higher sampling frequency that surpasses 100 MHz with the spatial interval of 0.2 mm and more than 2,000 measuring points. The lift-off distance was 100 mm which denotes completely non-contact detection. The more advanced 3D-SLDV system was also presented to detect Rayleigh waves on rail head (Masurkar et al., 2020), and at each sensing point 50 measurements were averaged to yield clearer and better waveforms. Though the sensing performance for LUT is rather impressive, one major drawback is that such non-contact and air-coupled method can only detect surface and sub-surface waves. This has prevented these methods from detecting deeply buried defects such as rail transverse cracks in the rail web. Assuming that it may be feasible to install laser equipment on an inspection vehicle, it is difficult to guarantee the scanning quality for field tests as many factors such as environment, humidity,

scanning speed, and even rail bumps may compromise signal fidelity.

2.2.4. Fiber Bragg grating (FBG)-based ultrasonic sensing

Compared with PZTs, EMATs and LUTs, optical fiber-based sensors would be a promising substitute to be installed on railway tracks considering their natural immunity to EMI. Additionally, optical fiber sensing can significantly save power consumption and integration cost in long-period continuous monitoring scenarios (X. Sun et al., 2022).

Optical FBG sensors and distributed optical fiber (DOF) sensors are common optical sensing instrumentations in the field of railway structural health monitoring, but the sensing performance for these two types of sensors differs significantly. DOF can achieve continuous measurement for long-range railway tracks but with the spatial resolution of approximately 1 meter; FBGs feature higher sensitivity to structural deformation but the limited grating length of FBGs limits the sensing range. Distributed acoustic sensing (DAS) is categorized under DOFs that can achieve ultrasound-level sampling rate, but it has only been implemented as trackside sensing systems. Recent developments in high-speed optical interrogation technology have enabled UGW sensing using FBGs. Unlike DAS, FBGs can be attached to structural surface to detect minor changes in structural deformation. According to literatures (Artagan et al., 2020; Dirks et al., 2015), commonly discovered defects within railway track material are of

small dimensions, which requires the deployment of UGWs with shorter wavelengths. Consequently, the FBG sensor should be an excellent candidate to be installed for on-site testing on rail track online monitoring due to their high sensitivity to UGWs with shorter wavelengths.

FBGs are commonly acknowledged for their high sensitivity to longitudinal strains. Nevertheless, it is still a major challenge to interrogate the FBGs at ultrasonic-level frequencies (>20 kHz). The commonly used approach for FBG demodulation is to either emit a broad-bandwidth light to the grating or deploy a tunable laser with a concentrated wavelength to sweep within a specified period of light wavelength. The reflected light of a designated wavelength is measured, which is defined as the Bragg wavelength λ_B, as illustrated as,

$$\lambda_B = 2n\Lambda \quad \textbf{(2-1)}$$

where n denotes the effective refractive index of the FBG; Λ represents the grating period. Although this interrogation strategy has been widely used as the principle to design FBG interrogators, the sampling frequency can hardly surpass 5 kHz, while ultrasound frequency surpasses 20 kHz. To solve this issue, the method of edge-filtering technique has been proposed to achieve high-speed demodulation of FBGs with higher frequency sampling bands. Unlike traditionally used broad-bandwidth light emission, a laser source that generates high-power narrow-bandwidth light is deployed. The light precisely meets the 3-dB position of the reflective spectrum of the FBG being

demodulated. Then, the grating wavelength shift caused by macrostrains can be sensed and transformed to laser optical power intensity change. This process is demonstrated in **Figure 2-5**. It should be noted that FBGs are known to be sensitive to longitudinal strain, but insensitive to shear strain (Wee et al., 2017). The directionality of FBG sensing has raised much attention and a phased array system was developed based on this theory (Tian et al., 2019). Such characteristic of direction-dependent sensing of FBGs enables damage location in plate-like structures. However, the complexity of wave modes on rail guides can bring more challenges when considering the directionality of FBGs in ultrasonic sensing.

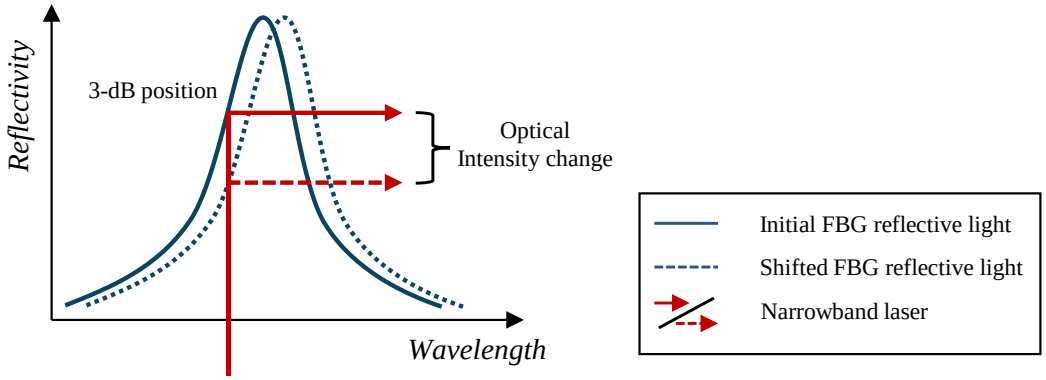

Figure 2-6. Schematic of ultrasound high-speed FBG demodulation using edge-filtering technique.

Apart from sensing directionality, multiplexing of FBGs should also be considered when deploying into GWT for railway tracks. The large volume of railway system requires equally massive sensor networks for daily maintenance and health monitoring (Cao et al., 2020). This has prevented FBGs from being massively utilized because in

most scenarios multiplexing characteristics are greatly valued, to obtain a more comprehensive damage detection performance by covering a larger inspection area. The solutions to designing multiplexed FBG systems have been explored by numerous researchers. Pang et al. (2018) proposed an effective FBG sensor network to achieve acoustic emission source localization on an Aluminum 2-D plate; to this regard, a FBG network configuration which shares similarities was also developed to locate acoustic emission sources in literatures (Sai et al., 2016). Nevertheless, the methods proposed in the above research methods have only been validated in experiments on plate-like structures where the dominant UGW mode is Lamb waves. The directionality of FBG sensing determines that those sensors can only be assumed to be sensitive to longitudinal strain of the grating area. This feature brings an obvious advantage, that is, the pressure waves can be picked up with little interference from the shear waves in solid media, which is quite different from traditional piezoelectric sensors. However, there have been little research addressing the utilization of FBGs in field applications.

2.2.5. Comments on sensing technologies

Table 2-1 provides a comprehensive and detailed comparative analysis of various techniques for generating and detecting guided waves. Traditional sensing instruments, such as PZTs and EMATs, have been thoroughly validated and are known to be effective for this purpose. However, they possess inherent drawbacks, including susceptibility to EMI and the requirement for an external power source.

Table 2-1. Guided wave generation and detection methods.

Type of method	UGW generation	UGW detection	Advantages	Limitations
PZT	applicable	applicable	high sensitivity; mature techniques; high-frequency response	high-voltage electricity supply needed; disturbed by EMI; unendurable (brittle)
EMAT	applicable	applicable	capable of excite SH guided wave modes; non-contact and no coupling agent needed; high sensitivity	high-voltage electricity needed; affected by lift-off effect; disturbed by EMI; Narrow-band sensing
LUT	applicable	applicable	high sensitivity; non-contact; high spatial resolution	Expensive; redundant system; disturbed by EMI and ambient effects; fast energy attenuation; can only detect surface or sub-surface waves; low SNR
FBG	not applicable	applicable	immune to EMI; high sensitivity; no external electricity supply needed; small dimensions; disposable	difficult to demodulate optical signals; difficult to multiplex; cannot actively excite UGWs; sensitive to temperature change

In contrast, FBGs are inherently immune to EMI and do not require electrical wiring, thanks to their optical operational principle. Consequently, FBGs are anticipated to advance significantly in ultrasonic inspections within complex railway on-site environments due to their superior adaptability. Nevertheless, the research exploring

the full capabilities of FBGs in GWT remains sparse. While existing literature confirms the feasibility of FBGs for detecting UGW and acoustic emission signal in simple 3-D wave guides such as aluminum plates and longitudinal pipelines (Yao et al., 2023), their practical application in more challenging configurations, specifically railway tracks with much more perplexing propagation routes and guided wave modes, requires further investigation.

2.3. Signal Processing Techniques for Guided Wave Testing

An effective NDT & E methodology not only relies on advanced sensing equipment but also robust and reliable models for signal processing and structural evaluation. Ultrasonic signals collected on the railway can be highly perplexing due to reflections and refractions resulting in difficulties in demodulation.

2.3.1. Data pre-processing

Data pre-processing is essential for later analysis, not only to improve SNR but also to extract useful information from raw guided wave signals (Rokach et al., 2023). It has been suggested that for a machine learning process, UGW signals polluted by environmental conditions, specimen boundary conditions, and noise caused by vibration and the electronic system can result in model overfitting (W. Liu et al., 2021). To solve this problem, normalization of the guided wave signal is crucial, before the data preparation begins. Adaptive filtering and split spectrum approaches have been

adopted to enhance SNR (Diogo et al., 2022), although their principles are completely different. Filtering-based pre-processing aims at reducing the impact of dispersive modes of UGW signals by functioning as a linear filter with a transfer function. The split spectrum approach calculates and determines distinct interferograms for spectral sub-bands, thus, to eliminate the effects of unwanted dispersive modes.

The input for ML models can either be a combination of features with physical meaning or timeseries. Commonly used features such as waveform (Hilbert) envelope, skewness, kurtosis, peak-to-peak amplitude, etc., can be simply calculated and used to represent the signal characteristics. Energy-based and time-frequency analysis-based features have also been proved to be useful (Hei et al., 2020; X. L. Lu et al., 2024; C. Su et al., 2019). The above features extracted are effective input to the ML models. The underlying implication between each feature type and the damage conditions can be revealed by powerful ML algorithms, usually through projecting into a higher-dimensional latent space. In comparison, with the rapid development of research progress on natural language processing (NLP), time-series ML models have been extensively deployed to the application of processing and representing ultrasonic signals (Flores Cuenca et al., 2024).

There are also time-domain and frequency-domain pre-processing methods, which are essentially created to prepare data for later ML model training. For instance, Hilbert transform is the most used approach to extract signal envelope (Dang et al., 2024),

effectively revealing the time-domain characteristics of the ultrasonic signal and improving the precision in calculating the time of flights. The Hilbert energy spectrum has also been proposed to assist damage detection using UGW inspections (C. Su et al., 2019). Apart from time-domain features, researchers have discovered that frequency-domain features are also important for analysis (Z. Yang et al., 2023). However, in most cases frequency-domain features, such as the power spectrum density functions, are not solely used for analysis. That is because the frequency spectrum may not reflect local characteristics of a signal. The common solution is to obtain and integrate time-frequency-domain features, using short-time Fourier transform (STFT) (S. X. Chen et al., 2021; Dang et al., 2023), Wavelet transform (WT) (D. Li et al., 2021; Rostami et al., 2020), and Hilbert-Huang transform (HHT) (C. Su et al., 2019). **Figure 2-7** shows a typical data pre-processing scheme using STFT to effectively extract useful information embedded in the raw signal, which is 1-dimensional time-domain data. The STFT results are transformed into RGB images which make 3-dimensional input for a convolutional neural network (CNN). Then, the convolution layer of the CNN further expands the dimension of the input RGB images. From this example, it can be observed that the optimal purpose for conducting such data processing is to increase the efficiency of data analysis for later damage diagnosis (Lomazzi et al., 2023). Similar conclusions were drawn from the work of Setshedi et al. (2024) and Arias-Vergara et al. (2021), that ML models can effectively extract useful representations from the spectrograms of UGW signals.

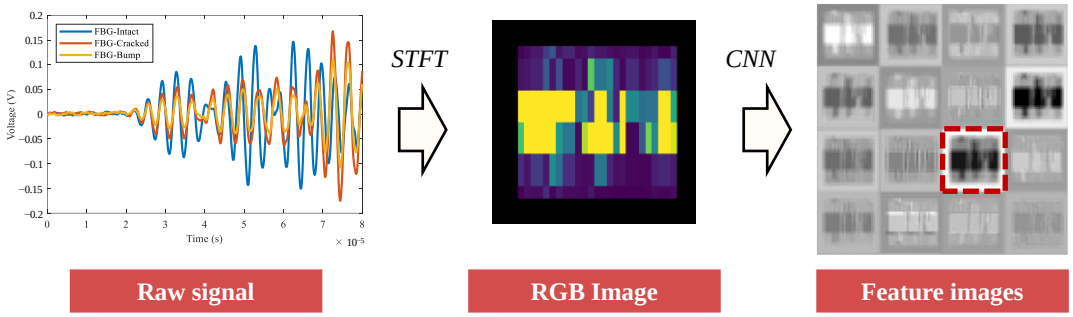

Figure 2-7. The data pre-processing scheme adopted by Dang et al. (2023).

2.3.2. Conventional approaches

In this section, the author defines conventional approaches as those methods utilizing DSFs that are directly derived from UGW signals. There exist distinguishable features in UGW signals acquired from rail segments of healthy and damaged conditions. Based on that assumption, rail health evaluation is carried out through analyzing DSFs extracted from the waveform.

2.3.2.1. Ultrasonic imaging

Ultrasonic imaging is a powerful tool in NDT to display defects or flaws of a material. This technique enables clear interpretations via a scanning multi-probe system. In the context of railway track inspection, B-scan is mostly utilized to collect abundant data to reveal railway defects (Huang & Lanza di Scalea, 2024; Spada et al., 2022; Yu et al., 2024). **Figure 2-8** shows an ultrasonic B-scan method that comprehensively detects rail head defects with high precisions.

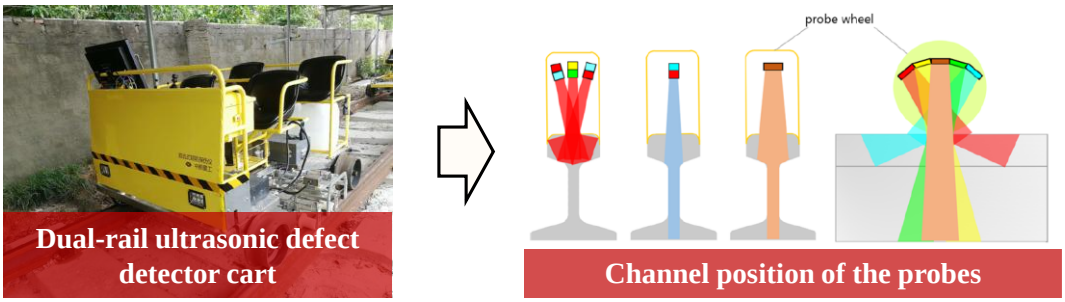

Figure 2-8. An ultrasonic B-scan method proposed by Z. Chen et al. (2021).

Although ultrasonic imaging has been extensively studied and demonstrated excellent performance specifically on plate-like structures (De Castro et al., 2022; Sha et al., 2021; Tian et al., 2019; X. Yang et al., 2022), the author shockingly learns that few successful attempts have been made in guided wave imaging of railway tracks. Thereupon, two possible reasons are presented based on the author's observation:

(1) It can be concluded that Lamb wave is currently the most popular choice for imaging because its dominant modes (namely Symmetric and Antisymmetric modes) are simple enough to control and manipulate (X. Yang et al., 2022). However, it is difficult to excite Lamb waves with few modes in rails, in consequence, most imaging techniques do not apply to rails. The intricate geometric characteristics of a railway track segment also complicate the application of imaging techniques (Hu et al., 2021).

(2) Ultrasonic imaging requires a scanning procedure to sample spatial information, which brings challenges in sensing techniques. Most UGW transducers are contact sensors, meaning that it takes a full ultrasonic sensor array pre-implemented to diagnose rail health which apparently is not cost-efficient. There are solutions proposed by

researchers (Hu et al., 2021; C. Zhou et al., 2017) where advanced sensing technology and sensor placement were deployed to achieve ultrasonic imaging; however, the current methods are still not suitable for long-range monitoring of massive railway lines.

Due to the above reasons, ultrasonic imaging is still too 'luxurious' for railway monitoring applications, because for most circumstances it is preferred to increase the inspection range at the cost of lower spatial resolution for railway GWT.

2.3.2.2. Energy attenuation-based DSFs

Energy attenuation is a basic phenomenon for guided wave propagation and such a process can be quantified by various means, such as wavelet packet transform-based transmissive wave energy (Hei et al., 2020). Z. Su et al. (2014) systematically compared linear and nonlinear signal features of guided wave and conclusions are drawn that nonlinear features are more sensitive to damage on an aluminum plate. A 3-step damage detection method was proposed by Z. F. Tang et al. (2021), considering guided wave energy transmission and reflection. The energy-based damage index (EDI) adopted by X. Sun et al. (2022) is based on guided wave attenuating pattern which allows multiple wave modes to exist in rails. The EDI can be formatted as follows:

$$EDI = \sqrt{\frac{\sum_{j=1}^{2^n}\left(E_j - E_{b,j}\right)^2}{\sum_{j=1}^{2^n}\left(E_{b,j}\right)^2}} \quad \textbf{(2-2)}$$

where E_j denotes the j-th wavelet packet energy of a signal, which is compared to the j-th baseline wavelet packet energy level $E_{b,j}$. It can be observed that if EDI approaches 1 it is most likely that the signal deviates from the baseline, meaning that there is interference induced by rail damage. In their work, it can be found that proposed EDI has the potential to characterize rail damage severity. An alternative index proposed H. Sun et al. (2024) adopted guided wave relative energy coefficient, which can be derived from virtual time reversal method instead of wavelet packet transform. This method, compared to the former one, can indicate rail web defect in a more specific and quantitative manner. Through analytical, numerical, and experimental studies, it has been proved that the DSF can accurately reflect the dimensions of the defect.

2.3.2.3. Waveform distortion-based DSFs

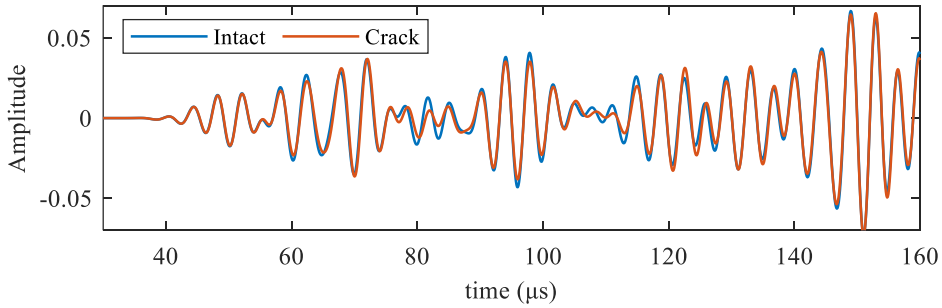

Figure 2-9. Waveform distortion induced by rail crack.

It is well-known that defects and flaws in rail can cause waveform distortion in time domain, as shown in **Figure 2-9**. Researchers have proposed numerous DSFs to characterize the change in time-domain waveform. Although ToF is a classic index for ultrasonic inspection, it lacks generalization when it comes to local damage with minimum sizes. In this sense, local temporal coherence (LTC) is adopted to quantify

the signal changes induced by rail damage. Sun et al. (2022) adopted LTC for each fixed time window in time domain, which is defined as the peak coherence. The composed DSF in their work, which is named peak coherence change (PCC), can be calculated as follows:

$$PCC = \max_{\tau}\big(LTC(\tau,t)\big) - \overline{LTC(\tau,t)} \quad \textbf{(2-3)}$$

where τ should be defined as a time interval by which the damaged signal is translated in time domain; t generally denotes the specific time window. An important advantage of PCC is that it automatically removes temperature effect on guided wave propagation.

The above DSFs are baseline dependent. However, the baseline condition may vary through different ambient factors thus for engineering applications it is difficult to apply. To address this issue, a benchmark-less evaluation method is proposed by K. Wang, Cao, et al. (2020). The DSF calibrates the level of decorrelation between guided wave signals acquired before and after the passage of a train, and it is formatted as:

$$R_{cc} = 1 - \frac{\int X(t)Y(t)dt}{\sqrt{\int X(t)^2dt \int Y(t)^2dt}} \quad \textbf{(2-4)}$$

Where $X(t)$ and $Y(t)$ denote the signal acquired before and after train pass-by. R_{cc} denotes the remnant cross correlation. Assuming that a crack is located on the testing range of a rail segment, crack extension caused by train dynamic loads will be reflected

by R_{cc} due to the guided wave field change. Through experimental studies, this baseline-free method was verified and proved to be sensitive to rail defects of minimum dimensions.

2.3.2.4. Comments

Nevertheless, the author would declare that those conventional approaches are not necessarily less effective in every scenario than those recently proposed by numerous researchers. In contrast, those methods are simple and direct enough and have been proven to be feasible through long-lasting engineering field tests. However, the rapid development of the railway system does require more intelligent railway maintenance strategies, and in this sense, traditional GWT generally lacks efficiency. Most methods introduced in literature that can be referred to were only verified on an analytical or laboratory experimental basis, where there is still a gap to fill to meet engineering requirements.

2.3.3. Sparse representation of UGW signals

The rail is a highly complex 3-D waveguide resulting in perplexing waveforms in time domain. In this sense, the technology of sparse representation has been proposed to retrieve valuable information from overlapping UGW signals (Song et al., 2023; B. Tang et al., 2024; Y. Yang et al., 2024). There are 2 ways of deploying such methods in ultrasonic signal processing. The first approach aims at conducting compressive sensing

(CS) and minimizing the data size while maintaining the wave characteristics in both time and frequency domains. This method is commonly used in acoustic emission-based monitoring projects where data storage is challenging. In contrast, the second approach attempts to reconstruct certain wave characteristics in time domain so that defect detection can be achieved. The focus of this study is structural health monitoring (SHM) of rails by means of GWT thereupon both approaches will be discussed in this section.

2.3.3.1. Compressive sensing

CS has been introduced to signal processing of UGW signals. The main goals of deploying CS-based techniques in GWT can be summarized as lost data recovery, signal denoising, dimensionality reduction, and data storage optimization. CS can be briefly defined as a signal processing technique that allows for the reconstruction of signals from a small number of measurements, provided the signal is sparse in a certain spatial domain. The mathematical expression of a typical CS model can be written in the following format (X. Wang, Li, et al., 2022):

$$d_{sparse} = \Phi d_{rec} = \Phi \Psi s = \Theta s \quad \textbf{(2-5)}$$

where, d_{sparse} and d_{rec} are the projection and reconstruction of the detection signals; Φ denotes the measurement matrix; Ψ and s represent the sparse transformation basis and the sparse representation coefficient of the original detection signals; and

finally, $\Theta = \Phi\Psi$ is the sensing matrix.

In recent years, the popular deployment of CS in processing UGWs is by combining with high-performance ML methods. Powered by a deep learning neural network, X. Wang, Li, et al. (2022) proposed a CS method to address the practical problem that the ultrasonic imaging quality is restricted by the number of transducers in service. K. Yang et al. (2023) proposed an unsupervised learning-based CS approach tailored for ultrasonic guided wave data for compression, denoising, and damage detection, which was proved effective via a dataset composed of seven million guided wave measurements collected over 2 years. The sparse representation can be actively integrated into ultrasonic imaging, as demonstrated in case studies introduced in literature (Z. Tang et al., 2021; X. Wang, Li, et al., 2022; Z. Wang, Huang, et al., 2022; Zang et al., 2023).

To briefly conclude, the current applications of CS in GWT mainly focus on preliminary signal processing, and enhancement in damage imaging techniques. There are still a lack of efficient and successful implementations in railway monitoring scenarios, where the UGW signals are more perplexing than those sampled from pipelines and plates. The sensor array placement (X. Wang, Li, et al., 2022) and ambient factors (K. Yang et al., 2023) can also significantly affect the detection accuracies, which should be addressed in future research.

2.3.3.2. Matching Pursuit

Matching pursuit (MP) is an adaptive signal time-frequency-domain processing technique that can sparsely decompose a target signal into a linear expansion of components (i.e., atoms) that belong to a redundant dictionary of waveforms (Cai & Wang, 2011; X. Hong et al., 2019; Sawant et al., 2021). By deploying a customized redundant dictionary with atoms of interest, a signal can be effectively represented and expanded using various combinations of dictionary components (i.e., atoms) with numerous time-frequency or time-scale characteristics. In practical uses, MP-based methods are extensively used in those scenarios where the knowledge of signal time-frequency features is priorly available for signal processing. Consequently, MP can be comprehended as an inverse solution to which case that the signal to be processed can be approximated. Compared to rails, there had been prior research where MP-based defect frameworks were deployed on cylinder-like structures (J. C. Hong et al., 2005; Y. Li et al., 2021; Rostami et al., 2017; Tse & Wang, 2013; X. Wang et al., 2010), and plate-like structures (B. Wu et al., 2017). Researchers have successfully demonstrated the feasibility of MP-based methods in SHM, nevertheless, it is a significantly more challenging research topic to deploy similar approaches on rails considering their much more complex geometrical characteristics.

Recent advances in MP-based rail health monitoring have brought much attention. Song et al. (2022) proposed an acoustic signal reconstruction method based on an improved

MP algorithm and an adaptive modular dictionary, and the reconstruction results of acoustic signals of rails demonstrated lower root mean square error (RMSE) compared to other methods. This part of research has provided useful guidance for real-time signal analysis, which contributes to their later research on acoustic emission-based SHM of rails (Song et al., 2023). Research outcomes of K. Wang, Hao, et al. (2020) also support this finding. To this extent, it has been verified that MP is capable of reconstructing ultrasonic signals as complex as rail acoustic signals. Followed by this conclusion, Y. Chang et al. (2017) proposed an inspiring methodology where sparse representations were utilized to distinguish overlapping echoes of UGW in complex 3-D structures. This theory was then proved to be applicable on rails by Ghafoor et al. (2021) who successfully detected defect echo using MP and different dictionaries. This piece of work shares similar spirit with the method previously deployed to detect railway bumps by using sparse representation of vehicle vibration data (Lederman et al., 2017). In this case, MP is considered an aid to reconstruct wave packets of interest (the defect echo in the case of SHM) given a priorly dictionary where the knowledge of characteristics of wave packets. The schematic in **Figure 2-10** shows a basic workflow of such methods. The defect echo is sparsely represented via the MP algorithm with a modulated adaptive dictionary. It is thus obvious that the accuracy of detecting defects rely on not only the choice of MP algorithms but also the prior dictionary. Tse & Wang (2013) studied the characteristics of pipeline crack induced guided wave echo and deployed an optimized dictionary, which is named dictionary of Interference Reflective

Components (IRC), to characterize general defect echoes. In literatures (Ghafoor et al., 2021; Ng et al., 2022; X. Wang et al., 2010), the components in the dictionary are retrieved from both numerical and experimental UGW signals.

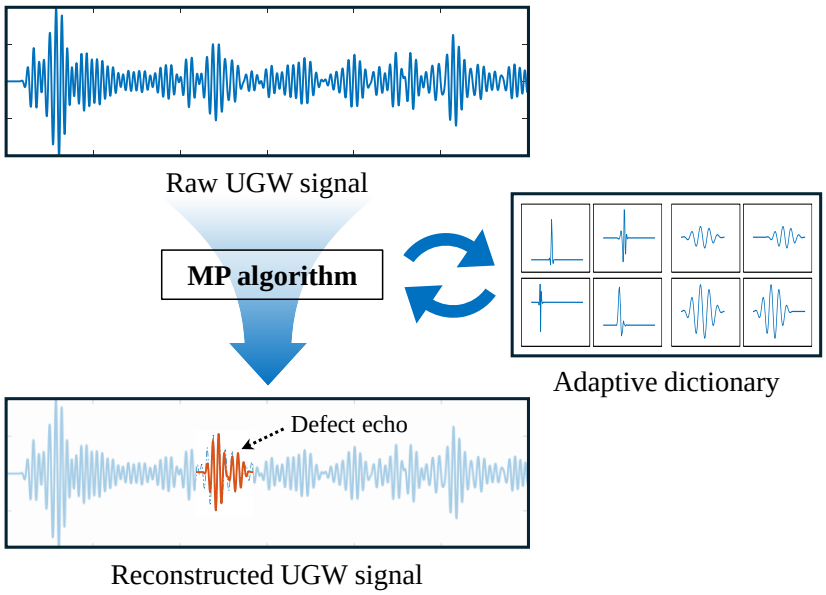

Figure 2-10. Schematic of MP-based defect detection using UGW.

However, it is worth noting that previous attempts were based on laser-induced GWT where Lamb waves were the dominant mode, meaning the time-domain characteristics of defect echo could be easily identified even by human intuition. Although this approach is highly effective for detecting surface and subsurface rail head defects using LUT-based methods, the UGW propagation mechanisms remains a major influence when deploying such methods. The complex waveforms are usually highly overlapped, thereby the reconstructed crack reflected waves can hardly be straightforwardly observed in an intuitive manner. Consequently, the potential feasibility and effectiveness of using MP-based methods to detect and localize rail cracks remains to

be studied. Furthermore, it is challenging to characterize the defect location and size based on reconstruction results which will require more systematic research.

2.3.4. Machine learning-based methods

2.3.4.1. An overview of current applications

The recent applications where ML are deployed to model the UGW propagation and aid the damage detection process are organized and listed in **Table 2-2**. It can be concluded that the exceptional ML algorithms have been extensively utilized to process the UGW signals acquired on railway tracks. In many works of modern publications, it has been mentioned that the perplexity of UGW signals is the motivation for deploying data-driven ML approaches to address the difficulties in damage detection for railway tracks. Based on current studies, the following conclusions can be drawn about the research progress on ML-powered GWT in railway inspection:

(1) Most of the applications are based on supervised learning approaches. Represented by classifiers and regressors, the supervised ML models have exceptional fitting performance and are especially suitable for automatically extracting damage-sensitive features from UGW signals. This brings significant convenience in damage detection process. However, those methods generally lack interpretability and generalizability. The practical use of these techniques can be extremely limited, because they tend to overfit upon a designated UGW dataset.

(2) The proposed ML models rely on abundant datasets for the training process, which is quite demanding in practical applications. As mentioned, the ML models tend to overfit on the training sets, resulting in inaccurate predictions on other datasets that are obtained with varying conditions. This drawback should be addressed by introducing probabilistic analysis to the damage detection process to enhance robustness and reliability (Y. Zhang et al., 2024).

Table 2-2. ML-powered ultrasonic testing applications in railway damage detection.

Model	Author(s)	Application	Summary
Variational mode decomposition	X. Zhang, Sun, et al. (2020)	Rail crack detection	The weak crack-induced signal can be effectively retained from acoustic emission signals
CNN	D. Li et al. (2021)	Rail crack detection	Classification of surface and internal crack-induced ultrasound
DNN (Transfer Learning)	S. X. Chen et al. (2021)	Rail crack early-stage identification and evaluation	Transfer learning was adopted to process and classify the acoustic emission signals
Hybrid probabilistic DNN	Y. Zhang et al. (2024)	Rail defect identification	The probabilistic deep learning can demonstrate the uncertainty in rail damage recognition
GAN	X. L. Lu et al. (2024)	Rail defect detection and quantification	The method reconstructs ultrasound-based 3D rail defects

Continued

Model	Author(s)	Application	Summary
DNN (Transfer Learning)	Z. Chen et al. (2021)	Rail defect detection and recognition	DNN for B-scan image recognition of rail defects with high precision
CNN	Mahajan & Banerjee (2023)	Rail crack localization	The method can accurately predict the crack location validated via a rail bending test
CNN	Dang et al. (2023)	Rail crack detection	UGW spectrograms are classified to indicate rail damage
DNN (Transfer Learning)	Yu et al. (2024)	Rail defect detection	An improved transfer learning-based model was proposed to classify the B-scan images of rail defects
Support vector machine (SVM)	W. Liu et al. (2021)	Rail foot defect detection	The method can identify the rail foot damage using multiple features extracted from UGW signals
CNN	Ghafoor et al. (2022)	Rail head defect classification	The proposed CNN model can classify various types of railhead damages against noise
DNN	Y. Wu & Yang (2023)	Rail defect localization	The acoustic emission signals are utilized to train DNN models to localize the rail flaw
Regressive models	Zarembski et al. (2016)	Rail defect detection	The method predicts the life of a rail defect in the presence of track geometry defects

In the following contents of the section, supervised and unsupervised approaches will be introduced respectively, showcasing each strength and disadvantages.

2.3.4.2. Supervised learning-based frameworks

Classifiers and regressors are powerful tools for data analysis and features extraction. Numerous supervised models have been developed to conduct effective NDT & E owing to their excellent fitting performance and robustness. Prior research has been undertaken, mapping complex ultrasonic signals that cannot be directly interpreted utilizing supervised learning methods (Bao & Li, 2021; Dang et al., 2023; D. Li et al., 2021; Suwansin & Phasukkit, 2021; T. Wang, Zhang, et al., 2022). Moreover, Rautela et al. (2021) designed a physical knowledge-assisted ML framework to detect damages using UGWs. Deeper networks were also proposed to reveal more information indicating damages hidden within the acoustic signals (Du et al., 2023; Ebrahimkhanlou et al., 2019; Lee et al., 2021; Mahajan & Banerjee, 2023; Suwansin & Phasukkit, 2021; Yun et al., 2021; Z. Zhang et al., 2022). Besides, ultrasonic imaging methods combined with deep learning have been deployed into NDE and the results showed promising potential to be massively utilized on railway inspections (Cui et al. 2022; Zhou et al. 2017). Despite the exceptional fitting performance, these ML models are label-dependent, indicating that they require a manually labeled dataset for supervised training. However, most engineering scenarios won't meet this requirement due to the insufficiency in acquiring fully labeled datasets, especially when the amount of data is

massive. For example, in the context of NDT for rails, the abundance of rail defect types brings inevitable difficulties in obtaining effective training data.

High-performance classification algorithms are essential for long-term acoustic emission monitoring scenarios to identify the nature of obtained acoustic emission events (J. Wang et al., 2018). On-site railway monitoring usually comes with high-operational noise, complex railway cracking conditions and mass data (Dang et al., 2024; X. Sun et al., 2022). Thereupon, DNN was adopted by D. Li et al. (2021) to identify and filter the samples to automatically extract cracking-induced acoustic emission events. Regardless of the powerful performance of this method has demonstrated, it should be noted that data labelling remains to be extremely labor-costly for training a complex DNN model. A similar approach was adopted by S. X. Chen et al. (2021), where in their case study the whole life cycle of rail crack growth was recorded. Useful information related to cracking was buried within strong train-pass-by impact background, and DNN naturally became the prior option for accurate features extraction. A deep transfer learning model was developed and through the visualization of the bottleneck features the clustering phenomenon was observed, indicating a possibility of unsupervised crack identification. However, to the best of the author's knowledge such potential has yet to be fully explored. S. X. Chen et al. (2022) previously proposed a novel ultrasound analysis method based on semi-supervised adversarial adaptation (SADA). Similar ideas have been proposed by Listou Ellefsen et

al. (2019). This approach addresses the challenge of transferring knowledge from well-controlled experimental or monitoring data (source domain) to real-world operational conditions (target domain). A two-level marginal and conditional domain adaptation is used to effectively reduce discrepancies in data distributions caused by operational differences. This framework significantly overcomes the reliance on data labels. Based on this research, a task similarity transfer learning (TSTL)-based method was proposed to further address the overfitting of traditional transfer learning (S. X. Chen et al., 2025). By analyzing the visualized feature space of source models constructed, the ultrasonic signals acquired on-site demonstrate an intuitively distinguishable distribution, meaning that there exists a promising potential for unsupervised detection of railway defects.

To sum up, despite the remarkable fitting performance of the supervised classifiers that have been extensively used to solve engineering problems, it remains a major challenge to develop automatic damage detection approaches using unsupervised algorithms to meet practical engineering applications where only unlabeled datasets can be accessed. For example, variational autoencoders were used by Yuan et al. (2021) to develop unsupervised detection and localization methods of light rail squats; K. Wang, Hao, et al. (2020) successfully detected broken rails using long-range UGWs and data-driven models considering various ambient factors.

2.3.4.3. Unsupervised learning-based frameworks

Unsupervised damage detection frameworks have also been proposed based on various machine learning models, such as autoregressive (AR) models, autoencoders (AEs), generative adversarial networks (GANs), and other generative models, owing to their excellent performance to learn nonlinear representations of nonlinear systems (Dunphy et al., 2022; Hao et al., 2021; W. Li et al., 2023; Luo et al., 2023; Sajedi & Liang, 2022; Silva et al., 2021). Those methods do not rely on labelled datasets but generally require a baseline condition for comparison.

The frameworks to be introduced in this section generally take advantage of excellent fitting performance of ML algorithms to help extract damage sensitive features. The 3-step damage detection process can be concluded, namely (step I) signal preprocessing, (step II) model training, and (step III) model transfer and anomaly detection. Several representatives are demonstrated as follows, to illustrate the methodologies deployed in existing literature.

(1) Paradigm 1: Autoregressive models

The first category of ML models are autoregressive models. **Figure 2-11** shows an anomaly detection framework based on an AR neural network. The AR model is first trained using the acquired data available, and anomaly detection can be conducted by feeding input signals to the trained network. The high-level reconstruction error

between the predicted signal and measured signal can indicate anomalies related to structural damage. It has been concluded that such methods are sensitive to anomalies buried in time series (A. Liu et al., 2019; J. H. Yang et al., 2021), and can also eliminate ambient factors such as wind load and temperature. Likewise, a nonlinear autoregressive neural network was adopted by Yan et al. (2013) and by Umar et al. (2021). The novelty in their methods lies in the exogenous inputs of neural network assists with the anomaly detection process, followed by probabilistic analysis of the nonlinear autoregressive model output.

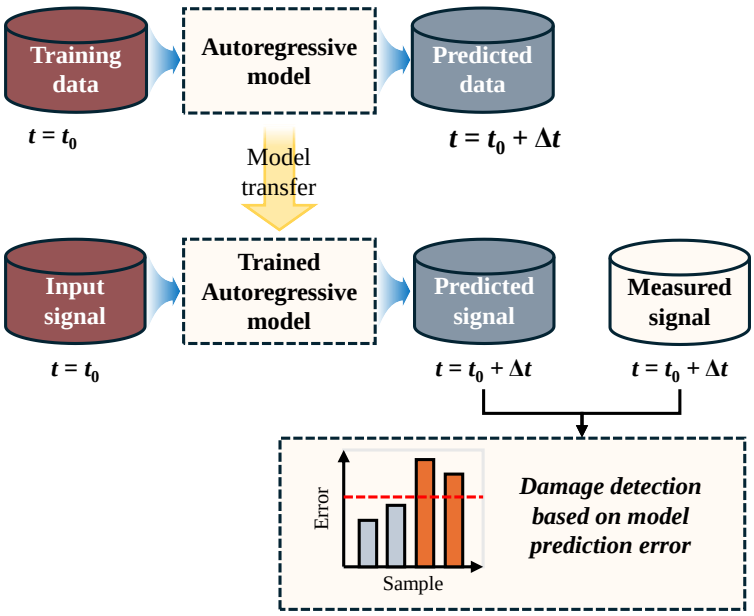

Figure 2-11. Workflow of a damage detection framework based on an AR model.

(2) Paradigm 2: Autoencoders

Unlike AR models, AE models typically do not possess the concept of time-series characteristics. The AE is composed of an encoder and a decoder structure, aiming at minimizing the reconstruction errors of training data. The training phase simultaneously

update the parameters of the encoder and the decoder. **Figure 2-12** shows an anomaly detection framework based on an AE. Different from the training phase of an AR model which predicts time series, AEs learn nonlinear representations through encoding and decoding the training data in batches. Then, much like the framework shown in Figure, the reconstruction error is also utilized for damage detection. For instance, an AE-based approach was deployed where AEs were trained on Lamb wave data proposed by Lee et al. (2021), based on which an automatic damage diagnosis framework was proposed. Pandey et al. (2022) also developed a novel data-driven approach for damage detection of a 2-D plate-like structure using Lamb wave. Both studies demonstrate high accuracies in the detection of damage, but plate-like specimens used in these literatures are obviously less complex in geometry than the rail segment resulting in simpler UGW modes. It thus remains unclear whether such methodology can be further extended to diagnose rail damage.

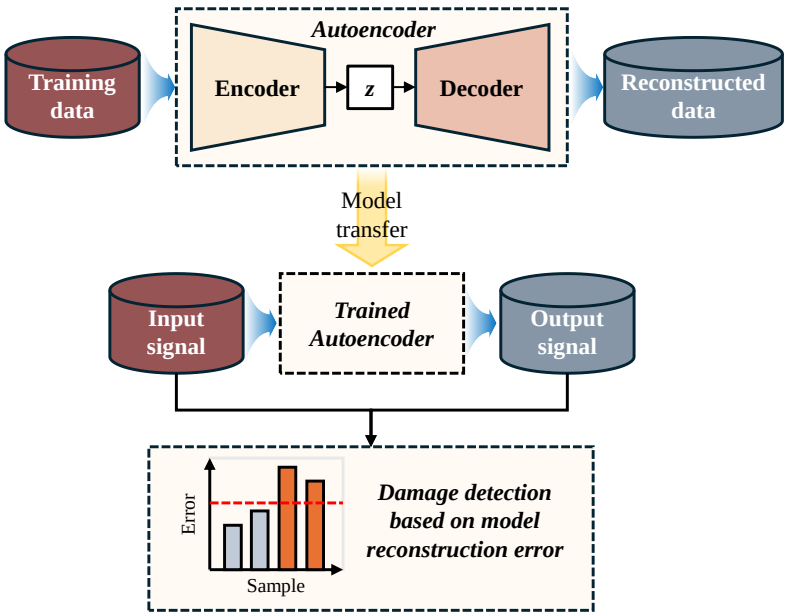

Figure 2-12. Workflow of a damage detection framework based on an AE.

So far, it can be concluded that the implementation of autoregressive models and AE models relies on analyzing the reconstruction or prediction error level to diagnose the structural defects. This requires much careful fine tuning to ensure that the ML models are well-trained to be sensitive to signal abnormalities so that they can reveal defects happening within the structure. And of course, a baseline dataset is always necessary for the training process where the models can learn nonlinear representations of the baseline signal while overcoming interference of data noise (Mo et al., 2021, 2025).

Apart from normally adopted damage indicators that focus on reconstruction error of an AE, the latent variable z also has the potential to be utilized for damage detection, as it demonstrates compressed yet informative representation of input signals. In this sense, latent variables were also utilized for anomaly analysis (Zemouri et al., 2023). Much alike principal component analysis (PCA), the latent variable vectors encoded by AEs show spatially distinguishable characteristics, except for that AEs can learn a nonlinear manifold (Mao et al., 2021). Although research has been conducted on studying features extraction based on AEs or AE-based structures (Anaissi et al., 2023; Pollastro et al., 2023), probabilistic analysis can hardly be applied to the latent variable distributions because they are randomly sparse and lack statistical features.

(3) Paradigm 3: Generative models

Figure 2-13 demonstrates a novel data anomaly framework proposed by Mao et al.

(2021), who innovatively combined a GAN and an AE as a novel framework for anomaly detection. The GAN and AE are trained simultaneously, while the generator is transferred and functioning as the decoder. In the anomaly detection phase, the input signal is firstly encoded to generate a latent variable z_1; the signal is then reconstructed and z_2 can be encoded using the reconstructed signal as input; finally, the latent loss is calculated, i.e., the second-order regularization of the error. This framework can be effective when the training data is defined as class-imbalanced and class-incomplete (Boppana & Bagade, 2023; Dai et al., 2023; W. Li et al., 2021), though the overall training and anomaly detection process can be redundant.

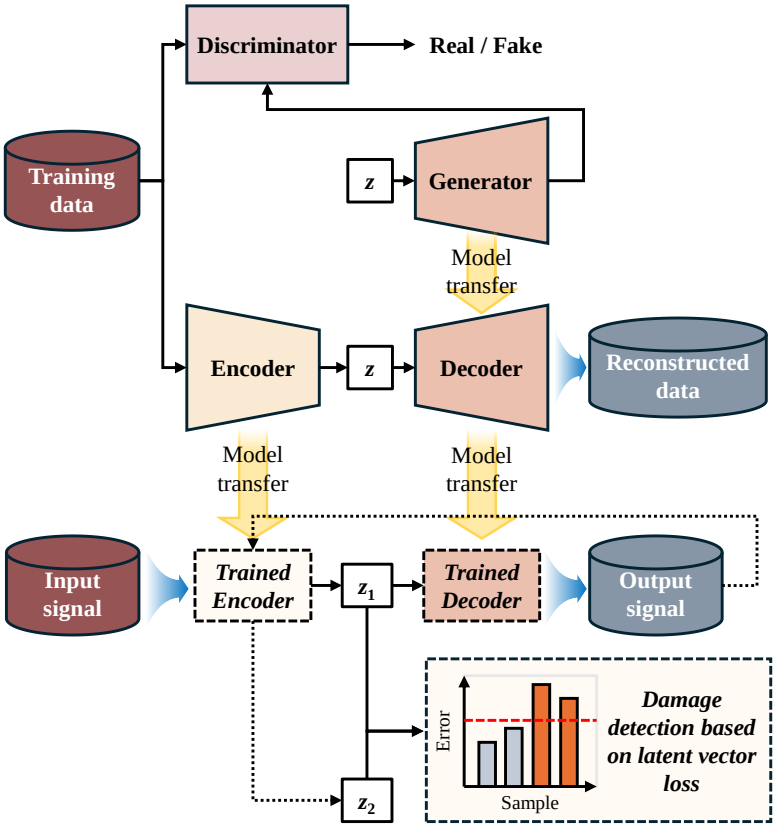

Figure 2-13. Workflow of a damage detection framework based on an AE and a GAN (Mao et al., 2021).

There are also applications mentioned in literature (Dunphy et al., 2022; Maggipinto et al., 2022; Pei et al., 2021; Setshedi et al., 2024; X. Wang et al., 2023; Zhong et al., 2023) where a trained GAN was utilized for data augmentation to ultimately enhance the classification networks, but such applications are not directly related to unsupervised damage detection process. For instance, a GAN model was designed by Luleci, Catbas, et al. (2023) that shows incredible robustness and is highly capable of both data augmentation and damage detection with excellent accuracy; similar work has been undertaken to create surrogate models of structural responses, such as accelerations and deformations (Luleci, Necati Catbas, et al., 2023; Ma et al., 2020; Shim et al., 2022). Nevertheless, few researchers have researched the feasibility of training GANs using ultrasonic signals as input.

The existing damage detection frameworks demonstrated and concluded in this section, although aided by implementing different types of ML algorithms, share similar concepts. Compared to supervised methods such as classifications and regressions, such unsupervised methods can effectively learn nonlinear representations within the input signals. The output of the ML models can indicate the level of abnormality through further comparison with the baseline conditions. Nevertheless, the current limitation for deploying such methods is that the damage quantification can yet be achieved. For most circumstances, a threshold is manually defined based on the level of network output, which lacks explanatory and robustness. One possible solution towards solving this

problem may be introducing probabilistic analysis into neural network training process so that the network output can contain useful information of damage status.

2.4. Concluding remarks

2.4.1. Towards enhancing UGW sensing reliability and robustness

Achieving a balance between the sensing range and the inspection resolution presents an almost contradictory challenge in railway field GWT. The excitation frequency determines the wavelength of UGW and the attenuation rate, thus restraining the propagation range. Higher frequency range (i.e., shorter wavelengths) results in faster attenuation but higher sensitivity to rail defects or flaws. Taking the engineering application in the literature (Ramatlo et al., 2022) as an example, the guided wave sensing system installed on railway tracks can cover more than 300 meters longitudinal rail line. But this system was designed to conduct rail weld monitoring and was incapable of detecting rail cracks of small dimensions. In fact, most modern GWT systems are known to be implemented for broken rail detection (Bombarda et al., 2021; Loveday et al., 2020). To detect early-stage rail cracks, it obviously requires a more precise inspection sensing system. To address this problem, researchers have proposed optimal mode selection schemes through analytical, numerical, and experimental investigations (R. Chen et al., 2021; P. Zhang et al., 2021), aiming at exciting certain types of guided wave modes that are prone to rail defect interferences. But such

approaches can be easily affected by uncontrollable ambient effect such as temperature, and to the best of author's knowledge there have yet been successful implementations on in-service railway lines.

Another problematic issue that could possibly prevent the advancement of online GWT sensing techniques is the harsh environmental condition of railway site. The solar thermal radiation can cause significant temperature difference on the railway surface, challenging the stability of ultrasonic sensors. The severe EMI can compromise the fidelity of acquired signals (Dang et al., 2023). The anti-EMI coatings and shells for piezoelectric sensors can be easily worn off if not maintained properly. Furthermore, the durability of a sensing system should also be valued when it comes to long-term monitoring of railway lines.

Consequently, it is rational and applicable to install more sensors on railway lines to compensate for the relatively insufficient guided wave sensing range, but it will significantly cost more. Research development in optical fiber-based ultrasonic sensing has brought promising applications in massive railway lines owing to its low cost and durable performance. The optical sensors are naturally immune to EMI, and optical signal can be transmitted via armored optical fiber installed along the railway lines, which is notably more cost-effective compared to electric wiring. Additionally, FBGs can be multiplexed in each acquisition channel, contributing to reliable, efficient, and applicable GWT for such large volume of railway lines. Yet there remain numerous

unsolved problems, for example the temperature compensation for FBG spectrum shift should be priorly configured.

2.4.2. Towards filling the gap between laboratory settings and engineering applications

Current research progress has been made on the basis of laboratory proof-of-concept. Most methods proposed require further validation on in-service railway lines, where the harsh environmental conditions need to be considered. Apart from deploying durable and reliable sensing techniques, it is equally important to develop more effective signal processing techniques with generalized performance. Nevertheless, few methods proposed by researchers have taken ambient factors of railway site into account even though it is an obvious factor for guided wave propagation.

The optimal goal for an advanced GWT system for railway tracks should be to discover rail defects or manufacturing flaws at an early stage, thus tragical accidents can be prevented. It is essential that our sensing system, integrated with highly capable signal processing techniques, can raise alarm for early-stage railway defects. The sensing system should be capable of real-time monitoring of railway tracks, ruling out potential rail defects that may endanger the safe operation of railway systems. To this end, it is suggested that future research should focus on long-range rail safety inspection and health monitoring of key railway components.

CHAPTER 3 PZT-MFBG HYBRID SENSING SYSTEM FOR RAILWAY GUIDED WAVE TESTING

3.1. Introduction

Conventional piezoelectric ultrasonic sensors often face challenges in harsh operational environments, which has somewhat limited the widespread adoption of ultrasonic testing. A key issue is the significant degradation of signal quality caused by strong EMI in railway settings (X. Sun et al., 2022). This sensitivity to EMI stems from the inherent electrical properties of PZT materials, particularly near exposed electrodes. In contrast, fiber-optic sensors present a viable alternative due to their superior EMI resistance, making them well-suited for railway track installations. Moreover, optical fiber sensing systems offer notable advantages in long-term continuous monitoring, including reduced power consumption and lower integration costs (H. P. Wang et al., 2019; H. P. Wang, Gong, et al., 2022). Among fiber-optic solutions, FBG sensors and distributed optical fiber (DOF) sensors are widely used for ultrasonic detection, though their performance varies considerably. FBGs excel in identifying subtle defects and are typically deployed on critical structural components. Conversely, DOF sensing is better suited for large-scale monitoring, albeit with reduced spatial resolution and demodulation frequencies. Given that rail defects often exhibit minimal dimensions in both length and depth (Dirks et al., 2015), short-wavelength ultrasonic waves are more effective for detection. Consequently, FBGs are considered highly suitable for rail track

inspections due to their enhanced sensitivity to high-frequency ultrasonic signals. Previous studies, such as the PZT/FBG hybrid system developed by X. Sun et al. (2022), have demonstrated the feasibility of FBG-based ultrasonic detection. However, optimal damage assessment requires multiple measurement points along the rail. Researchers have explored various solutions, including FBG sensor networks for acoustic emission source localization on aluminum plates proposed by Pang et al. (2018) and impact detection (Sai et al., 2016, 2020). While these methods have proven effective for simple structures dominated by Lamb waves, their applicability to complex rail geometries remains unexplored. The subsequent sections will detail an advanced edge-filter demodulation technique designed for synchronized ultrasound detection using a multi-FBG array.

A novel hybrid sensing system is designed for ultrasonic testing on rails. The system excites ultrasound using high-voltage piezoelectric transducers glued onto rail surface and ultrasonic signals are sensed through a multiplexed FBG array. The main novelty of this system lies in the interrogation plan for the multi-channel FBG sensors, which is concisely illustrated in later sections. A damage diagnostic framework is also proposed in this study using regression neural networks to demonstrate nonlinear characteristics of ultrasonic signals recorded by the proposed system. Several rail intact and damaged conditions are considered, and the damage detection results are obtained after model fine-tuning.

3.2. Multiplexing of FBGs using edge filter-based interrogation

FBGs are commonly acknowledged for their high sensitivity to longitudinal strains. Nevertheless, it is still a major challenge to interrogate the FBGs at ultrasonic-level frequencies (>20 kHz). The commonly used approach for FBG demodulation is to emit a broad-bandwidth light to the grating or deploy a tunable laser with a concentrated wavelength to sweep within a specified period of light wavelength, which is demonstrated via **Equation 2-1**. For a multiplexing configuration, the same principle also applies on the premises that the Bragg wavelengths of multiplexed FBGs are not overlapped on the reflected spectrum, which is consistent with current practical applications for commercialized FBG interrogators.

Figure 3-1(a) and **3-1(b)** shows 2 mainly used FBG interrogation schemes on multiplexing. The FBGs are multiplexed through continuously bonded optical fiber, with spreading Bragg wavelengths. In the broadband light configuration, the reflected FBG spectrum shows 3 peak wavelengths that are automatically identified and used for measuring wavelength shift via photodetectors. This process can also be achieved via a sweeping laser source, as shown in **Figure 3-1(b)**.

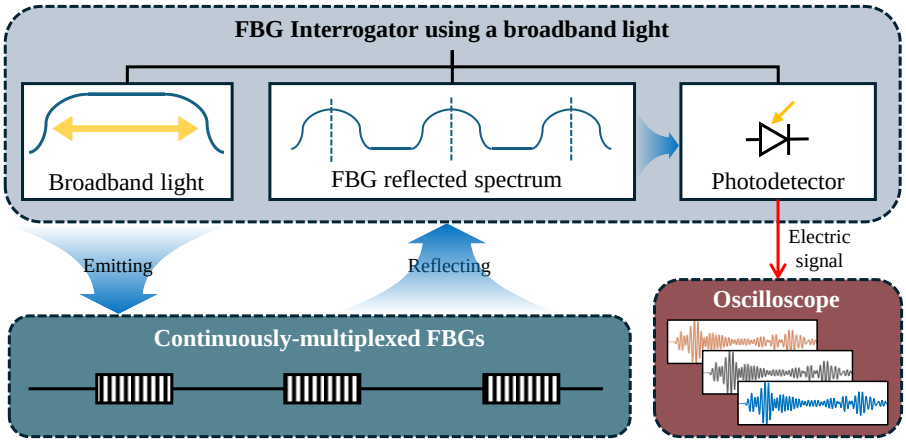

(a)

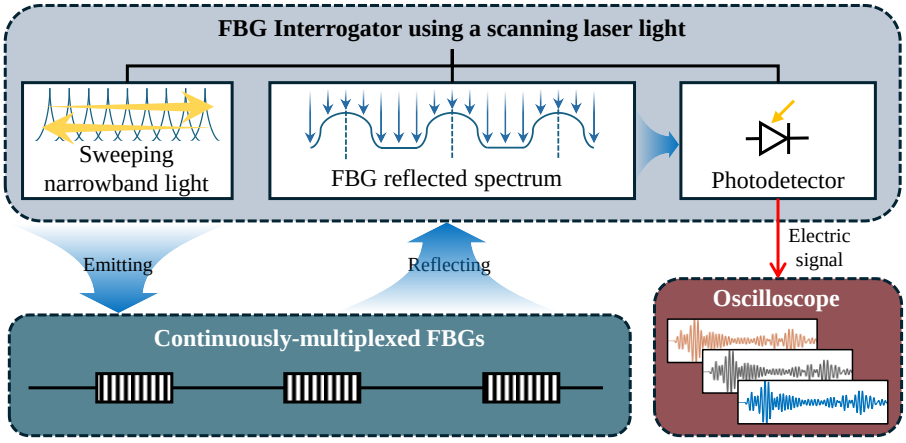

(b)

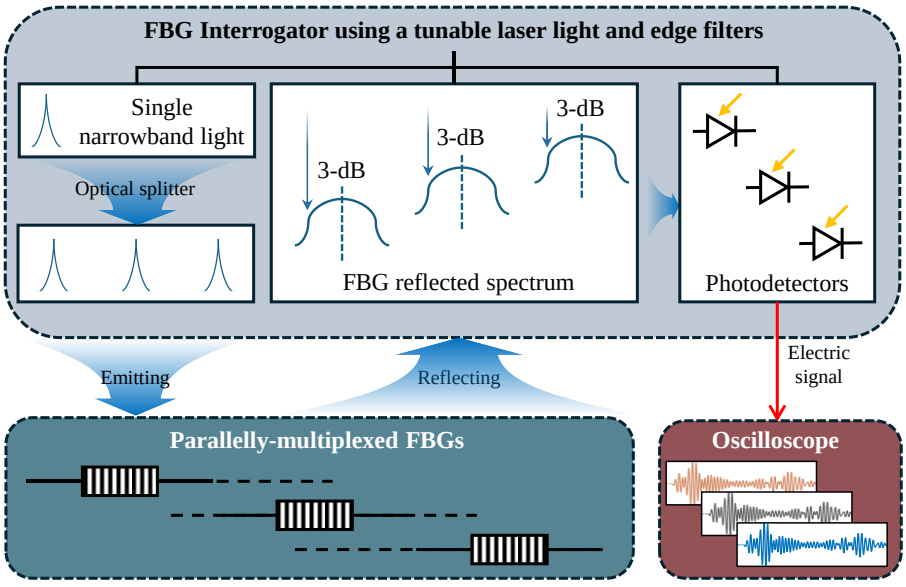

(c)

Figure 3-1. Comparison between 3 multiplexing schemes for FBG demodulation: (a) scanning laser-based, (b) broadband light source-based, (c) edge filter-based.

By constantly changing the laser emitting wavelength at a high speed, the multiplexed FBG spectrum can be obtained. Compared to the approach using a broadband light, this scheme can effectively improve the measurement resolution. The above 2 approaches introduced are commonly used for commercialized FBG interrogators. However, the sampling frequency for those interrogation systems can hardly surpass 5 kHz, limited by the demodulation strategies. This has ultimately prevented multiplexed FBGs from sensing ultrasound in solid media.

The most convenient and efficient solution to demodulating FBGs at an ultrasound-level sampling frequency is to adopt the edge filters which is illustrated in Chapter 2. The multiplexing for edge filters is extremely difficult as the wavelength of the emitting laser light is fixed at the 3-dB position of a single FBG spectrum. Therefore, to solve this problem this study proposes a novel scheme using an optical splitter to demodulate parallelly multiplexed FBGs which share the aligned Bragg wavelengths (**Figure 3-2**). The tunable laser emits narrowband laser light at the 3-dB position of the FBG reflected spectrum. The laser light is evenly distributed by a Planar Lightwave Circuit (PLC) splitter, and the laser power is emitted into multiple optical fibers, with each optical port transmitted to a 3-port optical circulator to emit and transmit reflected light from FBGs. Then the grating wavelength shift can be mapped to laser optical power intensity change via photodetectors. The above process is visualized and demonstrated in **Figure 3-1(c)**. In this setup, laser intensity variations can be measured for each FBG within the

array. Unlike conventional single-FBG systems, this multiplexed configuration offers a key advantage: the ability to capture richer ultrasonic signal data across multiple sampling channels concurrently.

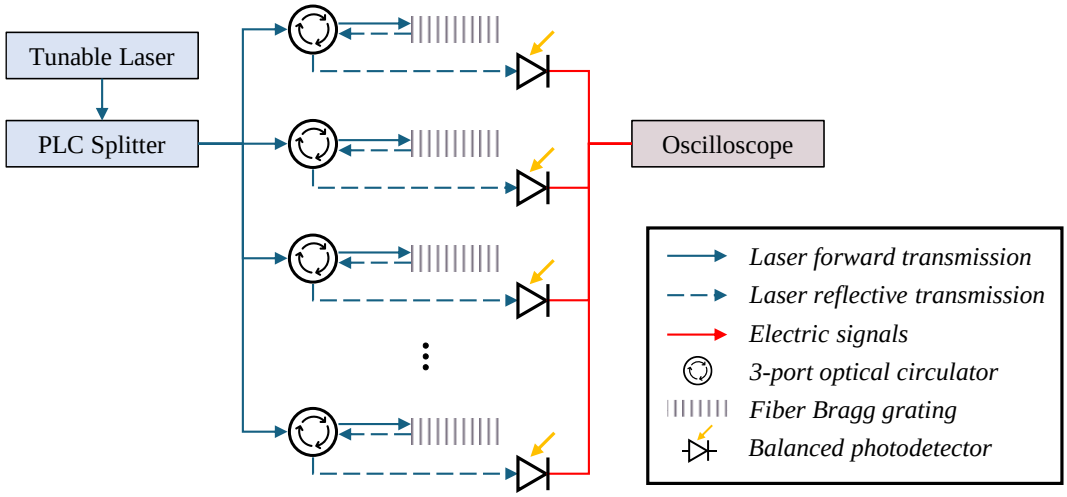

Figure 3-2. Schematic of demodulating an ultrasonic FBG array.

3.3. Hybrid sensing system design and implementation

3.3.1. System design

A hybrid sensing system designed for the high-speed interrogation of an FBG array is introduced in this study, consisting of mainly the actuation module and the transducing module as shown in **Figure 3-3(b)**. This system is defined as a PZT-multiplexed-FBG (PZT-MFBG) hybrid sensing system. To further demonstrate the superior performance and the innovative design of the demodulation strategy, **Figure 3-3(a)** also shows the FBG high-speed demodulation strategy proposed in literature (X. Sun et al., 2022), which is essentially based on the edge filtering technique. As opposed to the previous

hybrid sensing system, the multiplexing feature enables a more comprehensive ultrasonic sensing performance. A total of 8 FBG sensors (maximum) can be demodulated simultaneously, at the sampling frequency of 10 MHz (maximum). To conclude, the following updates are made to the previous system:

(1) FBG sensors: as mentioned above, the wavelengths for each FBG should be consistent with a deviation within 0.1 nm. The wavelength of 1550 nm is selected based on the responsivity spectrum of the balanced photodetectors (BPDs) to achieve the optimal measurement performance.

(2) Tunable laser source: due to the split laser power, the emission power of the tunable laser source output is updated to 15 dBm. The signal amplitude decline brought by split laser power is inevitable in this multiplexing configuration.

(3) BPDs: the optical light reflected from the gratings cannot be induced into the same optical channel, because the reflective light wavelength should be theoretically identical. Thereupon, an update is made by introducing a multi-channel BPD to receive and transmit the reflective light from multiple optical circulators.

(4) Oscilloscope: due to the multi-channel sensing characteristics, the oscilloscope should be equipped with multi-channel display and data storage functions to achieve successful measurements.

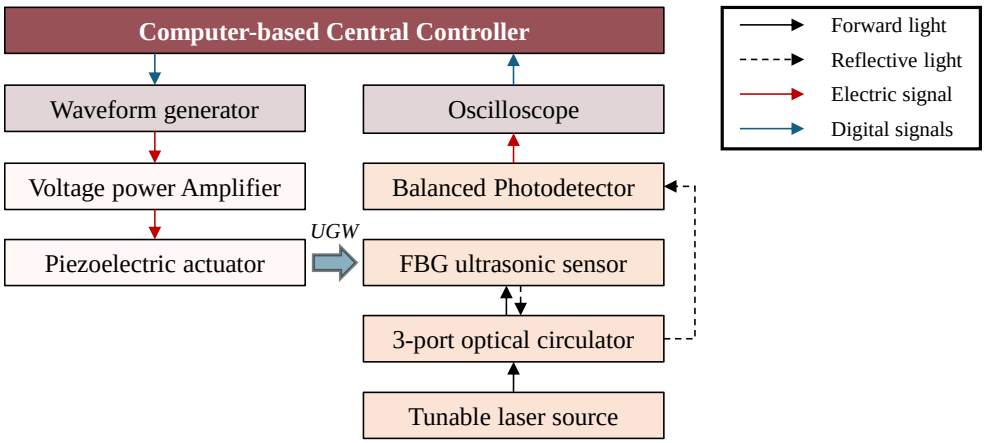

(a)

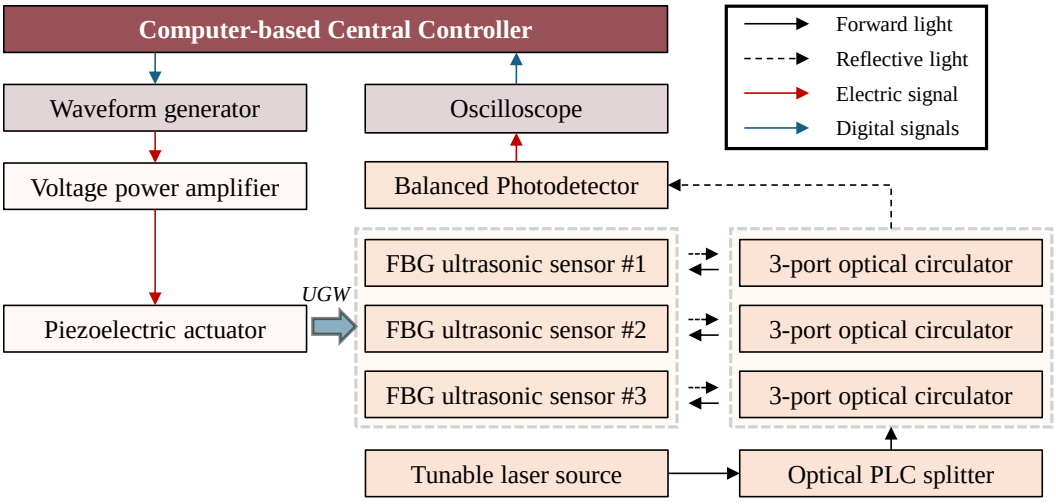

(b)

Figure 3-3. Schematics of the FBG edge-filter demodulation setup. (a) the system introduced in literature (Sun et al., 2022); (b) the system proposed in this study.

The PZT-MFBG hybrid sensing system, depicted in **Figure 3-4**, integrates piezoelectric actuation with fiber Bragg grating (FBG) array detection through a carefully designed experimental setup. A computer-controlled arbitrary waveform generator (PXI-5412, National Instruments) produces input signals that are amplified 200 times by a power amplifier (HVA-400-A, Ciprian), delivering a 200 V excitation to the PZT actuator. This excitation generates mechanical displacements that are subsequently captured by

the FBG array. The optical demodulation system employs an edge-filtering technique, where a narrow-bandwidth laser source (TLB-6700, Newport) is precisely tuned to the 3-dB point of the FBG spectrum. An optical coupler splits the laser output into 3 channels for simultaneous interrogation of FBG sensors, with their reflected signals being converted to electrical output via balanced photodetectors (2117-FC, Newport) capable of 10 MHz detection bandwidth.

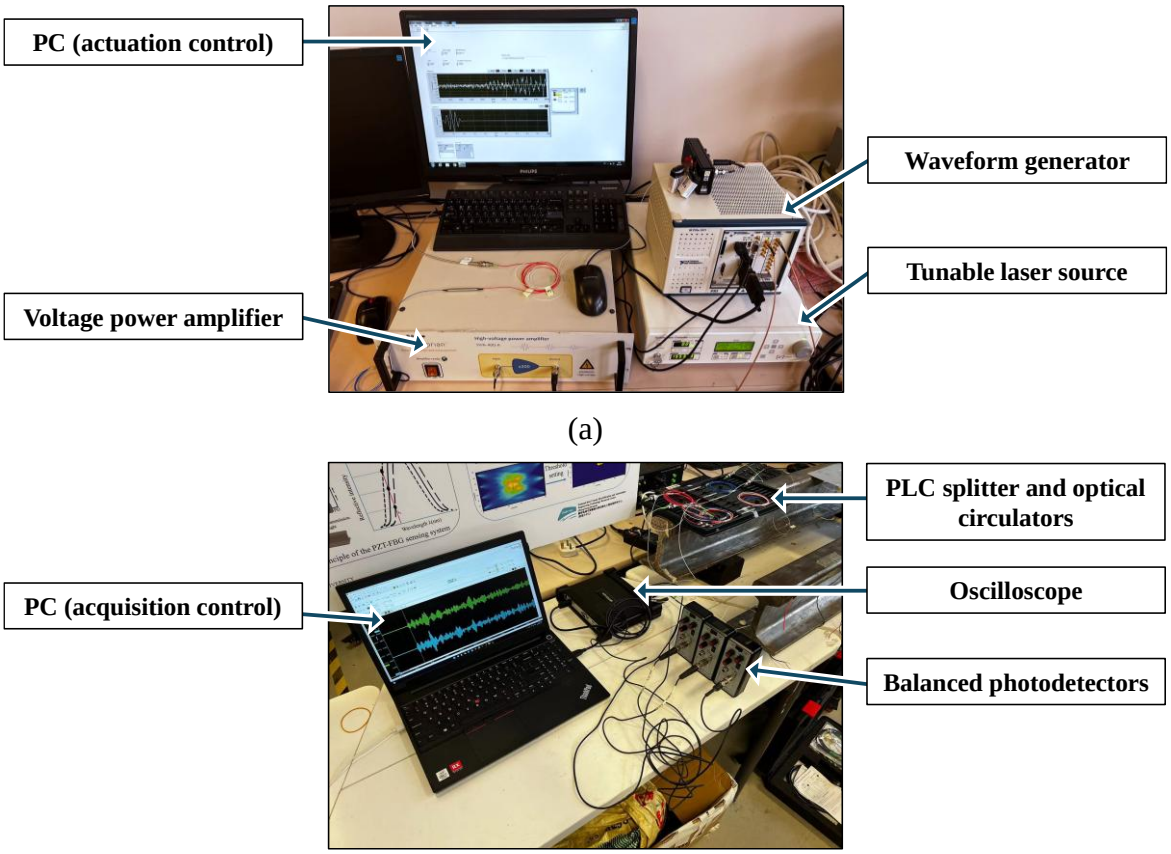

Figure 3-4. Experimental setup of the PZT-MFBG hybrid sensing system: (a) the excitation module, and (b) the transducing module.

Table 3-1. Specifications for PZT.

Parameters	Value
Diameter × thickness	8×1 (mm)
Material	PZT-5H
Resonant frequency	~2 (MHz)
Dielectric constant ε_{r3}^{T}	3200
Piezoelectric constant $d31$	275 (-1012 m/v)
Acoustic velocity v_t	3900 (m/s)

Table 3-2. The parameters of the hybrid sensing system.

Module	Equipment Name	Descriptions	Key Parameters
actuation module	Arbitrary Waveform generator	Generating a 5-cycle sinusoidal tone bursts at different frequencies	Max. output: 1 V
	Power amplifier	Amplifying the digital signals and output electrical signals	Voltage gain: 200 times Max. input: 1 V Max. output: 200 V
	PZT	Receiving the electrical signals and generating ultrasonic waves	Displacement at 200 V: 9 μm
transducing module	Tunable laser source	Emitting narrow-bandwidth laser	Laser wavelength: 700-1600 nm Laser power: 50 W
	FBG array	Receiving ultrasonic waves	Bragg wavelength: 1560.0 nm Grating length: 10 mm Fiber type: bare fiber
	BPD	Transforming light wavelength shifts into electrical signals	Detector material: InGaAs Responsivity: 1 A/W
	Oscilloscope	Receiving electrical signals and sample the time series under trigger mode	Sampling frequency: 10 MHz Sample length: 1

This configuration enables multi-channel ultrasonic measurement while maintaining high sensitivity, with complete system specifications detailed in **Table 3-2**. Under this configuration, the detectable length for FBGs ranges from 1 to 3 meters, depending on the excitation frequency of the UGW. To leverage the detection range and inspection accuracy, the choosing of central excitation frequencies is vital to obtain satisfactory results.

It is also worth noting that BPDs are adopted to improve the SNR by reducing the laser intensity noise. The BPDs receive both reflection and transmission light so that the voltage obtained by two parts of BPD would simultaneously experience changes with the same amplitudes but opposite phases (Q. Wu & Okabe, 2012). The voltage output of a BPD V can be calculated below:

$$V = 2R\Delta\lambda_b GP \quad \textbf{(3-1)}$$

where G denotes the grating slope of the 3-dB position of the FBG being demodulated, R is the response factor of the photodetector considering the gain factor, and finally P is the laser power of the tunable laser source. It can be observed that the use of BPDs can double the voltage amplitude of obtained signals improving the SNR at the same time.

When multiplexing is being deployed, it can be assumed that the split optical power P_n will not affect other parameters in **Equation 3-1**. In this case, P_n specifically denotes

the split laser power under a 1-to-n multiplexing configuration. To theoretically demonstrate the amplitude of the signal acquired, the optical power of the system output is calculated.

To simplify the calculation, assume that the coupling ratios for each port of the PLC splitter should remain constant when the insert light wavelength is centered at 1550 nm, so that the theoretical power output for each port should be consistent. The power loss due to the optical connectors are not considered in this case, because under ideal circumstances fiber fusion splicing should be preferably used. While the insertion loss for a typical 3-port optical circulator should be approximately 0.8 dB (1.6 dB for both 1-2 and 2-3 transmitting), the typical insertion loss for PLC splitters with varying number of output ports are quite different, which is demonstrated in **Table 3-3**. Therefore, the optical power P_n can be calculated by:

$$P_n = \frac{P}{n} \times 10^{-\sum \frac{L_i}{10}} \quad \textbf{(3-2)}$$

where $\sum L_i$ should include the insertion losses for both optical components. It should be mentioned that this equation does not include sophisticated optical power loss due to reflections and refractions within the optical fiber transmission process.

Table 3-3. Typical insertion loss of PLC splitters with varying number of ports *n*.

n	1	2	4	8	16
insertion loss (dB)	0	3.7	7.7	10.7	13.5

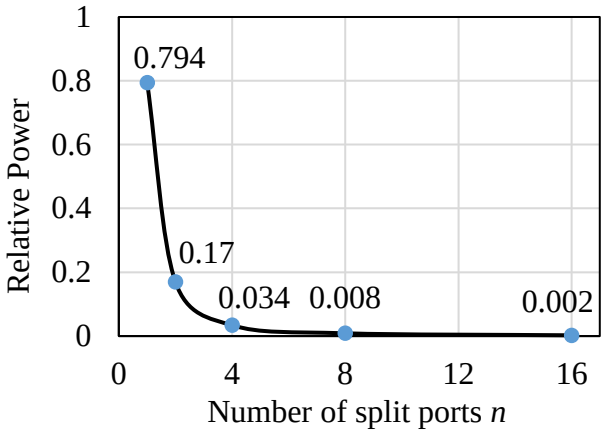

Figure 3-5. Relative optical power regarding different multiplexing configurations.

The relative power calculated regarding varying number of multiplexed ports is shown in **Figure 3-5**. It can be obviously observed from the curve that the optical power loss is significantly increased with the number of split channels within an optical system. Thereby, 2 solutions are proposed to possibly address this challenge: 1) try using tunable laser sources with more transmitting channel, or 2) simply increase the laser power. The first solution is recommended because though the cost for instrumentations may be raised, it does guarantee better signal acquisition quality. The second solution may cause a higher level of noise in signal acquisition, which may bring inconvenience in signal processing.

The reflective optical spectrum of the three FBGs installed on the rail segment, along with the tunable laser source intensity, is presented in **Figure 3-6**. As clearly demonstrated in the figure, all three FBGs exhibit nearly identical Bragg wavelengths (λ_B) centered at approximately 1550.31 nm. The narrow-band laser source, carefully tuned to 1550.22 nm, aligns precisely with the 3-dB point at the edge of the FBGs' pass-

band wavelength period, optimizing the system's detection sensitivity. Notably, the laser source demonstrates exceptional performance characteristics, including a mode-hop-free fine-tuning range of 240 pm and outstanding wavelength stability of ±2 pm, ensuring high-precision measurements. This precise spectral alignment between the FBGs and the laser source is critical for achieving optimal system performance in ultrasonic wave detection.

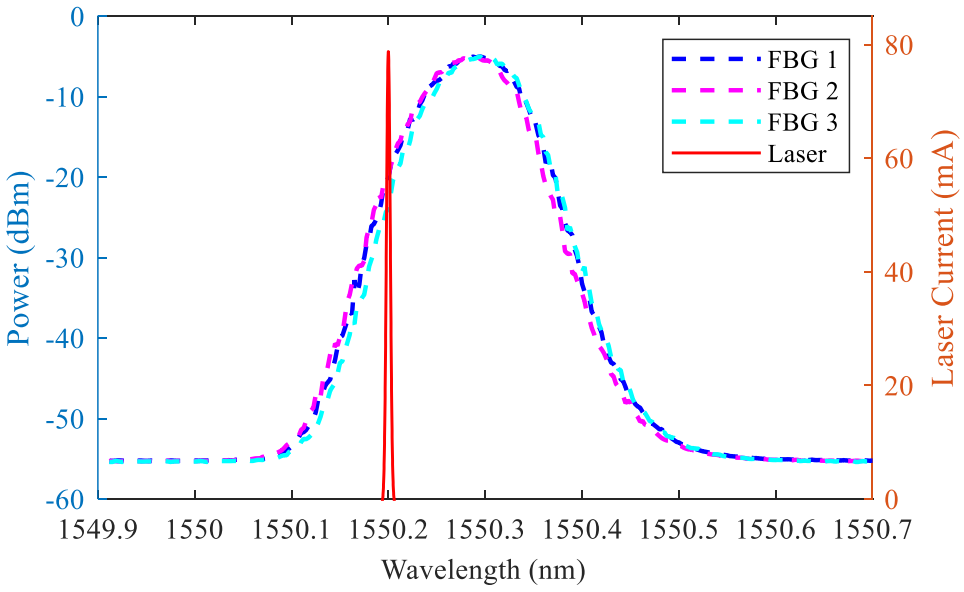

Figure 3-6. Reflective optical spectrum of FBGs and the tunable laser intensity.

3.3.2. System performance testing

3.3.2.1. Bonding quality tests of PZT sensors

To effectively ensure the effectiveness of PZT wafers in generating UGWs in railway tracks, repeatability tests are conducted. Specifically, the PZT wafers are first installed to excite UGWs before being removed from the rail surface. The above process is

repeatedly conducted and the signals obtained from each testing procedure are compared.

The excitation signal input to the power amplifier is shown in **Figure 3-7**, which demonstrates both time and frequency domains. To improve time-domain signal resolution and clarity, the system employs a five-cycle sinusoidal tone burst modulated with a Hanning window function. This specific waveform configuration is generated by PXI-5412 (the central terminal instrument). The Hanning window modulation effectively reduces spectral leakage while maintaining good frequency resolution, and the five-cycle duration provides an optimal balance between time localization and frequency content for ultrasonic detection applications. This carefully designed excitation signal significantly enhances the system's ability to resolve ultrasonic wave features in the time domain while minimizing noise interference. The peak amplitude of the signal is 1 V, which is then amplified 200 times to excite the piezoelectric material of the PZT wafer.

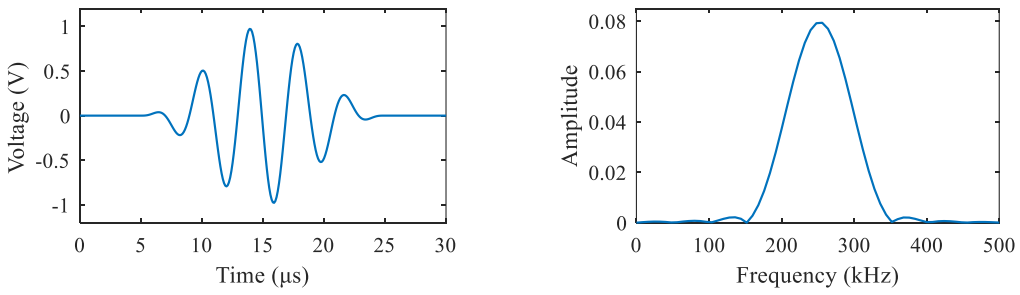

(a) (b)

Figure 3-7. Excitation signals (250 kHz) in this experiment in (a) time domain, and (b) frequency domain.

The repeatability testing result is shown in **Figure 3-8**, where clearly proves the feasibility and reliability of the ultrasonic excitation of the proposed hybrid sensing system. To evaluate the difference between each testing, the acquired UGW signals are compared to demonstrate the repeatability. Based on the observation, it can be thus concluded that the bonding quality of PZT is guaranteed to be constant.

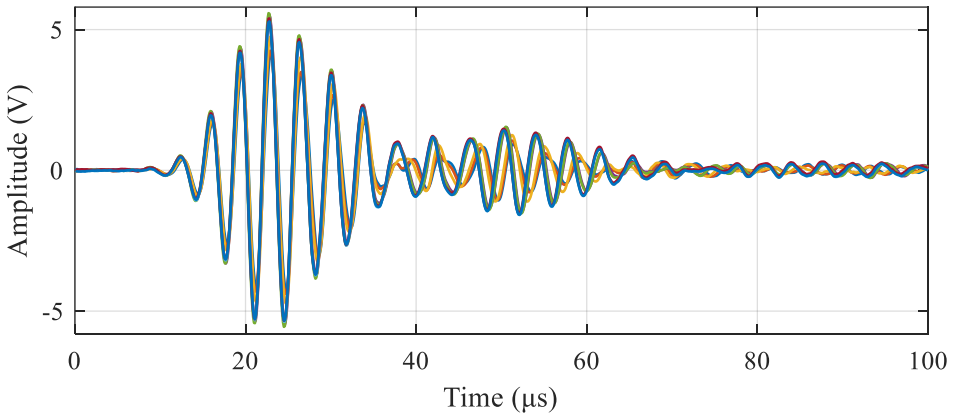

Figure 3-8. Repeatability testing results.

3.3.2.2. FBG frequency response

The sensing quality of FBGs is also studied. Specifically, the bonding agent is primarily considered as an important factor in ultrasonic sensing. Therefore, 3 types of adhesives, namely Cyanoacrylate, Epoxy, and Silicone adhesives, are respectively used to install FBGs. The gratings of the fiber is coated with acrylate to protect them from mechanical damage, moisture, and environmental factors. Some basic prior knowledge about the bonding performance in regard to each adhesive involved in this evaluative experiment is listed in **Table 3-4**. Considering the overall performance, Epoxy adhesives are apparently ideal candidates for this specific utilization, because of the durability,

reliability, and minimum interference with optical fiber sensing quality. Although it takes much longer to install the FBG using Epoxy adhesives than others, the low degradation rates can guarantee long-term use without much maintenance work.

Table 3-4. Performance comparison between adhesives.

Adhesives	Cyanoacrylate	Epoxy	Silicone
Interactions with the coatings	Yes	No	No
Mechanical stress during curing	Low	Low	High
Curing time	Fast	Slow	Slow
Bond strength and elasticity	High	High	Low
Bond degradation	Significant	Insignificant	Insignificant
Thermal resistance	Poor	Excellent	Good

The experimental evaluation is conducted by comparing the peak-to-peak amplitudes of FBG response under the same excitation modes. The FBGs are bonded using the 3 candidate adhesives on the same position of the railway surface (**Figure 3-9**). Higher levels of response amplitudes indicate better sensing quality with higher SNR. A series of excitation frequency bands are adopted, ranging from 100 kHz to 500 kHz, and the corresponding peak-to-peak amplitudes are demonstrated in **Figure 3-10**. For each excitation frequency, the UGW acquisition is repeated 10 times to calculate the average response. It can be clearly observed that both Cyanoacrylate and Epoxy has a relatively higher frequency-domain sensitivity to UGW propagating in railway tracks. Figure 3-9 also indicates that FBGs, when bonded as instructed in this study, have higher response amplitude towards UGWs of 150 - 300 kHz. This frequency range also

indicates that for the hybrid sensing system, it is feasible and applicable to excite UGWs within this range. In comparison, the performance of Silicone adhesive is much less satisfactory.

(a) (b) (c)

Figure 3-9. The bonding of FBGs using different types of adhesives: (a) Cyanoacrylate; (b) Epoxy; (c) Silicone.

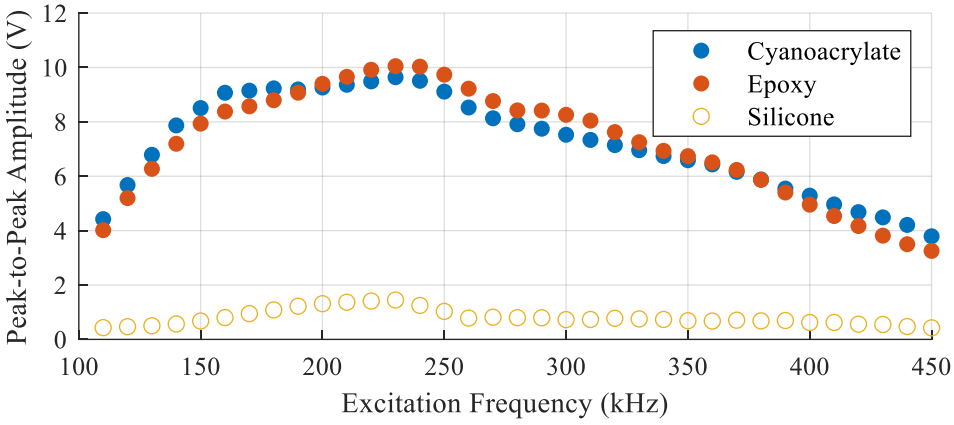

Figure 3-10. The effect of excitation frequency: FBG response (peak-to-peak amplitudes) with varying excitation frequencies (f).

Thereby, the following conclusions and suggestions are given based on the research findings in this section:

(1) The Cyanoacrylate adhesives can be used for temporary bonding of FBGs on railway tracks due to its fast-curing characteristics. The measurements can be instantly carried out after bonding.

(2) Epoxy is more suitable for permanent installation of FBGs owing to its reliable bonding performance and high sensitivity towards a wide range of ultrasound excitation frequencies.

(3) The Silicone-based adhesive is outperformed in terms of frequency-domain sensitivity which results in poor ultrasonic measurements, thus is not recommended.

3.3.3. Cost-effectiveness evaluation

Besides the excellent sensing quality of the proposed hybrid sensing system, one significant advantage it offers is the cost-effectiveness. To intuitively demonstrate the savings, **Table 3-5** presents detailed break-down costs (in HKD) regarding the proposed hybrid system. A comparative system is also considered, retrieved from a representative work from S. X. Chen et al. (2021). The data is collected based on the quotations provided by local agents or suppliers.

Three system functions are compared, namely interrogation, sensor, and transmission. For the interrogation function, the proposed system, which uses an 8-channel interrogation setup with a relatively more expensive tunable laser source and optical

components costs twice as much as the commercial ultrasonic system. For the sensor function, the proposed system uses disposable FBG sensors, achieving significant savings of 98.8%. Lastly, for transmission, the proposed system uses armored single-mode optical fiber, whereas the ultrasonic system uses electric cables with EM shielding costing significantly more, yielding savings of 87.5%. Overall, the proposed system demonstrates notable cost reductions in the sensor and transmission functions but incurs higher costs for interrogation. Thereby it can be concluded that the proposed system is suitable for deployment of a large sensor network where the number of sensors and the signal transmission lengths are considerably enormous.

Table 3-5. Break-down costs (HKD) of the proposed hybrid system in comparison with the ultrasonic system proposed by Chen et al. (2021).

System functions	Proposed system		D. Li et al. (2021)		Savings
	Descriptions	Price	Descriptions	Price	(%)
Interrogation	8-channel interrogation, including a tunable laser source, balanced photodetectors and optical components	80,000	8-channel oscilloscope with high resolution and deep memory	50,000	-60.0%
Sensor	8 FBGs with acrylate coating	400	8 high-frequency piezoelectric sensors	24,000	98.3%
Transmission	Armored single-mode optical fiber	800 (1 km)	Electric cable with EM shielding	6,000 (1 km)	86.7%

3.4. Numerical investigations: proof-of-concept

To further reveal the UGW propagating mechanisms and verifying the effectiveness of the proposed hybrid system, a finite element model (FEM) is developed to model the UGW generating and receiving processes. Finite element modeling provides a highly efficient approach for studying ultrasonic guided wave propagation in rail structures, as it allows direct acquisition of transient wave signals under precisely controlled conditions. This numerical method eliminates many experimental constraints, enabling researchers to systematically examine wave behavior while maintaining complete command over all test parameters. Consequently, numerical investigations are carried out based on the constructed FEM representation of a BS100R rail, and UGWs are excited through applying velocity history towards rail surface. Detailed analysis is conducted in this section.

3.4.1. FEM configuration

3.4.1. Overview of the FEM

A numerical model is constructed via COMSOL Multi-physics, a commercial FEM software. The solid mechanics module is deployed to study guided wave propagation mechanisms in rails with complex cross-section. The BS100R rail segment shown in **Figure 3-11**is modelled. The section geometry is demonstrated in **Figure 3-11(a)**. To demonstrate the realistic ultrasound generation of the PZT wafer adopted in

experimental studies, the PZT wafer and the railway track are simultaneously modelled, and the 2 components are assembled (**Figure 3-11b**), forming an identical boundary pair that can accurately simulate the displacement induced by piezoelectric effects. The length of the railway track modelled in this study is 1,000 mm. The geometry parameters of the PZT component is configured based on the experimental PZT wafer as described in **Table 3-1**. An artificial crack is also placed on the same rail web plane where the PZT is bonded. The crack is simulated by creating a parametric surface which reflects the guided waves. Both the depth and the width of the crack are 2 mm, and the length of the crack is 10 mm, which is demonstrated in the perspective graph of **Figure 3-11(b)**.

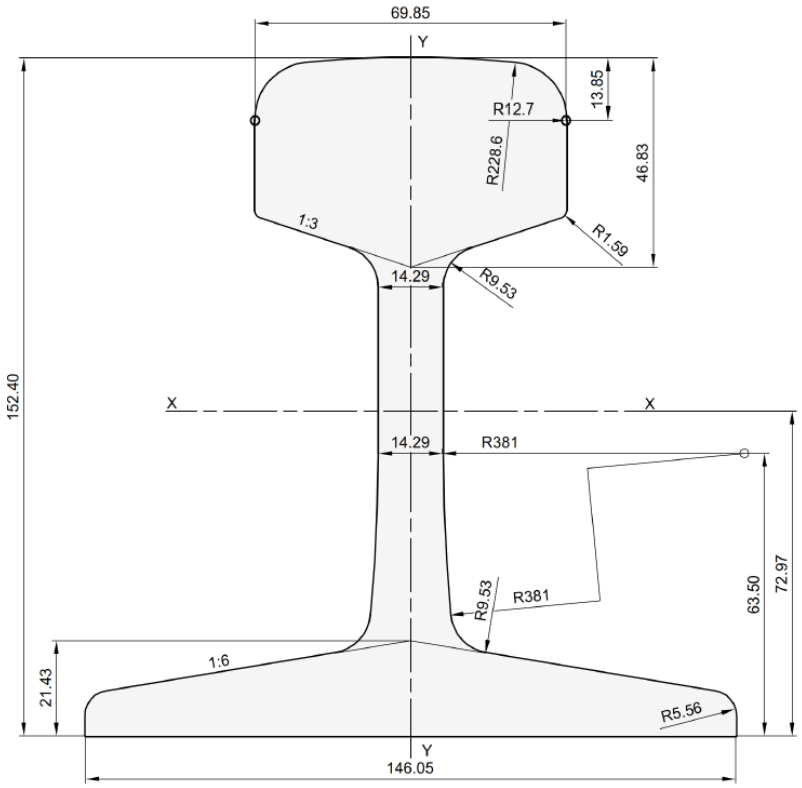

(a)

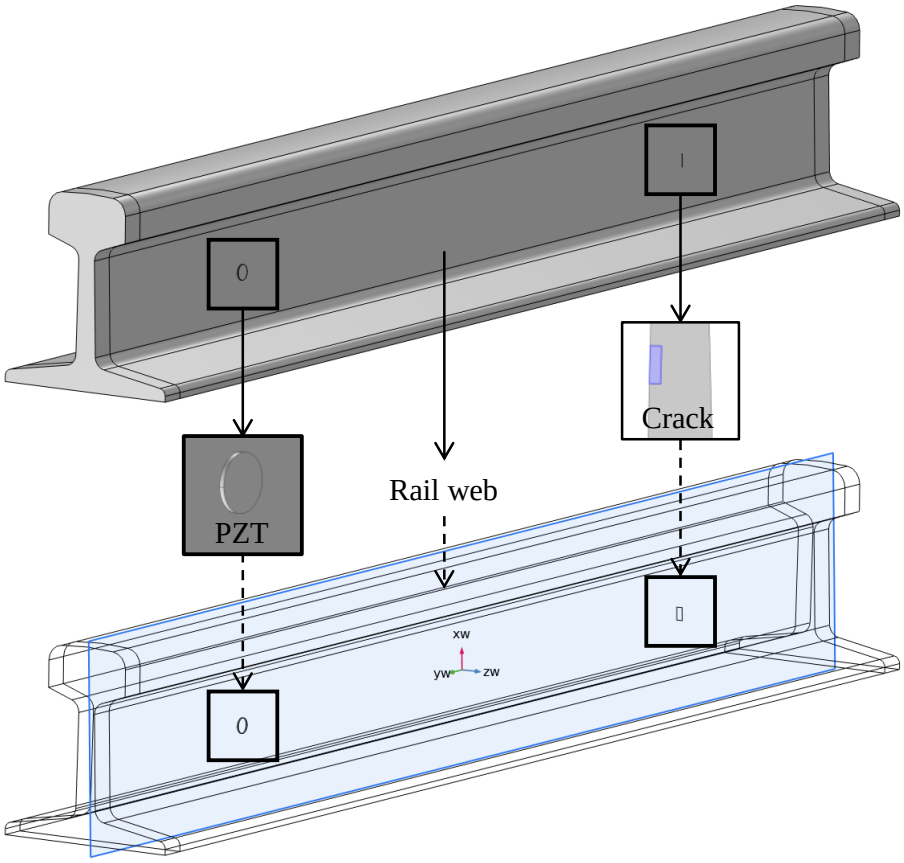

(b)

Figure 3-11. 3D rail numerical model profile: (a) section specification; (b) an overview of the rail component.

3.4.2. Material properties

The material properties of the PZT and rail components are shown in **Table 3-6**. The calculation formulas between Young's modulus, Poisson's ratio and other material properties are given as follows:

$$E = \rho(c_s)^2 \cdot \frac{3{c_p}^2 - 4{c_s}^2}{{c_p}^2 - {c_s}^2} \qquad \mu = \frac{{c_p}^2 - 2{c_s}^2}{2\left({c_p}^2 - {c_s}^2\right)} \tag{3-3}$$

Table 3-6. Material properties of the FEM components.

Variable	Descriptions	Components		Unit
		PZT	Rail	
ρ	Density	7,500	7,800	kg/m³
E	Elastic Module	7.0678×10^{10}	2.0078×10^{11}	Pa
μ	Poisson's ratio	0.3767	0.2889	/
c_p	Longitudinal wave speed	4,160	5,800	m/s
c_s	Shear wave speed	1,850	3,160	m/s

3.4.3. Mesh grid configuration

The maximum mesh grid size is restricted to one eighth of wavelength. As the central excitation frequency is set to be 300 kHz, it is estimated that the maximum mesh sizes for rail and PZT components are respectively 1.5 mm and 0.8 mm, assuming that shear wave is the dominant propagation mode. For both components, the free tetrahedral mesh grid type is deployed. Thereby the mesh grid results for each modelling component are demonstrated in **Figure 3-12**.

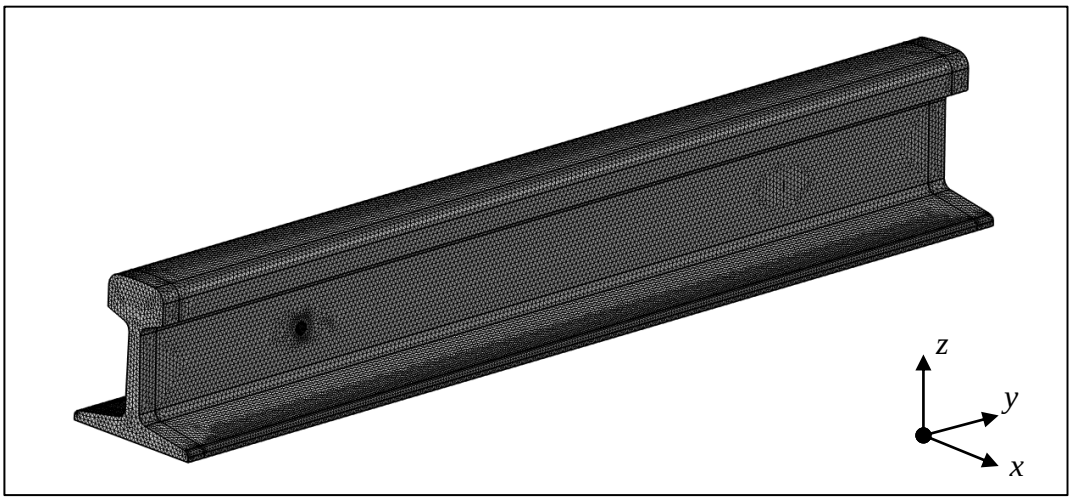

(a) an overview

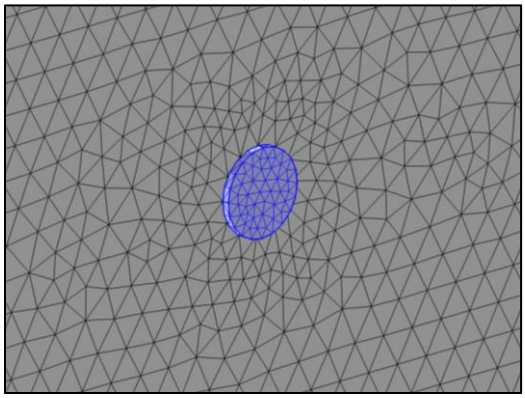

(b) the PZT component

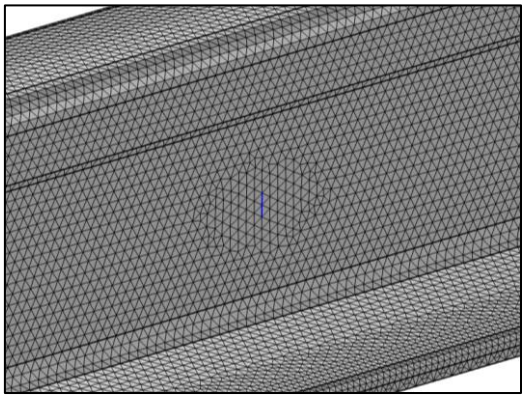

(c) the crack area

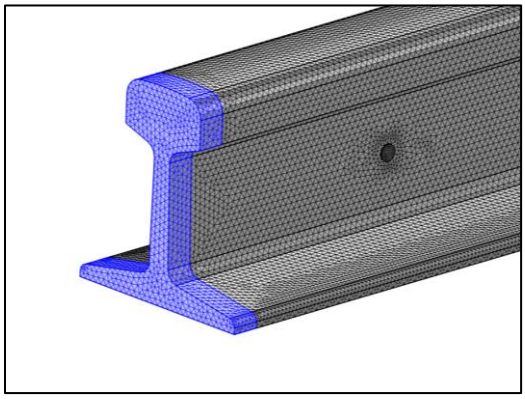

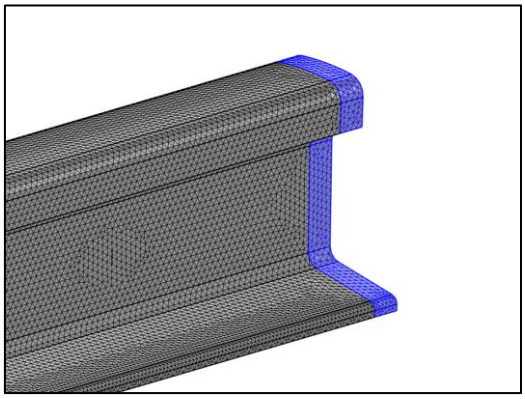

(d) the infinite domains of both ends

Figure 3-12. The meshing grid configuration of the FEM.

3.4.4. Infinite domains

To effectively reduce computational costs, the infinite domains and low-reflectivity boundaries are configured, where the damping can eliminate reflections and avoid interference brought by end reflections. The length of both infinite element domains is 20 mm as shown in **Figure 3-12(d)**. This configuration can effectively simulate UGW longitudinal propagation in a long railway track. The radial mesh width of the infinite domain is set to 6-unit lengths to ensure that the infinite domain can provide effective damping for the weakening of P waves and S waves (**Figure 3-12d**).

3.4.5. UGW generation and sensing

To simplify piezoelectric effects in this numerical model, UGWs are generated by applying a dynamic velocity history towards the piezoelectric layer of the PZT component. The peak value equals typical compression wave velocity in railway materials, which is approximately 5,800 m/s. The input signal history is composed of a five-cycle sinusoidal tone burst demodulated by a Hanning window, as is often utilized in previous research. Thereupon, the time history input can be formatted as follows,

$$P(t) = \frac{v_0}{2} \cdot \left[1 - \cos\left(\frac{2\pi f_0 t}{n}\right)\right] \cdot [\sin(2\pi f_0 t)] \quad \textbf{(3-4)}$$

where v_0 denotes the compression wave velocity, f_0 denotes the central excitation frequency which in this case equals to 300 kHz, and n equals to 5 which is the number of cycles of sinusoidal tone burst. The signal is plotted in **Figure 3-13**. The geometry characteristics of the FBG sensor are also reasonably simplified. In this numerical study, the ultrasonic signal acquired by FBG is represented by the average longitudinal dynamic strain, on the premise that the grating period is insensitive to shear strain. The sampling frequency is set to be 10 MHz, thereby the time step for transient function is 0.1 μs with the total time step of 500 μs.

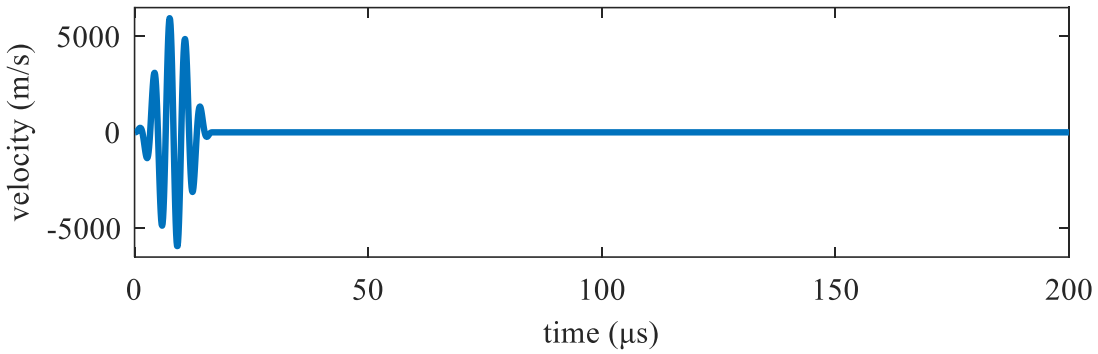

Figure 3-13. Input history of the FEM.

3.4.2. Guided wave propagation mechanisms

3.4.2.1. Wave propagation analysis

The 3-D displacement fields corresponding to 3 key time slots have been reconstructed via FEM and demonstrated in **Figure 3-14**. The UGW is generated through the radical vibration of the PZT bonded on the railway web, as shown in **Figure 3-14(a)**. Through multiple scatterings and reflections, the UGW starts to propagate via the longitudinal direction (**Figure 3-14b**). Then when $t = 180$ μs, several groups of waveforms encounter the artificial crack. It can be clearly observed that the existence of the crack interfere with the wave propagation causing reflections. This phenomenon is the basic principle based on which defect detection is carried out.

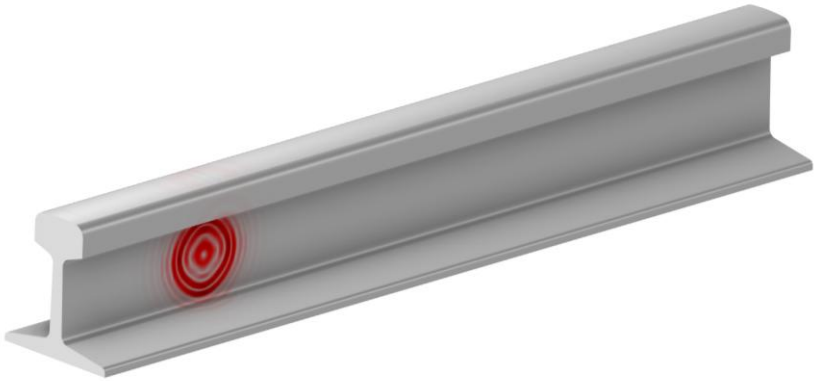

(a) t = 20 μs

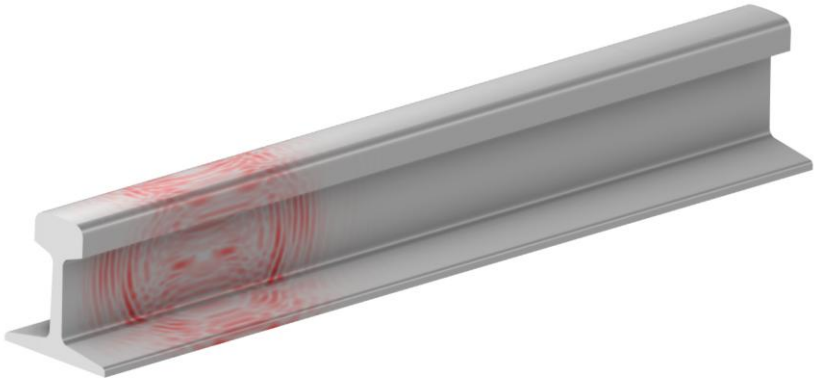

(b) t = 50 μs

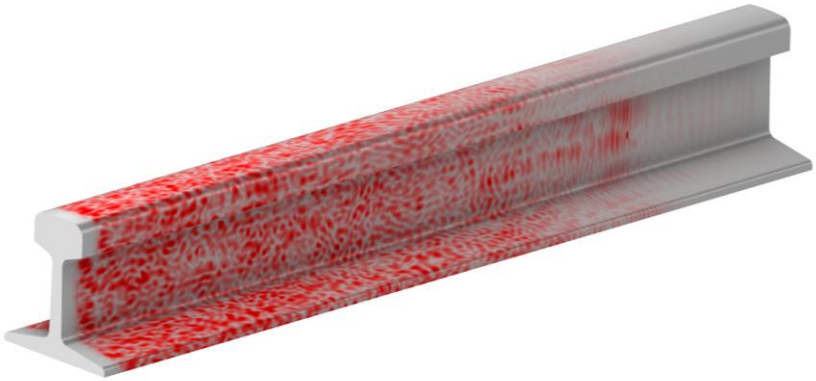

(c) t = 180 μs

Figure 3-14. Reconstruction of 3-D displacement fields.

To further clearly study the UGW propagation process under the configured excitation mode, the railway web surface is extracted to construct 2-D velocity fields. **Figure 3-**

15(a) shows the excitation of UGW creates radical wave velocities propagating from left to right (longitudinal direction). Then later when t = 50 μs, it can be observed that the longitudinal wave-dominant wave group (Group 1) travels faster than Group 2 which is defined as a group of mixed modes (**Figure 3-15b**). When t = 100 μs, another wave group (Group 3) is formed, as the result of reflections and scatterings from the railway boundaries (**Figure 3-15c**). Then Group 1 and Group 2 encounters the artificial crack at the time of approximately 180-200 μs, as shown in **Figure 3-15(d)** and **(e)**. In comparison, the waves in Group 1 result in weaker amplitude of reflections due to the rail crack than Group 2. It indicates that the longitudinal waves may not be sensitive to the existence of the vertical crack simulated in this case. The mixed mode wave group, i.e., Group 2, contains higher energy while the longitudinal wave-dominant wave modes, i.e., Group 1, travel faster but also attenuates faster which is not suitable for defect detection. Finally, the wave velocity field turns too complex to comprehend after reflections and scattering (**Figure 3-15f**). What could be intuitively derived from studying the propagation process of the rail web surface is that under this specified PZT excitation configuration, UGWs with the central frequency of 300 kHz are generated and, because of the thickness of the railway web, the rail can be approximated as an interface waveguide where Rayleigh waves are predominant travelling through the surface and subsurface of the rail. This conclusion can be derived from the observations that surface displacement is more significant than internal displacement.

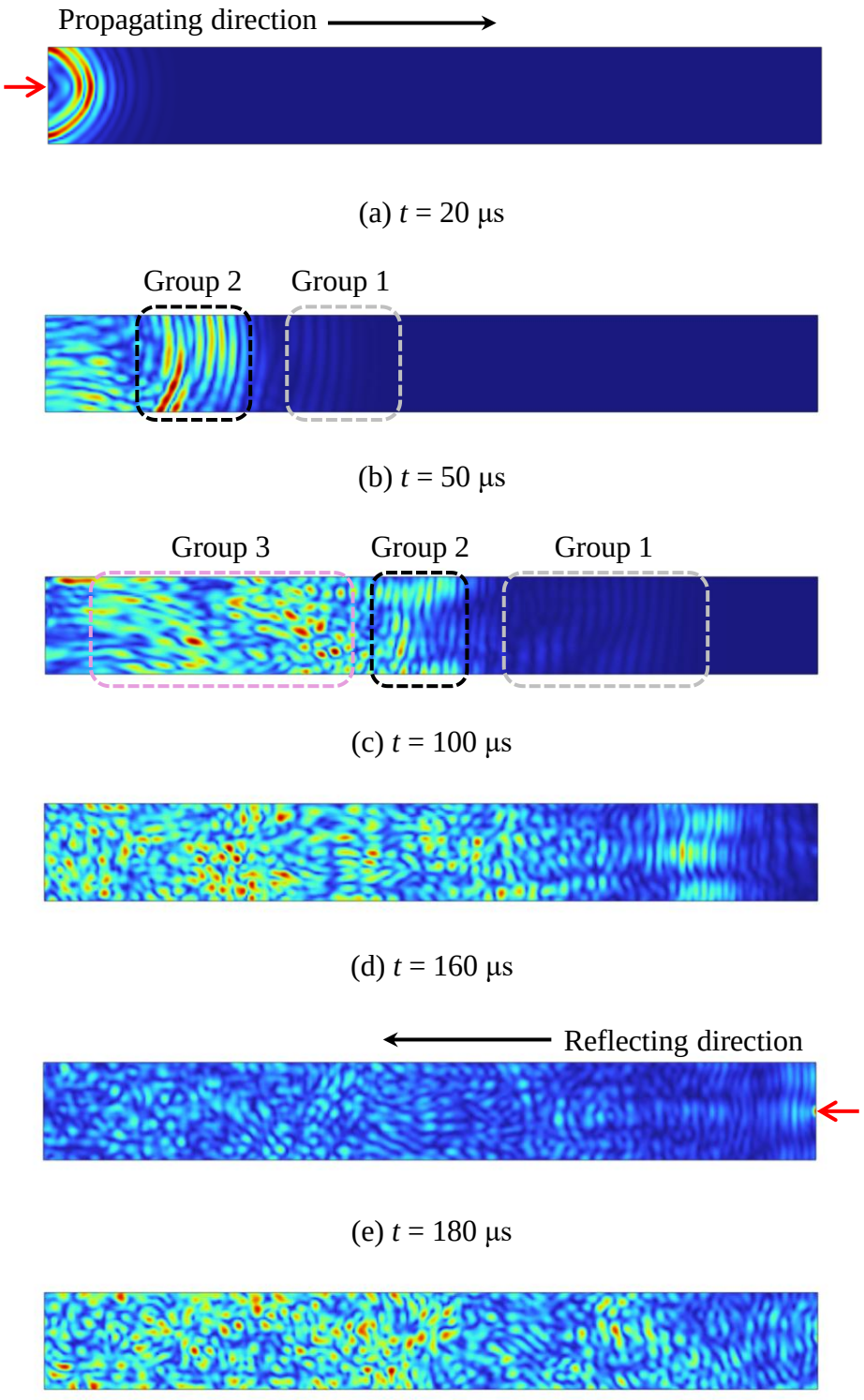

Figure 3-15. Reconstruction of 2-D wave velocity fields of the rail web vertical (y-z) surface.

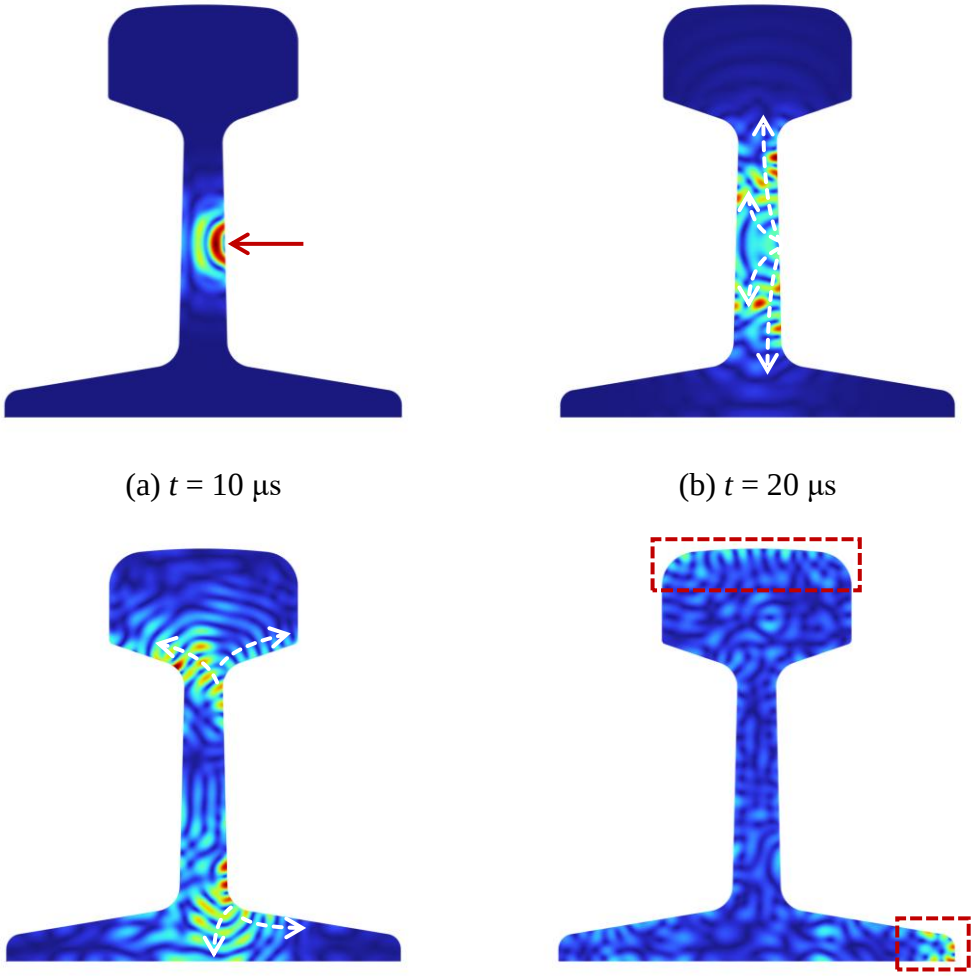

(a) t = 10 μs (b) t = 20 μs

(c) t = 30 μs (d) t = 50 μs

Figure 3-16. Reconstruction of 2-D wave velocity fields in the transverse (x-z) plane.

The transverse rail section where the PZT is located is also extracted from the FEM to reconstruct the 2-D velocity field, which is shown in **Figure 3-16**. The UGW is excited from the PZT and starts to propagate on both sides of the rail web as shown in **Figure 3-16(a)** and **(b)**. As the wave groups reach the boundary where the web and the head joins, the waves are split into 2 divisions (**Figure 3-16c**). Part of the waves keep travelling via rail head surface while the rest propagates into the rail head until they reach the top surface of the rail. Similar findings can be found in rail foot. Finally, the

waves meet at the surface of the rail head and foot, respectively, as demonstrated in **Figure 3-16(d)**. This finding is perfectly aligned with previous observations of guided wave propagation mechanism of the rail web surface. When the ultrasonic frequency increases, the shorter wavelength would automatically satisfy the semi-infinite wave guide assumption. Through reconstructing the wave field, the wave power is more concentrated on the railway surface than the internal materials, which further proves that the surface waves are predominant.

The following part of the section provides theoretical proof of the existence of Rayleigh waves by calculating the wave velocity. Under the excitation configuration where the PZT wafer is bonded on the railway web surface, Rayleigh waves are generated that travels on rail surface and subsurface. The wave propagation obey Navier's governing equation is first given as,

$$(\lambda + \mu)\nabla(\nabla \cdot \boldsymbol{u}) + \mu\nabla^2\boldsymbol{u} = \rho\frac{\partial^2\boldsymbol{u}}{\partial t^2} \quad \textbf{(3-5)}$$

in which $\boldsymbol{u}$ is the displacement vector, and λ, μ are Lame constants. The displacement vector $\boldsymbol{u}$ can be divided into two components, ϕ and ψ, indicating the longitudinal and transverse wave, respectively:

$$\boldsymbol{u} = \nabla\phi + \nabla \times \psi \quad \textbf{(3-6)}$$

Then, the original governing equation can be separated into two simple wave equations, representing dilatational waves and one for rotational or shear waves,

$$\nabla^2\phi - \frac{1}{{c_l}^2}\ddot{\phi} = 0$$
$$\nabla^2\psi - \frac{1}{{c_s}^2}\ddot{\psi} = 0 \quad \textbf{(3-7)}$$

Considering that the PZT is a cylinder object and that the force is applied directly to the rail surface (z-directional), the 2-dimensional case is deployed by only considering the displacement in the sagittal plane formed by the x and z unit vectors. Finally, the harmonic solution can be obtained,

$$\phi = A_1 e^{-kqz} e^{ik(x-ct)}$$
$$\psi = B_1 e^{-ksz} e^{ik(x-ct)} \quad \textbf{(3-8)}$$

where

$$q = \sqrt{1 - \left(\frac{c_R}{c_l}\right)^2}, s = \sqrt{1 - \left(\frac{c_R}{c_s}\right)^2}, c = \frac{w}{k}$$

and both A_1 and B_1 are arbitrary constants. By satisfying the constitutive equation for homogeneous isotropic materials, and the boundary conditions, the theoretical Rayleigh wave velocity c_R then can be intuitively estimated as a function of Poisson's ratio μ. The detailed derivation process can be retrieved from the work of Rose (2012).

The following equation is given,

$$c_R = \frac{0.87 + 1.12\mu}{1 + \mu} \cdot c_s \quad \textbf{(3-9)}$$

where in this case, the theoretical velocity should be 2926.8 m/s which agrees with the

simulation results. The above equation assumes that the waveguide is isotropic, homogeneous, elastic solid media, with a free surface and semi-infinite material boundary condition. Rayleigh waves travelling in an interface are sensitive to surface and subsurface defects or any geometry inconsistencies, which is the basis of defect detection for railway tracks. The above equation also indicates that Rayleigh surface waves are nondispersive.

To briefly conclude the section, the characteristics of UGWs propagation in railway tracks are revealed and analyzed. Through reconstructing the displacement and velocity fields, the PZT configuration is proved to be cable of effectively generating UGWs that interacts with railway cracks, which are mainly composed of a group of mixed-mode waves. The predominant waves travelling on the railway surface and subsurface are Rayleigh waves which are highly sensitive to railway defects. The above findings provide useful information and guidance for railway defect detection design.

3.4.2.2. Defect detection

The interactions between UGWs and the railway crack is statistically studied in this section. Several sensing probes are configured on the UGW propagation route, which are shown in **Figure 3-17**. For each probe, the y-direction displacement is extracted to output the time-domain signals. This configuration intents to simulate the FBG sensing results. It should also be noted that Probe 1 and 2 are located on the left side of the crack

which means that the crack reflections can be recorded. Probe 3, however, is located on the right side of the crack which would block part of the waves.

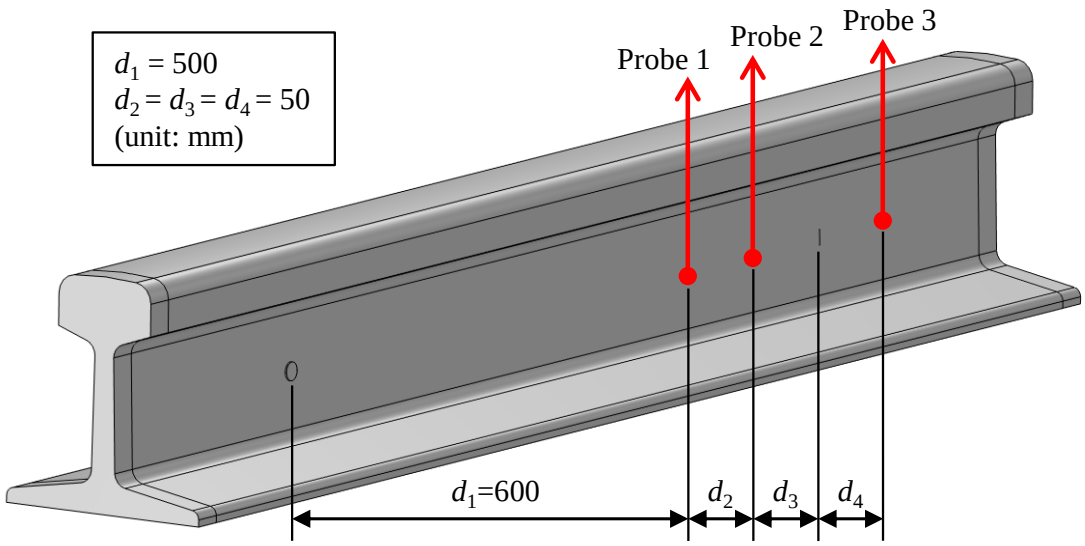

Figure 3-17. FBG probes configured on the propagation routes of the rail web.

The physical waves are demonstrated in **Figure 3-18**. From the time-domain waveforms, the influence of railway cracks can be intuitively observed. For Probe 1 and 2, the reflected waves can be seen at approximately 250 μs and 260 μs, respectively. However, the amplitude of the reflected waves are lower than other waves which may cause difficulty in identifying the waveforms in practical applications. As for the signals acquired by Probe 3, the waveform distortion and amplitude decline caused by crack interference can be extremely difficult to intuitively observe (**Figure 3-18c**). This is because UGWs can travel through obstacles such as corners and welds, minimizing the effects of defect interference.

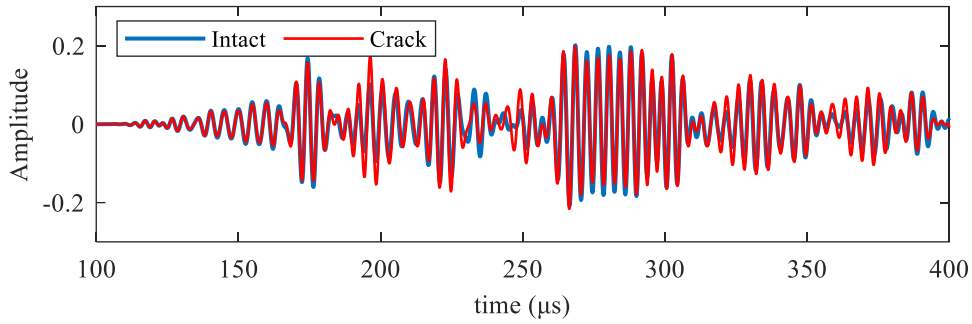

(a)

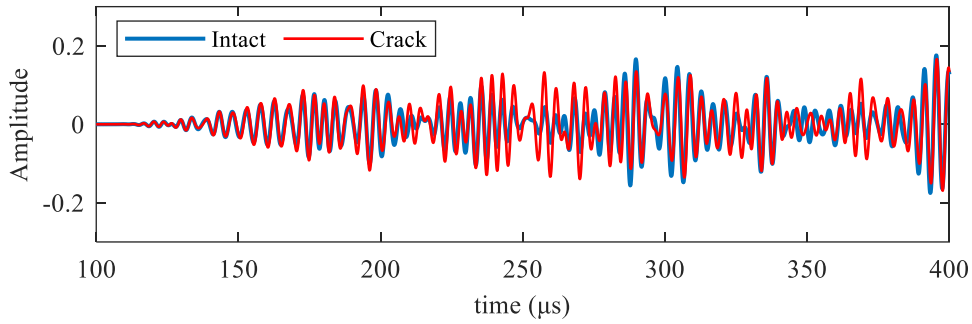

(b)

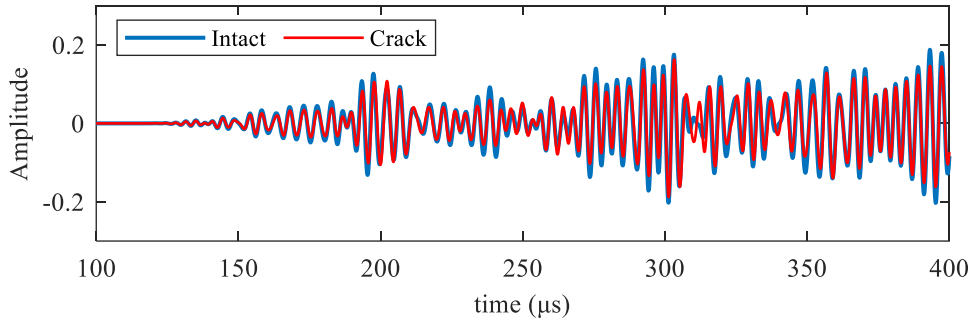

(c)

Figure 3-18. Ultrasound signal acquired by FBG probes under baseline and defect conditions: (a) Probe 1; (b) Probe 2; (c) Probe 3.

3.5. Summary

This chapter introduces a novel PZT-MFBG hybrid sensing system for railway guided wave online testing. The multiplexing scheme is first discussed in this chapter. Traditional FBG interrogation can hardly meet the requirements of ultrasonic sensing,

which is the motivation of proposing an edge filter-based multiplexing scheme specified for railway GWT. The system is set up in the laboratory, followed by a series of performance tests and cost-effectiveness evaluations. The last section of this chapter focuses on numerical investigations to validate the effectiveness of the proposed hybrid sensing system. The FEM is introduced, and the guided wave propagation mechanism including the interactions with railway cracks is studied and demonstrated. The following conclusions can be drawn from this chapter:

1 The proposed FBG multiplexing scheme is suitable for ultrasonic testing on railway tracks, featuring high-speed demodulation and high sensitivity towards UGWs.

2 The system performance is fully evaluated via experimental investigations in the laboratory. The bonding quality tests of both PZT and FBGs facilitate the reliability of the measurements, and the cost-effectiveness of the hybrid system indicates its engineering applicability.

3 The proof-of-concept for the proposed hybrid system is carried out via numerical investigations. The guided wave propagation mechanism in this configuration provides valuable prior knowledge for practical applications. It has been found that the propagation mechanism of PZT-induced UGW in railway consists of mixed modes where the predominant Rayleigh wave propagates on railway

interface that are proved to be sensitive to geometry inconsistencies.

4 The UGW generated by PZT interacting with railway cracks is modelled, and through reconstructing wave velocity fields and extracting time-series responses, the results provide numerical evidence for the feasibility of damage detection using the proposed hybrid sensing system.

CHAPTER 4 RAILWAY TRACK DEFECT DETECTION BASED ON NONLINEAR AUTOREGRESSIVE MODELS WITH EXOGENOUS INPUTS

4.1. Introduction

A robust NDE methodology requires both advanced sensing hardware and precise mathematical models for signal analysis. Ultrasonic waves in rail structures exhibit complex overlapping patterns caused by boundary reflections and wave scattering, making signal demodulation particularly challenging. Recent advances have employed supervised learning for ultrasonic signal processing (Bombarda et al., 2021), including physics-informed machine learning for damage detection proposed by Rautela et al. (2021) and deep networks to extract defect-related features from acoustic signals (Cui et al., 2022; Ebrahimkhanlou et al., 2019; S. Guo et al., 2022; Z. Zhang et al., 2022), demonstrating promise for such methods in rail inspections. However, developing unsupervised detection methods remains critical for field applications where labeled data is unavailable. Notable unsupervised approaches include variational autoencoders for light rail squat detection proposed by Yuan et al. (2021), data-driven broken rail prediction models developed by X. Wang, Liu, et al. (2022), and big data analytics linking track geometry to rail defects introduced by Zarembski et al. (2016).

While time-series models are emerging in NDE, they have proven effective for

structural health monitoring (SHM) of civil infrastructure (Q. Han et al., 2023). These methods predict structural responses using real-time sensor data, where prediction errors indicate damage. Linear models like AR and ARX have analyzed structural dynamics (Cheng et al., 2021; A. Liu et al., 2019), while nonlinear systems require Bayesian approaches (Y. W. Wang & Ni, 2020), or Bayesian-ARX models (Saito & Beck, 2010; J. H. Yang et al., 2021). For rail tracks with nonlinear boundary conditions, nonlinear autoregressive networks with exogenous inputs (NARX) demonstrate superior fitting capability (Rai & Upadhyay, 2017; Yan et al., 2013), particularly for multi-sensor systems where they can reveal cross-channel relationships - making them ideal for ultrasonic rail inspection (Bao & Li, 2021). These networks enable simultaneous processing of multi-dimensional inputs, making them particularly suitable for structural health monitoring (SHM) applications involving multiple sensor channels. Their nonlinear autoregressive capabilities allow for revealing complex inter-channel signal relationships. These characteristics align perfectly with the requirements of railway NDE systems employing multi-sensor arrays, motivating our investigation of NARX models for ultrasonic signal processing.

This chapter integrates an FBG sensing network with NARX modeling for rail NDE. Section 4.2 details the methodology and health evaluation framework, followed by experimental validation (Section 4.3) including sensitivity optimization. Large-scale testing (Section 4.4) confirms the method's robustness, demonstrating how data-driven

models combined with advanced sensing enable accurate rail condition assessment.

4.2. Methodology

4.2.1. NARX

As introduced in the previous chapter, the proposed FBG array for rail track monitoring brings multiplexed data channels. Consequently, a robust and multi-input approach for data processing is required, specifically, a data-driven model capable of processing ultrasonic time-domain signals and learning nonlinear representations from multi-dimension inputs. In this sense, NARX makes the ideal candidate due to its optimal advantages that it is not only trained in an unsupervised manner (Umar et al., 2021) but also can adapt to time-domain data with multiple input channels. To illustrate the proposed damage detection framework where the NARX is implemented, the nonlinear autoregressive algorithm is firstly introduced below.

Considering a multi-input single-output (MISO) system where the input channels contain both the regression target and exogenous inputs, model *F* can be written as,

$$\hat{y}(t) = F\left[b_0 + \sum_{h=1}^{Nh} W_{h0} \cdot f\left(b_h + \sum_{i=1}^{d_x} W_{ih} x(t-i) + \sum_{j=1}^{d_y} W_{jh} y(t-j)\right)\right] \quad \textbf{(4-1)}$$

where y and $\hat{y}$ are the original and predicted targets, respectively; the x denotes the input time-series; and d_x and d_y refer to the time delays of the exogenous input and

the target that the prediction is performed by. The weights and the bias matrixes of the hidden layers in this equation is referred to as W_h and b_h, respectively, with the input being either the target y or the input x. While F representing the nonlinear function, f is the activation function of the neurol nodes. It is also worth noting that the dimension of the exogenous vector x is determined by the specific scenarios, in the format shape of [(Number of exogenous inputs), (length of the exogenous inputs)].

The schematic of using a NARX to detect abnormalities of a MISO system is illustrated in **Figure 4-1**. The time delay d is crucial to the training of the neurol nodes, which determines the number of the input series. As for the hidden layers, each neurol node has basic trainable parameters, the weight and bias matrixes, which are utilized to fit the nonlinear series. And a linear function is utilized for normalizing the output of each neurol node. The numbers of neurol nodes and hidden layers are considered key hyperparameters when it comes to optimizing model performance. Finally, the output layer, except for the regular trainable weights and bias, is equipped with a SoftMax function to help output the final predictions.

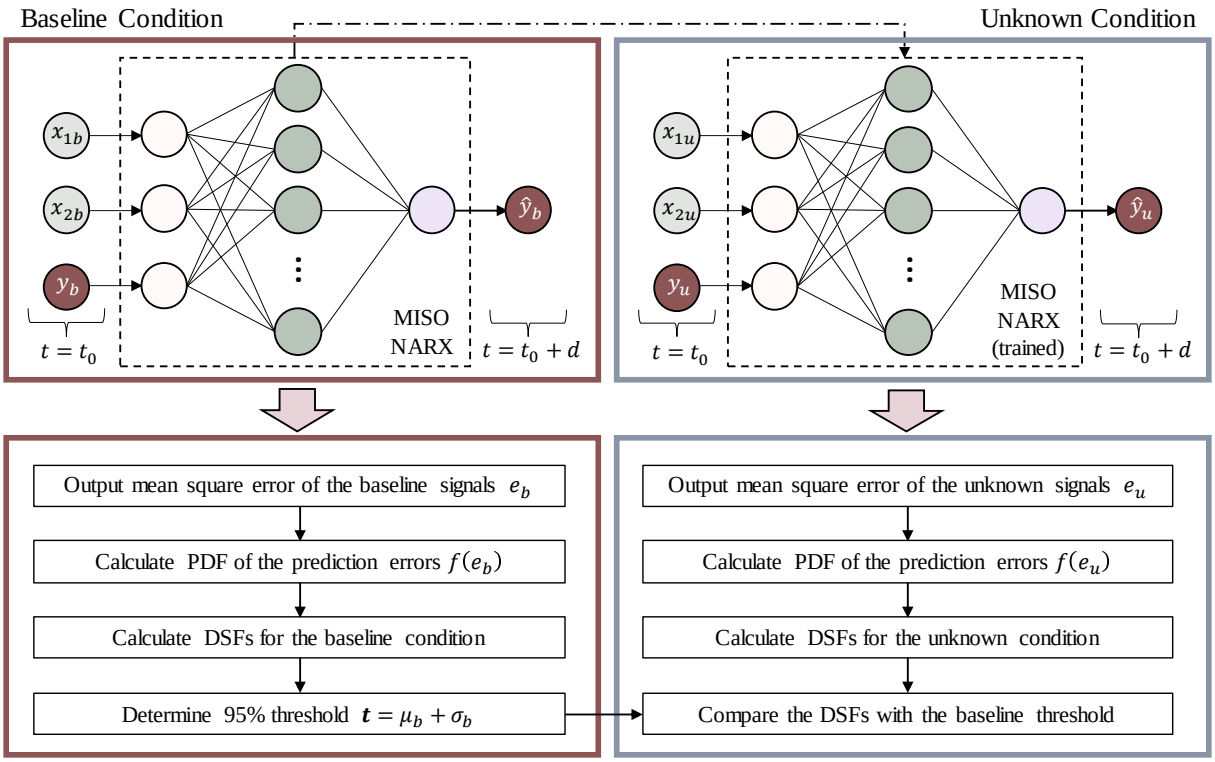

Figure 4-1. Schematic of using a MISO NARX neural network with 2 exogenous inputs to conduct damage detection.

For a multi-FBG system, e.g., a sensor array, the input to a nonlinear autoregressive model as such can obtain time-domain ultrasonic wave signals on the rails. The signals are approximated through the nonlinear function F with the signals acquired by other FBGs as the exogenous inputs. To this regard, the NARX models can effectively learn nonlinear representations from time-domain signals, both from the autoregression and the exogeneous inputs.

The mean square error (MSE) of the predictions, which is defined as the difference between the target y and $\hat{y}$, denotes the performance of the NARX model. Under normal circumstances (regarding as the baseline condition), the level of MSE should

maintain at a certain level, which can be demonstrated using a PDF. While the tested rail is damaged, the MSE values are supposed to deviate due to the abnormality within the time series since the parameters of the trained model remain the same. Based on this theory, DSFs can be extracted to characterize potential damages. Thresholds for DSFs can be obtained when testing on the baseline condition. For future unknow conditions, the calculated DSFs can be utilized to compare to the thresholds so that damage detection can be achieved. The above is the basic principle of using a NARX model to determine the health status of a tested rail track.

4.2.2 Probability density function-based features extraction

The baseline models can be utilized to identify the health status of the rail track, specifically, by analyzing the prediction error and comparing it to a certain threshold. However, while determining the difference between the prediction error distribution of the baseline condition with that of an unknown condition, DSFs are required to be configured to represent the possible damages on the rails. Thus, PDF is deployed in this study. Firstly, the baseline model is trained with the baseline condition datasets as input. Then, the same model is utilized to make predictions of the unknown condition, through which the prediction error distribution is also obtained. Both the training error of the baseline condition and the prediction error of the unknown condition can be represented by PDF with significant Gaussian distribution characteristics. Thus, the standard deviation and the mean value of the error e, σ and μ, can be obtained accordingly via

the following equation,

$$G(e) = \frac{1}{\sigma\sqrt{2\pi}} \exp\left[-\frac{(e-\mu)^2}{2\sigma^2}\right] \quad \textbf{(4-2)}$$

Consequently, the DSF is constructed using the features extracted from the PDFs of both the baseline and the unknown condition. Umar et al. (2021) introduced a PDF-based DSF where the prediction error is utilized. An ambient vibration based DSF was also proposed, given systematic dynamics derivations to verify the relations between the proposed features and the structural conditions (Azim & Gül, 2019). The basic discriminative principal is to compare the error distribution of the baseline condition $G(e_b)$ and that of an unknown condition $G(e_u)$.

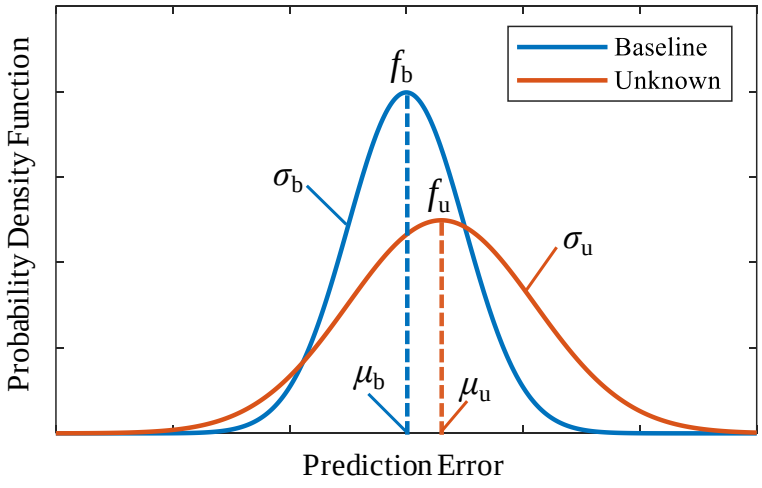

Figure 4-2. Schematic of extracting statistic parameters form typical PDFs.

The following equation is given, which describes the proposed DSF in this study,

$$DSF = \log\left(\frac{\sigma_u f_b}{\sigma_b f_u} + 1\right) \quad \textbf{(4-3)}$$

where f_b, f_u are the peak values of the PDFs, and σ_b, σ_u are the standard variance of the baseline and unknown conditions, respectively. The statistical parameters are extracted from the PDF curves, schematically shown in **Figure 4-2**.

4.2.3. Damage detection framework

To sum up and integrate the methodologies introduced above, a complete flowchart is given in **Figure 4-3** to illustrate the 3-step damage detection process proposed in this study. First, in the aspects of sensing hardware, PZT is utilized to excite ultrasonic waves with a certain central frequency range so that the FBG array can receive the signals using the demodulation configuration introduced in Chapter 3. The 3-channel FBG array receives ultrasonic signals simultaneously, with 2 time series serving as the exogenous input and another 1 being the target input of NARX model. Then, the baseline and unknown conditions are separately considered in the model training process, using the methodology introduced in Section 4.2.2. The thresholds are priorly determined using the baseline datasets considering the 95% confidence level; then, the DSFs calculated using the prediction residuals of an unknown condition are compared with the configured threshold, based on which the rail track condition is assessed. It should be noted that in practical engineering applications, it makes sense to conduct ultrasonic testing using different excitation frequency bands to ensure that ultrasonic

wavelengths shall not surpass the physical size of the defect because sub-wavelength defects are generally more difficult to detect. However, the defect size is hardly priorly known to engineers in practice. In addition, it should be taken into consideration that shorter wavelengths would result in faster attenuation in signal amplitudes, which restricts the propagation distance. Leveraging the above factors, the excitation frequency band of PZT varies within the range of 160 to 350 kHz, with the internal gap of 10 kHz (i.e., 160 kHz, 170 kHz, …, 350 kHz), which covers the wavelength of 5 to 30 mm. For each excitation frequency band, an independent baseline NARX model is trained, meaning that 20 MISO NARX models are trained separately.

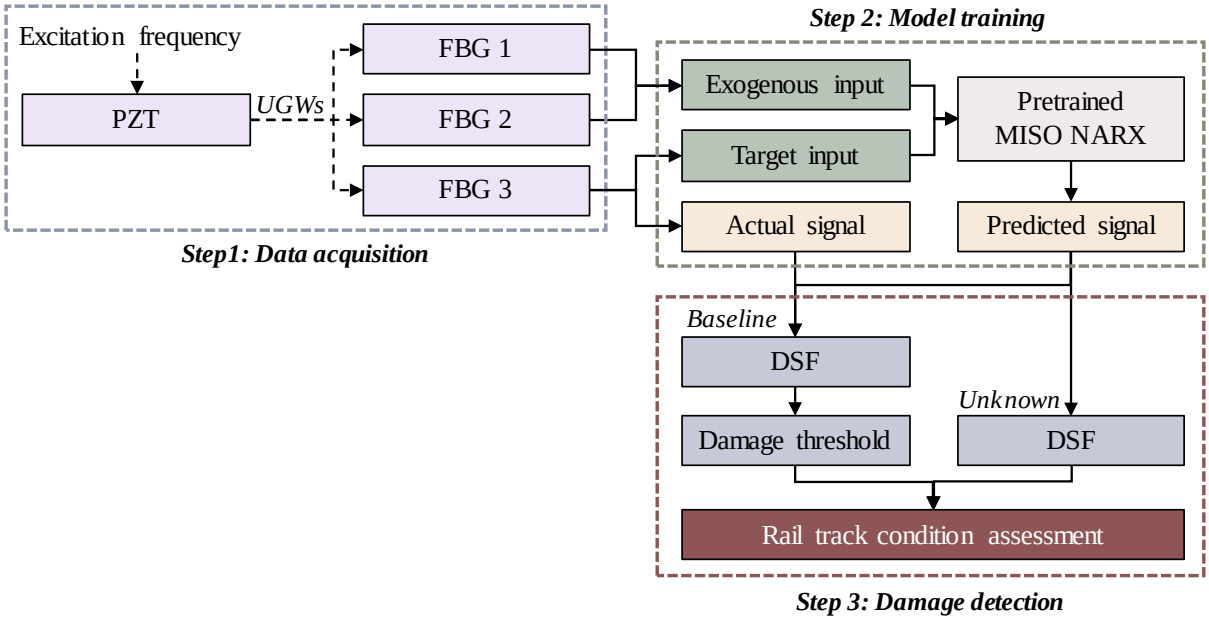

Figure 4-3. Flowchart of the damage detection strategy proposed in this study.

4.3. Experimental investigations

In this section, the laboratory experiments carried out and the datasets obtained are

thoroughly illustrated, based on which the proposed methodologies are verified. The damage detection process is also demonstrated, and the preliminary results are discussed at the end of the section.

4.3.1. Experimental procedures

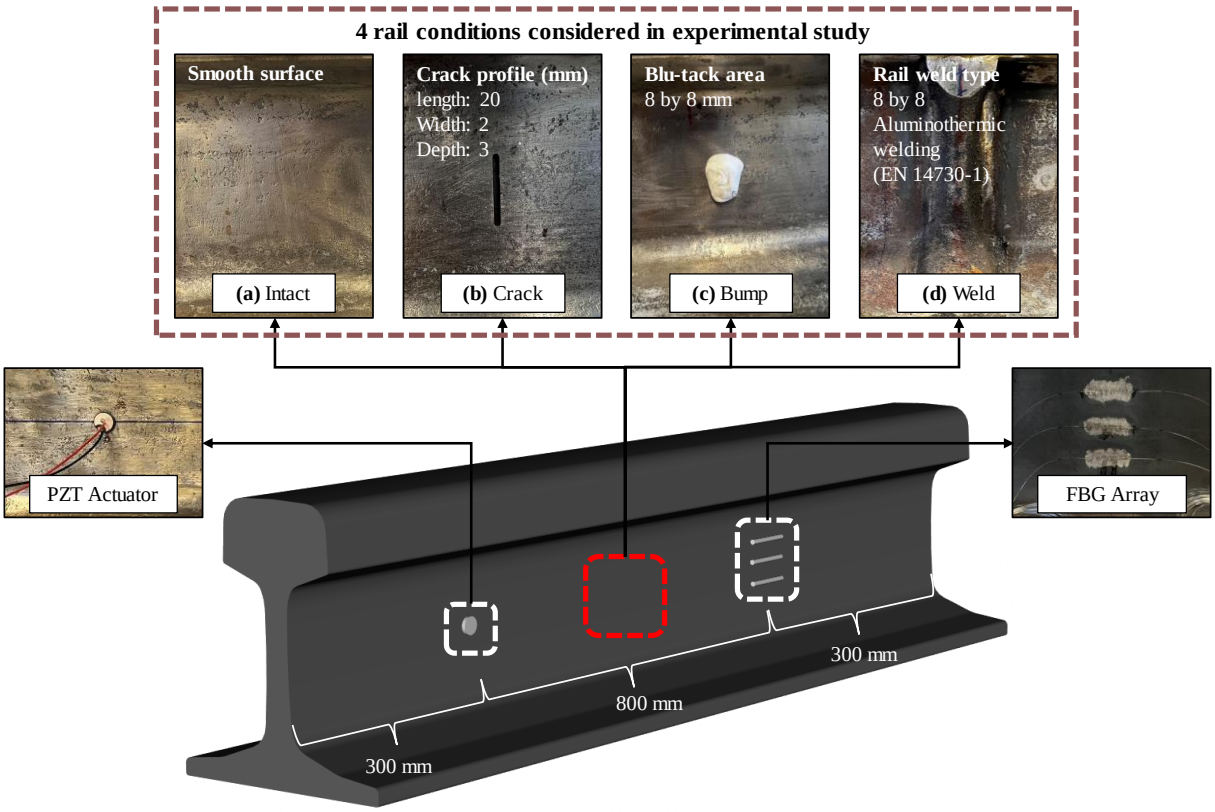

Figure 4-4. Experimental configuration of rail track conditions.

To verify the feasibility of the proposed damage detection method, 1 intact condition **(Figure 4-4a)** and 3 abnormal conditions (**Figure 4-4b, 4-4c, 4-4d**) that are assumed to commonly happen on rails are considered, namely crack, bump, and weld.

Cracks that grow on the rail web are easily neglected in most cases because they are often too minor to be observed. But once the crack has developed, the damage it caused

would most likely bring major safety hazards to the railway operation. Since it is crucial to provide an early-stage warning of the cracks on the rail web, an artificial damage is created by cutting a shallow crack on the surface, as shown in **Figure 4-4(b)**, with the dimension of 20×2×3 mm (length×width×depth) to simulate an early-stage cracked condition that endangers railway safety.

Apart from the rail cracks, the irregular objects attached onto the rail may also compromise the safe operation of the rail system. To simulate a similar abnormal bump onto the rail web in the laboratory, the authors adopt the commonly used blu-tack adhesives and glue them covering rail surface area of approximately 8 mm by 8 mm (**Figure 4-4c**), making sure no hollow area exists between the adhesives and the rail web. The assumption is made that such bump can absorb certain amounts of ultrasonic waves during their propagation route, because of the complex reflections and refractions.

The last condition considers the influence of aluminothermic welds on ultrasonic waves, as is shown in **Figure 4-4(d)**. Compared with the two damage conditions mentioned, a rail weld would have the more obvious influence onto the signals obtained by the ultrasonic NDT & E (Loveday, 2012; Ramatlo et al., 2022; Z. Zhang et al., 2022). For one thing, aluminothermic welds are the protruding material out of the rail web surface that can absorb a significant amount of wave packets; for another, the materials used to fill in the gap between are somewhat different from the original materials of the rail

tracks (Y. Liu et al., 2021). The change in material properties would cause interface reflections and refractions, which will be embodied in the observed ultrasonic waves.

In this experimental study, both PZT and FBGs are installed onto the vertical midpoint of rail web surface using adhesives. The propagation distance of ultrasonic waves, i.e., the distance between PZT and FBG array is 800 mm. Four rail conditions (intact, crack, bump and weld) are configured as illustrated in Figure 8. It is assumed that defects that exist on the propagation route between PZT and FBG array will interfere with the acquired ultrasonic signals as part of waves are reflected backwards, causing distortions in waveforms compared to the baseline condition. In other words, as long as the defect exists in between the PZT and FBG array, the proposed NARX-based evaluation method will be sensitive to any minor distortions of waveforms. Therefore, in this sense, the location of defects is not priorly considered in this study.

Some samples corresponding to 4 different rail track conditions are acquired and shown in **Figure 4-5**. It can be observed that rail damages generally bring changes to waveform shapes in time domain. From this perspective, DSFs that are related to the ultrasonic wave propagation can be utilized to indicate potential damage. The detailed DSF calculation process is introduced in the next content.

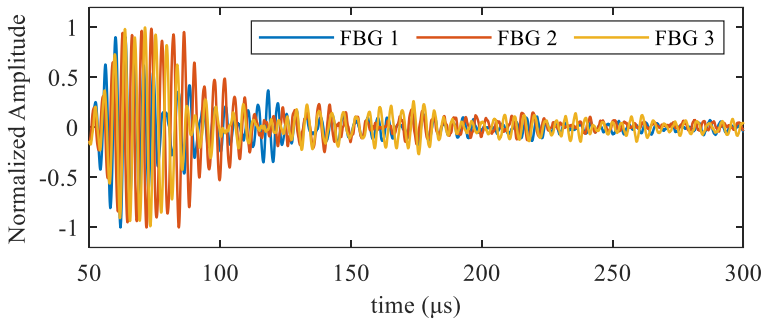

(a)

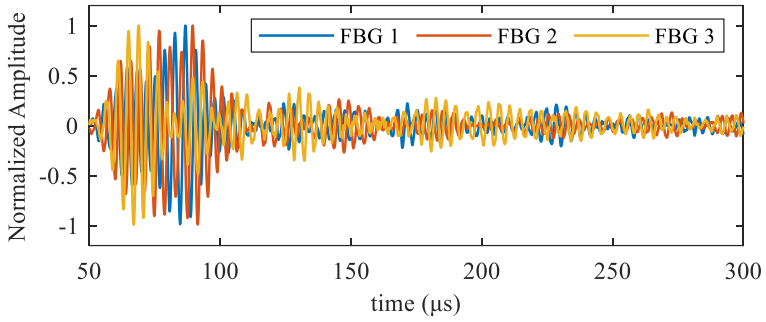

(b)

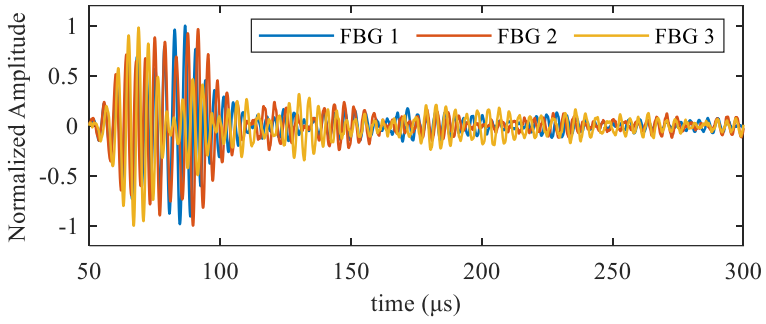

(c)

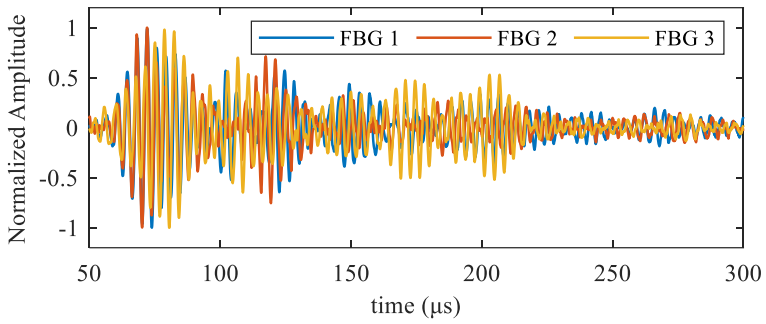

(d)

Figure 4-5. Sampled ultrasonic signals sampled under the excitation of 250 kHz in various rail track conditions: (a) Intact; (b) Crack; (c) Bump; (d) Weld.

4.3.2. Construction of the NARX model

4.3.2.1. Hilbert envelope of the UGW signal

To maximally achieve better prediction results, it is critical to firstly analyze and extract the valid information from the obtained ultrasonic signals. Referring to the previous research work regarding one-dimension signal processing (Schmidt et al., 2014; X. Yang et al., 2022), various features of both time and frequency domain are selected to represent the characteristics of the signals.

Considering that the rail track is so highly nonlinear that the obtained ultrasonic waves are rather complex in time domain, the raw signals being directly fed to the nonlinear regressor would consume much unnecessary computer power and training time. Additionally, the excitation frequency for each NDE is fixed, and the frequency dispersion effect can almost be neglected for this case because the propagation route is rather short. Consequently, the frequency domain of the signals should not contain little useful information. In this experiment, the envelopes of the ultrasonic signals are calculated as the input vectors because they are assumed to be simpler than the raw data while preserving most of the information possibly indicating rail damages.

Hilbert transform (HT) is adopted to calculate the discrete-time analytic signals. Due to the conjugate Symmetry characteristics of Fourier transform of real signal, the HT is regarded to be equivalent to an orthogonal filter without changing the amplitudes. The

discrete Hilbert envelope spectrum of this signal series is calculated in such format,

$$h(t) = \sum_{t}^{\infty} \frac{1}{f} a(t) e^{-j2\pi f t} \tag{4-7}$$

where f denotes the sampling frequency of the discrete signals, $a(t)$ denotes the instantaneous amplitude of the discrete signals expressed in the exponential form.

To clearly demonstrate the results of the envelope calculations, **Figure 4-6** shows one of the Hilbert envelopes calculated using ultrasonic signals. It can be observed that most peaks of the signals are concluded by the generated envelope. For each calculated envelope, the length is equal to that of the raw data. In the meanwhile, a smooth function is adopted to eliminate the effect brought by the nonlinear calculation of the fluctuations of the Hilbert envelope.

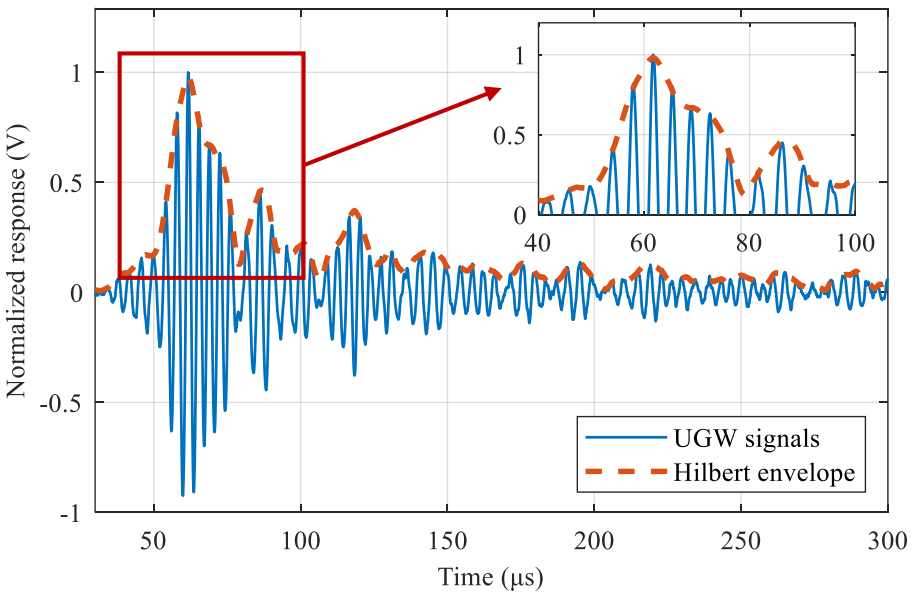

Figure 4-6. An example of the features extraction using Hilbert envelope.

4.3.2.2. Parameter settings

To obtain well-trained baseline NARX models, some parameters are set to accelerate the fitting process. For a nonlinear fitting problem, the key parameter is usually the number of neural nodes and the gradient descent function. Generally, the more neural nodes are adopted to train the network, the better the fitting performance, especially if the target vector is extremely nonlinear. However, more nodes would indicate the significant number of parameters, the weight and bias matrixes, resulting in redundant training which is rather time-consuming. In this experiment, each NARX model possesses 20 neurol nodes to fit the extracted Hilbert envelopes of different conditions. The SoftMax function is utilized for each node for normalization and transmits the information to the output layer where a linear regression function is adopted to predict the target vectors. The time delay for each prediction equals 10 data points, to achieve predictions with lower MSE.

4.3.2.3. Training functions

Training functions are vital when constructing and training the NARX. To achieve better prediction performance, the choice of training function is seen to be a hyper-parameter to be optimized in this case. In this sense, there are 3 different functions, namely quasi-Newton (QN) function, scaled conjugate gradient (SCG) descent function, and Levenberg-Marquardt (LM) method, respectively adopted so that comparative

study can be carried out to further explore optimized rail health evaluation method.

4.3.2.4. Training the baseline model

The proposed method aims at achieving rail damage diagnosis in an unsupervised manner, therefore, in the training stage, only ultrasonic signals collected under the intact rail condition are utilized as the input to feed NARX. The ultrasonic testing procedure is repeatedly conducted using different excitation frequency bands, and for each frequency band, an individual NARX is trained. And for each NARX model that corresponds to a singular excitation frequency band, 3 training functions have been respectively used for back-propagating parameters. In the training session, only the data collected on an intact rail is utilized because a baseline model is required for later comparison to identify the existence of defects. Therefore, it is essential that the training dataset is collected when the rail is intact.

Figure 4-7 shows a part of training and validation curves of NARX, specifically at the excitation frequency of 160 kHz, 200 kHz, 240 kHz, and 280 kHz. It can be obviously observed that NARX using LM method can achieve faster fitting convergence and lower MSE on the training set. Detailed training MSE values of baseline models using 3 training functions are listed in **Table 4-1**, with the lowest MSE intentionally underlined. The overall training performance of LM method stands out among QN and SCG methods.

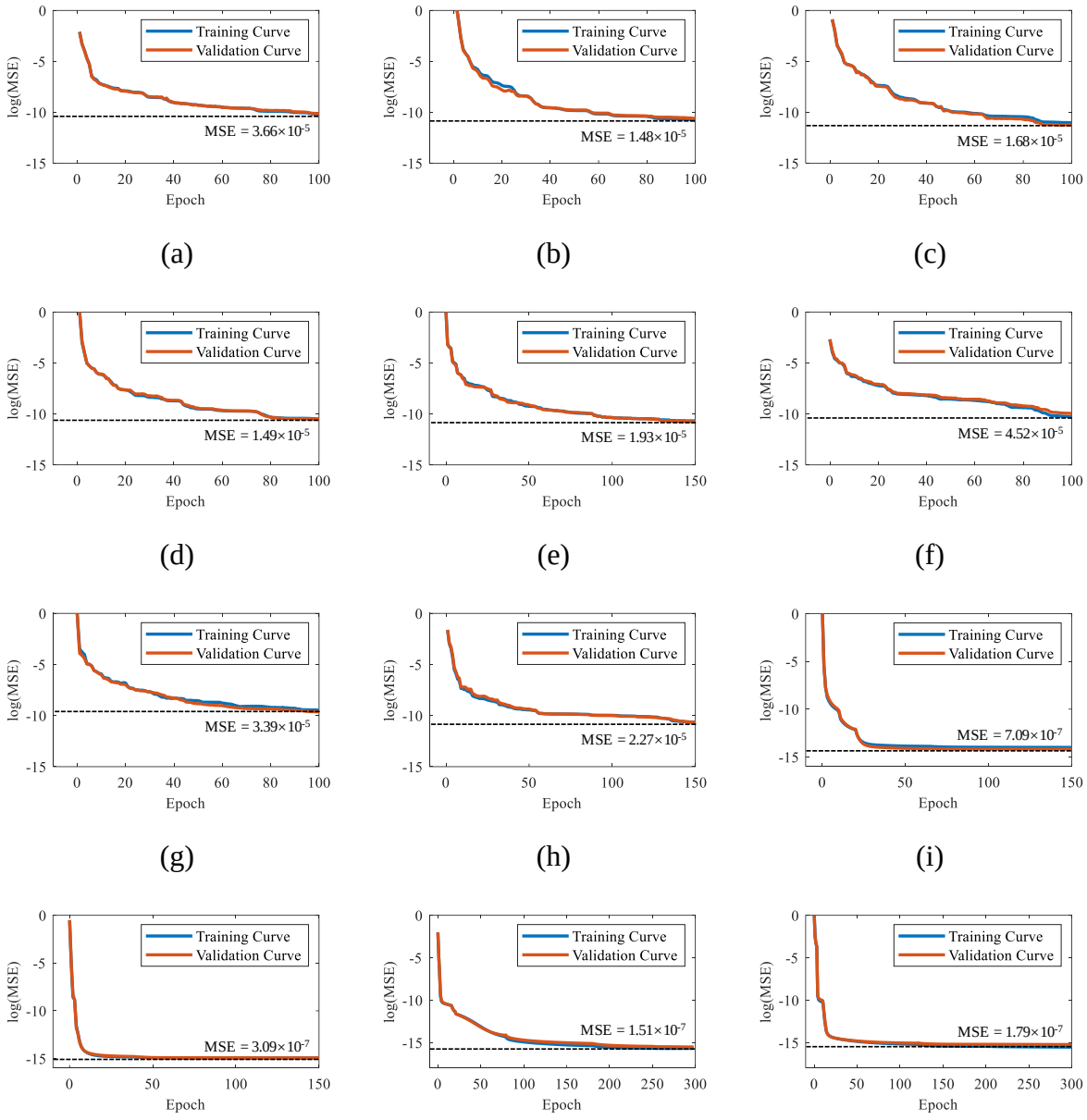

Figure 4-7. Training and validation curves under various excitation frequencies using (a)-(d) QN method, (e)-(h) SCG method, and (i)-(l) LM method.

Table 4-1. The MSE values of the baseline models trained using 3 different training functions under all excitation frequencies (the underlined denotes the lowest MSE).

Training functions	160 kHz	170 kHz	180 kHz	190 kHz	200 kHz
QN	3.66×10^{-5}	3.97×10^{-5}	5.91×10^{-5}	4.03×10^{-5}	1.48×10^{-5}
SCG	1.93×10^{-5}	9.99×10^{-5}	1.83×10^{-5}	4.89×10^{-5}	4.52×10^{-5}
LM	7.09×10^{-7}	3.50×10^{-7}	4.71×10^{-7}	4.13×10^{-7}	3.09×10^{-7}
Training functions	210 kHz	220 kHz	230 kHz	240 kHz	250 kHz
QN	1.40×10^{-5}	1.24×10^{-5}	3.57×10^{-5}	1.68×10^{-5}	1.68×10^{-5}
SCG	3.01×10^{-5}	8.21×10^{-5}	2.05×10^{-5}	3.39×10^{-5}	3.91×10^{-5}
LM	1.50×10^{-7}	1.29×10^{-7}	8.27×10^{-8}	1.51×10^{-7}	1.51×10^{-7}
Training functions	260 kHz	270 kHz	280 kHz	290 kHz	300 kHz
QN	6.78×10^{-5}	9.80×10^{-6}	1.49×10^{-5}	8.63×10^{-5}	1.49×10^{-5}
SCG	1.49×10^{-5}	2.88×10^{-5}	2.27×10^{-5}	7.05×10^{-5}	5.56×10^{-5}
LM	2.07×10^{-7}	1.57×10^{-7}	1.79×10^{-7}	1.42×10^{-7}	2.18×10^{-7}
Training functions	310 kHz	320 kHz	330 kHz	340 kHz	350 kHz
QN	8.14×10^{-5}	2.51×10^{-5}	8.37×10^{-5}	6.51×10^{-5}	5.05×10^{-5}
SCG	5.18×10^{-5}	6.83×10^{-5}	8.94×10^{-5}	2.87×10^{-5}	6.97×10^{-5}
LM	3.07×10^{-7}	3.70×10^{-7}	5.80×10^{-7}	5.35×10^{-7}	7.38×10^{-7}

4.3.2.5. Determination of the thresholds

The DSF thresholds are priorly determined, before evaluating rail health conditions. The uncertainty brought by model training is considered. Thus, ultrasonic signals are repeatedly sampled and equally split into ten folds, with one fold utilized to train a baseline NARX and the other nine folds utilized to feed the trained NARX. Through this process, DSFs are calculated nine times, according to the methodology previously illustrated in Section 4.2. As a result, a total of 180 DSFs are calculated through NARX training, i.e., 20 (NARX models) multiplies 9 (DSFs for each NARX model). Last, thresholds are determined based on the 95% confidence level of 180 DSFs calculated. It is assumed that once given a certain excitation frequency of ultrasonic testing, the rail track is indicated to be damaged if its DSF is measured higher than the threshold priorly determined.

The thresholds corresponding to NARX trained by 3 training functions are drawn in **Figure 4-8**. It can be observed that the calculated threshold for LM-based method is the lowest, compared to those for QN and SCG method. This can be comprehended that the MSEs for LM method are relatively lower, resulting in lower threshold of DSFs. It can be assumed that LM-based rail damage evaluation method can be more damage-sensitive because the threshold is relatively lower.

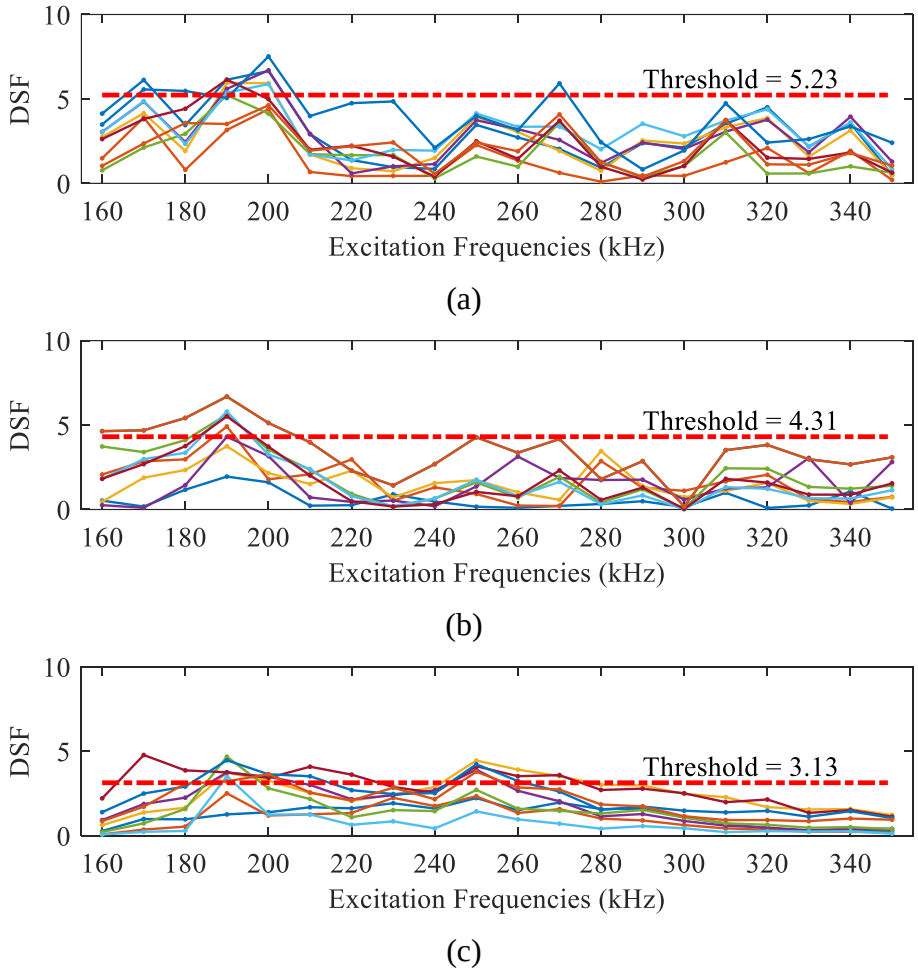

Figure 4-8. Threshold determination using 3 different training functions: (a) QN; (b) SCG; (c) LM.

4.3.3 Damage assessment results

The ultrasonic signals acquired on rails of crack, bump, and weld conditions are fed to the trained NARX. The corresponding DSFs are calculated to be compared with the thresholds as shown in **Figures 4-9**, **4-10**, **and 4-11**, where the blue bars mean that DSF is below threshold, i.e., the rail is diagnosed to be 'intact' while red ones indicate otherwise.

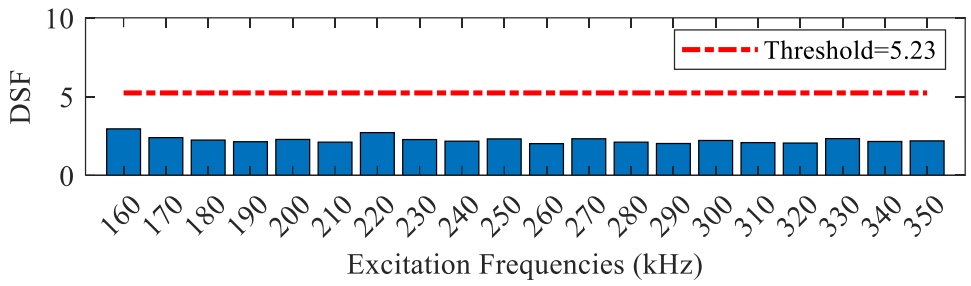

(a)

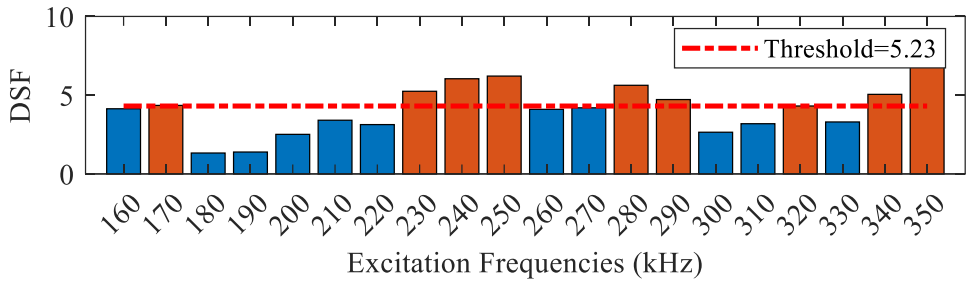

(b)

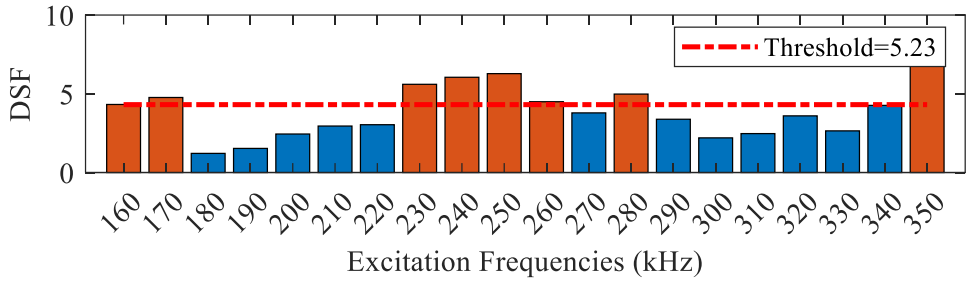

(c)

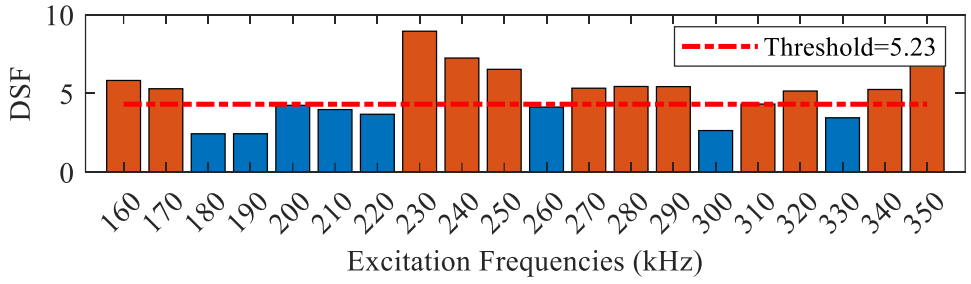

(d)

Figure 4-9. Damage detection results of QN method: (a) Intact; (b) Crack; (c) Bump; (d) Weld.

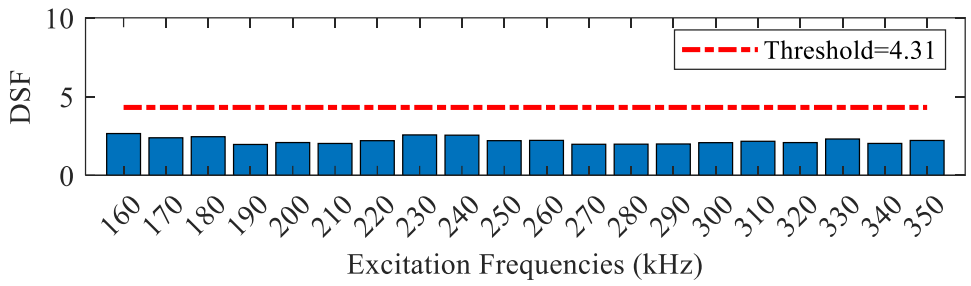

(a)

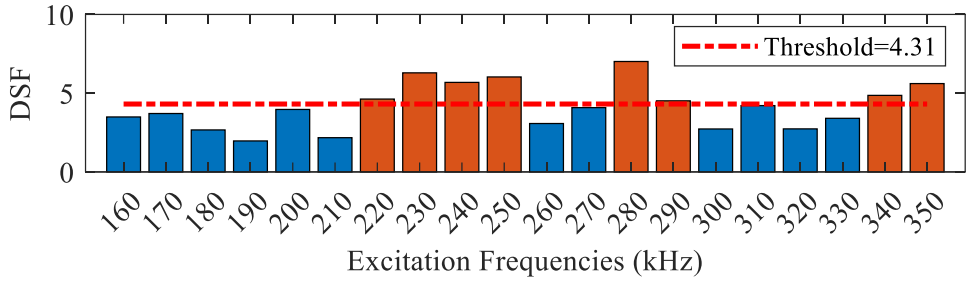

(b)

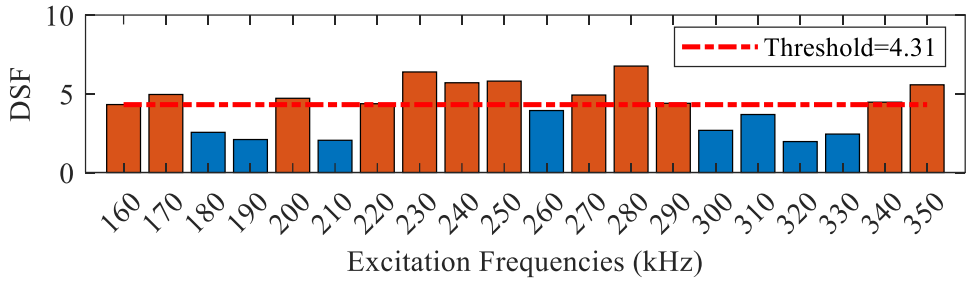

(c)

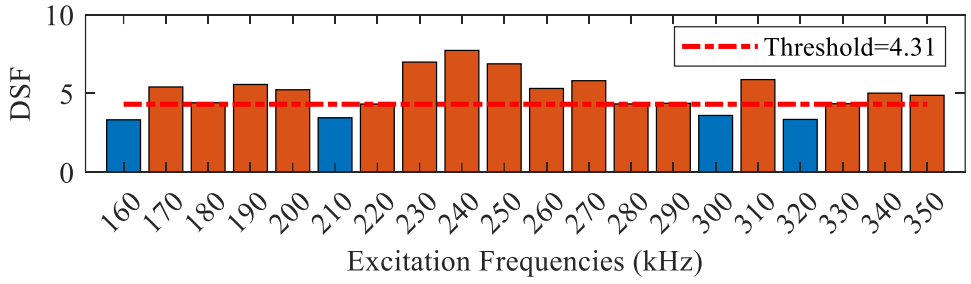

(d)

Figure 4-10. Damage detection results of SCG method: (a) Intact; (b) Crack; (c) Bump; (d) Weld.

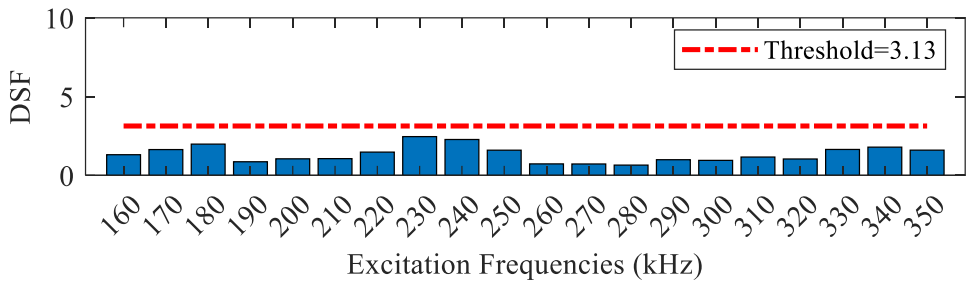

(a)

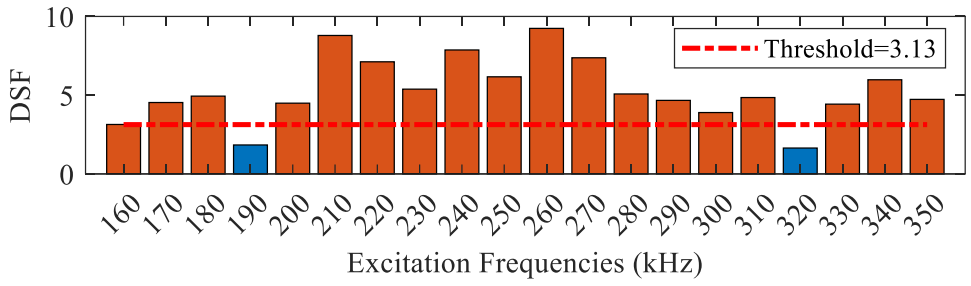

(b)

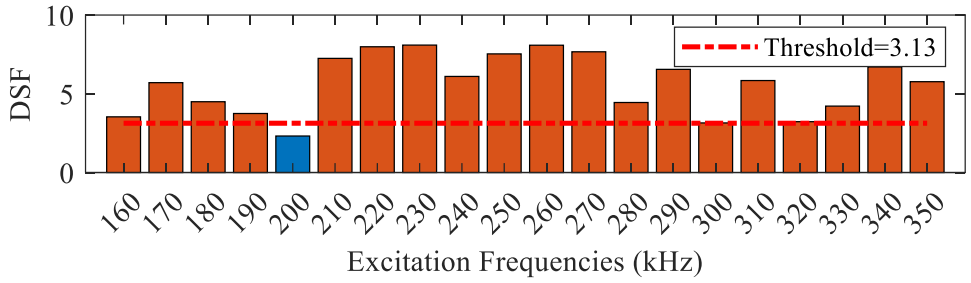

(c)

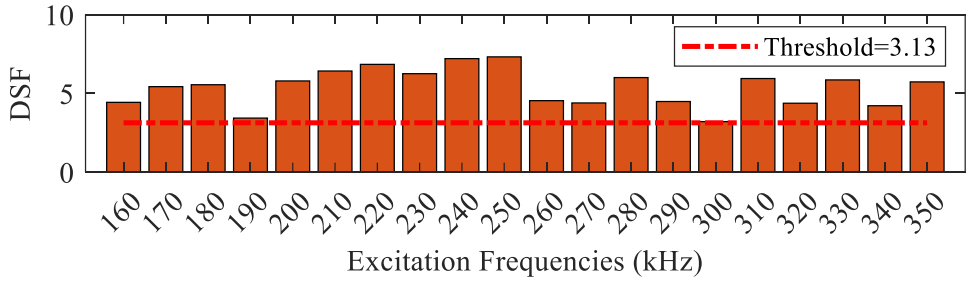

(d)

Figure 4-11. Damage detection results of LM method: (a) Intact; (b) Crack; (c) Bump; (d) Weld.

In comparison, it is obvious that the LM method achieved the best results. First, regarding the 'intact' rail condition, all three methods are fully capable of making correct diagnosis. However, when it comes to irregular conditions, the LM method clearly outperforms the other 2 methods, with only a limited number of mistakes being made. In stark contrast, QN and SCG methods are not reliable for they failed to report rail damaged conditions in many excitation frequencies. In conclusion, LM method undoubtedly contributes to a more sensitive damage evaluation diagnosis.

4.3.4. Visualization of the model prediction

To successfully distinguish between the 'intact' condition and the damaged ones, the trained NARX models are supposed to perform better predictions on the 'intact' datasets while biased predictions bringing larger MSE values would contribute to damage diagnoses.

To visually demonstrate the fitting performance of NARX, the predicted and actual wave packet envelopes (taking the excitation frequency of 250 kHz for an instance) are drawn together for comparison (**Figure 4-12**). The predicted envelope is closely approaching the actual one for the 'intact' condition, as shown in **Figure 4-12(a)**, which indicates that the tested rail is most likely to be in good condition. In dark contrast, the prediction errors can be visually inspected for the rest of the conditions, demonstrated in **Figure 12(b)-(d)**. The evenly distributed values of MSE would possibly increase the

possibility of raising a warning, according to the methodology proposed in this study.

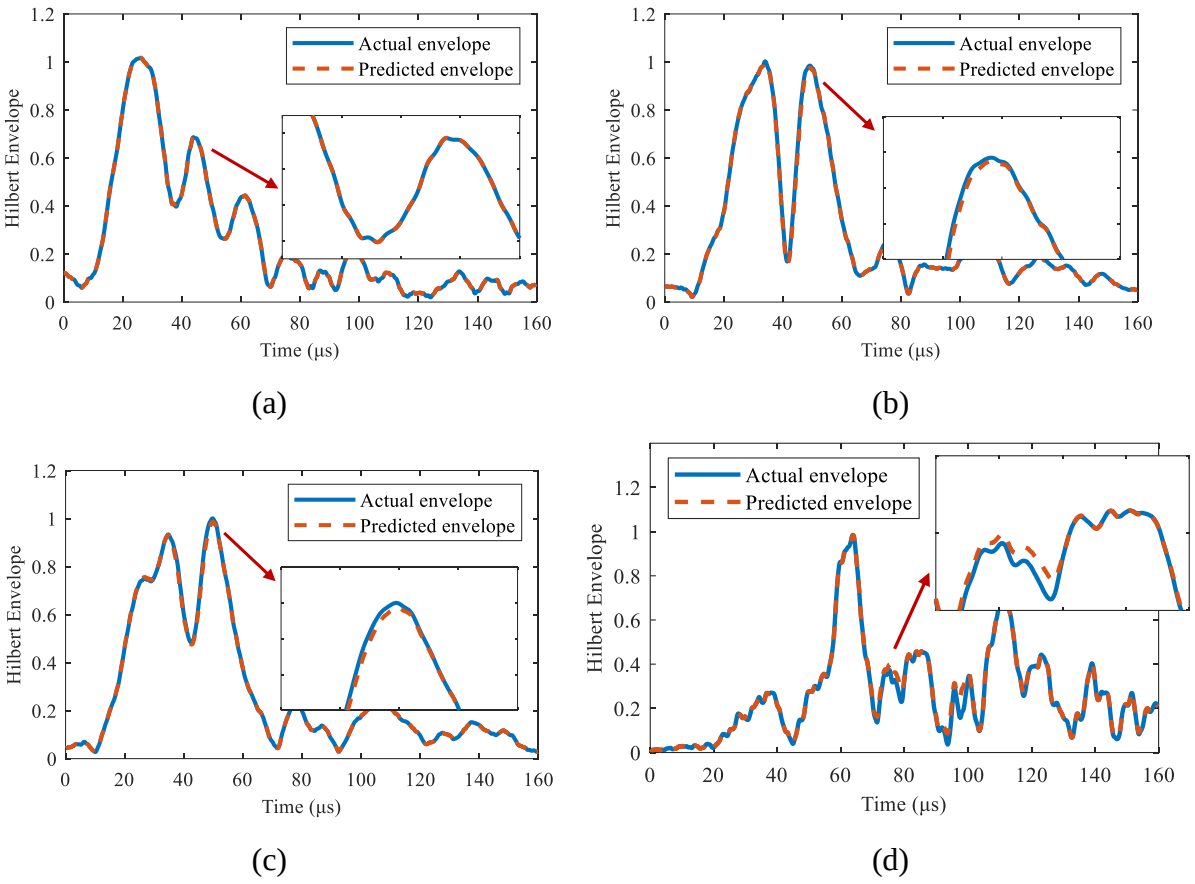

Figure 4-12. Predicted results of the NARX model trained using LM method at the excitation frequency of 250 kHz: (a) Intact; (b) Crack; (c) Bump; (d) Weld.

To quantify the prediction errors, the PDFs are calculated corresponding to the 4 conditions (using the baseline and the prediction of the 250 kHz NARX model for instance). The more errors the models perform on the testing sets, the smaller peak values and larger standard deviations are obtained. From **Figure 4-13(a)**, it is obvious that the PDF curve for the 'intact' condition lies within the range of the baseline curve, with higher peak value and smaller standard deviation. While it is the opposite case for the damaged conditions, visible peak shifts are observed in **Figure 4-13(b)-(d)**. Such

changes in PDFs prove that damages on the rail tracks are reflected in the prediction results of the trained baseline NARX models.

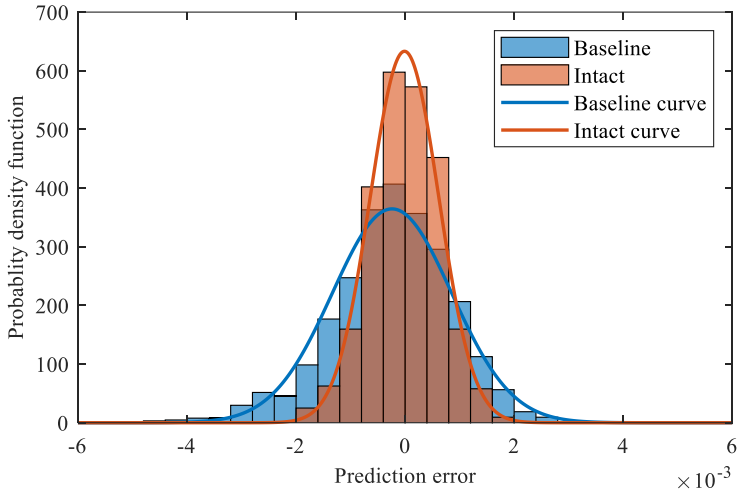

(a)

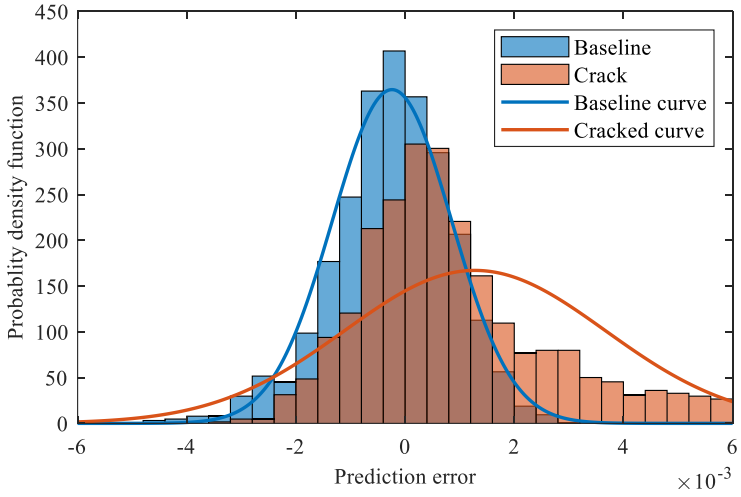

(b)

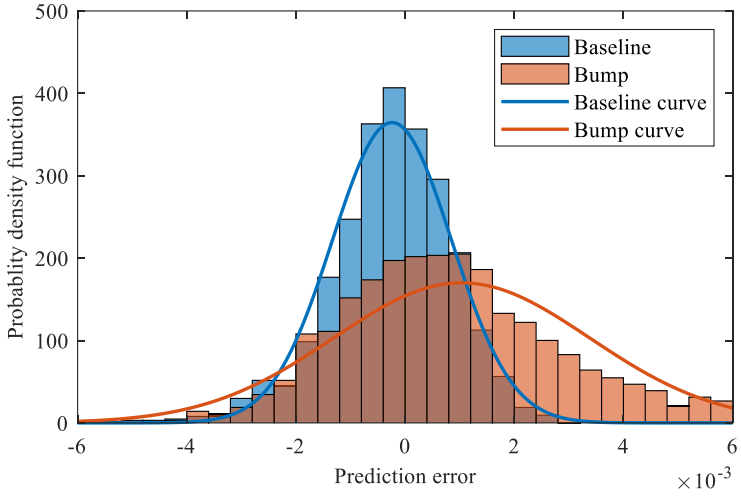

(c)

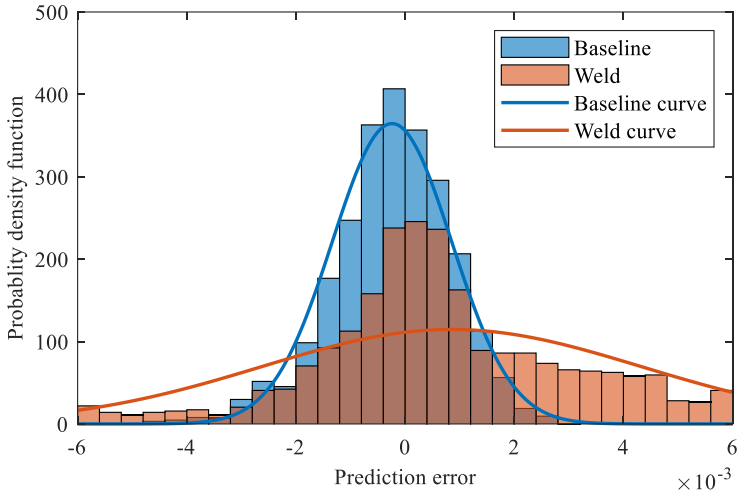

(d)

Figure 4-13. Probability density function of the prediction errors of the 250 kHz baseline model trained by LM method: (a) Intact; (b) Crack; (c) Bump; (d) Weld.

4.4. Large-scale testing

To further verify the damage detection performance of the proposed method, large-scale testing is conducted. Four new rail segments featuring intact, crack, bump, and weld conditions, that have not been used in previous experimental studies, are used in the

large-scale testing session. The length for each rail segment is 1,400 mm, on which PZT and FBGs are attached at the same locations as in the previous experimental study. Likewise, the sinusoidal wave modulated with a Hanning window of 5 cycles is used for ultrasonic excitation, which is aligned with previous study. To ensure the robustness and redundancy of the datasets, a 6-day test period was conducted. On each day, both the PZT and FBG sensors were uninstalled and replaced with new ones. This approach was designed to evaluate the consistency of the measurements and to test the robustness of the proposed method under varying conditions. By systematically replacing the sensors, potential biases or inconsistencies related to sensor performance were introduced to the datasets, thereby strengthening the reliability of the results.

A total of 6,000 ultrasonic samples are acquired in the laboratory using the excitation frequency of 250 kHz, of which 3,000 are acquired under intact rail condition and 1,000 for each defected condition (crack, bump, and weld). In previous experimental studies, the selected ultrasonic excitation frequency bands proved to be effective when conducting damage detections. Therefore, instead of repeating the same excitation configuration which denotes a wide range of ultrasonic frequencies being deployed, a 250 kHz excitation is representatively configured in large-scale testing should be adequate to verify the feasibility of proposed method in large-scale testing.

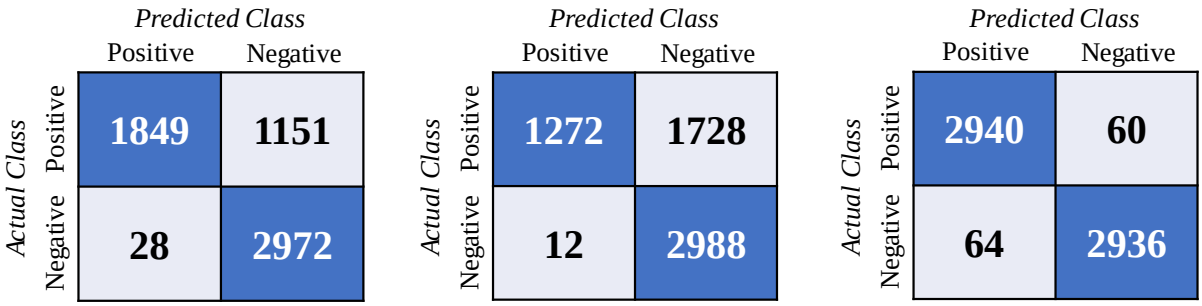

(a) (b) (c)

Figure 4-14. The damage detection results of large-scale testing using (a) SCG method; (b) QN method; (c) LM method.

The NARX models trained using SCG, QN, and LM functions are individually tested using the same testing set. The results of large-scale testing are demonstrated in the format of matching matrixes as shown in **Figure 4-14**. In each matrix, Positive' denotes that damage is diagnosed while 'Negative' refers to the judgement that the rail is of a healthy statue. Through comparison, the main advantage of using the LM method in damage detection can be observed that the number of False Negative (FN) classifications is significantly lower, meaning fewer positive samples (of defected conditions) are neglected. This is vital to engineering application to guarantee the damaged rails are timely detected, requiring relatively conservative and redundant detection methods to be developed. Although the LM-trained model is outperformed by others on negative samples collected on healthy rails, it is still preferable to train a preservative model that gets more false alarms than let the model ignore critical damage when conducting fault diagnosis. In this sense, it is of no doubt that the NARX model trained by LM outperforms the other two models. The optimized NARX model is very

sensitive towards UGW data anomaly patterns induced by rail defects. Therefore, in future studies, leveraging model robustness against noise and prediction accuracies towards various types of rail damage should be addressed.

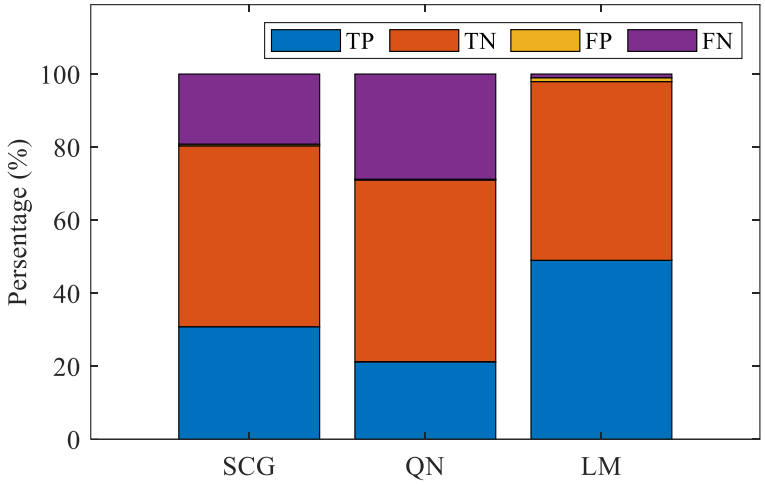

Figure 4-15. Stacked bar chart of damage detection results of large-scale testing.

The damage detection performance for each model is also visualized in **Figure 4-15**, where the proportion of True Positive (TP), True Negative (TN), False Positive (FP), and False Negative (FN) results are calculated. The overall accuracy, recall, and precision values of LM method are comparatively better, thus making it a better model to conduct large-scale NDT & E tasks.

4.5. Summary

In this chapter, an innovative rail defect detection method is developed, which is based on UGW signals acquired by the hybrid system introduced in the previous chapter. NARX models, which are tailored to characterize MISO systems, are utilized in this

study to process the multi-channel UGW signals, enhancing the reliability and sensitivity of the defect detection functions. Apart from the exceptional nonlinear fitting performance of NARX, the novelty of the proposed damage detection framework lies in the development of DSF, which is extracted from the PDF of network residuals. The feasibility of the proposed method is fully validated via comprehensive experimental investigations. Through model optimization and visualization, the exceptional damage detection accuracies are achieved. Further large-scale testing proves the effectiveness and robustness of the proposed method in practical applications. The following findings are summarized:

1 The NARX-based damage detection framework can effectively diagnose railway health status using a specified DSF which is based on model residuals. This framework is tailored to coordinate with the proposed hybrid sensing system, with multiple input channels of FBG ultrasonic sensors.

2 The NARX models are optimized to achieve optimal damage detection accuracies. Experimental studies show that lower MSE during training results in higher sensitivity towards railway damage. This is due to that the accurate detection of railway tracks rely on a shift in PDF spectrum, which could be more obvious if the training MSE is lower.

3 The visualization of the NARX model predictions effectively reveal the nature of

damage detection, which is based on PDF of the model prediction residuals. A higher error level increases the probability of defect cases. Due to the linear or nonlinear interference caused by the existence of cracks, the waveform distortion can affect the PDF of the model prediction residuals.

4 The large-scale testing further concludes that the proposed method features excellent robustness and reliability for engineering applications.

CHAPTER 5 RAILWAY TRACK DEFECT IDENTIFICATION USING ORTHOGONAL MATCHING PURSUIT

5.1. Introduction

Cracks are the most common type of defects on railway tracks, threatening safe and smooth operation of rail system (S. X. Chen et al., 2021; Ghafoor et al., 2022; Y. Zhang et al., 2024). Although minor cracks may not undermine the overall rail integrity, they may grow so rapidly into huge cracks (J. Chen et al., 2018; Chowdhury & Sehitoglu, 2016; Q. Wu et al., 2019) that there will be only limited time left for railway maintenance and management department to react before disastrous incidents happen. Consequently, damage detection methods, which can detect cracks at an early stage where they are still harmless to railway integrity, are expected to be developed and implemented. However, it is extremely challenging to accurately detect and locate such minor defects. Advanced sensing techniques of NDT are utilized to conduct on-site inspections (Rostami et al., 2020).

When it comes to GWT-based damage detection methods, it is vital to carefully determine and adopt feasible and effective damage indices extracted from UGW signal. Several solutions have been proposed to characterize UGW waveform to reveal health conditions of structures or objectives under testing. X. Sun et al. (2022) deployed

damage features based on energy attenuation and waveform distortion and compared their sensitivity to railway defects. Such waveform analysis-based damage indices require a priorly obtained baseline for comparison, which in most engineering scenarios is hardly available. K. Wang, Cao, et al. (2020) implemented ultrasonic receivers onto in-service railway turnouts and extracted the defect growth-induced changes in diffused ultrasonic wave signals to warrant the integrity, which does not require any specific baseline thresholds to be priorly obtained. Although this method can accurately detect the existence of railway defects, the exact location of defects cannot be estimated. Another typical engineering paradigm is a long-range UWG active detection device developed by the Institute of Maritime Technology (IMT) (Loveday, 2012) permanently installed in a railway route in South Africa to monitor rail fractures and rail weld defects. It has been reported that 3 defects have been successfully discovered during a 15-month monitoring period. However, there are obvious limitations regarding this UGW monitoring system, specifically its insensitivity to minor rail cracks with smaller dimensions.

To reveal defect characteristics such as location in rails, efforts have been made to study waveform reconstruction of waves reflected by cracks in time domain. To this regard, the MP algorithm has been utilized to analyze and represent various stationery and non-stationery signals. MP is known to excel at linear decomposition of ultrasonic signals using a redundant dictionary composed of atoms which is preset to ensure the

reconstruction quality. Numerous researchers deployed MP algorithms to reconstruct UGW signals on simple structures, such as plain plates (B. Wu et al., 2017) and composite structures (Cui et al., 2022; H. Lu et al., 2024; Sha et al., 2021; B. Tang et al., 2024) where Lamb waves are the dominant guided wave component. Tse and his research team have been devoted to studying signal representation techniques in processing UGW signal and detecting defect-reflected waves in pipelines (Fang & Tse, 2019; Ng et al., 2022; Rostami et al., 2017; Tse & Wang, 2013; X. Wang et al., 2010). Nevertheless, for complex infrastructures like rails within which multiple reflections and scatterings of UGW are expected to take place, it is still an unexplored area whether MP-based methods can be successfully applied in a similar manner. Ghafoor et al. (2022) utilized MP to detect defects using laser-generated Rayleigh waves to minimize the drawback of having unwanted wave packets reconstructed. This approach is highly effective when applied to surface and subsurface rail head defects. There are special scenarios, however, where UGW propagation mechanisms are so complex causing highly overlapped waveforms in time domain. Thus, the reconstructed crack reflected waves may not be as straightforwardly observable as those reconstructed on the rail heads. Consequently, the potential feasibility of using MP-based methods to identify rail cracks in more complicated signals remains to be explored.

This chapter presents a novel crack identification method using optical fiber sensing to conduct GWT on railway tracks. OMP is adopted to process the UGW signals and

reconstruct the crack reflection related wave packets in time domain, thus accurate locations can be determined. A specially designed dictionary is constructed for rail crack reflected wave representation. Numerical simulations are conducted in this research to fully reveal the UGW propagation mechanisms in rail webs while the simulated signals are utilized to verify the proposed OMP-based rail crack identification method. Then, experimental investigations are designed to further prove the applicability of the proposed method. Various experimental configurations are considered so that scientific proof can be provided to support the identification results of a rail crack. Linear regression is deployed to characterize the crack reflected wave time slot and the crack location so that the crack position can be accurately predicted for any scenarios. This research provides a novel and straightforward damage detection method for railway track web. The research outcome significantly contributes to the development of efficient railway track maintenance strategies enhancing railway safety.

5.2. Methodology

5.2.1. Orthogonal matching pursuit

MP is an adaptive signal time-frequency-domain processing technique that can sparsely decompose a target signal into a linear expansion of components (i.e., atoms) that belong to a redundant dictionary of waveforms (Cai & Wang, 2011; J. Wang et al., 2012). By creating a customized redundant dictionary, target signal can be expanded

and represented using various combinations of dictionary components with varying time-frequency or time-scale characteristics. This makes MP applicable in those scenarios where the knowledge of signal time-frequency features is priorly available for processing. Therefore, MP can be comprehended as an inverse solution where the target signal approximated using a given dictionary. To solve such inverse problems, iterative reconstruction strategies have been extensively proved to be effective (M. Chang et al., 2022; J. C. Hong et al., 2005; B. Wu et al., 2017) in the field of machine learning.

To illustrate the OMP deployed in this study, the basic MP algorithm is first introduced. A dictionary Λ that consists of representative atoms. Then, the MP process can be mathematically formatted,

$$b = \sum_{i=1}^{k} x_i a_i + r \qquad \textbf{(5-1)}$$

where x_i represents the amplitude correction coefficient for atom a_i selected at the i-th iteration; r is the residual term for optimal approximation that is formatted using L_2 normalization. For each time new atoms are selected from the dictionary, r is updated until it meets the optimum residual constant that is configured based on the noise level of b, which is the target signal to be represented.

In the above process, the atoms are not mutually orthogonal vectors. It is thus rational

that the residual r calculated after each iteration is subtracted based on the subsequent ones, resulting in components that are not orthogonal to be selected for representation. In this manner, accurate approximation can be achieved. However, in some cases such as identifying reflected waveforms interfering with unwanted wave packets that overlap onto each other, it is vital to ensure that only the desired waveforms are reconstructed for accurate detection. Therefore, OMP is introduced, and a 5-step iterative process is introduced below.

Step 0: In the initialization phase (before iterations), the following parameters are initialized,

$$\begin{aligned} r_0 &\leftarrow b \\ \Lambda_0 &= \emptyset \\ k &\leftarrow 1 \end{aligned} \tag{5-2}$$

where r denotes the residual and Λ is the index set used to keep record of the selected atoms during previous iterations thus prevent duplicated selection. k is the iteration counter.

Step 1: At the k-th iteration, extract the atom in A that has the largest absolute value of correlation with the residue vector r_{k-1}, which can be expressed as the following equation,

$$\lambda_k = \text{arxmax}_{j \notin \Lambda_{k-1}} \left| \langle a_j, r_{k-1} \rangle \right| \tag{5-3}$$

through which it can be assured that an atom that has not been previously selected, i.e., λ_k is not included in Λ_{k-1}.

Step 2: Augment the index set,

$$\Lambda_k = \Lambda_{k-1} \cup \{\lambda_k\} \quad \textbf{(5-4)}$$

Step 3: Perform estimation by solving a linear regression problem,

$$x_k(i \in \Lambda_k) = \text{arxmin}_x \left\| A_{\Lambda_{k-1}} x - b \right\|_2 \quad \textbf{(5-5)}$$

where $A_{\Lambda_{k-1}}$ denotes a sub-matrix of A from which atoms (i.e., columns) are used to regressively estimate b.

Step 4: Compute the approximation using the coefficient vector x_k obtained in Step 3 at iteration k. This process is mathematically written in the following equation,

$$\hat{b}_k = A_{\Lambda_k} x_k(i \in \Lambda_k) \quad \textbf{(5-6)}$$

where $\hat{b}_k$ represents the approximation. The above equation is exactly aligned with the inverse problem introduced at the beginning of this section.

Step 5: Update the residual and repeat Step 1-5 until the residual is decreased below a pre-set level.

$$r_{k+1} \leftarrow b - \hat{b}_k \quad \textbf{(5-7)}$$

The above process can be intuitively summarized in the form of workflow demonstrated in **Figure 5-1**. For each iteration the set difference of the sparse dictionary is adopted for atom selection so that the atom vector for signal sparse representation remains nonorthogonal. The stopping criteria can either be a lower boundary of residual or simply the number of iterations.

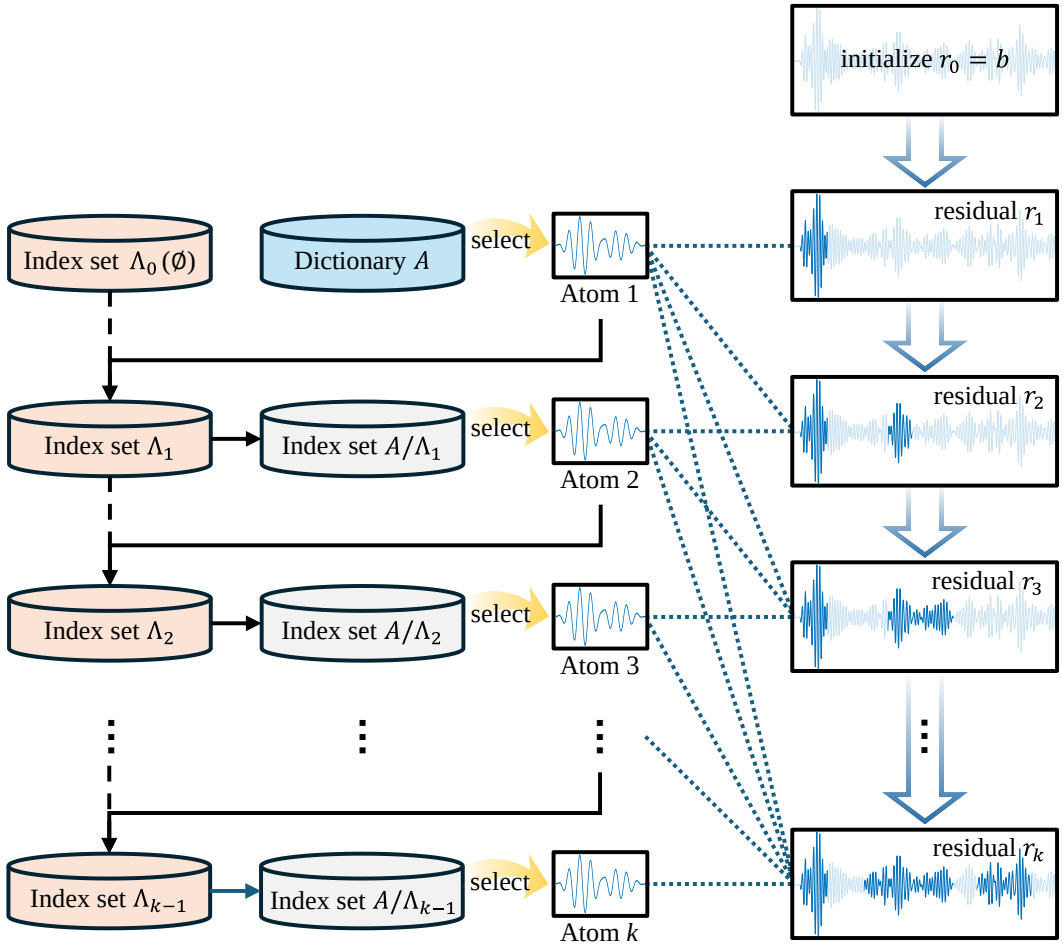

Figure 5-1. Schematic workflow of signal sparse representation using OMP.

OMP algorithms are constantly utilized to sparse signal recovery, feature selection, dimensionality reduction and denoising (H. Lu et al., 2024; Tse & Wang, 2013). In this study, the author deploys OMP to process overlapped UGW signals so that key

information that can reveal rail crack existence can be extracted. However, it must be priorly confirmed that the dictionary Λ used for OMP should contain useful information for reconstruction purposes, otherwise the residual r would maintain on a divergent level that cannot be easily reduced.

5.2.2. Dictionary of interfering reflection components

The propagation characteristics of UGW in rails are too complex to predict in most scenarios. However, previous research on studying UGW propagation mechanisms in pipelines (Y. Chang et al., 2017; J. C. Hong et al., 2005; Z. Zhang et al., 2022) can be utilized for reference. It is concluded that the reflection of guided waves from a defect primarily result from the interference between front-edge reflection and back-edge reflection. That is, theoretically, crack reflected wave packet should be composed of two reflection components that share similar waveform features, such as number of cycle and frequency band, but with varying amplitude and phase shift after colliding onto a geometrical defect. X. Wang et al. (2010) proved this characteristic of defect-reflected guided waves using experimental and numerical data of a pipeline structure. Then Tse & Wang (2013) also testified this discovery and successfully reconstructed defect reflected waves using an optimized dictionary based on two interfering reflection components (IRC). Although rail section is relatively more irregular and nonlinear than that of a pipeline, Rayleigh wave is found to be the dominant component of UGWs when propagating in the longitudinal direction of a rail track (Ghafoor et al., 2021;

Masurkar et al., 2020), which is almost identical to the case of pipelines considering the thickness of rail web is close to pipeline radial depth. Now that railway webs and pipelines share physical similarities in terms of both material properties and geometrical shapes, it is rational to assume that the UGW propagation mechanisms should also be aligned, or at least mechanistically applicable.

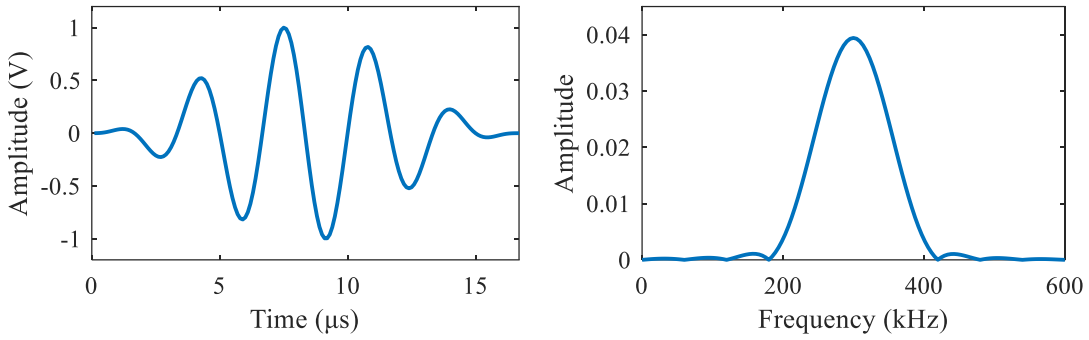

(a) (b)

Figure 5-2. The excitation signals in (a) time domain; and (b) frequency domain.

As stated earlier, it is reported that the reflection waveform is composed of two defect-edge reflected waves. In this research, a 5-cycle sinusoidal waveform modulated by a Hanning window is adopted as the excitation signal. The central frequency of the sinusoidal waveform is 300 kHz. **Figure 5-2** demonstrates the time-domain and frequency-domain excitation voltage tone burst, with the maximum voltage amplitude of 1 V, written in the format below,

$$a_0(t) = \left[1 - \cos\left(\frac{2\pi f_0 t}{5}\right)\right] * [\sin(2\pi f_0 t)] \quad \textbf{(5-8)}$$

where f_0 denotes the central frequency which is 300 kHz in this case.

Based on the waveform, time delay and amplitude decline are applied to construct the dictionary of IRC. The time delay applied to the second 5-cycle sinusoidal wave ranges from 10.1 to 15.0 μs; the amplitude decline of the delayed reflection wave ranges from 0 to 90%. The resolution of applying time delay and amplitude decline is 0.1 μs and 10%, respectively. Then there should be a total of 500 components (50×10), as shown in **Figure 5-3(a)**. Although a dictionary with more components can achieve better temporal reconstruction accuracies and more effective representations of a wider range of defect dimensions, the computational costs should also be addressed. Based on experimental results of previous studies (X. Wang et al., 2010), it can be priorly estimated that the IRC dictionary proposed in this study can effectively represent the reflective waves induced by cracks with the width ranging from 1 to 10 mm. For each iteration of OMP, a sliding window is applied to the original signal so that the atoms with maximum correlation and minimum fitting residual can be selected. The length of the window equals the length of each atom in the dictionary. The sliding step is 1 μs, which reflects the reconstruction resolution of OMP. **Figure 5-3(b)** demonstrates the OMP process for signal sparse representation. Taking a random atom retrieved from the dictionary atom *i* as an example, atom *i* is selected and linearly fitted into signal of each sliding window and corresponding residual vector $\boldsymbol{r}_i = [r_{i,1}, r_{i,2}, \dots, r_{i,n}]$ can be obtained. After repeating the above calculation for every atom in the dictionary, it can be determined which atom contributes to the maximum global residual reduction for sparse representation.

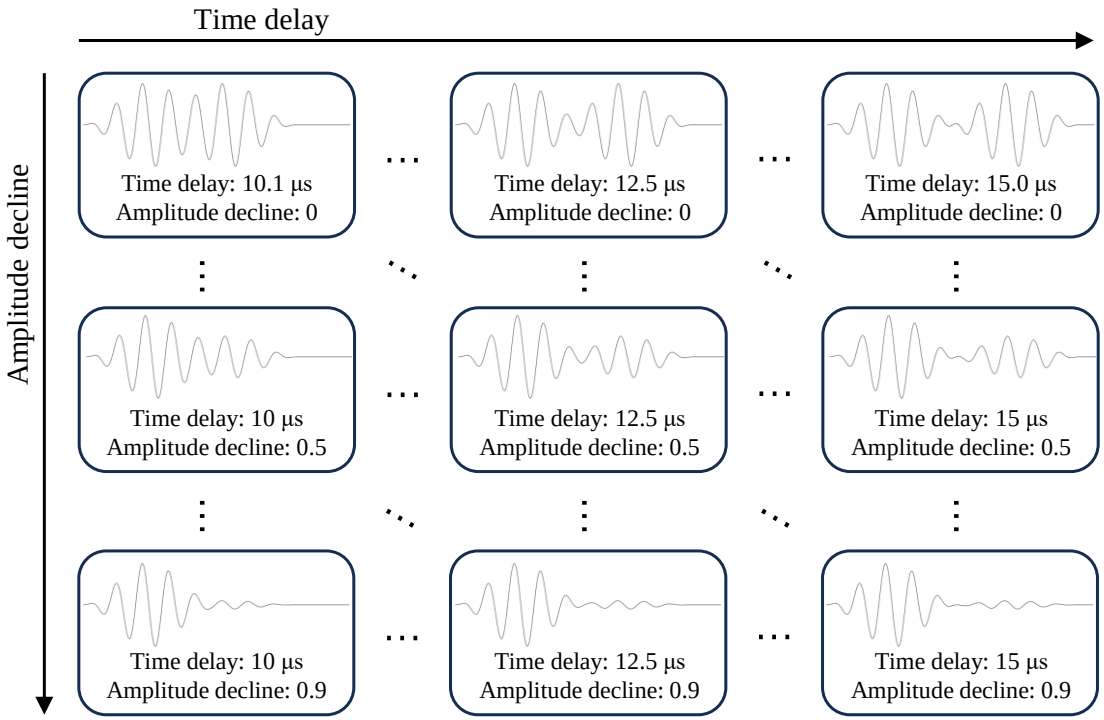

(a)

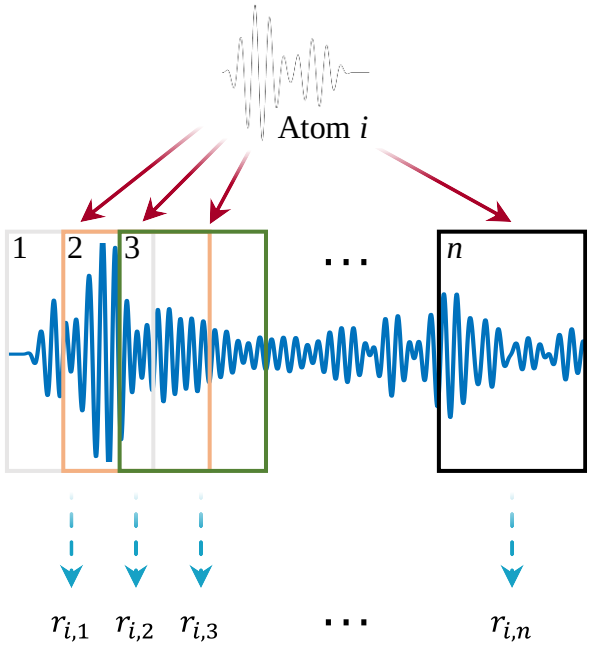

(b)

Figure 5-3. (a) The composition of IRC dictionary and (b) the schematic matching pursuit process for signal sparse representation.

To accurately represent the crack reflective wave in the time domain, it is generally preferable to utilize a large redundant dictionary constructed with smaller phase shift and amplitude decline steps. However, a larger dictionary would result in longer calculation time. In each signal reconstruction process performed on a signal of 2,000 data points, the computational time required for one iteration of OMP algorithm is approximately 1 second on a workstation equipped with an i7-11x CPU, 32 GB of memory, and a 3060Ti GPU, which is considered acceptable for practical application.

5.2.3. Rail crack identification framework

Based on the OMP algorithm and IRC dictionary introduced in this section, an integrated rail defect identification framework is proposed and shown in **Figure 5-4**. For starters, the IRC dictionary is constructed based on the excitation signals, following the steps introduced in section 5.2.2. Then, the acquired UGW signal is sparsely represented using OMP algorithm, which selects atoms from IRC dictionary. The reflection interval is defined as the time-domain window where crack reflective wave packets will possibly be reconstructed. It is important to have a prior knowledge of reflection interval as to rule out interference from wave packets induced by direct impact and end reflection. Once the reflected wave is reconstructed, the iterative loop breaks, and the framework outputs the representative atom of reflective wave consequently the crack location can be characterized.

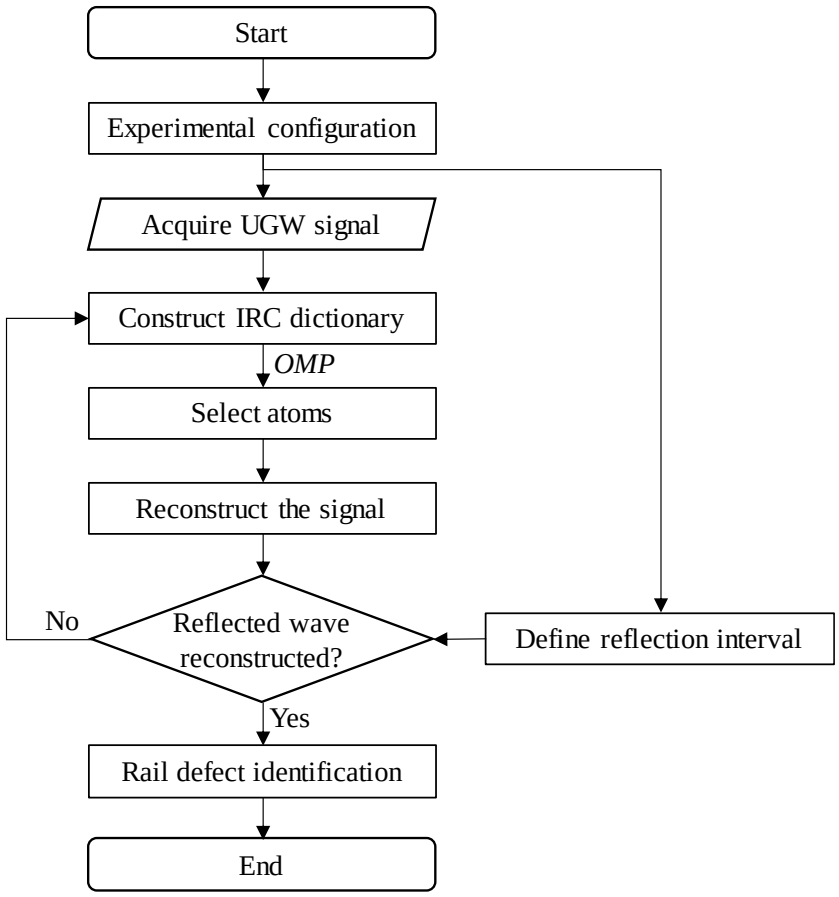

Figure 5-4. Flowchart of the proposed rail defect detection method.

5.3. Numerical investigations

In this section, FEW technique is deployed to investigate the feasibility of the proposed rail crack identification method using COMSOL Multiphysics Software. Specifically, it is significantly more convenient and facilitative to use FEM simulation to reveal the propagation mechanism of UGWs in railway because the transient responses desired can be easily obtained under any controllable conditions. Consequently, 3-D FEM is carried out and utilized to generate simulated UGW signal to verify whether the proposed method can successfully reconstruct the wave reflected by a rail web crack. The effectiveness of IRC dictionary is also verified by comparing reconstruction results

with other redundant dictionaries.

5.3.1. Finite element modelling configurations

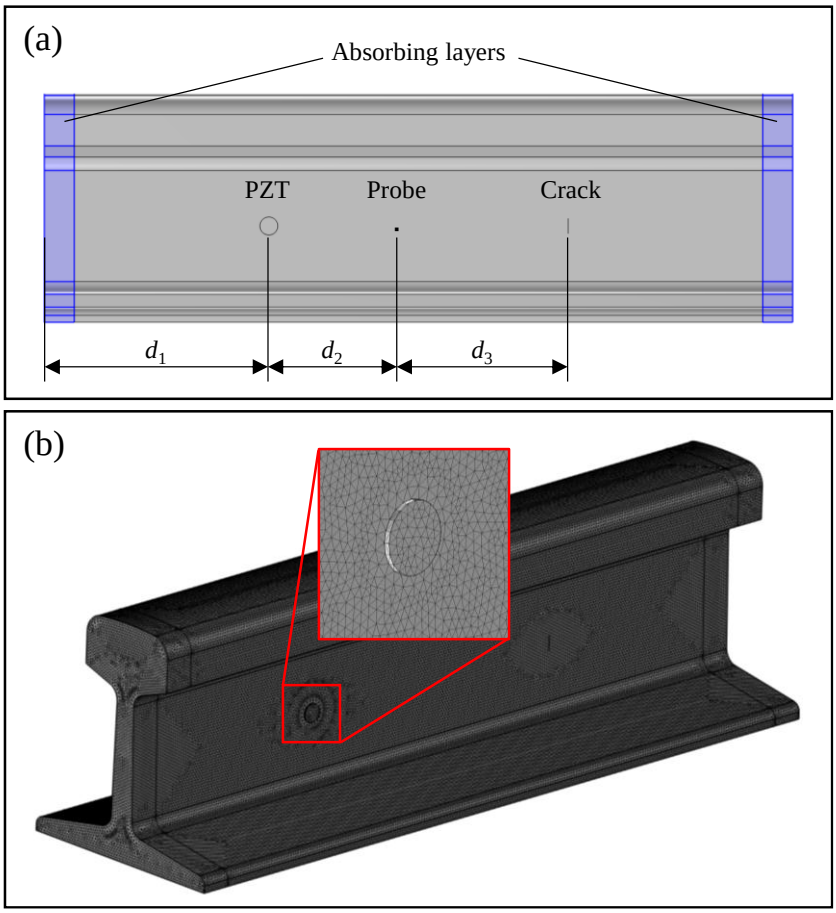

Figure 5-5. FEM configurations: (a) sensor layout; (b) the mesh grid of PZT and rail.

The FEM is an effective tool to study guided wave propagation as it can simulate complicated UGW interactions in complex 3-D structures such as pipelines and rails (S. W. Han et al., 2016; Jiang et al., 2021; X. Li et al., 2023; H. Sun et al., 2024). In this study, the 3-D model of the rail segment (model BS100R) with the length being 500 mm is imported, and an artificial crack is introduced to the rail web, as shown in **Figure 5-5**. The specific dimension of layout is given in **Table 5-1**, corresponding to a

schematic shown in **Figure 5-5(a)**. The crack is modelled by defining a parametric surface that is identified as a material fracture. The depth of the crack is 2 mm, and the vertical length is 10 mm.

Table 5-1. The configurations of numerical cases (unit: mm).

Case No.	d_1	d_2	d_3	Remarks
0	150	30	(no defect)	Control group
1	150	30	170	
2	150	50	150	Comparison group
3	150	70	130	

The main material properties for modelling the steel rail and PZT are given in **Table 5-2**. As shown in **Figure 5-5**, the rail and PZT are respectively modeled, and an identity boundary pair is configured at the contact area between the PZT and rail web surface ensuring continuity. The diameter of the PZT is 8 mm and the thickness is 1 mm. To simplify the piezoelectric effect, a velocity function written in the format of **Equation (5-8)** is applied perpendicularly to the PZT upper surface. The UGW generated inside PZT then propagates towards the rail, simulating a realistic experimental condition. For signal acquisition, a point probe is configured onto the rail web surface to pick up UGW signals. Considering the sensing directionality of FBG that it is more sensitive to fiber grating-longitudinal deformation than shear deformation (Dang et al., 2024), y-direction strain is recorded and extracted to simulate FBG directional measurement. The sampling rate for the FBG is 10 MHz. Additionally, an absorbing layer is

configured at both ends of the rail model, to simulate a free and non-reflective boundary condition. The maximum mesh size is defined as one eighth of wavelength. Considering the central excitation frequency is 300 kHz, it is thus estimated that the maximum mesh sizes for rail and PZT components are respectively 1.5 mm and 0.8 mm, assuming that shear wave is the dominant propagation mode. For both components, the free tetrahedral mesh grid is deployed (**Figure 5-5b**).

Table 5-2. Material properties of the FEM components.

Variable	Descriptions	Components		Unit
		PZT	Rail	
ρ	Density	7,500	7,800	kg/m³
E	Elastic Module	7.0678×10^{10}	2.0078×10^{11}	Pa
μ	Poisson's ratio	0.3767	0.2889	/
c_p	Longitudinal wave speed	4,160	5,800	m/s
c_s	Shear wave speed	1,850	3,160	m/s

For comparison purposes, 2 FEM models with the same dimensional configurations are adopted in this study, one with an artificial crack and the other without any damage on the rail web. **Table 5-1** demonstrates the model configurations of numerical cases. Case 0 is considered a control group where no defects are placed, while case 1-3 are rail segments with web cracks. The UGW signals for case 1-3 are sampled and extracted from Probe 1, 2, and 3, respectively.

5.3.2. UGW propagation routes

Given the configuration and sensor layout introduced in **Figure 5-6**, it can be predicted that 3 individual wave packets should be recorded by FBG sensor, namely the direct impact wave, the defect reflective wave, and the later arrival wave reflected from the near end, which are sorted by time order.

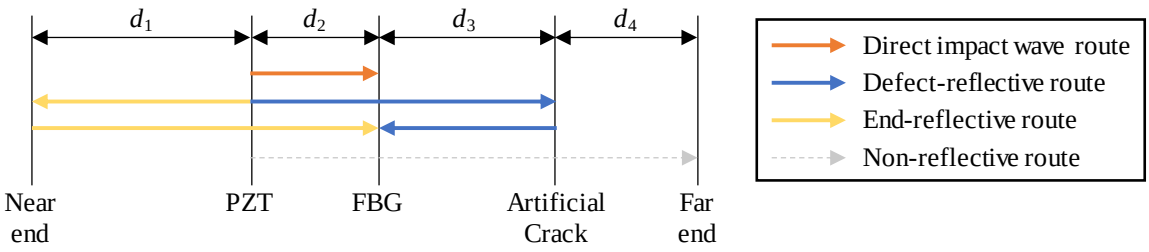

Figure 5-6. Schematic of UGW propagation routes.

The time slots in which they appear on this time series depends on the total length of their propagation routes. **Figure 5-6** comprehensively illustrates the propagation routes for each wave packet. Because of the existence of absorbing layer, it is assumed that far end-reflective wave cannot travel back to the sensing area within the sampling period, thus is labelled as non-reflective route in the schematic. Referring to the propagation routes, the direct impact wave is received first, followed by the defect-reflective wave packet (marked blue in **Figure 5-6**) travelling back after colliding onto the artificial crack. And the end reflected wave approaches FBG sensing area at last due to its travelling distance being the longest, which is the yellow route drawn in the schematic. The theory is that by calculating the propagation route of defect-reflective

wave route, the location of the defect can be revealed.

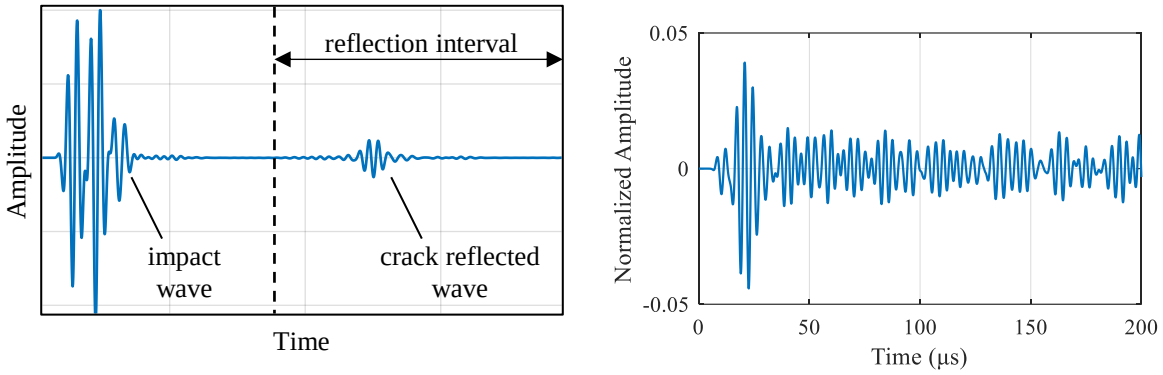

(a) (b)

Figure 5-7. The simulated UGW signals in time domain acquired on rails with (a) a schematic case with low-reflective boundaries, and (b) normal-reflectivity boundaries.

However, the above analysis is based on theoretical argumentation and analysis. The actual UGW signal is interfered with by multiple reflections in rail web. **Figure 5-7** schematically demonstrates the UGW signals with ideal low-reflective boundaries compared with normal-reflectivity boundaries. The low-reflectivity boundary is a special type of boundary condition whose primary purpose is to absorb outgoing waves and minimize their reflection back into the computational domain. This configuration can minimize the reflections induced at the rail geometric boundaries except for the artificial crack. In time domain, the wave packet of direct impact can be clearly observed in **Figure 5-7(a)**. Within the reflection interval, crack reflective wave can also be intuitively observed. But unfortunately, this only happens when the boundary is configured non-reflective. The actual signal simulated is shown in **Figure 5-7(b)**, where waveforms are highly overlapped due to reflections and scattering. This is

disadvantaged for crack identification. Therefore, OMP is proposed to reconstruct UGW signals aiming to filter the interfering factors while leaving useful information to be utilized to identify defects.

5.3.3. OMP reconstruction results using IRC dictionary

In this numerical study, OMP is utilized to reconstruct the sparse representation of the simulated UGW signal using atoms of the IRC dictionary. **Figure 5-8** shows the OMP reconstruction results in time domain. The crack reflective waves are reconstructed after the 3rd iteration of OMP sparse representation for case 1-3, shown in **Figure 5-8(b)**, 5-**8(c)**, and 5-**8(d)**.

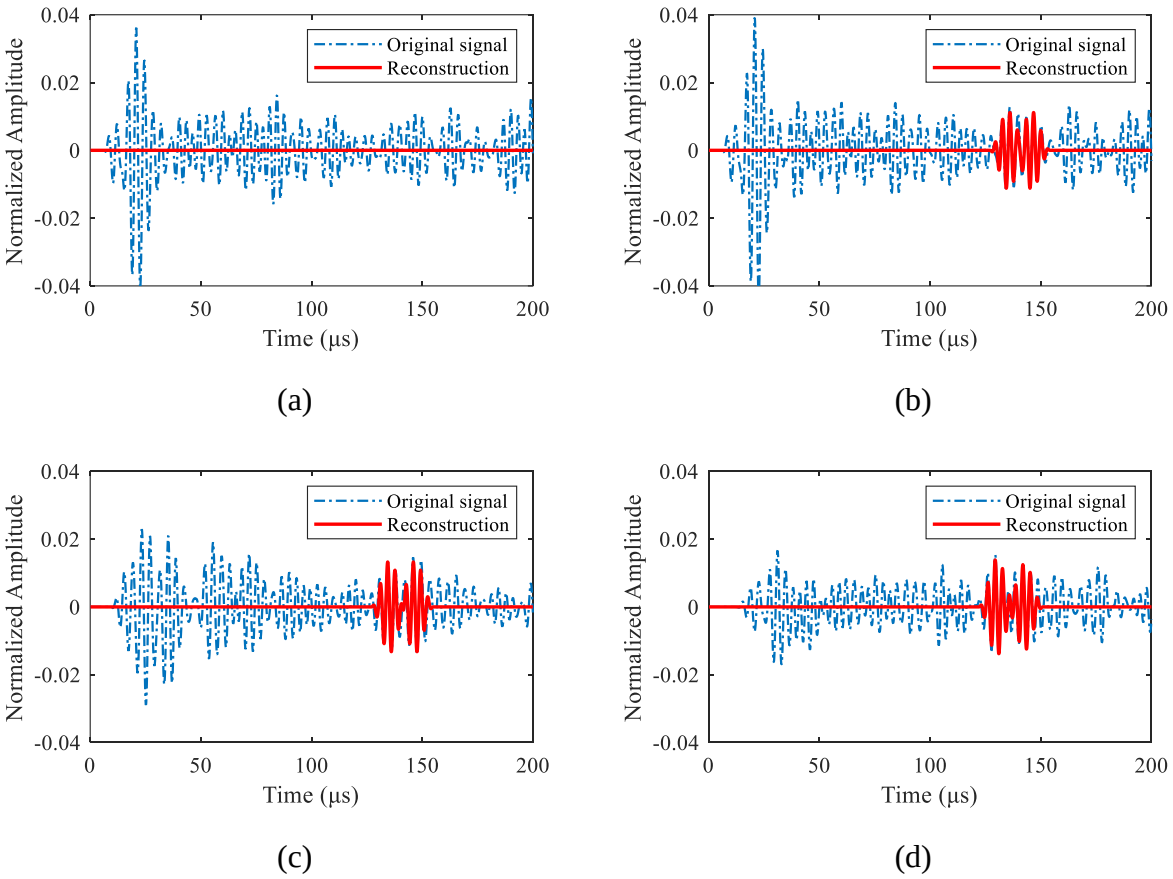

(a) (b)

(c) (d)

Figure 5-8. The OMP reconstruction results performed on UGW signals: (a) Case 0, (b)(c)(d) Case 1-3.

Despite the numerous interfering wave packets which can be deceitfully misleading when it comes to damage identification, the crack reflective wave packets are represented using the proposed approach. For comparison, no atoms are selected via OMP algorithm within 5 iterations to reconstruct the UGW signal within the crack reflection interval, which is defined between 100 and 200 μs in this case (**Figure 5-8a**). However, it still needs further proof to check whether the wave packet selected through OMP can be sourced back to the collision and reflection of the artificial crack.

To provide solid scientific proof to testify the authenticity of OMP results, the velocity field distributions throughout the simulation period are exported for analysis (**Figure 5-9**). As can be observed, UGW is excited by PZT and propagates in the rail. When t = 70 μs, the waves interact with the crack with some waves passing through while the rest are being reflected.

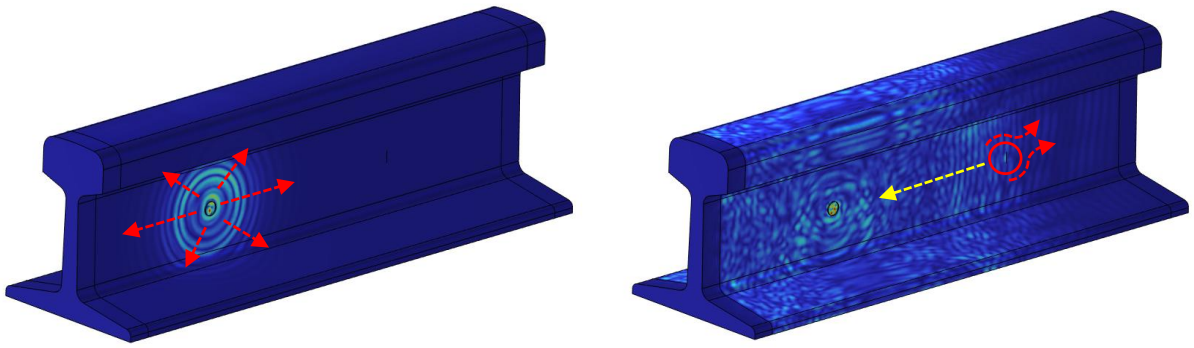

(a) (b)

Figure 5-9. The wave velocity field of the rail web at (a) t = 20 μ s, and (b) t = 70 μ s.

To further determine the exact time when crack reflective waves, the rail web horizontal cross section is selected to present 2D velocity field at various time slots. As shown in **Figure 5-10**, 6 key time slots are specifically selected to support the OMP reconstruction results. The UGWs are vertically excited by the PZT and are spreading into all directions, ending up bouncing back and forth within the narrow section of rail web. It is clearly visible that the surface waves are travelling longitudinally on both surfaces of the rail web, with clear periodical characteristics. Ahead of those surface waves are stress waves caused by extrusions between the elastic elements, featuring lower amplitude levels and longer wavelengths. At approximately 70 μs, the propagating wave packets collide with the artificial defect, resulting in some of the waves passing through while some are reflected. Then later at 100 μs, the waves are seen travelling backwards. When t = 119 μs, 125 μs, and 131 μs, the crack reflective waves approaches the coordinates where the FBG sensing points are placed in numerical cases 1-3, respectively. It is thus safe to assume that the OMP reconstruction results shown in **Figure 5-8** should be valid and accurate. **Figure 5-10** also reveals that throughout the impact wave and reflective wave propagation, the wave velocity fluctuates at the level of 3,000 m/s, which agrees with the FEM results demonstrated in Chapter 3.

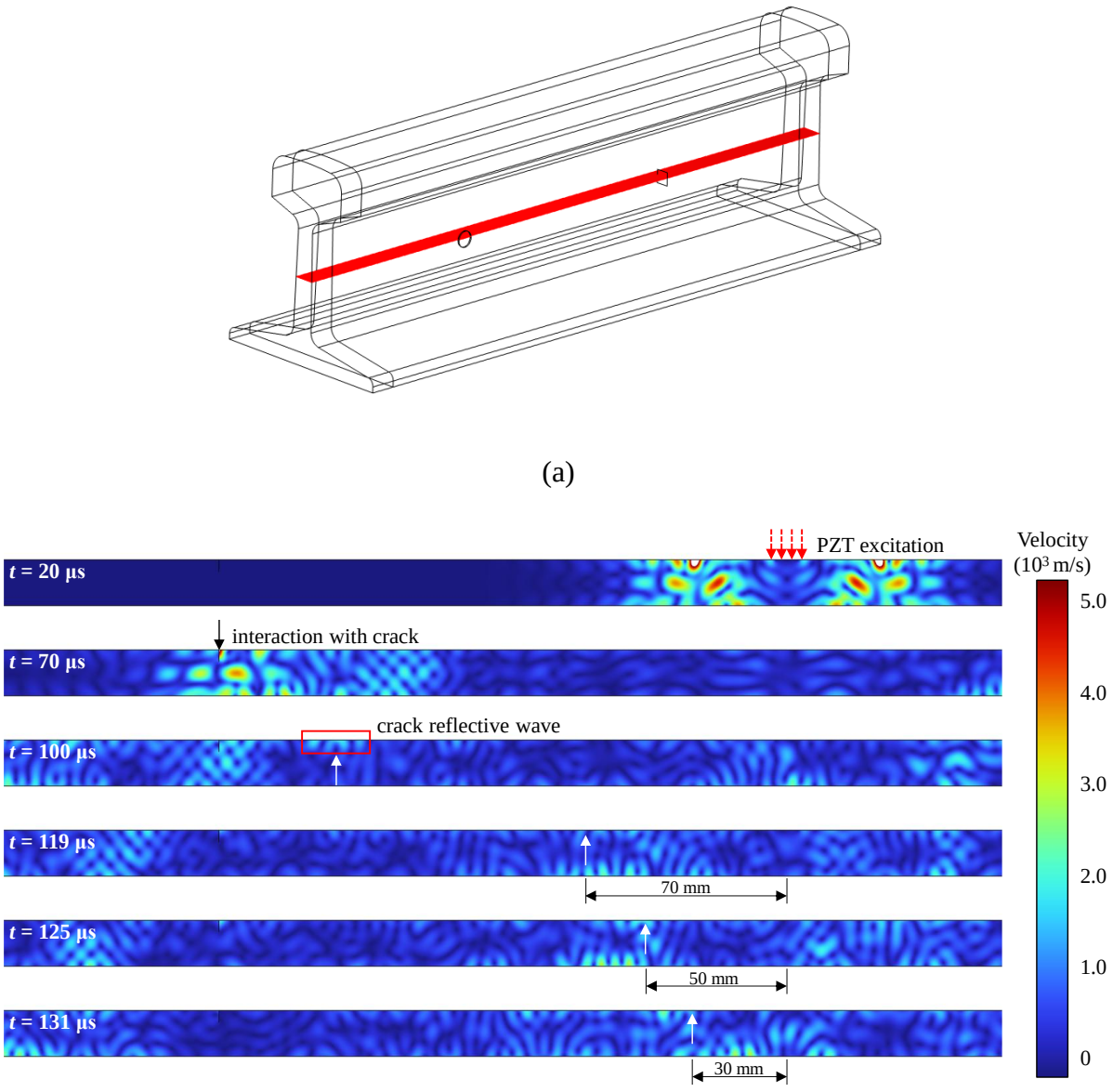

Figure 5-10. The wave velocity field of the rail web cross section: (a) the chosen cross section in 3D display, and (b) 2D velocity field at different time slots.

The above findings undoubtedly indicate that OMP with IRC dictionary is highly capable of differentiating the crack reflected wave from the raw signal where numerous wave packets are diverse and highly overlapped because of the complex reflections that repeatedly occur during propagation.

5.3.4 Comparative study of OMP reconstruction via alternative dictionaries

The reconstruction results illustrated in the last section prove the effectiveness of utilizing IRC dictionary to represent the characteristics of the crack reflected waves. In this section, alternative choices of dictionaries are considered to conduct comparative studies. Specifically, a default sinusoidal dictionary (DSD), a wavelet function dictionary (WFD) and a dictionary composed of single 5-cycle sinusoidal curves modulated by a Hanning window (SSHD) are respectively deployed to reconstruct the UGW signals simulated via FEM. Examples of the atoms in these three dictionaries are randomly selected to demonstrate the composition characteristics, shown in **Figure 5-11**. In DSD, numerous combinations of sine and cosine waveforms are presented; level-2 scaling functions, and level-1 and level-2 wavelet functions are utilized to compose WFD, e.g., the 'Haar' wavelet functions; The creation process of SSHD is quite similar to that of IRC dictionary where waveform amplitude decline and phase shifts are deployed, except for that there is a single 5-cycle sinusoidal wave in each atom.

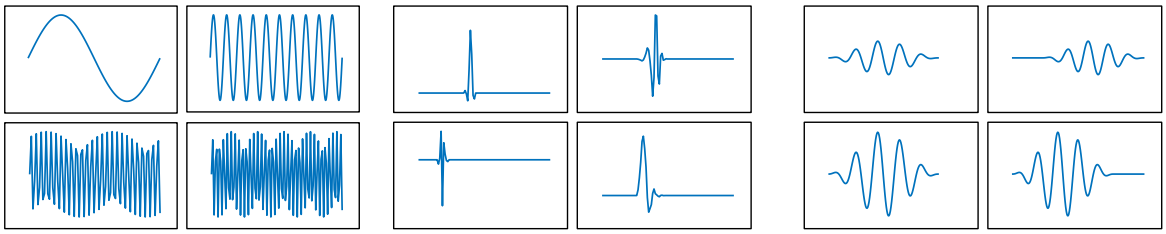

(a) (b) (c)

Figure 5-11. Atoms retrieved from dictionaries selected for comparison studies. (a) DSD; (b) WFD; (c) SSHD.

The representation results for case 1 are shown in **Figure 5-12**. It is clearly observable that OMP with DSD and WFD fail to reconstruct useful waveforms related to crack reflections. It cannot be intuitively differentiated which wave packet corresponds to the reflected waves caused by either the artificial crack or the near end of the rail web, because the atoms selected from DSD and WFD are not representatively effective for this specific reconstruction task. In stark contrast, the performance of OMP using SSHD is surprisingly better. After only 6 iterations, the wave responsible for crack reflection is successfully represented. Yet it remains unsatisfactory that several unwanted wave packets are also reconstructed (**Figure 5-12c**), which would terribly interfere with the defect identification process.

To briefly conclude, as for this numerical simulation case study, the IRC dictionary outperforms several other dictionaries, making it the best choice for reconstructions of crack reflected waves. It has also been indicated through comparative studies that the proposed IRC dictionary can achieve the best reconstruction accuracies because the atoms in this dictionary can perfectly characterize the crack reflective waves in time domain, which is based on the assumption of the 2-edge reflection mechanism previously discovered by Tse & Wang (2013).

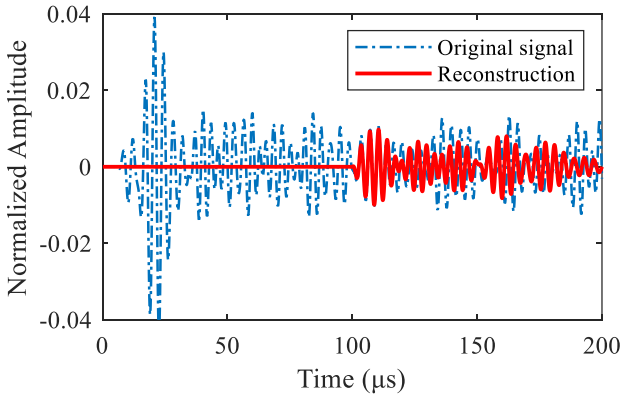

(a)

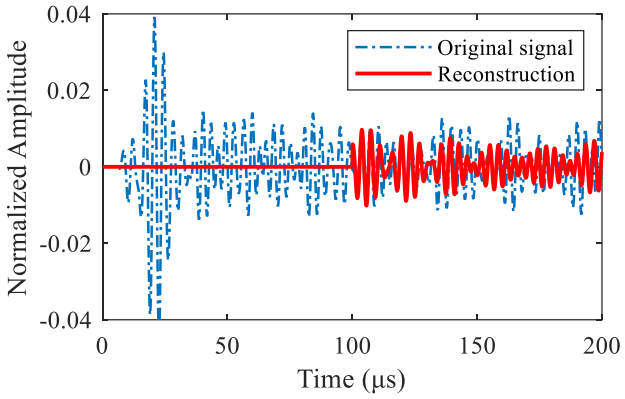

(b)

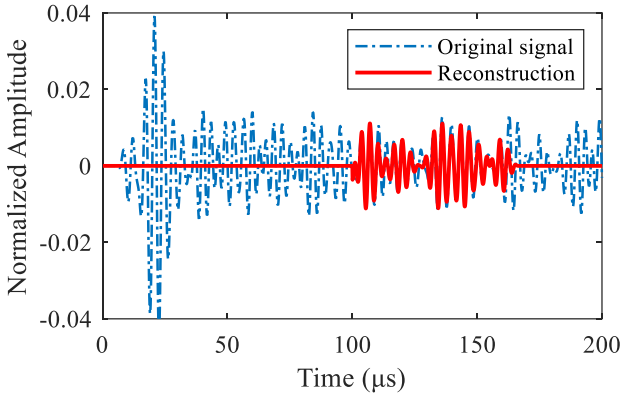

(c)

Figure 5-12. OMP reconstruction results using (a) DSD, (b) WFD, and (c) SSHD, after 6 iterations.

5.4. Experimental investigations

The proposed OMP method has proved to be highly feasible through numerical validations. However, it remains to be verified whether this method can eventually be utilized to process experimental UGW signals. In this section, experimental studies are designed and carried out considering multiple cases to respectively deploy OMP to reconstruct and identify the crack reflected wave packets. The proposed PZT/FBG hybrid sensing system is utilized to excite and receive UGWs on the rail web, which is demonstrated in detail in the following contents, followed by illustrations and further analysis of the experimental results.

5.4.1. Experimental design and configurations

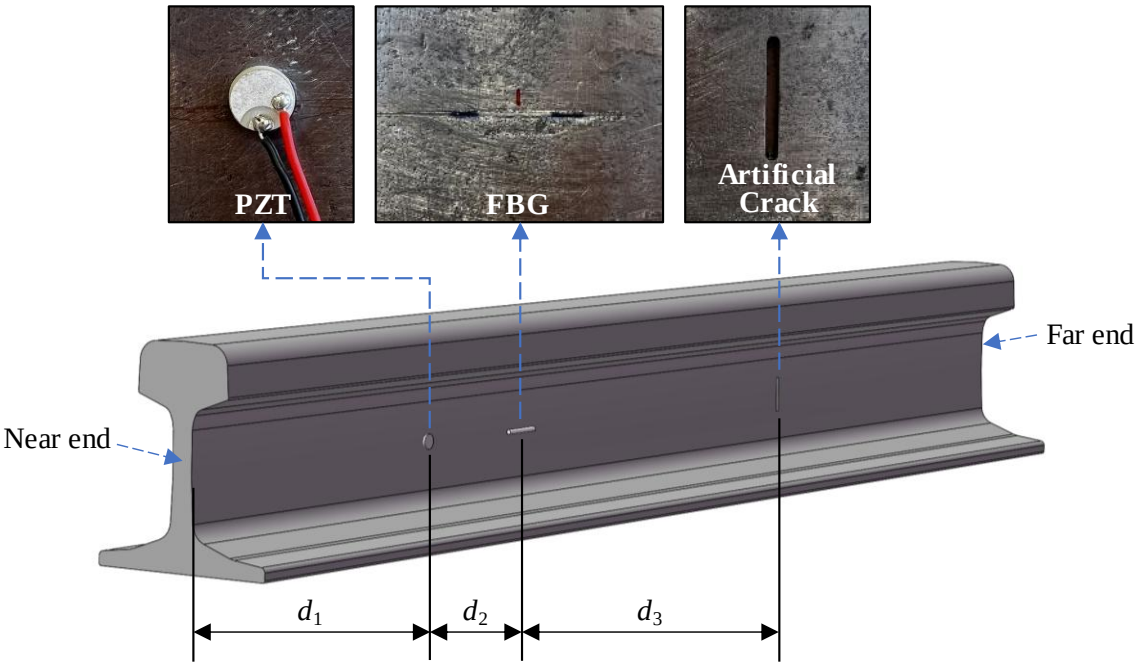

Figure 5-13. The rail segment under testing and the sensor layout.

Two rail segments (BS100R), both with the longitudinal length of 1,200 mm, are adopted in this experiment, one of which is intact with complete and smooth rail web surface, while the other is equipped with an artificial crack with the dimension of 2×2×20 mm (width×depth×length), shown in **Figure 5-13**.

Table 5-3. The configurations of experimental cases (unit: mm).

Case No.	d_1	d_2	d_3	Remarks
0	343	30	no defect	Control group
1	343	30	130	(1) Comparison group.
2	323	30	150	(2) **Case 1-9** were separately performed onto
3	303	30	170	the same rail segment, consequently, the sum
4	323	50	130	of d_1, d_2 and d_3 remains constant.
5	303	50	150	(3) For each experimental configuration, the
6	283	50	170	GWT was carried out 3 times to verify
7	303	70	130	reproducibility.
8	283	70	150	(4) Case 3, 5, and 7 shares the same d_2 and d_3
9	263	70	170	with the numerical case.

In this experimental study, various experimental conditions are considered, where multiple sensor layout varies to create various damage conditions so that the robustness of proposed method can be repeatedly and thoroughly verified. Case 0, acting as the control group, is performed on the intact rail segment without an artificial crack, while Case No. 1 to 9 are performed on the defected rail segment, with varying PZT and FBG sensor layout arrangements, introduced in **Table 5-3**. It should be worth mentioning that Case 3, 5, and 7 share the same the same d_2 and d_3 with the numerical cases 1-

3, to verify the consistency between numerical and experimental conditions.

Considering the sampling length for each guided wave testing is limited to 200 μs, rail end reflective wave theoretically cannot be recorded. Therefore, it is assumed that the UGW signals received by FBG should be aligned with that of the numerical simulation.

5.4.2. Results

The UGW signals acquired by FBG for each experimental case are reconstructed using IRC-dictionary based OMP method, and the results and number of iterations are noted for further analysis. First, it is essential to determine a certain interval in time domain from which reflected waves are expected to be identified. This can be roughly calculated by considering the UGW propagating speed and the distance between FBG and the artificial crack. Specifically in this experimental study, the period between 100 μs and 200 μs is selected and defined as the reflected waves area, for the sake of convenience in intuitive observations. The atoms used for representation of crack reflective waves are also remarked.

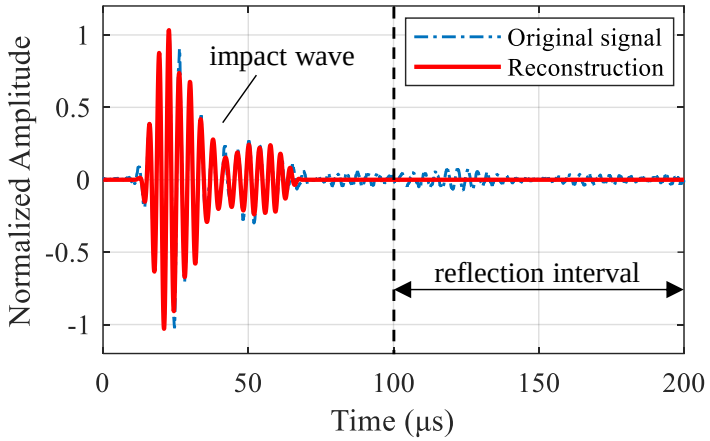

Figure 5-14. OMP reconstruction results of Case 0 after 20 iterations.

For case 0, whose representation results are shown in **Figure 5-14**, only those wave packets induced by first arrival impact and near end reflection are constructed by OMP. There are no waves reconstructed in the reflected waves area after the 20th iteration. It is therefore concluded that no defects are detected, as is the actual case.

The results for case 1-9 are shown in **Figure 5-15**. In stark contrast to the control group, obvious reflected waves are reconstructed in these cases, within the range of selected time interval. For each experimental case, the guided wave excitation and receiving were repeatedly conducted 3 times, to verify the reproducibility. The average time when the crack reflected wave is represented in time domain is marked in **Figure 5-15** by a vertical dashed line. It can be concluded that the estimated time of reflective wave for case 3, 5, and 7 are aligned with the numerical case, which proves the effectiveness and credibility of the proposed method. The average wave velocities for both numerical and experimental conditions are consistent, approximately at 3,000 m/s, with the dominant

wave type being defined as Rayleigh waves.

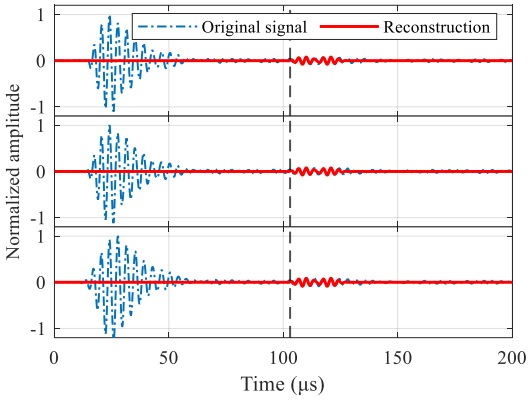

(a)

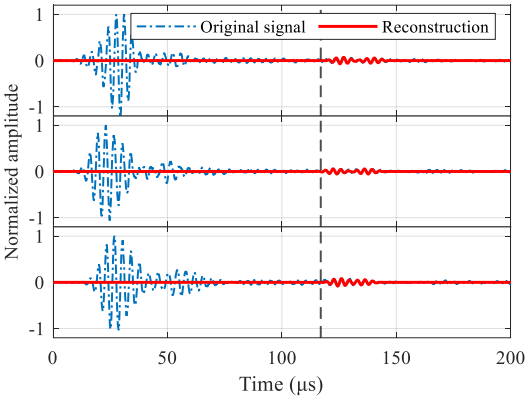

(b)

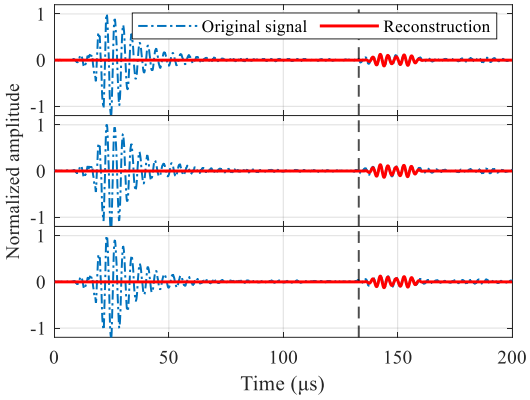

(c)

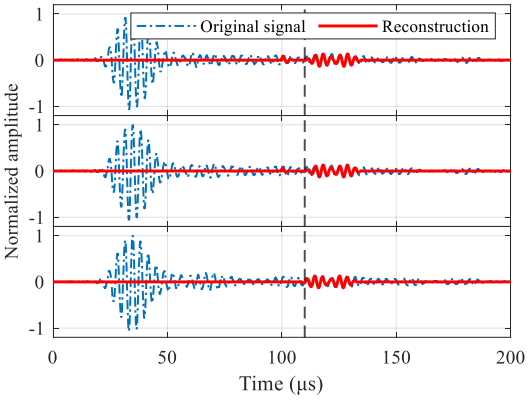

(d)

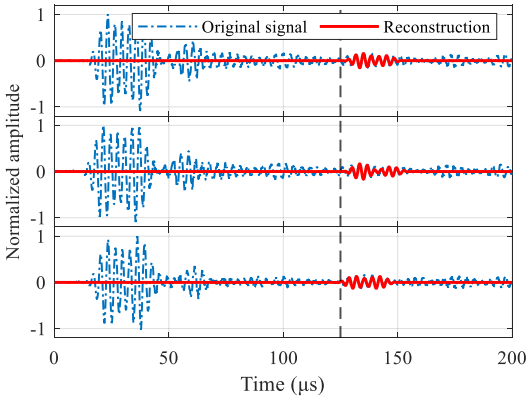

(e)

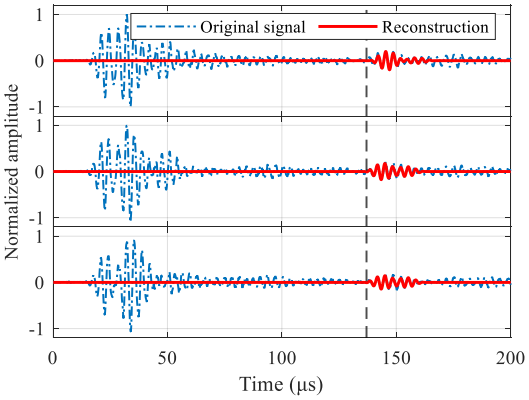

(f)

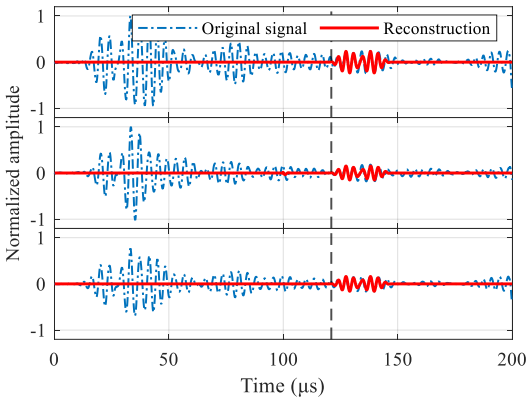

(g)

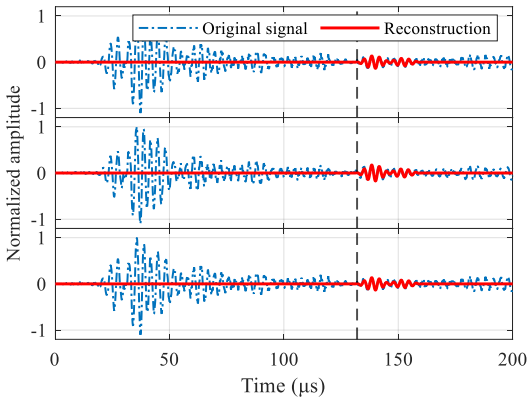

(h)

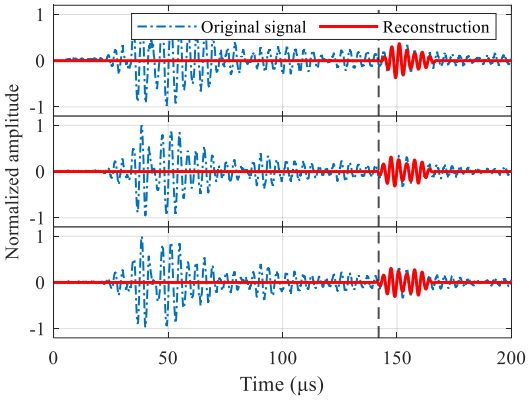

(i)

Figure 5-15. OMP reconstruction results of Case 1-9: (a)-(i) case 1-9.

It can be clearly seen that different sensor layout can cause a delay of time when the crack reflective waves are reconstructed. For example, for case 1-3, the value of d_3, i.e., the distance between FBG and the crack varies ranging from 130 to 170 mm. It can be intuitively observed that the appearing time slots of reflected waves reconstructed share a visible linear relation as d_3 linearly increases. Similar trends can also be concluded for other cases. This linear relation can be approximated and fitted by calculating the distance of UGW propagating route, which is defined as the format

given below,

$$d_{\mathrm{p}} = d_2 + 2 * d_3 \quad \textbf{(5-9)}$$

It should be easily comprehended that d_{p} represents the total travelling distance of UGW, starting from the beginning where it is excited and until the crack reflected wave is recorded by FBG. Similarly, t is used to represent the time when the crack reflected wave is received, according to OMP reconstruction results. Therefore, the relationship between d_{p} and t is obtained and shown in **Figure 5-16**. Although there is experimental error expected for each measurement because of inevitably biased operations, the overall crack reflected wave can be identified within an expectable range of no more than 5% (**Table 5-4**).

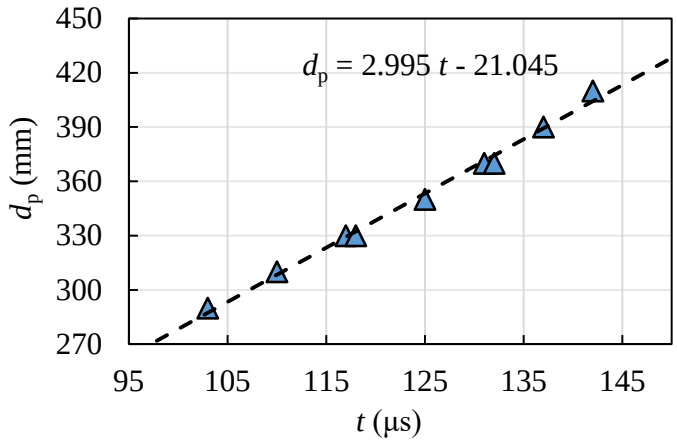

Figure 5-16. d_{p}-t linear fitting results for Case 1-9.

Table 5-4 shows statistics for the reconstruction results. It is intriguing that the number of iterations for damaged cases are significantly less than case 0 where there is no artificial crack. It can then be concluded that UGWs propagating in rails should retain

their fundamental time-domain features even after colliding with the artificial crack, which undoubtedly proves that the IRC dictionary adopted in this research can effectively characterize the waveforms of crack-reflective waves. As for the fitting accuracy, the level of error is controlled with the level of approximately 5 mm, which is sufficient when it comes to damage detection on railway webs with experimental error being considered. Limited by the precision of IRC dictionary adopted in this study, the crack reflected waves are identified with the time resolution of 1 μs. The fitting error could be further reduced if a more redundant dictionary is constructed. However, it would be costly and inefficient to perform OMP on a large-scale dictionary especially considering that the current resolution should be quite sufficient.

Table 5-4. The OMP reconstruction results for each experimental case.

Case No.	Number of iterations	t (μs)	$\widetilde{d_{\mathrm{p}}}$ (mm)	d_{p} (mm)	Fitting error (mm)
0	20	/	/	/	/
1	6	103	287.44	290.00	2.56
2	6	117	329.37	330.00	0.63
3	6	131	371.30	370.00	1.30
4	6	110	308.41	310.00	1.59
5	6	125	353.33	350.00	3.33
6	6	137	289.27	390.00	0.73
7	8	118	332.37	330.00	2.37
8	8	132	374.30	370.00	4.30
9	6	142	404.25	410.00	5.75

5.5. Discussions

5.5.1 Discussions on comparison between MP algorithms

To further verify the effectiveness of OMP algorithm over other time-domain signal reconstruction algorithms, a comparative study is conducted where basic matching pursuit (BMP) and weak orthogonal matching pursuit (WOMP) are also utilized for signal reconstruction. Detailed introduction for those methods can be found in literatures (J. Wang et al., 2012). The number of iterations taken by all three candidates for reconstructing crack reflective wave of each experimental case are calculated and shown in **Table 5-5**. It can be observed that OMP takes minimum iterations in locating the crack reflective wave in time domain. While both BMP and WOMP can achieve the same results, they do need more iterations and cost more computational power and time. Furthermore, BMP fails in detecting crack reflective wave of interest in case 8 and WOMP also fails in case 4, 7 and 8. Apparently the atoms retrieved from the IRC dictionary by BMP are nonorthogonal, meaning that to minimize residuals from previous iterations, components that are not orthogonal to the span of existing atom vector may be selected. This fact prevents the algorithm from reaching the reconstruction of waveform of interest, because the amplitude level of crack reflective wave is always lower than direct waves. Similar explanations can be applied to explain why WOMP is doing worse than OMP, because it features a more relaxed selection criterion compared to OMP.

Table 5-5. Reconstruction performance (number of iterations for each case) between OMP, BMP, and WOMP algorithms.

Reconstruction algorithm	Experimental case number								
	1	2	3	4	5	6	7	8	9
OMP	6	6	6	6	6	6	8	8	6
BMP	6	10	6	6	6	6	13	/	6
WOMP	10	12	6	/	10	6	/	/	6

5.5.2 Discussions on computational time

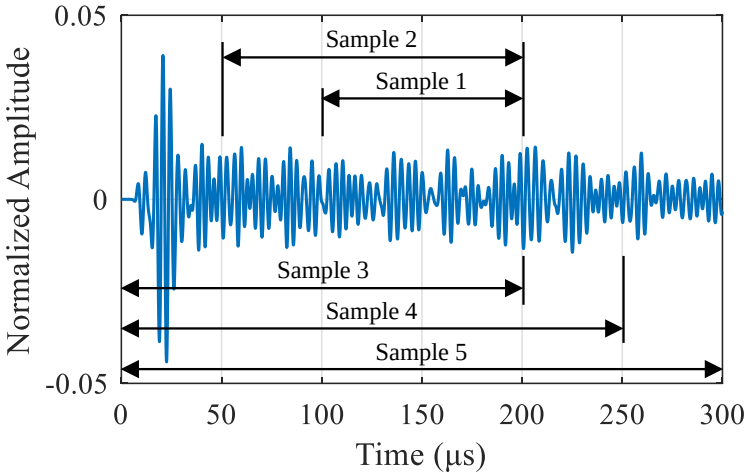

Figure 5-17. Data samples utilized for testing computational time. The lengths for Samples 1-5 are 1000, 1500, 2000, 2500, and 3000, respectively.

As stated in the previous section, the size of the redundant dictionary is critical in terms of reconstruction efficiency. Thereupon, in this section, the computational time consumption is evaluated via performing OMP on signals with various lengths, using IRC dictionaries with various sizes. The UGW signal from numerical case No. 1 is retrieved and utilized for computational time evaluation. The signal is first split into 4 samples, as shown in **Figure 5-17**.

The 4 samples with various data lengths varying from 1000 to 3000 are utilized for signal reconstruction, respectively, and the time consumption (unit: second) for each sample is recorded for comparison. After repeating each reconstruction 10 times, the averaged time consumption is demonstrated in **Figure 5-18**. The above tests were performed on the same workstation (i7-11x CPU, 32 GB memory, and 3060Ti GPU). It can be observed that the computational time consumption linearly increases as the length of processed signal increases. It can be therefore determined that the proposed method can perform accurate reconstruction quite efficiently and has the potential to achieve real-time analysis.

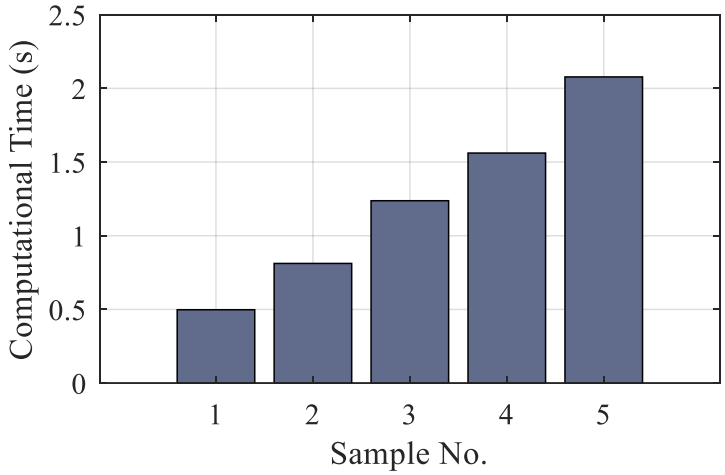

Figure 5-18. Computational time for each sample.

5.5.3 Discussions on crack location

Based on the experimental results in previous sections, a rail crack location method can be thus quantified and calculated. As stated earlier, d_3 denotes the distance between the FBG and the artificial crack, i.e., the representative longitudinal coordinate of crack

location. Therefore, a simple linear regression process is performed on the experimental results of case 1-3, using the obtained t values to predict the coordinate of the crack located onto rail web.

The fitting curve is drawn in **Figure 5-19**. And to further verify the accuracy of this curve, 2 extra experimental cases are considered, with their configurations and OMP reconstruction results stated in **Table 5-6**. The prediction error on both testing cases is far below the level of 5%, which proves the applicability and feasibility of proposed crack location scheme.

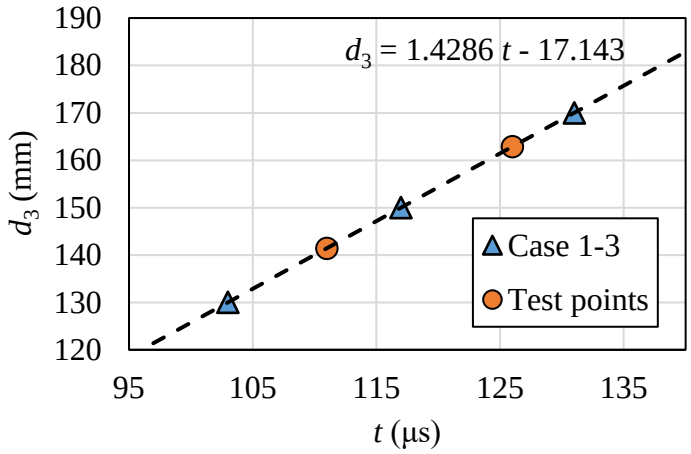

Figure 5-19. d_3-t linear fitting and crack location prediction results.

Table 5-6. The configurations of experimental cases.

Case No.	t (μs)	$\widetilde{d_3}$ (mm)	d_3 (mm)	Error (mm)
T1	111	141.43	140.00	1.43
T2	125	162.86	160.00	2.86

5.6. Summary

This chapter presents a novel railway track crack detection method using FBG sensing and OMP reconstruction algorithm that can straightforwardly reveal crack-reflective wave in time domain. A customized dictionary named IRC dictionary is constructed considering reflection of rail web cracks, ensuring that useful information can be extracted from UGW signals acquired. The proposed framework demonstrates exceptional accuracies in crack identification. The main findings and conclusions are as follows:

1 Given the knowledge of complexity and nonlinear boundary conditions of rail section, OMP can reconstruct the raw signals using orthogonal atoms selected from IRC dictionary, avoiding unwanted wave packets interfering with defect identification process.

2 An FEM simulation is first utilized to study the UGW propagation mechanism in rails and IRC dictionary based OMP is deployed to reconstruct impact wave packet, crack reflected wave packet and near end reflected wave packet. The reflected waveform resulted from the collision of an artificial crack is accurately represented in time domain. Comparative studies are carried out using alternative dictionaries where IRC dictionary successfully outperforms.

3 To further verify the feasibility of proposed method, experiments are conducted in

laboratory, considering various experimental configurations. For each experimental case in this research, wave packets are reconstructed within the reflected waves interval using IRC dictionary based OMP algorithm. The results are obtained showing highly linear relations between arrival time slots of defect reflected waves and longitudinal coordinates of the artificial crack.

4 The comparative study further proves that OMP algorithm outperforms other MP-based methods. The proposed method was also verified to be efficient in terms of computational time cost. Further discussions about the computational time are also conducted, demonstrating the feasibility of the proposed method in performing efficient and accurate reconstruction and even the potential of achieving real-time analysis.

5 Last, a regression model is developed to characterize the crack locations based on the reconstructed waveform of crack reflections. To verify the proposed crack location method, 2 extra experimental cases are considered, and their coordinates are accurately predicted with a minimum error level.

CHAPTER 6 RAILWAY TRACK RAPID DIAGNOSIS USING PENCIL LEAD BREAK AND ADVERSARIAL AUTOENCODERS

6.1. Introduction

Ultrasonic testing has been extensively deployed in rail maintenance and health evaluation, owing to its exceptional performance of detecting defects and measuring geometric contours. Portable ultrasonic detectors are commonly used to inspect rail health status by visualizing cracks with a high resolution. Such devices are also installed on inspection vehicles, using air-coupled ultrasound to measure rail profiles. Corrugation analysis trolleys (Grassie, 2005) are also deployed to measure acoustic roughness of in-service railway lines during maintenance window period, equipped with a portable wheeled instrument enabling convenient transportation. However, there are limitations of traditional ultrasonic methods in railway defect detection routines:

(1) Specialized ultrasound equipment are required, including ultrasonic probes and oscilloscopes, which makes it a considerable investment for purchasing, maintenance, and calibration.

(2) Professional skills and systematic training are required for railway workers to conduct on-site operations.

(3) The rough rail surface condition and complex rail section may undermine the quality of ultrasonic signals, interfering with damage detection.

(4) High-voltage electricity supply is necessary for transducing ultrasound, which is inconvenient for on-site conditions.

The above difficulties inevitably undermine the capability and effectiveness of such methods to be massively deployed on in-service railway lines. Therefore, prompt actions are needed to explore alternative approaches, specifically ones that not only possess the advantage of high accuracy but also can adapt to railway on-site inspection scenarios.

To address the limitations of traditional ultrasonic testing methods, this study proposes an ultrasonic testing method innovatively using pencil lead break (PLB) instead of traditional piezoelectric actuators. The PLB procedure is originated from acoustic emission experimental studies, where it is adopted as a reproducible wide-band acoustic emission source in laboratory (Hashim et al., 2021; X. Li et al., 2022; Prathuru et al., 2022). The pencil lead is intentionally pressed against the structural surface causing a static deformation and when the lead reaches the critical stress and breaks, an elastic acoustic wave is generated that propagates in the structure. This ultrasound excitation process is widely deployed in checking adhesive bonding, evaluating sensor performance, and wave mode demodulation (Yao et al., 2023), because of its simplicity,

convenience, reliability, and non-destructive operation. Thereupon, it is theoretically accessible to adopt such configuration to induce ultrasonic excitation on railway tracks. Instead of carrying heavy and complicated machines, on-site inspection can be simply accomplished by breaking a disposable pencil lead.

Nevertheless, little research has focused on studying PLB-induced ultrasonic waves on rails mainly owing to several uncontrollable factors that comprise the reproducibility of ultrasonic signals, such as variations in mechanical force applied to the pencil lead, the pencil lead diameter and length, the PLB location, and pencil lead angle against structural surface. Although PLB is considerably effortless and cost-effective compared to traditional ultrasonic testing procedures, it remains an unsolved problem how to derive damage sensitive features (DSFs) from PLB-induced signals to diagnose rail health status, especially when deliberating over the complexity of the rail section causes perplexing waveform. In this sense, the technology of ML provides a novel perspective of signal processing and analytics compared to traditional time-frequency analysis. ML algorithms automatically extract informative features buried within data, mapping a large amount of data towards designated tasks, such as anomaly detection (Mao et al., 2021; Mohanty et al., 2024; Sause, 2011; Xu et al., 2022) and condition assessment (S. X. Chen et al., 2021; Y. Zhou et al., 2023). Prior research has been undertaken, mapping complex ultrasonic signals that cannot be directly interpreted utilizing supervised learning methods (D. Li et al., 2021; Suwansin & Phasukkit, 2021; X. Wang et al.,

2023). Despite the exceptional performance, these methods are label-dependent, indicating that they require training datasets to be manually labeled for a supervised training phase. However, this normally does not apply to engineering scenarios because of the insufficient datasets. For example, in the context of rail damage detection, it is difficult to retrieve ultrasonic signals from rail segments with every type of defect. Thereupon, researchers have proposed various approaches in an unsupervised manner to extract DSFs of interest from raw ultrasonic signals (Dang et al., 2025; Hao et al., 2021; W. Li et al., 2023; Mahajan & Banerjee, 2023; Song et al., 2022, 2023; X. Zhang, Sun, et al., 2020; X. Zhang, Wang, et al., 2020), where generative models such as generative adversarial networks (GANs) and autoencoders (AEs) stand out owing to their excellent performance to learn nonlinear representations of nonlinear systems (Dai et al., 2023; Dunphy et al., 2022; Fan et al., 2023; Lee et al., 2021; Luleci, Catbas, et al., 2023; Luleci, Necati Catbas, et al., 2023; Sajedi & Liang, 2022; Silva et al., 2021). For instance, a robust GAN model was designed by Luleci, Necati Catbas, et al. (2023) that is capable of both data augmentation and damage detection with excellent performance; similar research has been undertaken to represent structural responses, such as accelerations and deformations ((Ma et al., 2020; Shim et al., 2022)). Additionally, attempts were made to train generative models using ultrasonic signals as input. For example, a deep autoencoder was trained using Lamb waves by Lee et al. (2021), and an automatic damage diagnosis framework was proposed. Similar work of Pandey et al. (2022) and Ramatlo et al. (2020) also presented a novel data-driven

approach for damage detection using Lamb wave. While the detection results showed high accuracy and robustness, the plate-like specimens used for experimental verification in these studies are less complex than the rail segment. It remains unclear whether such methodology can be further extended to diagnose rail damage, such as corrugation which has been previously studied as a common type of defects associated with rail noise and vibration (Gazafrudi et al., 2021; H. Yang et al., 2023).

This chapter presents a rapid and robust rail damage detection approach suitable for on-site diagnosis, powered by adversarial autoencoders (AAEs) with exceptional nonlinear representation learning performance. Compared with traditional ultrasonic testing procedures, a novel and simple on-site testing approach using PLB is utilized for rail damage diagnosis, which is readily achievable for non-technical railway inspectors. The damage diagnosis is powered by AAE algorithm, which integrates AE and a discriminator, featuring excellent performance in generative modelling. As for the experimental study, an AAE is designed and trained using PLB-induced ultrasonic signals obtained on rail segments, automatically extracting DSFs from the probabilistic distributions of the model output to conduct rail damage detection. Hyperparameter optimization and comparative studies are carried out. Field tests are also included in this study using the proposed damage detection method, considering various types of rail damage. Compared to traditional experience-based rail inspection and ultrasonic inspection vehicles, the proposed method outperforms featuring high robustness,

simple operation, low cost, and high accuracy.

6.2. Methodology

A 3-stage flowchart is given in **Figure 6-1** to schematically illustrate the proposed methodology. A sliding window scheme is priorly adopted to split the ultrasonic signals induced by PLB into samples with a fixed length. In Stage I, an AAE model is trained using data collected on a baseline rail segment with no damage. Then, in the second stage, the trained encoder and discriminator are transferred to evaluate rail segments with unknown conditions. The encoder, which is regarded as a generator in this case, encodes input signals into latent variables and passes towards discriminator. Last in Stage III, The Jensen-Shannon Divergence (JSD) between discriminator outputs of the baseline and unknown conditions is calculated as the damage indicator, based on which rail damage diagnosis is conducted.

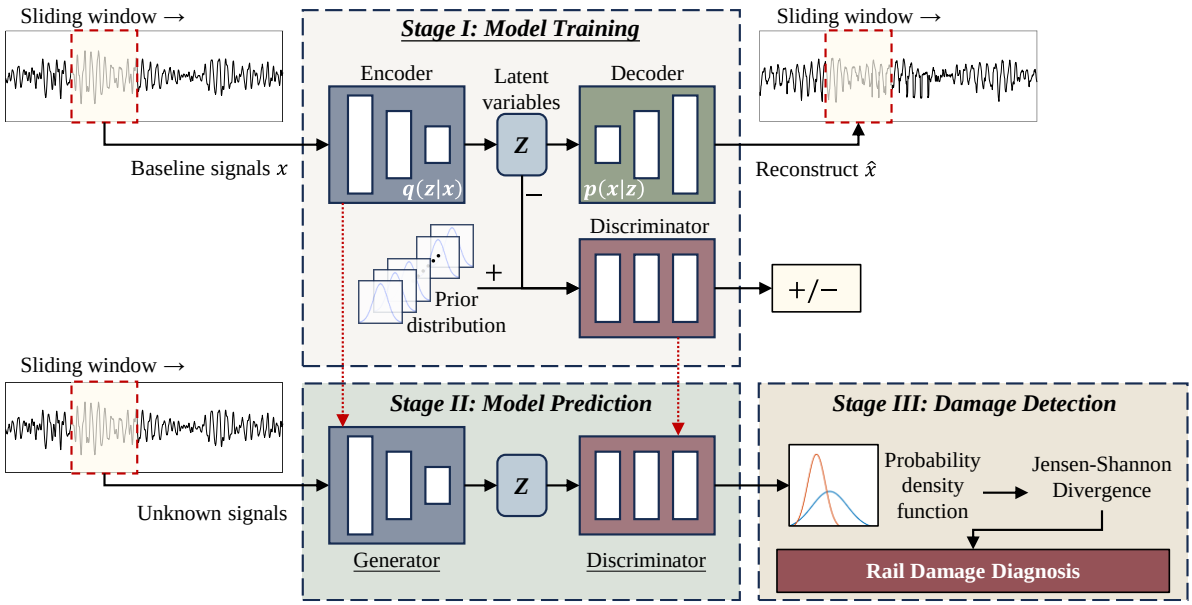

Figure 6-1. Damage detection framework proposed in this study.

It can be intuitively observed from the framework that the AAE model can automatically project the 1-D time series into the priorly designated latent space domain to reveal more representative features in data patterns. The discriminator output serves as the damage indicator for quantifying the probability of the damage status.

The mechanism of ultrasonic testing through PLB is priorly explained in this section, followed by detailed theoretical illustrations of proposed damage detection method in this study. The damage indicator utilized in this study is based on the AAE model input, combined with probabilistic analysis.

6.2.1. PLB-induced ultrasonic waves in rails

In this section, the mechanism of PLB is illustrated with further experimental verification conducted to perform PLB on rails. Referring to literatures ((De Almeida et al., 2015; X. Li et al., 2022; Prathuru et al., 2022)), the free length of pencil lead and the orientation angle of the mechanical pencil with respect to the structural surface are critical factors to PLB performance to ensure repeatability. The operation schematic is shown in **Figure 6-2(a)**. To maintain the consistent level of contact force applied to break the pencil lead, a mechanical pencil equipped with 2H type of pencil lead is used for repeatability tests. For each test, the orientation angle is 40 degrees with respect to horizontal rail head surface, and a vertical force is applied to break the pencil, releasing elastic potential energy. The free length of pencil lead for each test is approximately 3

mm. This signal is basically to simulate the passively acquired acoustics of rail-wheel interactions (Datta & Lanza di Scalea, 2022; Lanza di Scalea et al., 2018).

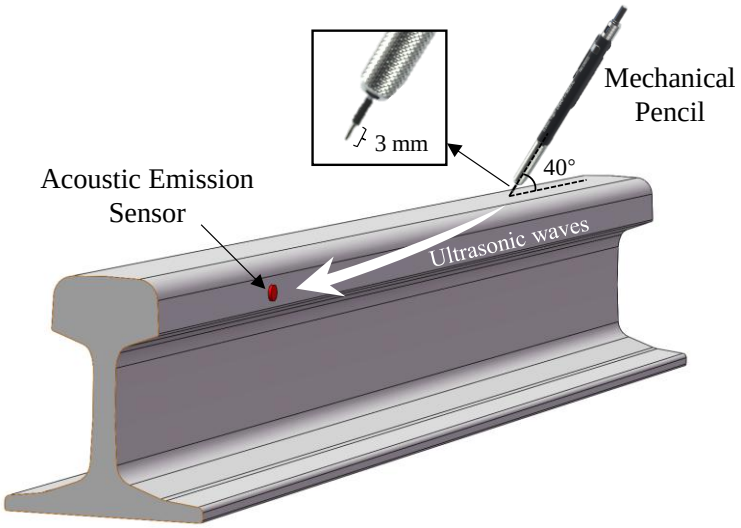

(a)

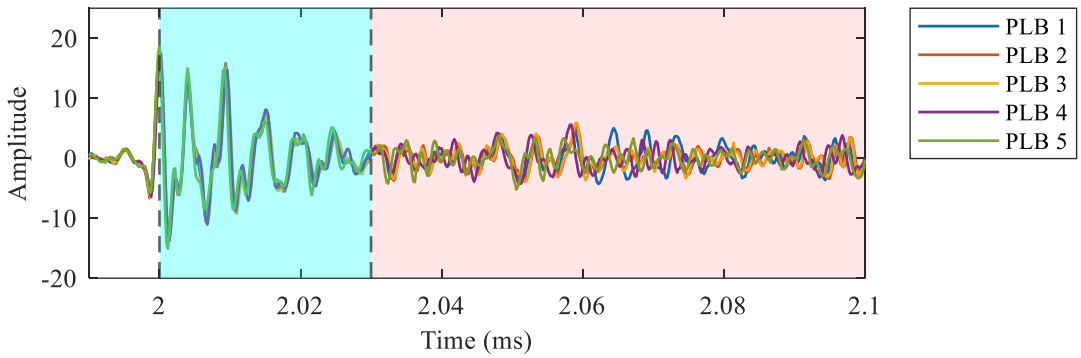

(b)

Figure 6-2. Schematic of performing PLB on rail surface: (a) operational method; (b) PLB-induced acoustic emission signals acquired for verifying repeatability.

Reproducible experiments are conducted to minimize the effect of deviations caused by experimental uncertainties, keeping the contact force generated by PLB consistent throughout the experiments. The acoustic emission sensor is mounted on the outer side of the rail segment and the distance between the acoustic emission sensor and the rail

surface where PLB is applied is 1 meter. This sensor location ensures high-quality data acquisition considering the PLB excitation is also placed at the railhead area. Besides, the installation of sensors should not overlap with the wheel-rail interaction area, which is also considered in this case.

Figure 6-2(b) demonstrates the repeatability of PLB tests on rails, where 5 PLB testing signals are presented. The triggering peak is located at 2 milliseconds for configuring synchronous acquisition. It can be observed that the waveforms are perfectly aligned for the first 30 μs starting from the triggering point (marked in blue in **Figure 6-2b**), followed by dramatical deviations in amplitude and phase (marked in red). This is due to the complicated scattering and reflections for ultrasonic wave propagation. Consequently, it is hardly accessible to directly analyze the time-domain waveforms and give an accurate and reliable diagnosis for rail status. Thereupon, given the prior observation that PLB-induced ultrasonic waveforms acquired from rails show little alignment in time domain, it can be derived that probabilistic patterns may apply to those acoustic emission samples if projected to a deeper dimension. In this sense, a probabilistic encoder is expected to be trained using PLB-induced ultrasonic samples, which can encode the acoustic emission signals into a preset probabilistic distribution. Rail damage diagnosis can be conducted using probabilistic analysis. The following contents of this section will focus on AAEs and their potential to engage in such an encoding process.

6.2.2. Adversarial autoencoder

6.2.2.1. Adversarial training of autoencoders

AEs are powerful tools to conduct denoising, reconstruction, compressive sensing, and features extraction in various engineering applications. A naive AE is often composed of an encoder and a decoder, enabling features extraction and data reconstruction processes (**Figure 6-3a**). The encoding process A can be comprehended as mapping an input $x \in \mathrm{R}^L$ the length being L, into the latent space $z \in \mathrm{R}^{d_z}$ ($d_z \ll L$), while decoder B reconstructs $\hat{x} \in \mathrm{R}^L$ to approach the input x from z. The following mathematical expression can be used to characterize the autoencoder working principle:

$$\hat{x} = B \circ A(x) \tag{6-1}$$

where we refer $A(x)$ as the bottle neck feature vector $z \in \mathrm{R}^{d_z}$, composed of d_z latent variables, as it demonstrates compressed yet informative representation of input x. Now we may see the encoding and the decoding process as a probabilistic mapping process. For a batch of signals, $\boldsymbol{x} \in \mathbb{R}^L$ with the original data distribution of p_d, the encoder A maps the input signals to a latent space $\boldsymbol{z} \in \mathbb{R}^{d_z}$. Thus, the reconstruction loss function ensures high fidelity of decoded signals:

$$L_{recon} = \mathrm{E}_{\boldsymbol{x} \sim p_d}[\|\boldsymbol{x} - B \circ A(\boldsymbol{x})\|^2] \tag{6-2}$$

Therefore, latent variables are often utilized for anomaly analysis (Makhzani et al.,

2015; Zemouri et al., 2023). Much alike PCA, the feature vectors composed of latent variables, encoded by an AE show spatially distinguishable characteristics, except for that an AE can learn a nonlinear manifold as stated in literature (Mao et al., 2021). However, probabilistic analysis can hardly be applied to such distributions because they are randomly distributed and lack statistical features (**Figure 6-3b**).

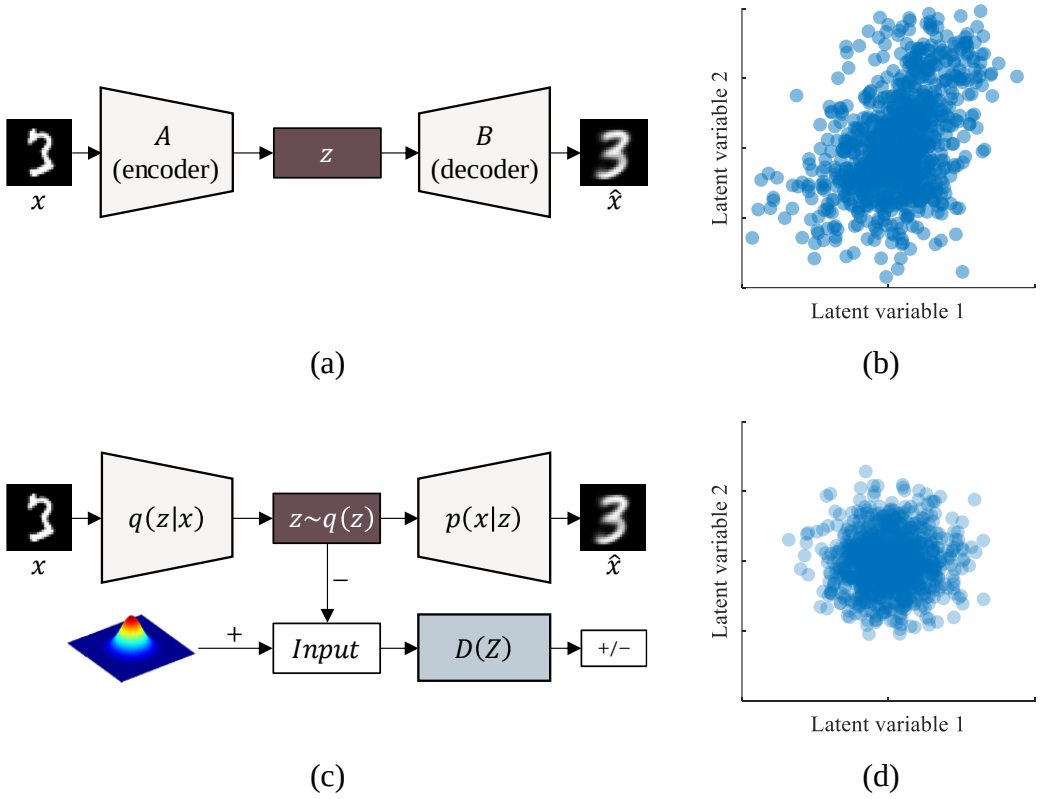

Figure 6-3. Schematics showing difference between AE and AAE: (a) and (b) show an AE architecture and its typical latent variable distribution; (c) and (d) show an AAE architecture and its typical latent variable distribution, with the premises that prior distribution is standard normal distribution. (In this case, latent variable vectors are 2-dimensional so that they can be visualized in 2-D scatter plots).

Based on previous research, instead of directly extracting damage indicators from counterbalance latent variables or reconstruction error of AEs, the authors propose an

adversarial training phase to create an independent discriminator that counterbalances the encoder, forcing the encoder to generate a series of latent variables that follow a specified prior distribution, as schematically illustrated in **Figure 6-3(c)** and **6-3(d)**. The discriminator then serves as an indicator itself, because through adversarial training it grows to be highly sensitive to even the slightest deviations occurring to latent space distributions.

To illustrate the comprehensive concept of an AAE, we regard encoding and decoding as dependent probabilistic distributions of input $\boldsymbol{x}$ and latent variable vector $\boldsymbol{z}$. Thus, the encoding function $q(\boldsymbol{z}|\boldsymbol{x})$ satisfies the following equation,

$$q(\boldsymbol{Z}) = \int q(\boldsymbol{z}|\boldsymbol{x}) p_d(\boldsymbol{x})\, dx \qquad \textbf{(6-3)}$$

where $q(\boldsymbol{Z})$ is defined as the aggregated posterior of latent variables, and $p_d(\boldsymbol{x})$ denotes the distribution of input data. Once given a prior distribution $p(\boldsymbol{Z})$, true samples are drawn from this arbitrary distribution and are fed to an independent discriminator architecture $D(\boldsymbol{Z}_{true}), \boldsymbol{Z}_{true} \sim p(\boldsymbol{Z})$.

While the encoder attempts to encode $\boldsymbol{x}$ into a latent variable distribution to confuse discriminator, written as $D(\boldsymbol{Z}_{fake}), \boldsymbol{Z}_{fake} \sim q(Z)$. In this regard, the encoder can be viewed as a generator that feed $\boldsymbol{Z}_{fake}$ to the discriminator. In the meantime, the encoder and decoder attempt to minimize the reconstruction error between input $\boldsymbol{x}$ and decoder output $\hat{\boldsymbol{x}}$. **Table 6-1** below concludes the training process of an AAE into a 2-

step training strategy.

Table 6-1. AAE training process.

Phase	Input	Output	Updated module(s)	Updated loss(es)
Phase 1 (reconstruction)	$\boldsymbol{x}$	$\hat{\boldsymbol{x}}$	Encoder, Decoder	Autoencoder loss
Phase 2 (Regularization)	$\boldsymbol{x}$	$D(\boldsymbol{Z}_{fake})$, $D(\boldsymbol{Z}_{true})$	Encoder, Discriminator	Generator loss, Discriminator loss

The autoencoder loss is defined as the MSE between x and $\hat{x}$. The generator loss and discriminator losses on fake and true samples are calculated using the format of sigmoid cross entropy (SCE),

$$S(\Lambda_{l1}, \Lambda_{l2}) = \max(\Lambda_{l1}, 0) - \Lambda_{l1} * \Lambda_{l2} + \log\left(1 + e^{-|\Lambda_{l1}|}\right) \quad \textbf{(6-4)}$$

where Λ_{l1} and Λ_{l2} denotes the output logit and label, respectively. Specifically, the generator A attempts to minimize $S\left(D\left(\boldsymbol{Z}_{fake}\right), 1\right)$ while the discriminator D struggles to discriminate fake samples from real ones, by minimizing $S\left(D\left(\boldsymbol{Z}_{fake}\right), 0\right)$ and $S(D(\boldsymbol{Z}_{true}), 1)$ simultaneously. The theoretical relationship between the discriminator output $D(\boldsymbol{Z})$ and expectation of SCE for both generator and discriminator losses are shown in **Figure 6-4**.

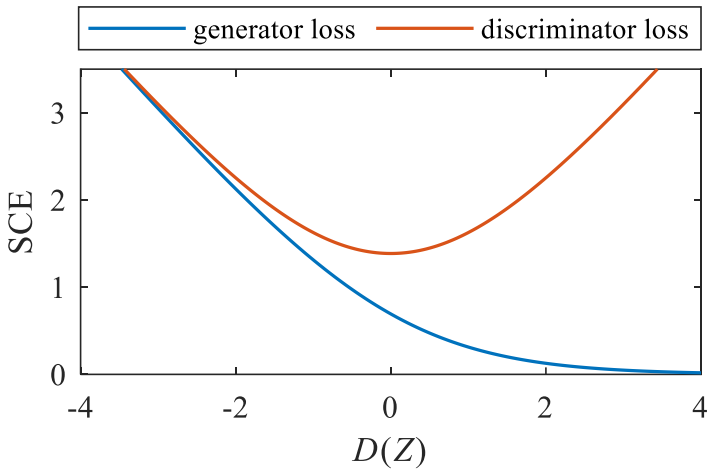

Figure 6-4. Theoretical loss functions of adversarial training phase of AAE.

The solution to the adversarial training phase can be interpreted in a minimax game:

$$\min_{A}\max_{D} \mathrm{E}_{\boldsymbol{z}\sim p(\boldsymbol{z})}\left[\log D(\boldsymbol{z})\right] + \mathrm{E}_{x}\left[\log\left(1 - D\left(A(\boldsymbol{x})\right)\right)\right] \qquad \textbf{(6-5)}$$

6.2.2.2. Anomaly detection based on AAE

With the basic model structure of AAE having been introduced, a novel damage indicator is developed, integrating discriminator output parameters and probability analysis. Previous studies have demonstrated the feasibility of using latent variable vector $\boldsymbol{Z}$ to identify abnormalities within a continuous dynamic system. Although $\boldsymbol{Z}$ undoubtedly demonstrates informative representation of data, it is still tricky to extract a generalized damage index from latent variable distributions. Another damage indicator that has been extensively used is the reconstruction error of an AE. It is assumed that abnormal conditions only occur if AE fails to reconstruct data with accuracy as good as that of training phase. However, AEs are initially designed to possess generalization performance, which is greatly valued. It is thus contradictory

that a more generalized AE model should conversely result in a decrease in its sensitivity to abnormality because it can recurrently reconstruct the input with high accuracies.

Therefore, instead of directly analyzing the latent variable distributions, it is rational to take advantage of adversarial training phase of AAE network through appointing the discriminator itself as an indicator. Specifically, a batch of input data $\boldsymbol{x}$ is fed to the encoder, and fake samples $\boldsymbol{Z}_{fake} \sim q(Z)$ are generated and passed to the discriminator. Then, the discriminator output can form a distribution $D(\boldsymbol{Z}_{fake})$ to indicate the anomalies in the original data pattern. Through the discriminator, the dimensionality of data is reduced from d_z (latent variable length) to 1. First, the discriminator output 1-D distributions obtained from a rail that is priorly known to be healthy is defined as the baseline distribution P_b. Then, by comparing a discriminator output distribution of an unknow data pattern P_u, it can be determined whether it fits the health status of the rail under inspection.

Thereby, the Jensen-Shannon Divergence (JSD) is introduced to characterize the similarity (or dissimilarity) between an unknown discriminator output distribution and the baseline distribution. Successful applications of JSD in evaluating structural integrity has been proved by Rashidi et al. (2020). Assuming the baseline distribution P_b is priorly obtained, the JSD values between the baseline P_b and an unknown distribution P_u is defined as:

$$\mathrm{JSD}(P_b \| P_u) = \frac{KL(P_b \| M) + KL(P_u \| M)}{2} \quad \textbf{(6-6)}$$

where M denotes the mixture distribution of P_b and P_u, and function KL is the Kullback-Leibler divergence (KLD) which is explained as:

$$\mathrm{KL}(P \| M) = \sum_i P(i) \cdot \log\left(\frac{P(i)}{M(i)}\right) \quad \textbf{(6-7)}$$

It can be concluded that the JSD values of 2 distributions must fall between 0 and 1. When JSD = 0 or 1, it means the 2 distributions are perfectly identical or maximumly different. In the context of this study, if the calculated JSD between an unknown discriminator output distribution and the baseline approaches 0, it is likely that the rail under detection is of a healthy state. Nevertheless, the effect of rail defects may disturb the PLB signal, causing a larger level of JSD values. To quantify a threshold for comparison, the JSD between every 2 baseline samples are calculated, and the 99% prediction interval is obtained as the upper and lower thresholds for anomaly detection. Specifically, the interval is based on 0.5% to 99.5% percentiles for any data distribution, which accounts for the variability of the individual data points regardless of whether the data distribution is normal. Thereupon, if a calculated JSD value falls between the interval, it is decided that this sample is collected from an intact rail. If not, it is flagged as a defective rail. The above reasoning process can be formatted as:

$$\mathrm{JSD}(P_b \| P_u) \in [\tau_{0.5}, \tau_{99.5}] \quad \textbf{(6-8)}$$

where $\tau_{0.5}$ and $\tau_{99.5}$ are defined as the 0.5% and 99.5% percentiles of baseline JSDs.

It should be mentioned that the above process is carried out in an unsupervised manner, meaning the proposed methodology possesses adaptive performance which is highly capable of conducting on-site inspections of in-service railway tracks with complicated conditions.

6.3. Experimental studies

Investigations are carried out in the laboratory, and experiments are designed to validate the feasibility of the proposed method. The AAE is trained using ultrasonic signals collected followed by damage detection.

6.3.1. Experimental setup

The rail segment in the laboratory is a BS100R standard rail component, with a length of approximately 1,500 mm, shown in **Figure 6-5**. The rail has never been implemented on in-service railway line, ruling out any potential damage that already existed before experiments. In this study, artificial damage is created by attaching a magnetic rectangular object onto the rail head surface. When ultrasonic waves propagate in rails, this external mass would absorb some of the travelling waves, which share similarities with that observed with real-world defects. Similar experimental configurations of artificial damages were also adopted in other research studies (Dang et al., 2023; K.

Wang, Cao, et al., 2020; K. Wang, Hao, et al., 2020). Although this configuration cannot fully represent the various defects that are formed through intense and long-term rail-wheel interactions, the simplicity and reproducibility allow preliminary attempts to verify the method's feasibility. Therefore, two rail conditions are considered in this experiment, one without and another with the magnet object, respectively. PLB testing procedures are performed on this rail segment according to the operation illustrated in Section 6.2.1. Guided waves propagate along the longitudinal direction of the rail head and are recorded by a high-performance acoustic emission sensor (Pico, Physical Acoustics, USA) mounted on rail head using cyanoacrylate and connected to a wireless ultrasonic oscilloscope (WS6, TiePie, the Netherlands). The mounting location is at the side of the rail head, which is determined by the rail geometry and sensing quality. The sensor is fixed via Cyanoacrylate adhesives, which is convenient for both installation and degumming, leaving no permanent marks on rail surface. The distance between the PLC excitation and the sensor is 1 meter in this experiment which is consistent with the previous testing configuration. The acquisition is configured as a triggering-recording mode, meaning that acoustic emission events are only recorded when acoustic emission sensor detects intense ultrasonic waves on rail surface. The sampling frequency was 5 MHz, and a built-in filter was utilized to clear out high-frequency background noise. The locations of PLB excitation and guided wave acquisition are respectively marked in **Figure 6-5(a)**. For both rail conditions (i.e., with and without the artificial defect), PLB is repeatedly conducted to ensure the redundancy of datasets. The time-domain

ultrasonic signals are shown in **Figure 6-5(b)** and **6-5(c)**. A 20 percent pre-triggering length is adopted in this experiment. The length for each PLB signal is 100,000, with 20,000 data points being the pre-triggering length. The difference between the 2 groups of signals cannot be intuitively observed in the time domain. It is thus critical to develop an analytical approach to reveal data patterns in a probabilistic manner. The PLB was performed 600 times on the intact rail and 100 times on the defect rail.

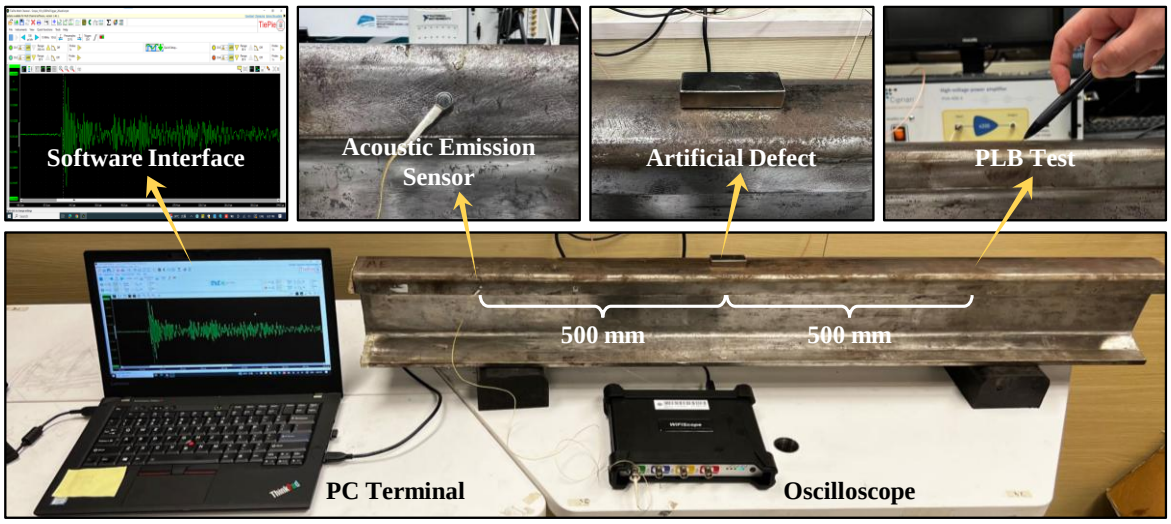

(a)

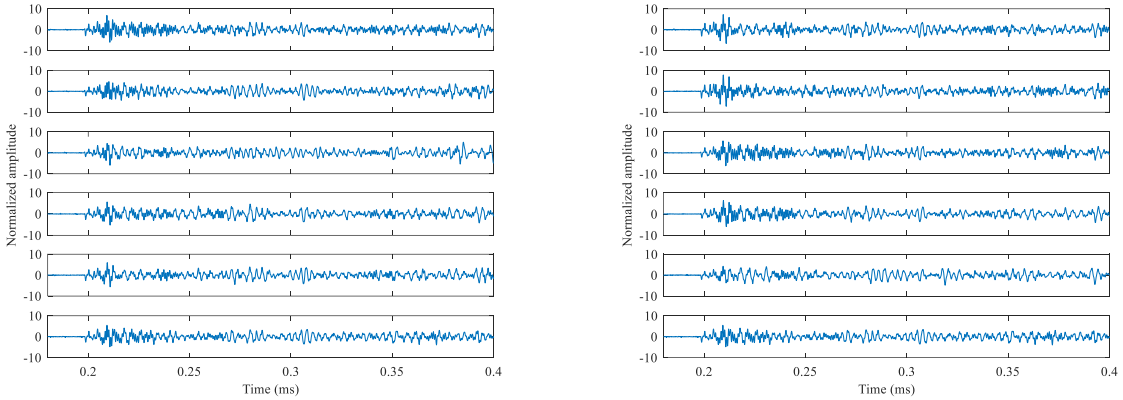

(b) (c)

Figure 6-5. Experimental configurations: (a) setup; and samples collected on (b) the baseline rail segment without any defect and (c) the rail segment with the artificial defect.

6.3.2. Data per-processing

The acquired PLB datasets are first cleaned to remove abnormal acoustic emission samples, especially mistakenly triggered acoustic recordings and those with waveforms polluted by electromagnetic noises. A sliding window scheme is adopted to pre-process the data collected, enhancing data diversity and improving converging performance.

Normalization is necessary for time-series input. Considering the highly nonlinear characteristics of guided waves propagating in rails, *Z*-score normalization method is implemented to centralize the mean and standard deviation for each time-series sample while the original properties of data are preserved, e.g., skewness and kurtosis. The data preprocessing steps can mitigate amplitude variations caused by external disturbances and ensure that the momentary noise spikes or anomalies should have minimum effects on the output results.

6.3.3. Model training

6.3.3.1. AAE hyper-parameters

In this study, fully connected (FC) layers are used to construct encoder, decoder, and discriminator, for 2-fold reasons. First, the input data is composed of 1-D time series with the length equal to the input layer dimension, in which case FC layer is adequate for processing. Second, compared to convolutional neural networks, multi-layer

perceptron (MLP) networks with FC hidden layers can achieve faster convergence speed due to fewer number of model parameters. To obtain optimal detection performance, hyperparameters of AAE are optimized through a grid search. In this case, different combinations of latent variable dimension (d_z), the sliding window length (l_x), and the batch size are configured to explore the best model for defect detection. The combinations are first split into 3 groups based on the batch size and the sliding window length, then under each group the effect of the dimension of latent variables is studied (**Table 6-2**).

Table 6-2. Experimental groups to study optimal model hyperparameters.

Group No.	Hyperparameters			
	learning rate	batch size	sliding window length l_x	latent variable dimension d_z
1	0.001	256	512	2, 8, 16, 32
2		128	1024	2, 8, 16, 32
3		64	2048	2, 8, 16, 32

In this case, it is ensured that the samples from the batch should compose a complete PLB signal with the length of 800,000 (the total of 100,000 minus the 20% of pre-triggering length). That is the reason the longer the sliding window length, the smaller the batch size. It should also be noted that the learning rate is constant for all 3 groups of AAE models considering that the models are relatively lightweight which minimizes the effect of learning rate. Each model of every group is repeatedly trained 5 times for 200 epochs to calculate the fluctuations in model performance. The other parameters

for the AAE models are set to be consistent, shown in **Table 6-3**.

Table 6-3. AAE architecture adopted in this study.

Module name of AAE	FC layers				Loss function	Optimizer
	Layer	Input dimension	Output dimension	Activation function		
Encoder	E_1	l_x	1024	relu	$MSE(\hat{X}-X)$; $S(D(\boldsymbol{Z}_{fake}),1)$	ADAM optimizer
	E_2	1024	512	relu		
	E_3	512	256	relu		
	E_output	256	d_z	None		
Decoder	D_1	d_z	256	relu	$MSE(\hat{X}-X)$	ADAM optimizer
	D_2	256	512	relu		
	D_3	512	1024	relu		
	D_output	1024	l_x	None		
Discriminator	Dc_1	z_d	512	relu	$S(D(\boldsymbol{Z}_{fake}),0)$ $+S(D(\boldsymbol{Z}_{true}),1)$	ADAM optimizer
	Dc_2	512	512	relu		
	Dc_3	512	1	None		

The training losses are first compared as it shows the adversarial state of the 3 parts of an AAE model, namely the encoder (generator), the decoder, and the discriminator. It can be concluded from **Figure 6-6(a)** that a higher dimension of latent variable $\boldsymbol{Z}$ would result in a higher reconstruction accuracy. A smaller batch size and longer sliding window would simultaneously reduce the reconstruction accuracy. As for the adversarial training process, it seems that the discriminator would prevail when the batch size is smaller, and the sliding window is longer. The higher the dimension of latent variable, the more instability it brings to generator and discriminator losses.

Nevertheless, it is yet to be verified the specific effects of AAE training performance on detection accuracy.

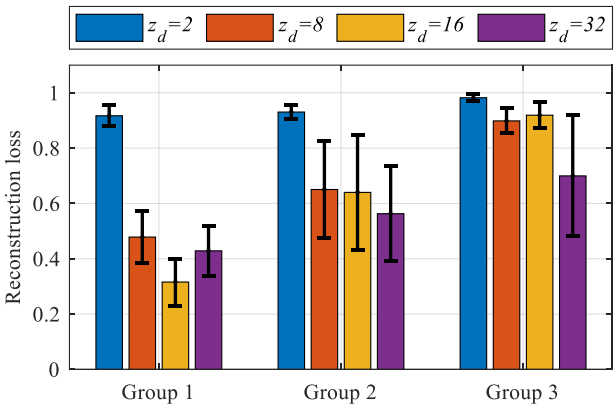

(a)

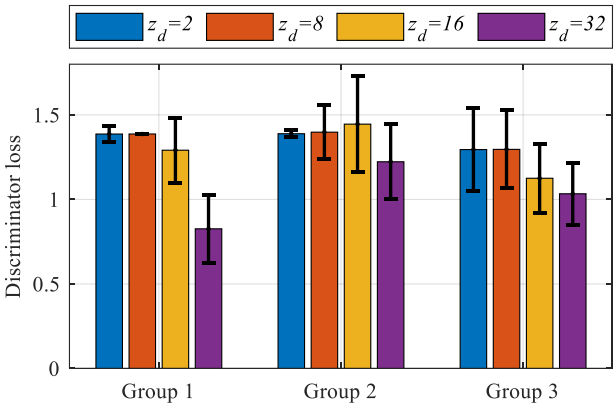

(b)

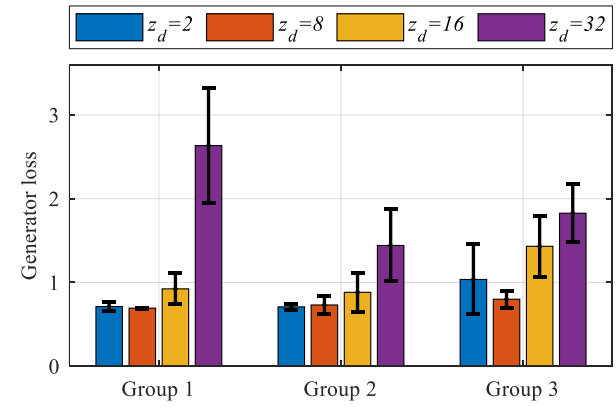

(c)

Figure 6-6. Training losses for Group 1, 2, and 3: (a) reconstruction loss; (b) discriminator loss; and (c) generator loss.

Table 6-4. Detection accuracy of AAE models with various hyperparameters.

Model No.	Latent variable dimension	Detection accuracy (%)	
		Intact samples	Defect samples
1.1	2	97	71
1.2	8	84	100
1.3	**16**	**100**	**100**
1.4	32	96	72
2.1	2	91	100
2.2	8	94	14
2.3	16	95	72
2.4	32	100	0
3.1	2	100	82
3.2	8	91	0
3.3	16	98	32
3.4	32	96	11

By defining the detection accuracy as the proportion of correctly determined samples (whether intact or defect) among all samples, quantitative evaluation can be carried out. For each AAE model trained in this section, the JSD values for samples under different rail conditions are calculated and the detection accuracies are demonstrated in **Table 6-4**. Apparently the AAE model of group 1, model 1.3 with the latent variable dimension being 16, achieves the optimal performance among all 12 candidates. For both intact and defect samples, the detection rates are both 100%. The other models are outperformed by model 1.3, with lower detection accuracies in both intact and defect samples. As for models 2.4 and 3.2, the models were clearly overfitted during the

adversarial training phase, causing 0% detection accuracies in detection anomalies.

The JSD values for baseline, intact, and defect samples processed by 4 models of Group 1 are shown in **Figure 6-7**, **6-8**, and **6-9**. It can be observed through comparison that models 1.1 and 1.4 are typically excelled at distinguishing intact samples, with detection accuracies above 95%, but cannot effectively detect anomalies. Both models 1.2 and 1.3 are quite capable of detecting both intact and defect samples, but the latter model outperforms the other. The lower reconstruction error may account for better detection accuracies.

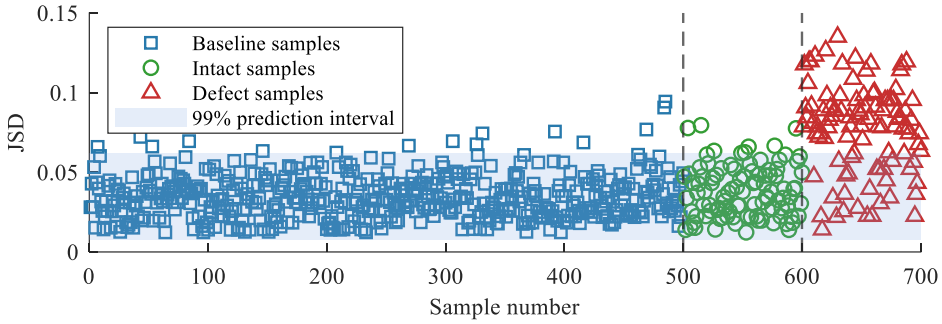

(a)

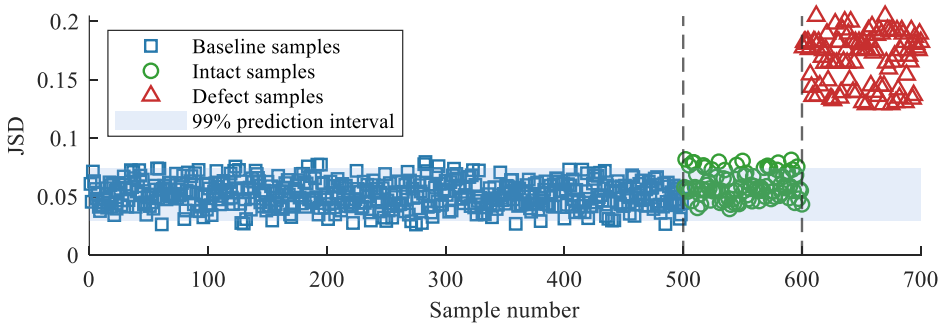

(b)

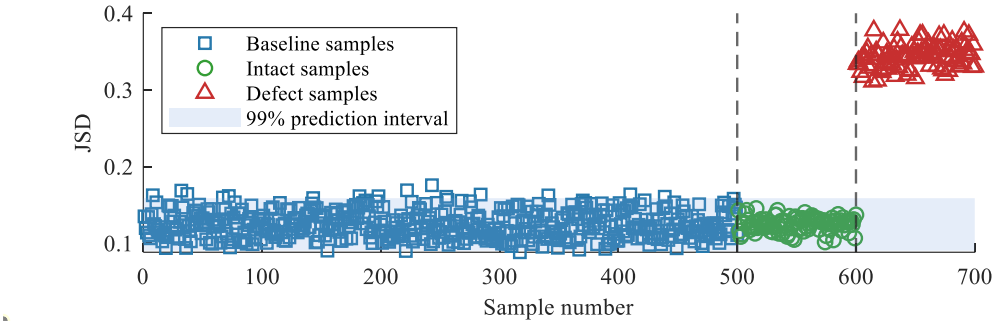

(c)

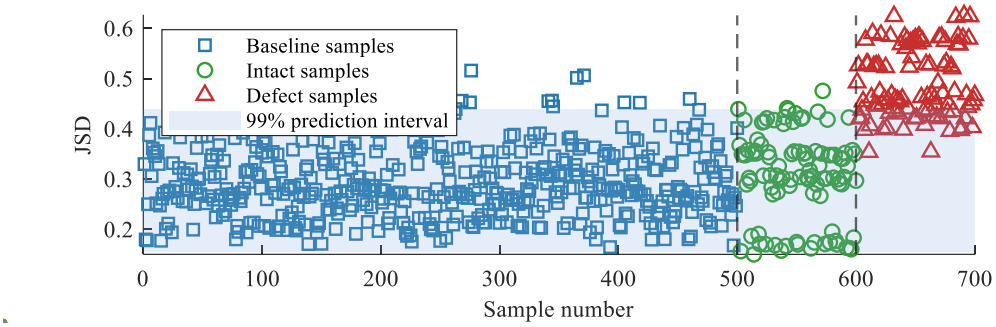

(d)

Figure 6-7. Defect detection results for AAE models of Group 1: (a) z_d=2, (b) z_d =8, (c) z_d =16, and (d) z_d =32.

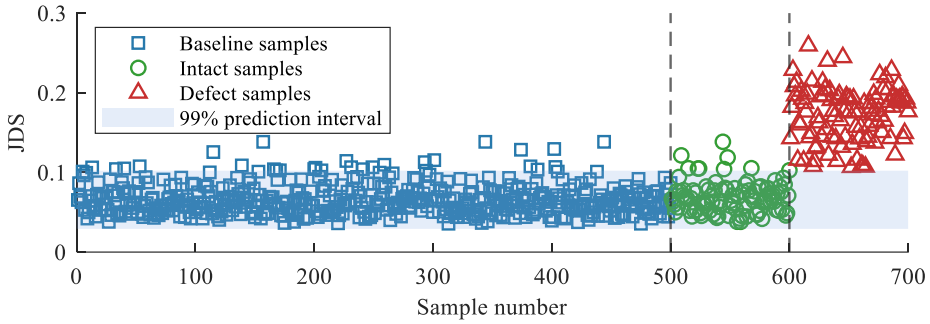

(a)

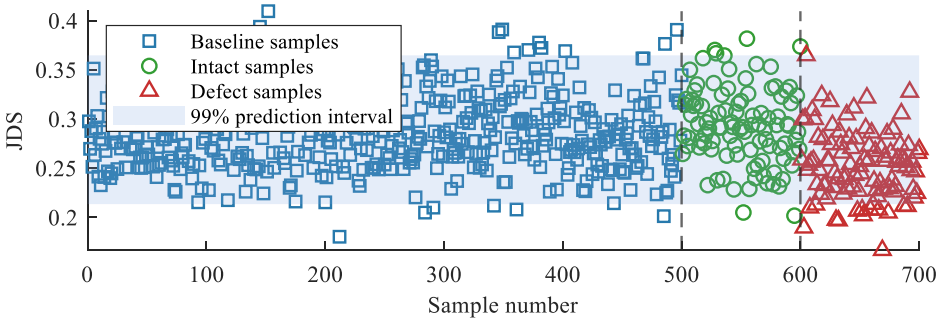

(b)

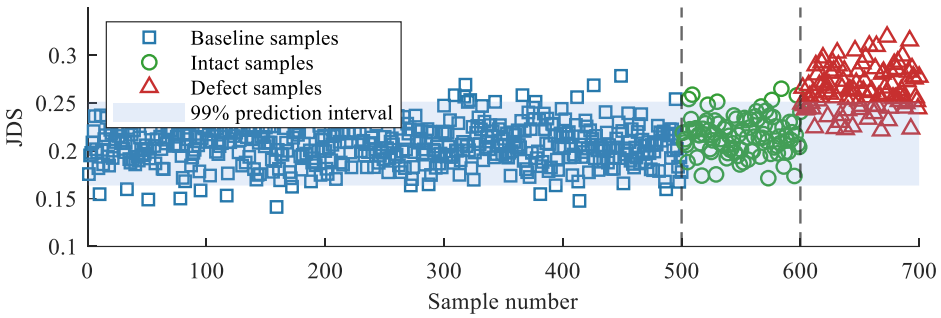

(c)

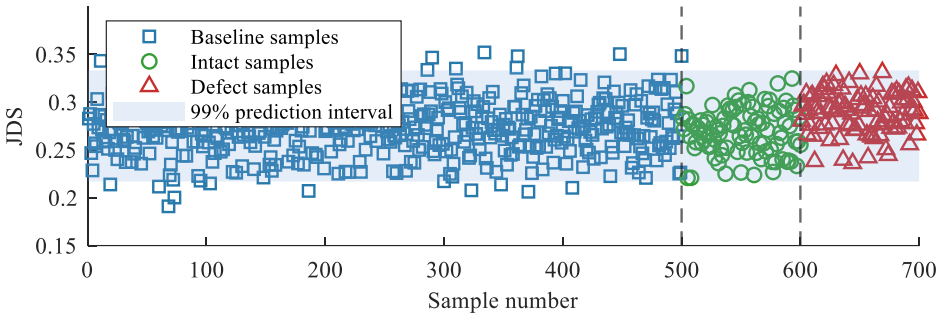

(d)

Figure 6-8. Defect detection results for AAE models of Group 2: (a) z_d=2, (b) z_d =8, (c) z_d =16, and (d) z_d =32.

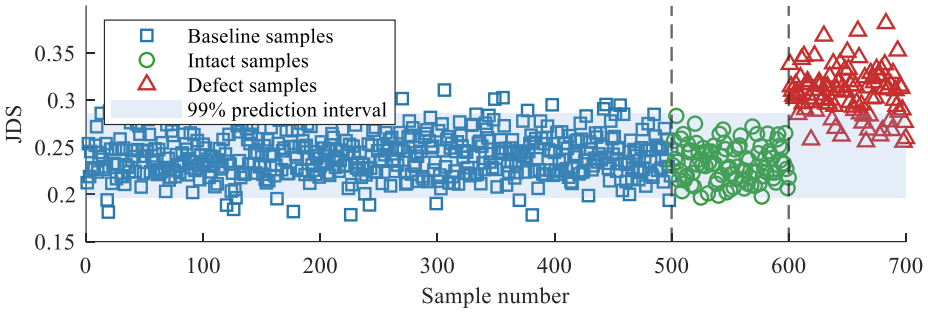

(a)

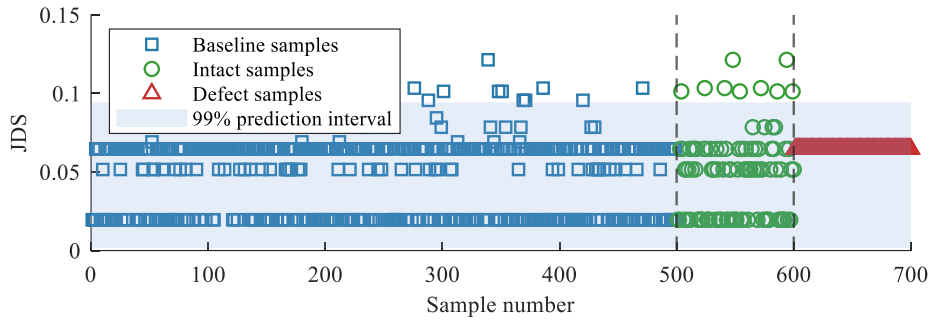

(b)

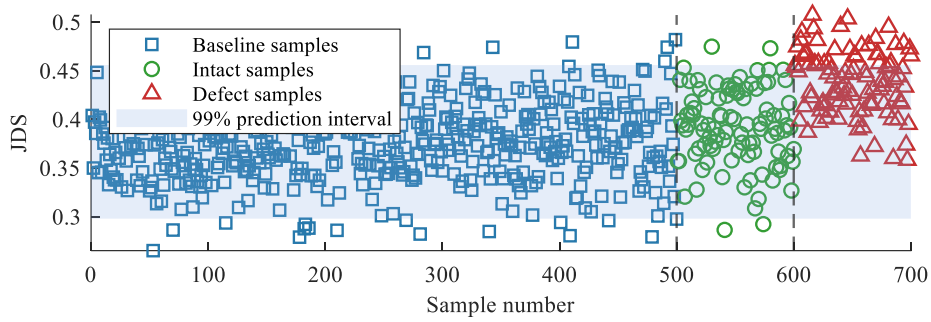

(c)

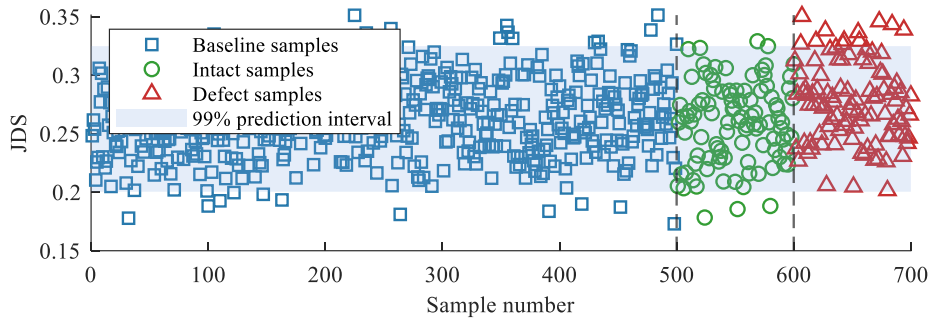

(d)

Figure 6-9. Defect detection results for AAE models of Group 3: (a) z_d=2, (b) z_d =8, (c) z_d =16, and (d) z_d =32.

6.3.3.2. Training process

The above training of AAE models have been completed on a workstation equipped with an Intel Core i7-11x CPU, 32 GB of RAM, and an NVIDIA GeForce RTX 3060Ti GPU (8 GB of RAM). The whole training process only took 57 minutes for 100 epochs, , which is due to the lightweight FC structure design.

The training history of loss functions is shown in **Figure 6-10**. After 200 epochs, the discriminator loss approaches 1.29 while the generator loss gradually stabilizes at the level of 0.91, indicating that for each epoch the generator is equally confused with real and fake samples, i.e., data drawn from prior distributions and encoded ultrasonic signals. The autoencoder loss, which is defined as the MSE between input data and reconstruction, is also plotted in **Figure 6-10**. A random segment of input and output (reconstructed) ultrasonic signal is presented in **Figure 6-11**. It can be intuitively concluded that the reconstructed waveform is basically aligned with original input, proving that the encoded latent variables are qualified representations of acoustic emission events.

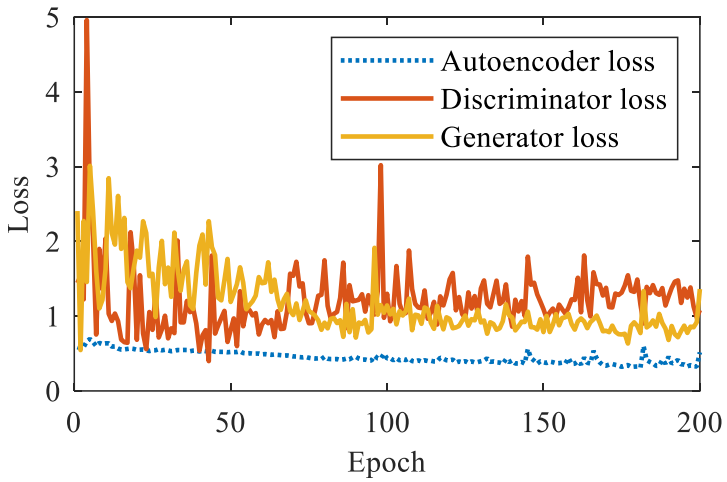

Figure 6-10. AAE training losses.

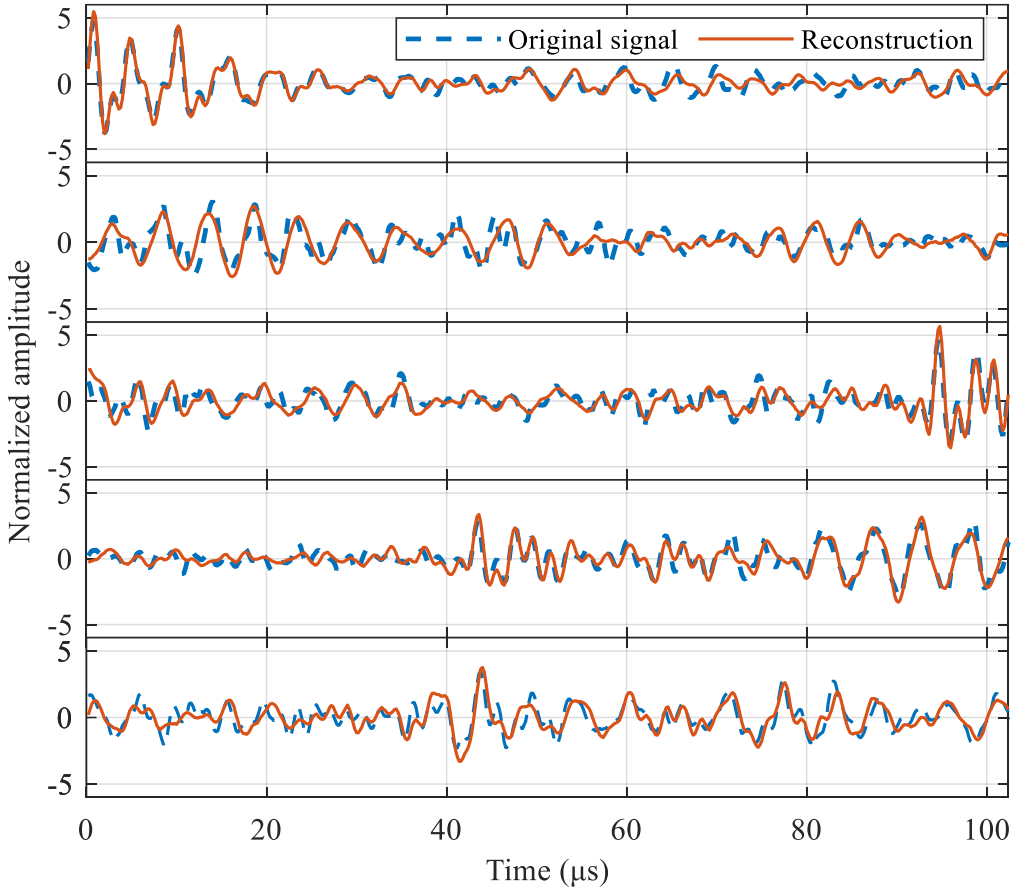

Figure 6-11. Randomly selected original (input) and reconstructed (output) signal processed by the trained AAE model.

The latent variables that the encoder outputs are a 1-dimonsion vector composed of d_z independent variables, each of which follows a priorly-set normal probability distribution,

$$Z_{fake} = \{z_1, z_2, \dots, z_{d_z}\}$$
$$z_i \sim N(0,1) \quad \textbf{(6-9)}$$

To visualize the latent variables from a lower dimension, the first 2 components of the latent variable vector, namely z_1 and z_2, are selected to display a 2-D distribution.

Exceptional difference can be clearly observed in 2-D distributions of latent variables encoded using different datasets shown in **Figure 6-12**. Specifically, the distribution of intact case shows similar statistical characteristics compared to that of baseline case, proving that the adversarial training is effective. The mean values and standard deviations are perfectly aligned, with both approaching the prior normal distribution (**Figure 6-12a**). This phenomenon can be comprehended as intuitive and direct proof that the input signals are of the same condition as the baseline case. In contrast, as for the defect case, significant distribution drift can be seen in **Figure 6-12(b)**. The center of the cluster drifts from the origin points for both z_1 and z_2.

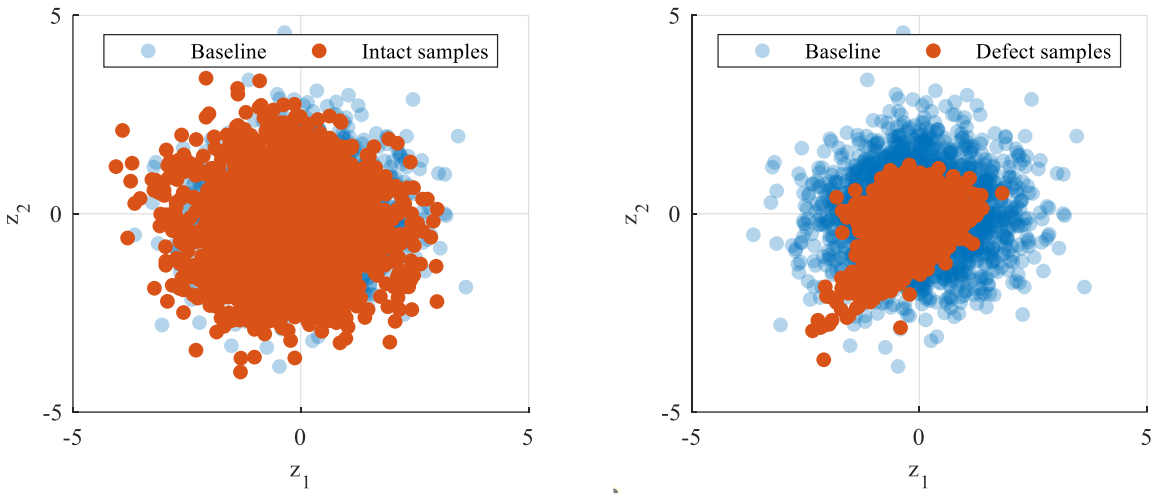

(a) (b)

Figure 6-12. 2-D distributions of the first 2 components in latent variable vectors of AAE: (a) baseline versus intact case, and (b) baseline versus defect case.

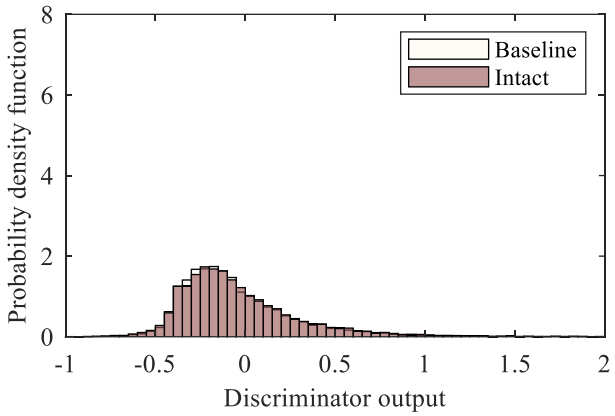

(a)

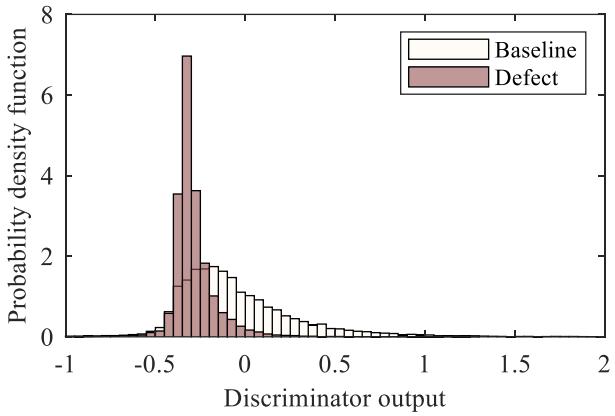

(b)

Figure 6-13. Probability density function of the distributions of discriminator output: (a) baseline versus intact case, and (b) baseline versus defect case.

The discriminator output values for 1 data batch can be drawn into probability density function (PDF) histograms (**Figure 6-13**). The baseline distribution is obtained on training dataset. It can be intuitively observed that the intact distribution is perfectly aligned with baseline. However, an obvious deviation is presented in **Figure 6-13(b)**. The deviations in PDF of discriminator output results in varying JSD values, thus revealing data anomaly caused by rail defects.

6.3.4. Comparative studies

In this section, the performance of the proposed method is further evaluated by comparing it with other models. The AAE model, as illustrated in previous sections, is essentially the combination of an AE and a GAN. Therefore, a GAN and an AE model are adopted for comparison. Considering the unsupervised nature of the proposed method and that the ultrasonic signals are initially time series, 2 popular methods that have been proved to be effective in processing time series, namely Long-Short Time Memory (LSTM) neural network and Recurrent Neural Network (RNN), are also included in comparative studies.

Table 6-5. Performance comparison results.

Model Name	Main hyperparameters	Detection accuracy (%)	
		Intact samples	Defect samples
AAE	See Section 6.3.3.1	100.0	100.0
GAN	The GAN uses the same generator and discriminator structures as the AAE	90.0	26.0
AE	The AE uses the same encoder and decoder structures as the AAE	99.0	79.0
LSTM	Number of hidden layers: 256 Number of hidden units per layer: 64 Optimizer: Adam Sequency length: 512	70.0	38.0
RNN	Number of hidden layers: 256 Number of hidden units per layer: 64 RNN cell: gated recurrent unit Sequency length: 512	79.0	33.0

The model structures and hyperparameters of GAN and AE models are set to be aligned with the AAE model selected in Section 6.3.3. After training, the JSD values are calculated based on the GAN output, for damage detection. As for the AE, the mean square error level of AE reconstructions is utilized as the damage indicator. Last, the input and output of LSTM and RNN are set to be the same time series, because no label information is priorly known for this case. The key model parameters and the results are shown in **Table 6-5**. Each model is trained for 200 epochs on the training dataset.

It is obvious that the proposed AAE-based defect detection approach achieved the best performance on both intact and defect samples. When the GAN is trained, it is assumed that the generator is constantly winning over the discriminator because the generator, through training, learns to encode arbitrary signals (whether intact or defect signals) to latent variables that always follow the prior distributions. The imbalanced training directly leads to failure in damage detection. The huge gap of anomaly detection performance between AAE and GAN resulted from the different training phases, specifically, the reconstruction phase of AAE ensures that the encoded latent variables are effective representations of input signals. In contrast, the impact of the distribution of input data $p_d(x)$ is weakened resulting in unsuccessful encoding. The generator can easily generate a series of fake samples that always confuse the discriminator without any constraint. As shown in **Figure 6-14**, the generator encodes abnormal samples into perfectly aligned Gaussian distributions. After training for 200 epochs, it is found that the generator output remains consistent even when the input is Gaussian noise. The prevailing generalization performance of the generator/encoder undermines the sensitivity for damage indicators to function accurately.

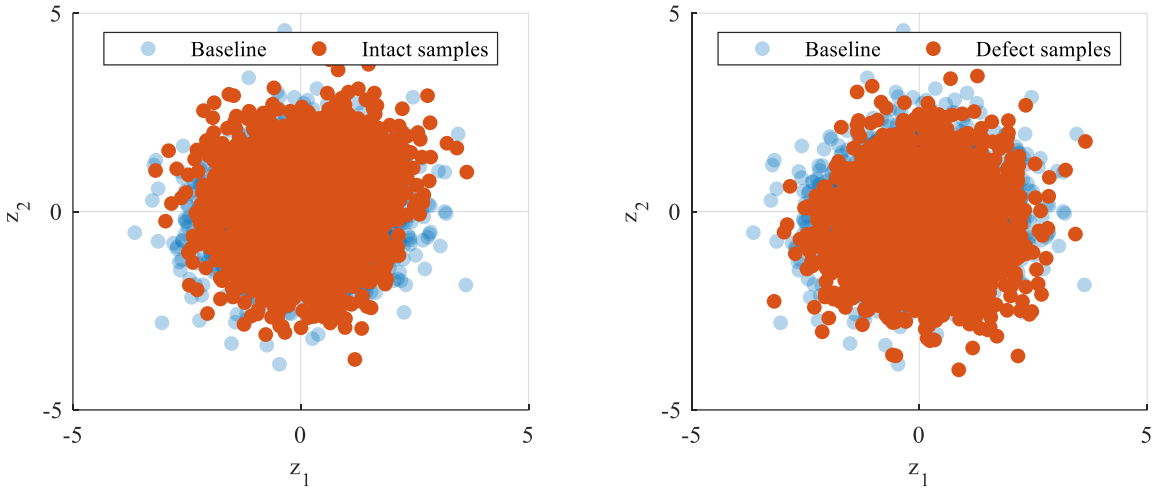

(a) (b)

Figure 6-14. 2-D distributions of the first 2 components in latent variable vectors of GAN: (a) baseline versus intact case, and (b) baseline versus defect case.

It can be also observed that the detection accuracies of defect samples for AE, LSTM, and RNN are poor. This may indicate that the MSE for reconstruction of abnormal samples is lower than expected. The drawback of using reconstruction error as the damage indicator is that the model must not possess generalizability. It is even preferable to train an over-fitted model to conduct anomaly detection because the reconstruction error may increase more extensively when the anomalous data is processed. However, this thought is in contrary to the field of machine learning where the model generalizability is greatly valued. Thereby, defect detection methods using model reconstruction or prediction error may not be as adaptive as the approach proposed in this study.

6.4. Field tests

The proposed method is applied and further validated on an in-service railway line in Hong Kong, China. First, an on-site inspection was conducted, and several rail segments within the inspection route had been selected featuring distinguishable rail health defects, such as corrugation and squat. Then, PLB tests were conducted on each segment and AAE models were trained to perform damage detection.

6.4.1. Overview

It has been previously reported that abnormal noise and vibration problems occurred on an in-service railway line in Hong Kong, China. The railway line under inspection is constructed inside an underground tunnel which connects the adjacent stations. Through an on-site inspection (**Figure 6-15**), the authors' research team obtained first-hand information about the railway line. Most rail defects, such as corrugation, fatigue cracks, wear, and squat, were observed near a curving road, resulting in high-pitch noise and intense vibration constantly interrupting railway operation. Therefore, for the sake of railway safety and ride comfort for passengers, a three-day field test was conducted during offline maintenance window period to detect rail damage and assess health conditions.

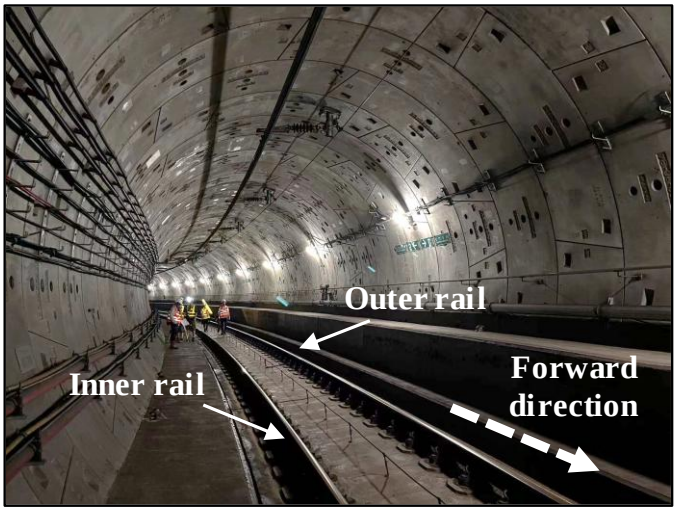

Figure 6-15. A pilot on-site inspection at an in-service railway line during maintenance window period.

6.4.2. Data acquisition

According to an official report provided by operation and maintenance department responsible for this railway line, most defects are frequently spotted on the inner rail rather than outer rail because heavier loads are applied onto the inner rail when trains pass by the curve road. Therefore, multiple rail segments are selected from both inner and outer rails featuring either intact or damaged condition, as shown in **Figure 6-16**. **Table 6-6** also gives detailed information about the rail condition for each segment. Three of all segments are evaluated to be intact (referring to ISO 23054-1), indicating that no obvious wear or defects ever exist that could potentially endanger operational safety. Rail segment No. 3 shows visible corrugation phenomenon on rail head surface with the dominant wavelength band measured lying in between 20 to 100 mm; rail segment No. 4 also shows corrugation but features a longer wavelength band

approximately at 200 to 300 mm. Rail segment No. 5, however, is assessed to be damaged because of an obvious squat. It is worth noting that corrugations and squats are the two most common and representative types of rail defects that could compromise ride comfort and operational safety. Corrugations refer to continuous surface irregularities while squats are localized defects. Those defects are likely associated with abnormal noise and vibration, compromising ride comfort and operational safety. This dataset is composed of various rail conditions to verify the robustness and effectiveness of the method.

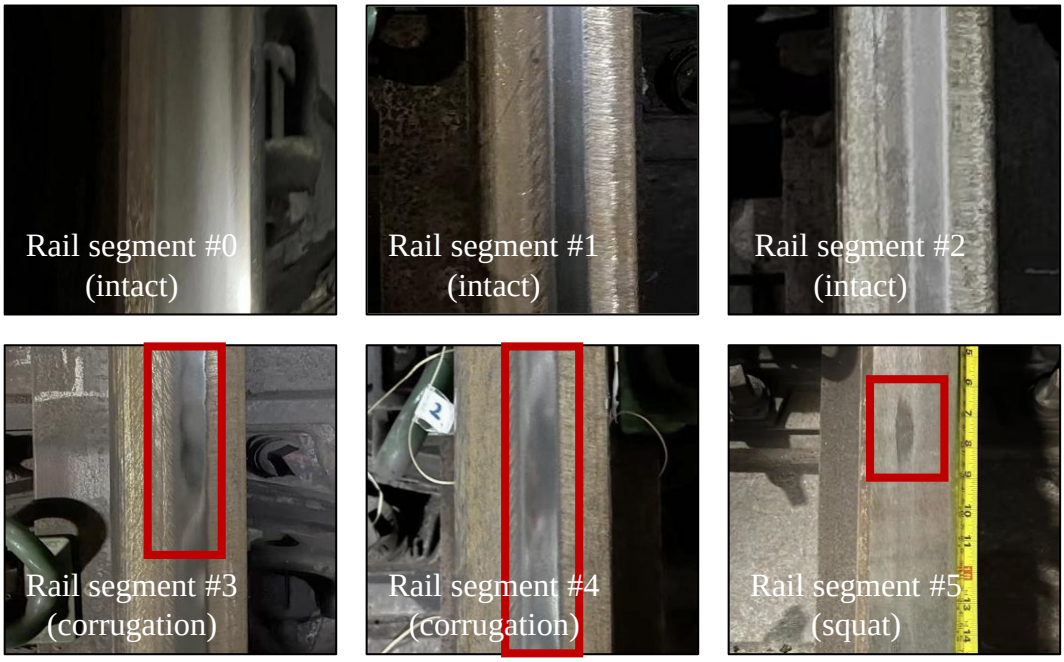

Figure 6-16. Rail segments of various conditions on which PLB tests are performed.

Table 6-6. Specification of selected rail segments.

Rail segment No.	Condition	Location	Defect profile	Remarks
0	intact	outer rail	None	Train set
1	intact	outer rail	None	
2	intact	inner rail	None	
3	corrugation	inner rail	20 to 100 mm (wavelength)	Test set
4	corrugation	inner rail	200 to 300 mm (wavelength)	
5	squat	inner rail	40×15 mm (squat size)	

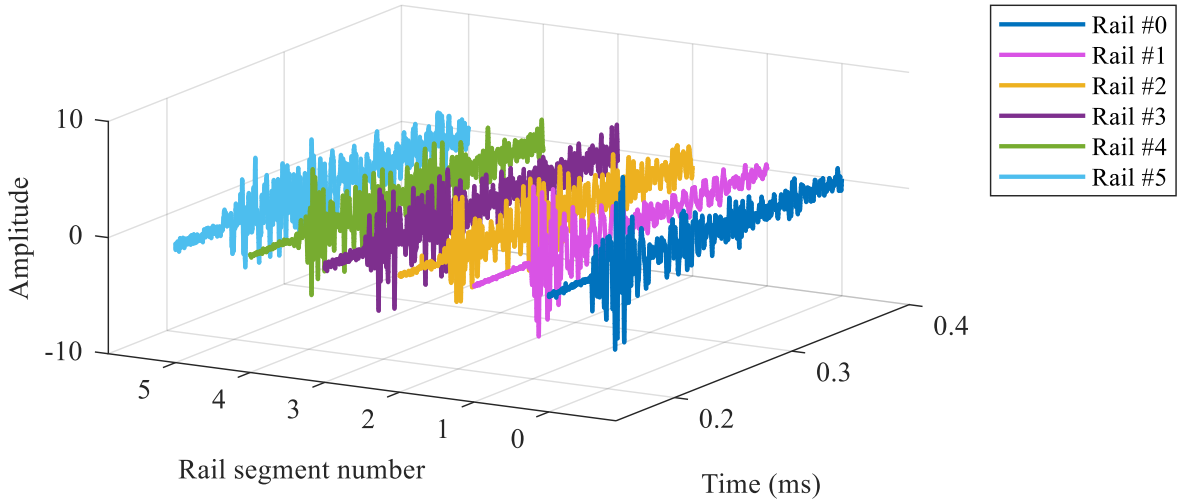

Figure 6-17. PLB-induced ultrasonic signals for each rail segment.

The representative PLB-induced ultrasonic samples for each rail segment are shown in **Figure 6-17**, which are normalized according to *Z*-score normalization method. The effect of on-site noise interference was minimized through the built-in filter of the acquisition system and data preprocessing. The train set is composed of 200 samples, enhanced using the same sliding window and pre-processing scheme as illustrated in

the previous section. For test sets, 100 samples are obtained from each rail segment through on-site PLB testing.

The testing setup is demonstrated in **Figure 6-18**. Acoustic emission sensors are attached to the rail head using cyanoacrylates agent. It should be noted that the sensor positioning in the field tests were aligned with that in the laboratory experiments, to ensure consistent data collection and minimize variability during testing. The oscilloscope is utilized to record acoustic emission events via Wi-Fi connection to a portable PC. For each rail segment under testing, PLB is manually performed multiple times, exactly 2 meters away from where acoustic emission sensor is installed, guaranteeing that the propagating acoustic signals can characterize structural condition of the rail segment.

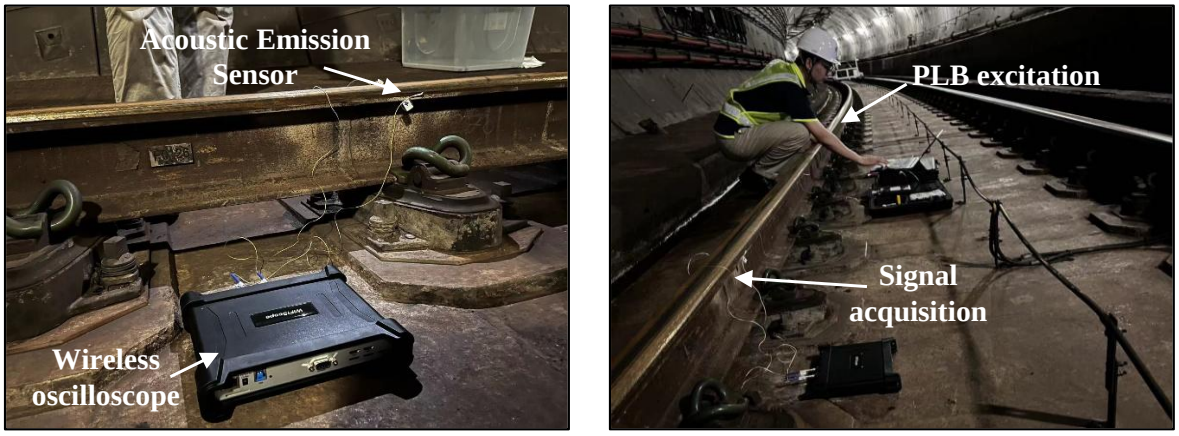

(a) (b)

Figure 6-18. Overview of on-site testing: (a) acquisition setup, and (b) PLB configuration.

6.4.3. Damage detection results

6.4.3.1. AAE training

It is worth noting that only the AE signals acquired on rail segment # 0 are regarded as baseline signals and are utilized for AAE training, with the rest of data being fed to a trained AAE for further validation. The AAE model utilized for this section possesses the same hyperparameters as the optimal model selected through grid searching in experimental studies. The model was trained for 200 epochs. The learning loss functions updating histories are shown in **Figure 6-19**.

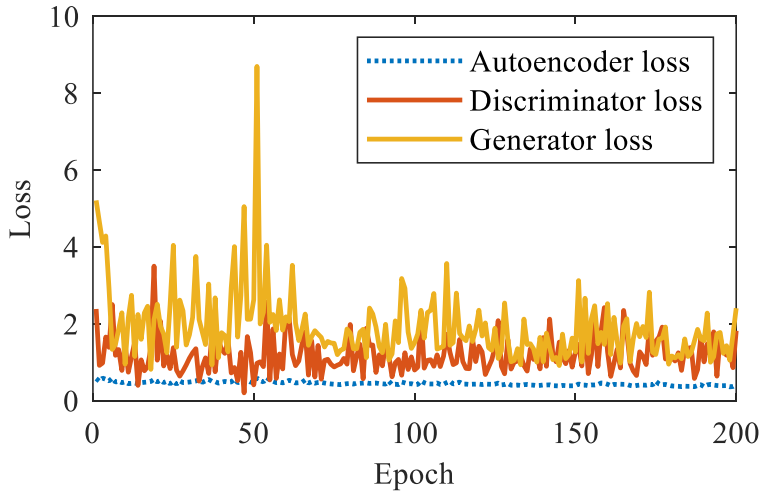

Figure 6-19. AAE training history.

6.4.3.2. Damage diagnosis on rail segments

The PDFs of discriminator output for 5 testing sets are shown in **Figure 6-20**. It can be intuitively observed that defected rail segments show more obvious deviations compared to the baseline rail in the distribution patterns of discriminator output. This

indicates that the discriminator senses the abnormalities in latent variables encoded by the generator. Slight deviations are shown for rail segments 1 and 2, i.e., those of intact condition, indicating similar rail conditions are applied to both rails. In comparison, PDF histograms for rail segment No. 3-5 are hardly aligned with the baseline distribution.

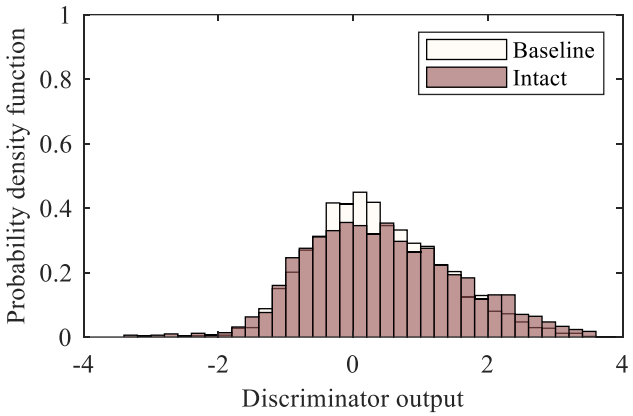

(a)

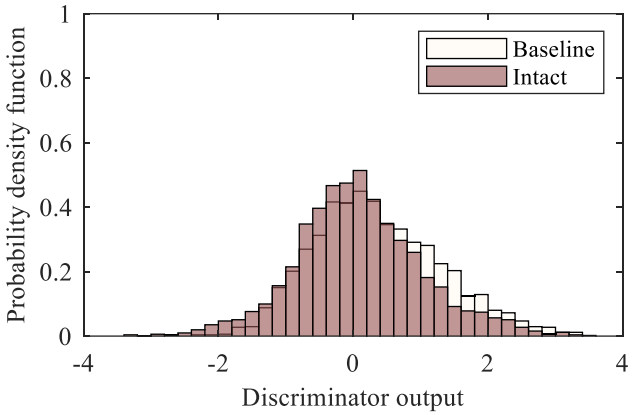

(b)

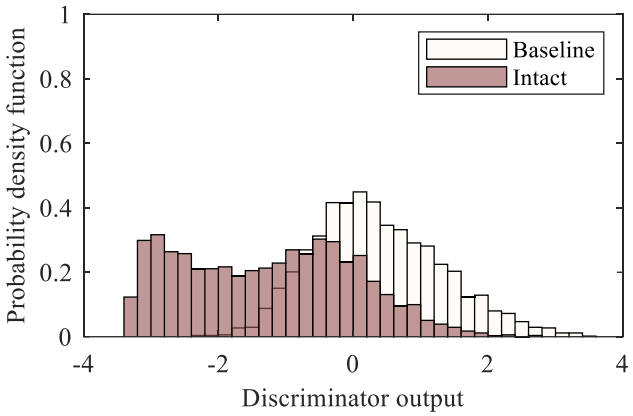

(c)

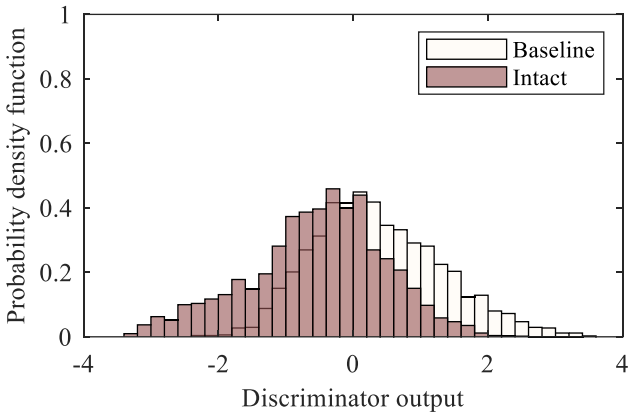

(d)

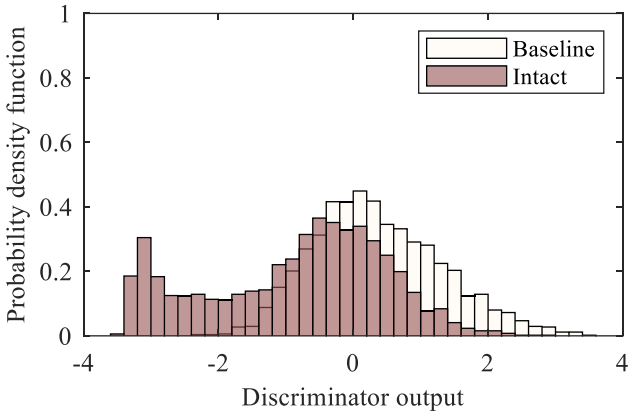

(e)

Figure 6-20. Probability density function of discriminator output for 5 testing sets, in comparison to the baseline condition.

Finally, the JSD values are calculated for each case for damage detection. Comparative studies are also conducted to further demonstrate the effectiveness of the proposed

method, with results shown in **Table 6-7** and **Figure 6-21**. It should be noted that for the AAE and GAN models, JSD values are used for determining the 99% prediction interval and the detecting anomalies. For the AE, LSTM, and RNN, reconstruction error is used as the damage indicator. From **Table 6-7**, the proposed AAE has achieved 95.5% and 97.3% overall detection accuracies in intact and defect samples, which shows excellent robustness. In comparison, the AE, LSTM, and RNN achieved satisfactory results in detecting intact samples but are not effective in detecting defect samples. Those methods are all based on signal reconstruction error, which demonstrates the typical drawback of those methods. As for GAN, the detection results for testing rail segments generally lack reliability. To conclude, the proposed approach features robustness against field testing noises, which has been effectively proved through comparative studies.

Table 6-7. Performance comparison results.

Model	Detection accuracy (%)					Overall performance (%)	
Name	Rail #1	Rail #2	Rail #3	Rail #4	Rail #5	Intact	Defect
AAE	97.0	94.0	100.0	94.0	98.0	95.5	97.3
GAN	34.0	96.0	47.0	27.0	81.0	65.0	51.7
AE	93.0	84.0	58.0	47.0	45.0	88.5	50.0
LSTM	82.0	76.0	3.0	1.0	3.0	79.0	2.3
RNN	97.0	98.0	2.0	3.0	0.0	97.5	1.7

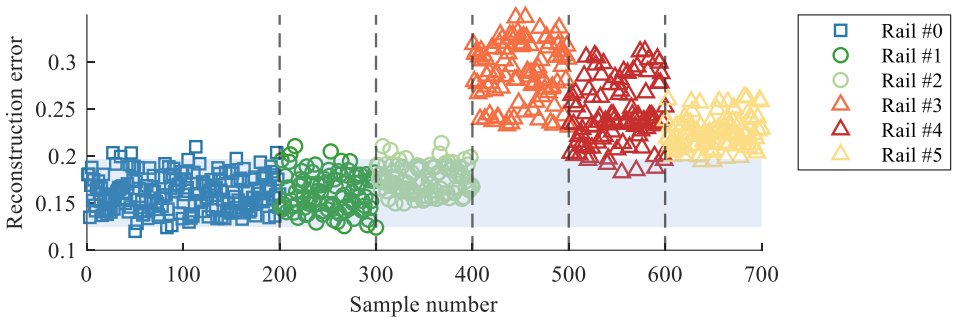

(a) AAE

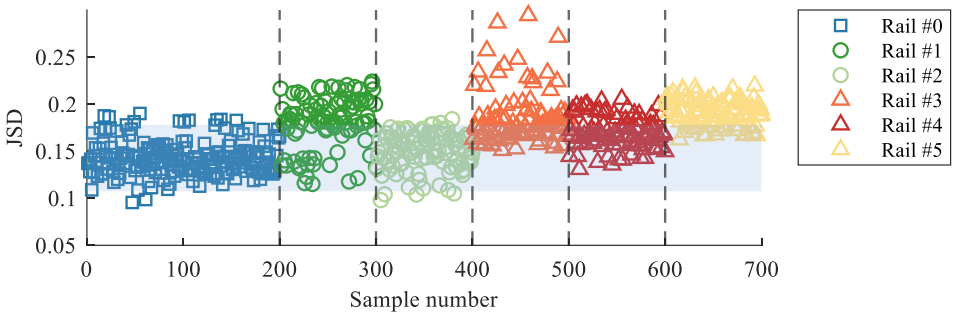

(b) GAN

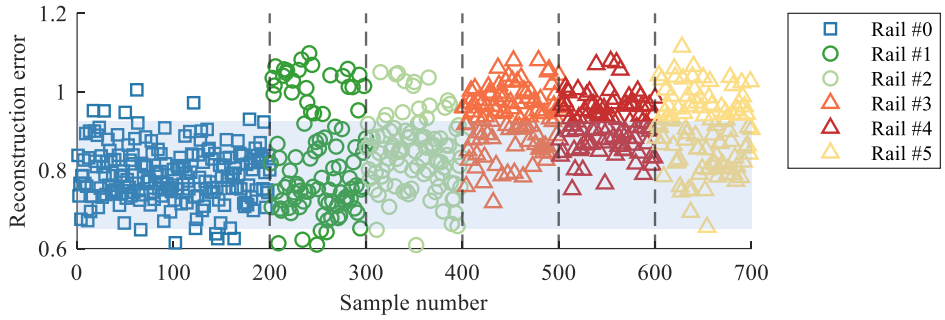

(c) AE

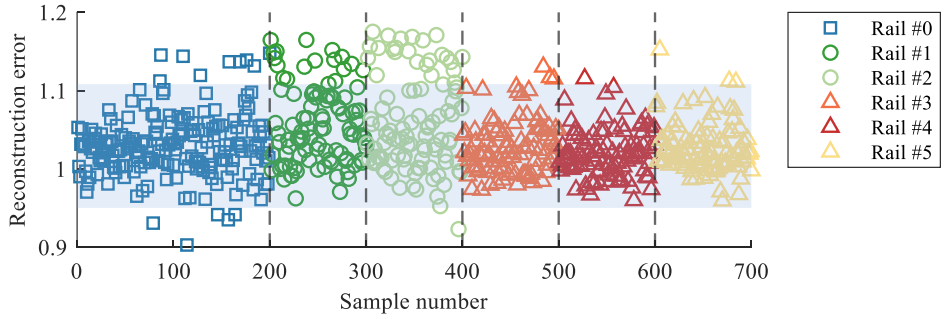

(d) LSTM

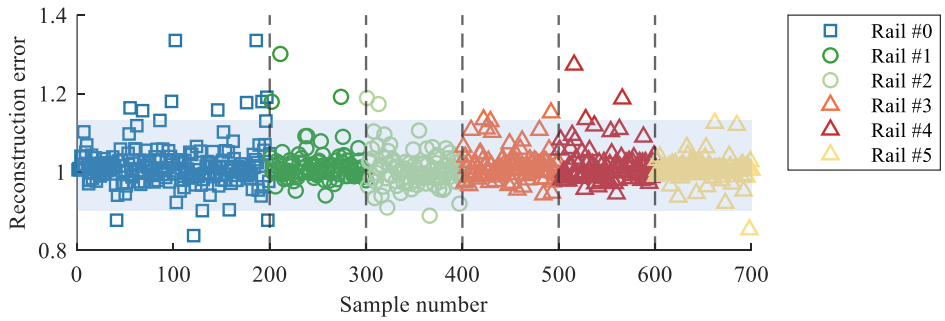

(e) RNN

Figure 6-21. Rail defect detection results (including the baseline Rail #0 and testing rails # 1-5) using different methods. The 99% prediction interval is adopted for each method as the threshold.

6.5. Discussions on scalability

6.5.1. Cost-effectiveness

The proposed method is highly scalable due to its low costs. Specifically, the following aspects are summarized to demonstrate the cost-effectiveness:

(1) The disposable mechanic pencil utilized for ultrasound generation is cost-effective and the operation is rather simple even for non-professionals. This unique feature enables large-scale implementations of the proposed method on railway lines.

(2) The signal processing is completed by AAEs, followed by probabilistic analysis, which generates reliable results. The lightweight AAE models and the sliding window introduced in this method also enhance data processing efficiency without consuming a lot of computational resources.

(3) The proposed method is initially designed as a supplementary approach for railway maintenance, featuring rapid and reliable performance. The PLB operation can be easily performed during inspections routines by any personnel and the AAE-based framework has the potential to be installed on digital devices such as laptops or even smart phones.

While using the PLB approach to generate ultrasound barely costs a dime, the sensors used in this study are also significantly more cost-effective than traditional ultrasonic devices or instruments. PLB signals have been proved to be compatible with most commercial ultrasonic sensors available, even disposable Lead Zirconate Titanate (PZT) disks (De Almeida et al., 2015; Prathuru et al., 2022; K. Wang, Cao, et al., 2020). Developing customized sensors tailored for rail inspections could also further reduce the costs, especially when it comes to large-scale implementations. As for maintenance, the sensors used are protected by durable stainless shields to adapt to harsh environments. They can also be easily checked or replaced during routine inspections.

In future applications, it is feasible to install sensors at critical locations prone to defects. For instance, the field tests introduced in this study were performed on curves where there had been complaints from the passengers about high-pitch noise and abnormal vibration of the car body. Additionally, the portable and electricity-free nature of the PLB method allows for flexible sensor placement.

6.5.2. Computational time

While excellent performance has been achieved, the AAE model-powered damage detection is not demanding on computational resources. The training of an AAE generally takes merely 4 to 5 minutes. And once trained, the proposed method will operate in an inference mode, meaning that only forward propagation of the neural network will be needed for calculating the damage indicators. The AAE can process each signal segment (with the length of 100,000) in less than 1 millisecond, followed by JSD calculation performed by a Python script, which takes even less computational time. The modularity of the proposed AAE framework ensures that it can be implemented on portable devices, from resource-constrained edge devices to high-performance servers. In engineering applications, continuous data streams can be imported to the trained AAE model for processing without noticeable delays.

6.5.3. Robustness against ambient factors

The probabilistic framework based on AAE models is designed to adapt to variations in signal patterns, as it does not rely on physical threshold-based criteria or predetermined defect characteristics. In addition, measures are undertaken to minimize the impact of ambient factors on signal quality. The built-in filter in the acquisition system was deployed and abnormal acoustic emission events were eliminated from the datasets. The data preprocessing steps can mitigate amplitude variations caused by

external disturbances. The sliding window used for splitting datasets can also effectively eliminate the ambient interference to acquired signals. Although the successful detection of various defect conditions in field tests demonstrates the robustness of the method against real-world railway tunnel nose interference, the method has yet to be tested under intense environmental fluctuations. Especially considering that the field test dates were adjacent and that the inside-tunnel ventilation system cannot effectively simulate outdoor environment, the temperature and humidity inside the tunnel remained consistent throughout the testing period (from 1:00 to 3:00 a.m.). It could be possible to conduct long-term experiments to study the impact of ambient effects and track degradation on defect detection results, using long-term monitoring data to train adaptive AAE models.

6.6. Summary

A novel ultrasonic testing method for on-site rail inspection is proposed in this study. Rail damage diagnosis is achieved by simply breaking a pencil lead on the rail under inspection. The rapid and accurate rail damage evaluation is empowered by the AAE model which is highly capable of learning nonlinear representations of PLB-induced ultrasonic signals and revealing slight deviations caused by rail damage in an unsupervised manner. Experimental studies are conducted firstly in the laboratory, followed by on-site tests for further verifications. The main conclusions can be drawn as follows:

1 A innovative ultrasound generation method is proposed by means of PLB. The method has never been proposed to conduct active inspection on railway tracks, featuring rapid and robust nature. Combined with AAE for signal processing, the valuable information lied in PLB-induced ultrasound signals can be fully revealed.

2 The laboratory investigations presented in this study preliminarily prove the feasibility of using AAE. A grid search is conducted to optimize the AAE model performance, which achieves the detection accuracy of 100% on intact and defect samples.

3 Further comparative studies also demonstrate the robustness and effectiveness of the AAE-based damage detection framework. The JSD-based probabilistic analysis clearly show the influence of rail damage on AAE model output. By comparing the AAE model performance with other models, it can be observed that AAE outperforms with effective defect detection rate on both intact and defect samples.

3 The on-site field tests prove the effectiveness of the proposed method. A total of 6 rail segments were selected and measured from an in-service railway line, and the results show that the proposed damage detection method can effectively reveal various types of rail defects. Comparative studies further also prove the robustness of the proposed method, against more complex field environments.

The significance of this study highlights achieving rail damage evaluation in a rapid and robust manner, contributing to a more efficient and sustainable railway system. The training of AAEs is not label-dependent, thus making it suitable for railway applications where defects have yet to occur. The underlying framework proposed in this study is designed to generalize to subtle changes in ultrasonic signals thus has the potential to identify a wide range of defects, not particularly restricted to corrugations and squats.

CHAPTER 7 CONCLUSIONS AND RECOMMENDATIONS

7.1. Conclusions

This thesis presents a comprehensive study on guided wave-based testing approaches of railway tracks, integrating high-performance sensing systems and state-of-the-art signal processing techniques. Traditional ultrasonic inspection routines can hardly meet the constantly expanding scale of the modern railway system. The instrumentations currently deployed, although proved to be effective in detecting various types of railway defects, are not efficient enough for timely reporting potential safety risks. Therefore, through system development, numerical and experimental studies, this study ultimately aims to make significant improvements in traditional railway ultrasound inspection routines, in terms of efficiency, accuracy, and reliability. The major contributions and findings of this thesis are summarized as follows:

1 **A novel hybrid sensing system for railway GWT using optical sensing is first designed, then assembled and installed, finally tested and optimized in laboratory.** Designed for railway online inspection, the hybrid system uses PZT and FBG sensors for generating and detecting UGWs. The exceptional performance of FBGs in EMI resistance, ultrasound sensitivity, and ambient durability is made best use of through a specially designed high-speed

interrogation strategy based on edge filters. The feasibility of the proposed system is comprehensively evaluated in this study, including both sensing performance and cost-effectiveness. A proof-of-concept validation is carried out via FEM tools to fully reveal the UGW propagation characteristics and interactions with railway defects. The results demonstrate that the predominant surface wave propagates on railway interface that are sensitive to geometry inconsistencies, which can be characterized via time-domain wave distortion and amplitude decline. However, for laboratory settings, high-precision ultrasound measurements and effective signal processing techniques are required for detection.

2 **A defect detection and evaluation framework for railway tracks is proposed based on nonlinear regressive models and a probabilistic damage indicator.** The UGW propagating in railway tracks possesses complex time-domain characteristics which makes it difficult to diagnose abnormalities directly from the raw waveforms. This proposed approach utilizes NARX models featuring exceptional fitting performance to process the Hilbert envelope of the UGW signals acquired by an FBG array. A DSF is proposed based on the PDF of the network residuals to predict the possibility of the occurrence of rail damages. The proposed framework is validated through experimental studies, where 3 different types of railway defects are configured to acquire training and testing datasets. The NARX models are optimized through hyperparameter optimization. The results of

defect detection demonstrate excellent accuracies. Further validation is conducted via large-scale testing, achieving the overall accuracy of 98.0%. Through experimental investigations, the robustness and effectiveness of the proposed method are fully verified.

3 **A railway defect identification method using OMP algorithm and a customized IRC dictionary is proposed and validated through numerical and experimental investigations.** The railway crack identification method is developed based on the previously proposed hybrid sensing system using PZT as the actuator and FBGs as receivers. This method integrates the sparse representation of OMP which actively reconstruct the UGW signals using atoms of the specified IRC dictionary. Numerical investigations have first been conducted to verify the effectiveness of the proposed approach. The OMP reconstruction successfully identifies the crack reflective waves which agrees perfectly with the simulation results. Comparative studies further verify the effectiveness of the IRC dictionary. In experimental investigations, various cases are configured, and the results show that the proposed method can accurately predict the crack location with the fitting error rate being less than 5 mm. Further discussions in this study focus on algorithm comparison and computational time, which prove that the proposed method is highly practical for engineering applications.

4 **A railway track rapid diagnosis approach using PLB-induced ultrasound and AAEs is proposed, followed by verifications in both laboratory and field tests.** For railway on-site inspection routines, specialized ultrasound equipment are expensive and generally require professionally trained personnel. High-voltage excitation of UGWs makes it even more inconvenient for offline inspection. In this sense, an ultrasonic testing method innovatively using PLB as the ultrasound actuator is developed. To effectively indicate and visualize the existence of railway defects, a probabilistic damage indicator is developed for health evaluation. To assist defect detection, an AAE-based framework is proposed to process the PLB-induced ultrasonic signals. The AAE hyperparameters are optimized to achieve optimal performance. Comparative studies demonstrate excellent damage detection rates in laboratory tests. The proposed railway track defect detection system is also validated in field tests. The results demonstrate 95.5% overall accuracy on intact rails and 97.3% on defect ones. Further discussions focus on the scalability of the proposed method in massive deployments on railway sites.

To conclude, the above findings have comprehensively addressed the main research gap in modern railway track GWT techniques, from sensing instrumentations to signal processing techniques. Empowered by state-of-the-art machine learning models, robust and efficient railway track damage identification and health evaluation methods are developed.

7.2. Recommendations

This thesis has laid a foundation for further studies but exhibits certain limitations. The following recommendations are given as guidance for future work.

1 To expand the proposed methodologies with high-priority rail head defects. A paramount next step is to adapt and validate the system for the detection of head defects, which are among the most common and critical failure modes in railways. Future work will investigate the optimal installation of FBG sensor arrays on the bottom of the rail head flange to probe this region. A key research question will be to determine how wave propagation patterns and signal characteristics differ between the web and head, as the head's larger mass and geometry will significantly alter guided wave behavior. For high-frequency excitation, the shorter wavelength would result in the predominance of Rayleigh waves in rail head. This analysis will be crucial for adapting the current damage identification algorithms to effectively interpret signals from head defects such as squats, shelling, and transverse fractures.

2 To conduct real-world validation and environmental robustness: a critical next-step development for this study involves transitioning the research from controlled laboratory settings to real-world operational environments. Although field tests were conducted and on-site data acquisition had validated the robustness of the

proposed frameworks, ambient factors were not considered, such as temperature fluctuations and humidity. Those factors are inevitable in field applications. Furthermore, the methods must be validated through long-term testing on full-length rail sections under dynamic loading conditions, such as fatigue cycle tests, to monitor the development of natural cracks rather than simplified artificial defects. Furthermore, the durability of sensor installation methods, particularly the proposed protection shields, must be proven under these demanding conditions to ensure data integrity and long-term system survival. This will prove the system's practicality, reliability, and durability for widespread deployment on active railway networks.

3 To further research on advanced railway defect characterization and enhance the performance of the ML algorithm. Future work will focus on moving beyond simple defect detection to sophisticated characterization. This involves enhancing the current algorithms, particularly the OMP method and IRC dictionary, to not only locate a crack but also accurately predict its dimensions, i.e., the length, depth, and width. A key challenge to address is to improve the algorithm's capability to adaptively learn and interpret the complex, nonlinear wave patterns generated by real-world defects. This also allows us to determine the minimum detectable crack size through more detailed analysis, for evaluating the practical value of the proposed frameworks in preventing rail failures, and ultimately supporting the

development of a scalable, cost-effective, and well-understood monitoring system for the industry.

CHAPTER 8 REFERENCES

Anaissi, A., Zandavi, S. M., Suleiman, B., Naji, M., & Braytee, A. (2023). Multi-objective variational autoencoder: an application for smart infrastructure maintenance. *Applied Intelligence*, *53*(10), 12047–12062.

Arias-Vergara, T., Klumpp, P., Vasquez-Correa, J. C., Nöth, E., Orozco-Arroyave, J. R., & Schuster, M. (2021). Multi-channel spectrograms for speech processing applications using deep learning methods. *Pattern Analysis and Applications*, *24*(2), 423–431.

Artagan, S. S., Bianchini Ciampoli, L., D'Amico, F., Calvi, A., & Tosti, F. (2020). Non-destructive Assessment and Health Monitoring of Railway Infrastructures. In *Surveys in Geophysics* (Vol. 41, Issue 3, pp. 447–483). Springer.

Azim, M. R., & Gül, M. (2019). Damage detection of steel girder railway bridges utilizing operational vibration response. *Structural Control and Health Monitoring*, *26*(11).

Bao, Y., & Li, H. (2021). Machine learning paradigm for structural health monitoring. *Structural Health Monitoring*, *20*(4), 1353–1372.

Bombarda, D., Vitetta, G. M., & Ferrante, G. (2021). Rail diagnostics based on ultrasonic guided waves: An overview. *Applied Sciences (Switzerland)*, *11*(3), 1–

42.

Boppana, T. K., & Bagade, P. (2023). GAN-AE: An unsupervised intrusion detection system for MQTT networks. *Engineering Applications of Artificial Intelligence*, *119*.

Cai, T. T., & Wang, L. (2011). Orthogonal matching pursuit for sparse signal recovery with noise. *IEEE Transactions on Information Theory*, *57*(7), 4680–4688.

Cao, W., Wang, K., Zhou, P., Yang, X., Xu, L., Liu, M., Fromme, P., Pang, B., Chi, R., & Su, Z. (2020). Nonlinear ultrasonic evaluation of disorderedly clustered pitting damage using an in situ sensor network. *Structural Health Monitoring*, *19*(6), 1989–2006.

Cawley, P. (2024). Guided waves in long range nondestructive testing and structural health monitoring: Principles, history of applications and prospects. *NDT and E International*, *142*.

Chang, M., Lu, Z., Huang, Q., & Yang, C. (2022). Parameter estimation for ultrasonic echo signals through improved matching pursuit and flower pollination algorithms. *Measurement: Journal of the International Measurement Confederation*, *194*.

Chang, Y., Zi, Y., Zhao, J., Yang, Z., He, W., & Sun, H. (2017). An adaptive sparse deconvolution method for distinguishing the overlapping echoes of ultrasonic

guided waves for pipeline crack inspection. *Measurement Science and Technology*, *28*(3).

Chen, J., Yuan, S., Qiu, L., Wang, H., & Yang, W. (2018). On-line prognosis of fatigue crack propagation based on Gaussian weight-mixture proposal particle filter. *Ultrasonics*, *82*, 134–144.

Chen, R., Hu, C., Xu, J., Gong, Z., Liu, L., Wang, P., & Chen, X. (2021). Research on guided wave propagation characteristics in turnout rails with variable cross-section. *Journal of Sound and Vibration*, *494*.

Chen, S. X., Zhou, L., & Ni, Y. Q. (2022). Wheel condition assessment of high-speed trains under various operational conditions using semi-supervised adversarial domain adaptation. *Mechanical Systems and Signal Processing*, *170*.

Chen, S. X., Zhou, L., Ni, Y. Q., & Huang, J. Z. (2025). Task similarity guided transfer learning for acoustic emission-based rail crack assessment. *Mechanical Systems and Signal Processing*, *227*.

Chen, S. X., Zhou, L., Ni, Y. Q., & Liu, X. Z. (2021). An acoustic-homologous transfer learning approach for acoustic emission–based rail condition evaluation. *Structural Health Monitoring*, *20*(4), 2161–2181.

Chen, Z., Wang, Q., Yang, K., Yu, T., Yao, J., Liu, Y., Wang, P., & He, Q. (2021). Deep

learning for the detection and recognition of rail defects in ultrasound b-scan images. In *Transportation Research Record* (Vol. 2675, Issue 11, pp. 888–901). SAGE Publications Ltd.

Cheng, L., Cigada, A., Lang, Z., Zappa, E., & Zhu, Y. (2021). An output-only ARX model-based sensor fusion framework on structural dynamic measurements using distributed optical fiber sensors and fiber Bragg grating sensors. *Mechanical Systems and Signal Processing*, *152*.

Chowdhury, P., & Sehitoglu, H. (2016). Mechanisms of fatigue crack growth - A critical digest of theoretical developments. In *Fatigue and Fracture of Engineering Materials and Structures* (Vol. 39, Issue 6, pp. 652–674). Blackwell Publishing Ltd.

Cui, R., Azuara, G., Lanza di Scalea, F., & Barrera, E. (2022). Damage imaging in skin-stringer composite aircraft panel by ultrasonic-guided waves using deep learning with convolutional neural network. *Structural Health Monitoring*, *21*(3), 1123–1138.

Dai, B., Frusque, G., Li, T., Li, Q., & Fink, O. (2023). Smart filter aided domain adversarial neural network for fault diagnosis in noisy industrial scenarios. *Engineering Applications of Artificial Intelligence*, *126*.

Dang, D. Z., Lai, C. C., Ni, Y. Q., Zhao, Q., Su, B., & Zhou, Q. F. (2023). Image Classification-Based Defect Detection of Railway Tracks Using Fiber Bragg Grating Ultrasonic Sensors. *Applied Sciences (Switzerland)*, *13*(1).

Dang, D. Z., Wang, Y. W., & Ni, Y. Q. (2024). Nonlinear autoregression-based non-destructive evaluation approach for railway tracks using an ultrasonic fiber bragg grating array. *Construction and Building Materials*, *411*.

Dang, D. Z., Wang, Y. W., & Ni, Y. Q. (2025). A novel guided wave testing method for identifying rail web cracks using optical fiber Bragg grating sensing and orthogonal matching pursuit. *Measurement: Journal of the International Measurement Confederation*, *243*.

Datta, D., & Lanza di Scalea, F. (2022). High-Speed Inspection of Rails by Passive Ultrasonic Monitoring. *Journal of Nondestructive Evaluation, Diagnostics and Prognostics of Engineering Systems*, *5*(4).

De Almeida, V. A. D., Baptista, F. G., & De Aguiar, P. R. (2015). Piezoelectric transducers assessed by the pencil lead break for impedance-based structural health monitoring. *IEEE Sensors Journal*, *15*(2), 693–702.

De Castro, B. A., Baptista, F. G., Ardila-Rey, J. A., & Ciampa, F. (2022). Baseline-Free Damage Imaging Algorithm Using Spatial Frequency Domain Virtual Time

Reversal. *IEEE Transactions on Industrial Informatics*, *18*(8), 5043–5054.

Lanza di Scalea, F., Zhu, X., Capriotti, M., Liang, A. Y., Mariani, S., & Sternini, S. (2018). Passive extraction of dynamic transfer function from arbitrary ambient excitations: Application to high-speed rail inspection from wheel-generated waves. *Journal of Nondestructive Evaluation, Diagnostics and Prognostics of Engineering Systems*, *1*(1).

Diogo, A. R., Moreira, B., Gouveia, C. A. J., & Tavares, J. M. R. S. (2022). A Review of Signal Processing Techniques for Ultrasonic Guided Wave Testing. *Metals*, *12*(6).

Dirks, B., Enblom, R., Ekberg, A., & Berg, M. (2015). The development of a crack propagation model for railway wheels and rails. *Fatigue and Fracture of Engineering Materials and Structures*, *38*(12), 1478–1491.

Du, F., Wu, S., Xing, S., Xu, C., & Su, Z. (2023). Temperature compensation to guided wave-based monitoring of bolt loosening using an attention-based multi-task network. *Structural Health Monitoring*, *22*(3), 1893–1910.

Dunphy, K., Sadhu, A., & Wang, J. (2022). Multiclass damage detection in concrete structures using a transfer learning-based generative adversarial networks. *Structural Control and Health Monitoring*, *29*(11).

Ebrahimkhanlou, A., Dubuc, B., & Salamone, S. (2019). A generalizable deep learning framework for localizing and characterizing acoustic emission sources in riveted metallic panels. *Mechanical Systems and Signal Processing*, *130*, 248–272.

Fan, G., He, Z., & Li, J. (2023). Structural dynamic response reconstruction using self-attention enhanced generative adversarial networks. *Engineering Structures*, *276*.

Fang, Z., & Tse, P. W. (2019). Demagnetization-based axial magnetized magnetostrictive patch transducers for locating defect in small-diameter pipes using the non-axisymmetric guided wave. *Structural Health Monitoring*, *18*(5–6), 1738–1760.

Flores Cuenca, M. F., Malikov, A. K. ugli, Kim, J., Cho, Y., & Jeong, K. S. (2024). A novel flaw detection approach in carbon steel pipes through ultrasonic guided waves and optimized transformer neural networks. *Journal of Mechanical Science and Technology*, *38*(7), 3253–3263.

Gazafrudi, S. M. M., Younesian, D., & Torabi, M. (2021). A High Accuracy and High Speed Imaging and Measurement System for Rail Corrugation Inspection. *IEEE Transactions on Industrial Electronics*, *68*(9), 8894–8903.

Ge, H., Chua Kim Huat, D., Koh, C. G., Dai, G., & Yu, Y. (2022). Guided wave–based rail flaw detection technologies: state-of-the-art review. In *Structural Health*

Monitoring (Vol. 21, Issue 3, pp. 1287–1308). SAGE Publications Ltd.

Ghafoor, I., Tse, P. W., Munir, N., & Trappey, A. J. C. (2022). Non-contact detection of railhead defects and their classification by using convolutional neural network. *Optik*, *253*.

Ghafoor, I., Tse, P. W., Rostami, J., & Ng, K. M. (2021). Non-contact inspection of railhead via laser-generated rayleigh waves and an enhanced matching pursuit to assist detection of surface and subsurface defects. *Sensors*, *21*(9).

Gong, W., Akbar, M. F., Jawad, G. N., Mohamed, M. F. P., & Wahab, M. N. A. (2022). Nondestructive Testing Technologies for Rail Inspection: A Review. In *Coatings* (Vol. 12, Issue 11). MDPI.

Grassie, S. L. (2005). Rail corrugation: Advances in measurement, understanding and treatment. *Wear*, *258*(7–8), 1224–1234.

Guo, S., Ding, H., Li, Y., Feng, H., Xiong, X., Su, Z., & Feng, W. (2022). A hierarchical deep convolutional regression framework with sensor network fail-safe adaptation for acoustic-emission-based structural health monitoring. *Mechanical Systems and Signal Processing*, *181*.

Guo, W., Yu, Z., Chui, H. C., & Chen, X. (2023). Development of DMPS-EMAT for Long-Distance Monitoring of Broken Rail. *Sensors*, *23*(12).

Han, Q., Ma, Q., Dang, D., & Xu, J. (2023). Modal Parameters Prediction and Damage Detection of Space Grid Structure under Environmental Effects Using Stacked Ensemble Learning. *Structural Control and Health Monitoring*, *2023*.

Han, S. W., Cho, S. H., Jang, G. W., & Park, J. H. (2016). Non-contact inspection of rail surface and internal defects based on electromagnetic ultrasonic transducers. *Journal of Intelligent Material Systems and Structures*, *27*(3), 427–434.

Hao, Q., Shen, Y., Wang, Y., & Liu, J. (2021). An adaptive extraction method for rail crack acoustic emission signal under strong wheel-rail rolling noise of high-speed railway. *Mechanical Systems and Signal Processing*, *154*.

Hashim, K. A., Nor, N. M., Abdullah, S., Aziz, F. F., & Idrus, J. (2021). Determination of Acoustic Emissions Data Characteristics under the Response of Pencil Lead Fracture Procedure. *Journal of Failure Analysis and Prevention*, *21*(6), 2064–2071.

Hei, C., Luo, M., Gong, P., & Song, G. (2020). Quantitative evaluation of bolt connection using a single piezoceramic transducer and ultrasonic coda wave energy with the consideration of the piezoceramic aging effect. *Smart Materials and Structures*, *29*(2).

Hong, J. C., Sun, K. H., & Kim, Y. Y. (2005). The matching pursuit approach based on the modulated Gaussian pulse for efficient guided-wave damage inspection. *Smart*

Materials and Structures, *14*(4), 548–560.

Hong, X., Zhou, J., & He, Y. (2019). Damage detection of anchored region on the messenger cable based on matching pursuit algorithm. *Mechanical Systems and Signal Processing*, *130*, 221–247.

Hu, S., Shi, W., Lu, C., Chen, Y., Chen, G., & Shen, G. (2021). Rapid detection of cracks in the rail foot by ultrasonic B-scan imaging using a shear horizontal guided wave electromagnetic acoustic transducer. *NDT and E International*, *120*.

Huang, C., & Lanza di Scalea, F. (2024). Application of Sparse Synthetic Aperture Focusing Techniques to Ultrasound Imaging in Solids Using a Transducer Wedge. *IEEE Transactions on Ultrasonics, Ferroelectrics, and Frequency Control*, *71*(2), 280–294.

Jamshidi, A., Faghih-Roohi, S., Hajizadeh, S., Núñez, A., Babuska, R., Dollevoet, R., Li, Z., & De Schutter, B. (2017). A Big Data Analysis Approach for Rail Failure Risk Assessment. *Risk Analysis*, *37*(8), 1495–1507.

Jiang, Y., Wang, H., Chen, S., & Tian, G. (2021). Visual quantitative detection of rail surface crack based on laser ultrasonic technology. *Optik*, *237*.

Lederman, G., Chen, S., Garrett, J. H., Kovačević, J., Noh, H. Y., & Bielak, J. (2017). Track monitoring from the dynamic response of a passing train: A sparse approach.

Mechanical Systems and Signal Processing, *90*, 141–153.

Lee, H., Lim, H. J., Skinner, T., Chattopadhyay, A., & Hall, A. (2021). Automated fatigue damage detection and classification technique for composite structures using Lamb waves and deep autoencoder. *Mechanical Systems and Signal Processing*, *163*.

Li, D., Wang, Y., Yan, W. J., & Ren, W. X. (2021). Acoustic emission wave classification for rail crack monitoring based on synchrosqueezed wavelet transform and multi-branch convolutional neural network. *Structural Health Monitoring*, *20*(4), 1563–1582.

Li, W., Shang, Z., Gao, M., Qian, S., Zhang, B., & Zhang, J. (2021). A novel deep autoencoder and hyperparametric adaptive learning for imbalance intelligent fault diagnosis of rotating machinery. *Engineering Applications of Artificial Intelligence*, *102*.

Li, W., Shang, Z., Zhang, J., Gao, M., & Qian, S. (2023). A novel unsupervised anomaly detection method for rotating machinery based on memory augmented temporal convolutional autoencoder. *Engineering Applications of Artificial Intelligence*, *123*.

Li, X., Naqi, A., Maqsood, Z., & Koseki, J. (2022). Verification of 3D AE Source

Location Technique in Triaxial Compression Tests Using Pencil Lead Break Sources on a Cylindrical Metal Specimen. *Applied Sciences (Switzerland)*, *12*(3).

Li, X., Wu, B., Gao, X., Liu, Y., Wang, H., & Liu, X. (2023). Ultrasonic SH guided wave detection of the defects of switch rails with 3D finite element method. *Measurement: Journal of the International Measurement Confederation*, *220*.

Li, Y., Zheng, F., Xiong, Q., & Zhang, W. (2021). A secondary selection-based orthogonal matching pursuit method for rolling element bearing diagnosis. *Measurement: Journal of the International Measurement Confederation*, *176*.

Listou Ellefsen, A., Bjørlykhaug, E., Æsøy, V., Ushakov, S., & Zhang, H. (2019). Remaining useful life predictions for turbofan engine degradation using semi-supervised deep architecture. *Reliability Engineering and System Safety*, *183*, 240–251.

Liu, A., Wang, L., Bornn, L., & Farrar, C. (2019). Robust structural health monitoring under environmental and operational uncertainty with switching state-space autoregressive models. *Structural Health Monitoring*, *18*(2), 435–453.

Liu, W., Tang, Z., Lv, F., & Chen, X. (2021). Multi-feature integration and machine learning for guided wave structural health monitoring: Application to switch rail foot. *Structural Health Monitoring*, *20*(4), 2013–2034.

Liu, Y., Tsang, K. S., Tan Zhi'En, E., Alagu Subramaniam, N., & Pang, J. H. L. (2021). Investigation on material characteristics and fatigue crack behavior of thermite welded rail joint. *Construction and Building Materials*, *276*.

Lomazzi, L., Fabiano, S., Parziale, M., Giglio, M., & Cadini, F. (2023). On the explainability of convolutional neural networks processing ultrasonic guided waves for damage diagnosis. *Mechanical Systems and Signal Processing*, *183*.

Loveday, P. W. (2012). Guided wave inspection and monitoring of railway track. *Journal of Nondestructive Evaluation*, *31*(4), 303–309.

Loveday, P. W., Long, C. S., & Ramatlo, D. A. (2020). Ultrasonic guided wave monitoring of an operational rail track. *Structural Health Monitoring*, *19*(6), 1666–1684.

Loveday, P. W., & Wilcox, P. D. (2010). Guided wave propagation as a measure of axial loads in rails. *Health Monitoring of Structural and Biological Systems 2010*, *7650*, 765023.

Lu, H., Chandran, B., Wu, W., Ninic, J., Gryllias, K., & Chronopoulos, D. (2024). Damage features for structural health monitoring based on ultrasonic Lamb waves: Evaluation criteria, survey of recent work and outlook. In *Measurement: Journal of the International Measurement Confederation* (Vol. 232). Elsevier B.V.

Lu, X. L., Gao, B., Woo, W. L., Xiao, X., Zhan, D., & Huang, C. (2024). Hybrid physics machine learning for ultrasonic field guided 3D generation and reconstruction of rail defects. *NDT and E International*, *146*.

Luleci, F., Catbas, F. N., & Avci, O. (2023). Generative adversarial networks for labeled acceleration data augmentation for structural damage detection. *Journal of Civil Structural Health Monitoring*, *13*(1), 181–198.

Luleci, F., Necati Catbas, F., & Avci, O. (2023). CycleGAN for undamaged-to-damaged domain translation for structural health monitoring and damage detection. *Mechanical Systems and Signal Processing*, *197*.

Luo, Y., Guo, X., Wang, L. K., Zheng, J. L., Liu, J. L., & Liao, F. Y. (2023). Unsupervised structural damage detection based on an improved generative adversarial network and cloud model. *Journal of Low Frequency Noise Vibration and Active Control*, *42*(3), 1501–1518.

Ma, X., Lin, Y., Nie, Z., & Ma, H. (2020). Structural damage identification based on unsupervised feature-extraction via Variational Auto-encoder. *Measurement: Journal of the International Measurement Confederation*, *160*.

Maggipinto, M., Terzi, M., & Susto, G. A. (2022). IntroVAC: Introspective Variational Classifiers for learning interpretable latent subspaces. *Engineering Applications of*

Artificial Intelligence, *109*.

Mahajan, H., & Banerjee, S. (2023). Acoustic emission source localisation for structural health monitoring of rail sections based on a deep learning approach. *Measurement Science and Technology*, *34*(4).

Makhzani, A., Shlens, J., Jaitly, N., Goodfellow, I., & Frey, B. (2015). *Adversarial Autoencoders*. http://arxiv.org/abs/1511.05644

Mao, J., Wang, H., & Spencer, B. F. (2021). Toward data anomaly detection for automated structural health monitoring: Exploiting generative adversarial nets and autoencoders. *Structural Health Monitoring*, *20*(4), 1609–1626.

Mariani, S., & Lanza di Scalea, F. (2018). Predictions of defect detection performance of air-coupled ultrasonic rail inspection system. *Structural Health Monitoring*, *17*(3), 684–705.

Mariani, S., Nguyen, T., Zhu, X., & Lanza di Scalea, F. (2017). Field Test Performance of Noncontact Ultrasonic Rail Inspection System. *Journal of Transportation Engineering, Part A: Systems*, *143*(5).

Masurkar, F., Rostami, J., & Tse, P. (2020). Design of an innovative and self-adaptive-smart algorithm to investigate the structural integrity of a rail track using Rayleigh waves emitted and sensed by a fully non-contact laser transduction system.

Applied Acoustics, *166*.

Miao, H., & Li, F. (2021). Shear horizontal wave transducers for structural health monitoring and nondestructive testing: A review. In *Ultrasonics* (Vol. 114). Elsevier B.V.

Mićić, M., Brajović, L., Lazarević, L., & Popović, Z. (2023). Inspection of RCF rail defects – Review of NDT methods. In *Mechanical Systems and Signal Processing* (Vol. 182). Academic Press.

Mitra, M., & Gopalakrishnan, S. (2016). Guided wave based structural health monitoring: A review. In *Smart Materials and Structures* (Vol. 25, Issue 5). Institute of Physics Publishing.

Mo, Z., Zhang, Z., Miao, Q., & Tsui, K. L. (2025). Extended Invariant Risk Minimization for Machine Fault Diagnosis with Label Noise and Data Shift. *IEEE Transactions on Neural Networks and Learning Systems*.

Mo, Z., Zhang, Z., & Tsui, K. L. (2021). The variational kernel-based 1-D convolutional neural network for machinery fault diagnosis. *IEEE Transactions on Instrumentation and Measurement*, *70*.

Mohanty, S. K., Nayak, P. K., Bera, P. K., & Alhelou, H. H. (2024). An Enhanced Protective Relaying Scheme for TCSC Compensated Line Connecting DFIG-

Based Wind Farm. *IEEE Transactions on Industrial Informatics*, *20*(3), 3425–3435.

Ng, K., Ghafoor, I., & Tse, P. (2022). A novel laser-based duffing oscillator system to identify weak ultrasonic guided wave signals related to rail defects. *Optics and Lasers in Engineering*, *157*.

Pandey, P., Rai, A., & Mitra, M. (2022). Explainable 1-D convolutional neural network for damage detection using Lamb wave. *Mechanical Systems and Signal Processing*, *164*.

Pang, D., Sui, Q., Wang, M., Sai, Y., Sun, R., & Wang, Y. (2018). Acoustic Emission Source Localization System Using Fiber Bragg Grating Sensors and a Barycentric Coordinate-Based Algorithm. *Journal of Sensors*, *2018*.

Pathak, M., Alahakoon, S., Spiryagin, M., & Cole, C. (2019). Rail foot flaw detection based on a laser induced ultrasonic guided wave method. *Measurement: Journal of the International Measurement Confederation*, *148*.

Pei, L., Sun, Z., Xiao, L., Li, W., Sun, J., & Zhang, H. (2021). Virtual generation of pavement crack images based on improved deep convolutional generative adversarial network. *Engineering Applications of Artificial Intelligence*, *104*.

Petcher, P. A., Potter, M. D. G., & Dixon, S. (2014). A new electromagnetic acoustic

transducer (EMAT) design for operation on rail. *NDT and E International*, *65*, 1–7.

Pollastro, A., Testa, G., Bilotta, A., & Prevete, R. (2023). Semi-Supervised Detection of Structural Damage Using Variational Autoencoder and a One-Class Support Vector Machine. *IEEE Access*, *11*, 67098–67112.

Prathuru, A., Faisal, N., Steel, J., & Jihan, S. (2022). Application of Pencil Lead Break (PLB) Point Source in the Detection of Interfacial Defects in Adhesive Bonds. *Journal of Nondestructive Evaluation*, *41*(4).

Rai, A., & Upadhyay, S. H. (2017). The use of MD-CUMSUM and NARX neural network for anticipating the remaining useful life of bearings. *Measurement: Journal of the International Measurement Confederation*, *111*, 397–410.

Ramatlo, D. A., Long, C. S., Loveday, P. W., & Wilke, D. N. (2020). A modelling framework for simulation of ultrasonic guided wave-based inspection of welded rail tracks. *Ultrasonics*, *108*.

Ramatlo, D. A., Long, C. S., Loveday, P. W., & Wilke, D. N. (2022). Physics-based modelling and simulation of reverberating reflections in ultrasonic guided wave inspections applied to welded rail tracks. *Journal of Sound and Vibration*, *530*.

Ramatlo, D. A., Wilke, D. N., & Loveday, P. W. (2018). Development of an optimal

piezoelectric transducer to excite guided waves in a rail web. *NDT and E International*, *95*, 72–81.

Rautela, M., Senthilnath, J., Moll, J., & Gopalakrishnan, S. (2021). Combined two-level damage identification strategy using ultrasonic guided waves and physical knowledge assisted machine learning. *Ultrasonics*, *115*.

Rizzo, P., Cammarata, M., Bartoli, I., Lanza di Scalea, F., Salamone, S., Coccia, S., & Phillips, R. (2010). Ultrasonic guided waves-based monitoring of rail head: Laboratory and field tests. *Advances in Civil Engineering*, *2010*.

Rokach, L., Maimon, O., & Shmueli, E. (2023). Machine Learning for Data Science Handbook: Data Mining and Knowledge Discovery Handbook, Third Edition. In *Machine Learning for Data Science Handbook: Data Mining and Knowledge Discovery Handbook, Third Edition*. Springer International Publishing.

Rostami, J., Tse, P. W. T., & Fang, Z. (2017). Sparse and dispersion-based matching pursuit for minimizing the dispersion effect occurring when using guidedwave for pipe inspection. *Materials*, *10*(6).

Rostami, J., Tse, P. W., & Yuan, M. (2020). Detection of broken wires in elevator wire ropes with ultrasonic guided waves and tone-burst wavelet. *Structural Health Monitoring*, *19*(2), 481–494.

Sai, Y., Jiang, M., Sui, Q., Lu, S., & Jia, L. (2016). Multi-source acoustic emission localization technology research based on FBG sensing network and time reversal focusing imaging. *Optik*, *127*(1), 493–498.

Sai, Y., Zhao, X., Wang, L., & Hou, D. (2020). Impact Localization of CFRP Structure Based on FBG Sensor Network. *Photonic Sensors*, *10*(1), 88–96.

Saito, T., & Beck, J. L. (2010). Bayesian model selection for ARX models and its application to structural health monitoring. *Earthquake Engineering and Structural Dynamics*, *39*(15), 1737–1759.

Sajedi, S., & Liang, X. (2022). Deep generative Bayesian optimization for sensor placement in structural health monitoring. *Computer-Aided Civil and Infrastructure Engineering*, *37*(9), 1109–1127.

Sandström, J., & Ekberg, A. (2009). Predicting crack growth and risks of rail breaks due to wheel flat impacts in heavy haul operations. *Proceedings of the Institution of Mechanical Engineers, Part F: Journal of Rail and Rapid Transit*, *223*(2), 153–161.

Sause, M. G. R. (2011). INVESTIGATION OF PENCIL-LEAD BREAKS AS ACOUSTIC EMISSION SOURCES. In *J. Acoustic Emission* (Vol. 29). https://www.ndt.net/?id=14487

Sawant, S., Banerjee, S., & Tallur, S. (2021). Performance evaluation of compressive sensing based lost data recovery using OMP for damage index estimation in ultrasonic SHM. *Ultrasonics*, *115*.

Schmidt, M., Baumert, M., Porta, A., Malberg, H., & Zaunseder, S. (2014). Two-dimensional warping for one-dimensional signals - Conceptual framework and application to ECG processing. *IEEE Transactions on Signal Processing*, *62*(21), 5577–5588.

Setshedi, I. I., Wilke, D. N., & Loveday, P. W. (2024). Feature detection in guided wave ultrasound measurements using simulated spectrograms and generative machine learning. *NDT and E International*, *143*.

Sha, G., Xu, H., Radzieński, M., Cao, M., Ostachowicz, W., & Su, Z. (2021). Guided wavefield curvature imaging of invisible damage in composite structures. *Mechanical Systems and Signal Processing*, *150*.

Shi, H., Zhuang, L., Xu, X., Yu, Z., & Zhu, L. (2019). An ultrasonic guided wave mode selection and excitation method in rail defect detection. *Applied Sciences (Switzerland)*, *9*(6).

Shim, S., Kim, J., Lee, S. W., & Cho, G. C. (2022). Road damage detection using super-resolution and semi-supervised learning with generative adversarial network.

Automation in Construction, *135*.

Silva, M. F., Santos, A., Santos, R., Figueiredo, E., & Costa, J. C. W. A. (2021). Damage-sensitive feature extraction with stacked autoencoders for unsupervised damage detection. *Structural Control and Health Monitoring*, *28*(5).

Song, S., Zhang, X., Chang, Y., & Shen, Y. (2023). An Improved Structural Health Monitoring Method Utilizing Sparse Representation for Acoustic Emission Signals in Rails. *IEEE Transactions on Instrumentation and Measurement*, *72*.

Song, S., Zhang, X., Hao, Q., Wang, Y., Feng, N., & Shen, Y. (2022). An improved reconstruction method based on auto-adjustable step size sparsity adaptive matching pursuit and adaptive modular dictionary update for acoustic emission signals of rails. *Measurement: Journal of the International Measurement Confederation*, *189*.

Spada, A., Capriotti, M., & Lanza di Scalea, F. (2022). Global–local model for three-dimensional guided wave scattering with application to rail flaw detection. *Structural Health Monitoring*, *21*(2), 370–386.

Su, C., Jiang, M., Liang, J., Tian, A., Sun, L., Zhang, L., Zhang, F., & Sui, Q. (2019). Damage Identification in Composites Based on Hilbert Energy Spectrum and Lamb Wave Tomography Algorithm. *IEEE Sensors Journal*, *19*(23), 11562–11572.

Su, Z., Zhou, C., Hong, M., Cheng, L., Wang, Q., & Qing, X. (2014). Acousto-ultrasonics-based fatigue damage characterization: Linear versus nonlinear signal features. *Mechanical Systems and Signal Processing*, *45*(1), 225–239.

Sun, H., Feng, Q., Li, J., Zheng, F., Peng, L., Li, S., Huang, S., & Xibei, Y. (2024). Rail Web Buried Defect Location and Quantification Methods in Hybrid High-Order Guided Wave Detection. *IEEE Transactions on Instrumentation and Measurement*, *73*, 1–12.

Sun, X., Guo, C., Yuan, L., Kong, Q., & Ni, Y. (2022). Diffuse Ultrasonic Wave-Based Damage Detection of Railway Tracks Using PZT/FBG Hybrid Sensing System. *Sensors*, *22*(7).

Suwansin, W., & Phasukkit, P. (2021). Deep learning-based acoustic emission scheme for nondestructive localization of cracks in train rails under a load. *Sensors (Switzerland)*, *21*(1), 1–19.

Tang, B., Wang, Y., Gong, R., & Zhou, F. (2024). Sparse reconstruction of ultrasonic guided wave signals of fluid-filled pipes by multistrategy hybrid DBO-OMP using dispersive Hanning-windowed chirplet model. *Measurement: Journal of the International Measurement Confederation*, *231*.

Tang, Z. F., Sui, X. D., Duan, Y. F., Zhang, P. fei, & Yun, C. B. (2021). Guided wave-

based cable damage detection using wave energy transmission and reflection. *Structural Control and Health Monitoring*, *28*(5).

Tang, Z., Liu, W., Yan, R., Zhang, P., Lv, F., & Chen, X. (2021). Application of compressed sensing in the guided wave structural health monitoring of switch rails. *Measurement Science and Technology*, *32*(12).

Tian, Z., Yu, L., Sun, X., & Lin, B. (2019). Damage localization with fiber Bragg grating Lamb wave sensing through adaptive phased array imaging. *Structural Health Monitoring*, *18*(1), 334–344.

Tse, P. W., & Wang, X. (2013). Characterization of pipeline defect in guided-waves based inspection through matching pursuit with the optimized dictionary. *NDT and E International*, *54*, 171–182.

Umar, S., Vafaei, M., & C. Alih, S. (2021). Sensor clustering-based approach for structural damage identification under ambient vibration. *Automation in Construction*, *121*.

Wang, H. P., Gong, X. S., Wang, X. Z., Feng, S. Y., Yang, T. L., & Guo, Y. X. (2022). Discrete curvature-based shape configuration of composite pipes for local buckling detection based on fiber Bragg grating sensors. *Measurement: Journal of the International Measurement Confederation*, *188*.

Wang, H. P., Ni, Y. Q., Dai, J. G., & Yuan, M. D. (2019). Interfacial debonding detection of strengthened steel structures by using smart CFRP-FBG composites. *Smart Materials and Structures*, *28*(11).

Wang, J., Kwon, S., & Shim, B. (2012). Generalized orthogonal matching pursuit. *IEEE Transactions on Signal Processing*, *60*(12), 6202–6216.

Wang, J., Liu, X. Z., & Ni, Y. Q. (2018). A Bayesian Probabilistic Approach for Acoustic Emission-Based Rail Condition Assessment. *Computer-Aided Civil and Infrastructure Engineering*, *33*(1), 21–34.

Wang, K., Cao, W., Xu, L., Yang, X., Su, Z., Zhang, X., & Chen, L. (2020). Diffuse ultrasonic wave-based structural health monitoring for railway turnouts. *Ultrasonics*, *101*.

Wang, K., Hao, Q., Zhang, X., Tang, Z., Wang, Y., & Shen, Y. (2020). Blind source extraction of acoustic emission signals for rail cracks based on ensemble empirical mode decomposition and constrained independent component analysis. *Measurement: Journal of the International Measurement Confederation*, *157*.

Wang, K., Zhang, X., Song, S., Wang, Y., Shen, Y., & Wilcox, P. D. (2022). Rail Steel Health Analysis Based on a Novel Genetic Density-based Clustering Technique and Manifold Representation of Acoustic Emission Signals. *Applied Artificial*

Intelligence, *36*(1).

Wang, T., Zhang, Z., Yang, F., & Tsui, K. L. (2022). Automatic Rail Component Detection Based on AttnConv-Net. *IEEE Sensors Journal*, *22*(3), 2379–2388.

Wang, X., Jiang, H., Liu, Y., Liu, S., & Yang, Q. (2023). A dynamic spectrum loss generative adversarial network for intelligent fault diagnosis with imbalanced data. *Engineering Applications of Artificial Intelligence*, *126*.

Wang, X., Li, J., Wang, D., Huang, X., Liang, L., Tang, Z., Fan, Z., & Liu, Y. (2022). Sparse ultrasonic guided wave imaging with compressive sensing and deep learning. *Mechanical Systems and Signal Processing*, *178*.

Wang, X., Liu, X., & Bian, Z. (2022). A machine learning based methodology for broken rail prediction on freight railroads: A case study in the United States. *Construction and Building Materials*, *346*.

Wang, X., Tse, P. W., Mechefske, C. K., & Hua, M. (2010). Experimental investigation of reflection in guided wave-based inspection for the characterization of pipeline defects. *NDT and E International*, *43*(4), 365–374.

Wang, Y. W., & Ni, Y. Q. (2020). Bayesian dynamic forecasting of structural strain response using structural health monitoring data. *Structural Control and Health Monitoring*, *27*(8).

Wang, Z., Huang, S., Shen, G., Wang, S., & Zhao, W. (2022). High resolution tomography of pipeline using multi-helical Lamb wave based on compressed sensing. *Construction and Building Materials*, *317*.

Wee, J., Hackney, D., Bradford, P., & Peters, K. (2017). Bi-directional ultrasonic wave coupling to FBGs in continuously bonded optical fiber sensing. *Applied Optics*, *56*(25), 7262.

Wu, B., Huang, Y., Chen, X., Krishnaswamy, S., & Li, H. (2017). Guided-wave signal processing by the sparse Bayesian learning approach employing Gabor pulse model. *Structural Health Monitoring*, *16*(3), 347–362.

Wu, Q., & Okabe, Y. (2012). High-sensitivity ultrasonic phase-shifted fiber Bragg grating balanced sensing system. *Optical Express*, *20*(27), 28353–28362.

Wu, Q., Wang, R., Yu, F., & Okabe, Y. (2019). Application of an optical fiber sensor for nonlinear ultrasonic evaluation of fatigue crack. *IEEE Sensors Journal*, *19*(13), 4992–4999.

Wu, Y., & Yang, N. (2023). Study of rail damage diagnosis and localization method based on intelligent wireless acoustic sensor network. *Measurement: Journal of the International Measurement Confederation*, *217*.

Xie, Q., Tao, G., He, B., & Wen, Z. (2022). Rail corrugation detection using one-

dimensional convolution neural network and data-driven method. *Measurement: Journal of the International Measurement Confederation*, *200*.

Xing, B., Yu, Z., Xu, X., Zhu, L., & Shi, H. (2019). Research on a rail defect location method based on a single mode extraction algorithm. *Applied Sciences (Switzerland)*, *9*(6).

Xing, B., Yu, Z., Xu, X., Zhu, L., & Shi, H. (2020). Mode Selection Model for Rail Crack Detection Based on Ultrasonic Guided Waves. *Shock and Vibration*, *2020*.

Xiong, L., Jing, G., Wang, J., Liu, X., & Zhang, Y. (2023). Detection of Rail Defects Using NDT Methods. In *Sensors* (Vol. 23, Issue 10). MDPI.

Xu, J., Dang, D., Ma, Q., Liu, X., & Han, Q. (2022). A novel and robust data anomaly detection framework using LAL-AdaBoost for structural health monitoring. *Journal of Civil Structural Health Monitoring*, *12*(2), 305–321.

Xue, Z., Xu, Y., Hu, M., & Li, S. (2023). Systematic review: Ultrasonic technology for detecting rail defects. In *Construction and Building Materials* (Vol. 368). Elsevier Ltd.

Yan, L., Elgamal, A., & Cottrell, G. W. (2013). Substructure Vibration NARX Neural Network Approach for Statistical Damage Inference. *Journal of Engineering Mechanics*, *139*(6), 737–747.

Yang, H., Liu, J., Mei, G., Yang, D., Deng, X., & Duan, C. (2023). Research on real-time detection method of rail corrugation based on improved ShuffleNet V2. *Engineering Applications of Artificial Intelligence*, *126*.

Yang, J. H., Kong, Q. Z., Liu, H. J., & Peng, H. Y. (2021). Efficient Bayesian model class selection of vector autoregressive models for system identification. *Structural Control and Health Monitoring*, *28*(9).

Yang, K., Kim, S., & Harley, J. B. (2023). Guidelines for effective unsupervised guided wave compression and denoising in long-term guided wave structural health monitoring. *Structural Health Monitoring*, *22*(4), 2516–2530.

Yang, X., Wang, K., Zhou, P., Xu, L., & Su, Z. (2022). Imaging damage in plate waveguides using frequency-domain multiple signal classification (F-MUSIC). *Ultrasonics*, *119*.

Yang, Y., Wang, P., Jia, Y., Jing, L., Shi, Y., Sheng, H., Jiang, Y., Liu, R., Xu, Y., & Li, X. (2024). Rail fracture monitoring based on ultrasonic-guided wave technology with multivariate coded excitation. *Ultrasonics*, *136*.

Yang, Z., Yang, H., Tian, T., Deng, D., Hu, M., Ma, J., Gao, D., Zhang, J., Ma, S., Yang, L., Xu, H., & Wu, Z. (2023). A review in guided-ultrasonic-wave-based structural health monitoring: From fundamental theory to machine learning techniques. In

Ultrasonics (Vol. 133). Elsevier B.V.

Yao, X., Vien, B. S., Rajic, N., Rosalie, C., Rose, L. R. F., Davies, C., & Chiu, W. K. (2023). Modal Decomposition of Acoustic Emissions from Pencil-Lead Breaks in an Isotropic Thin Plate. *Sensors*, *23*(4).

Yu, C., Liu, Y., Cao, Y., Sun, Y., Su, S., Yang, W., & Wang, W. (2024). Improved YOLOv8 for B-scan image flaw detection of the heavy-haul railway. *Measurement Science and Technology*, *35*(7).

Yuan, Z., Zhu, S., Chang, C., Yuan, X., Zhang, Q., & Zhai, W. (2021). An unsupervised method based on convolutional variational auto-encoder and anomaly detection algorithms for light rail squat localization. *Construction and Building Materials*, *313*.

Yun, H., Rayhana, R., Pant, S., Genest, M., & Liu, Z. (2021). Nonlinear ultrasonic testing and data analytics for damage characterization: A review. *Measurement: Journal of the International Measurement Confederation*, *186*.

Zang, X., Xu, Z. D., Lu, H., Zhu, C., & Zhang, Z. (2023). Ultrasonic guided wave techniques and applications in pipeline defect detection: A review. In *International Journal of Pressure Vessels and Piping* (Vol. 206). Elsevier Ltd.

Zarembski, A. M., Einbinder, D., & Attoh-Okine, N. (2016). Using multiple adaptive

regression to address the impact of track geometry on development of rail defects. *Construction and Building Materials*, *127*, 546–555.

Zemouri, R., Ibrahim, R., & Tahan, A. (2023). Hydrogenerator early fault detection: Sparse Dictionary Learning jointly with the Variational Autoencoder. *Engineering Applications of Artificial Intelligence*, *120*.

Zhang, P., Li, S., Núñez, A., & Li, Z. (2021). Multimodal dispersive waves in a free rail: Numerical modeling and experimental investigation. *Mechanical Systems and Signal Processing*, *150*.

Zhang, X., Sun, T., Wang, Y., Wang, K., & Shen, Y. (2020). A parameter optimized variational mode decomposition method for rail crack detection based on acoustic emission technique. *Nondestructive Testing and Evaluation*, 1–29.

Zhang, X., Wang, K., Wang, Y., Shen, Y., & Hu, H. (2020). Rail crack detection using acoustic emission technique by joint optimization noise clustering and time window feature detection. *Applied Acoustics*, *160*.

Zhang, Y., Dang, D. Z., Wang, Y. W., & Ni, Y. Q. (2024). Damage identification for railway tracks using ultrasound guided wave and hybrid probabilistic deep learning. *Construction and Building Materials*, *418*.

Zhang, Z., Pan, H., Wang, X., & Lin, Z. (2022). Deep Learning Empowered Structural

Health Monitoring and Damage Diagnostics for Structures with Weldment via Decoding Ultrasonic Guided Wave. *Sensors*, *22*(14).

Zhong, J., Huyan, J., Zhang, W., Cheng, H., Zhang, J., Tong, Z., Jiang, X., & Huang, B. (2023). A deeper generative adversarial network for grooved cement concrete pavement crack detection. *Engineering Applications of Artificial Intelligence*, *119*.

Zhou, C., Zhang, C., Su, Z., Yue, X., Xiang, J., & Liu, G. (2017). Health monitoring of rail structures using guided waves and three-dimensional diagnostic imaging. *Structural Control and Health Monitoring*, *24*(9).

Zhou, Y., Shu, X., Bao, T., Li, Y., & Zhang, K. (2023). Dam safety assessment through data-level anomaly detection and information fusion. *Structural Health Monitoring*, *22*(3), 2002–2021.